Published in Journals: Applied Sciences, Energies,
Geosciences, Minerals and Water

Topic Reprint

Porous Flow of Energy & CO2 Transformation and Storage in Deep Formations

Edited by
Jianjun Liu, Yuewu Liu, Zhengming Yang,
Yiqiang Li, Fuquan Song, Rui Song and Yun Yang

mdpi.com/topics

MDPI

Porous Flow of Energy & CO_2 Transformation and Storage in Deep Formations

Porous Flow of Energy & CO_2 Transformation and Storage in Deep Formations

Editors

Jianjun Liu
Yuewu Liu
Zhengming Yang
Yiqiang Li
Fuquan Song
Rui Song
Yun Yang

MDPI

Basel • Beijing • Wuhan • Barcelona • Belgrade • Novi Sad • Cluj • Manchester

Editors

Jianjun Liu Chinese Academy of Sciences Wuhan China	Yuewu Liu Chinese Academy of Sciences Beijing China	Zhengming Yang Chinese Academy of Sciences Beijing China
Yiqiang Li China University of Petroleum Beijing China	Fuquan Song Zhejiang Ocean University Zhoushan China	Rui Song Chinese Academy of Sciences Wuhan China
Yun Yang University of Calgary Calgary Canada		

Editorial Office
MDPI
St. Alban-Anlage 66
4052 Basel, Switzerland

This is a reprint of articles from the Topic published online in the open access journals *Applied Sciences* (ISSN 2076-3417), *Energies* (ISSN 1996-1073), *Geosciences* (ISSN 2076-3263), *Minerals* (ISSN 2075-163X), and *Water* (ISSN 2073-4441) (available at: https://www.mdpi.com/topics/PFECO2).

For citation purposes, cite each article independently as indicated on the article page online and as indicated below:

Lastname, A.A.; Lastname, B.B. Article Title. *Journal Name* **Year**, *Volume Number*, Page Range.

ISBN 978-3-7258-1383-4 (Hbk)
ISBN 978-3-7258-1384-1 (PDF)
doi.org/10.3390/books978-3-7258-1384-1

Contents

energies

MDPI

Editorial

Porous Flow of Energy and CO_2 Transformation and Storage in Deep Formations: An Overview

Rui Song [1,2,*] **and Jianjun Liu** [1,2]

[1] State Key Laboratory of Geomechanics and Geotechnical Engineering, Institute of Rock and Soil Mechanics, Chinese Academy of Sciences, Wuhan 430071, China; jjliu@whrsm.ac.cn
[2] University of Chinese Academy of Sciences, Beijing 100049, China
* Correspondence: rsong@whrsm.ac.cn

The transformation and storage of energy and carbon dioxide in deep reservoirs include underground coal gasification, the underground storage of oil and gas, the underground storage of hydrogen, underground compressed air energy storage, the geological utilization and storage of carbon dioxide, etc., which are related to the realization of low-carbon development, green development, and sustainable development. Fluid mechanics in porous media with a consideration for multiphysics coupling processes is one of the key disciplines supporting the above-mentioned large-scale projects. In order to strengthen the deep integration of seepage mechanics theory and engineering, as well as promote the development of emerging interdisciplinary subjects, we launched a call for papers with the support of relevant academic journals. A total of ten papers related to energy or CO_2 transformation and storage in deep formations were accepted and published in this Special Issue.

As a promising way to enhance oil recovery and carbon sequestration, the multiphase flow mechanism of CO_2–formation water has attracted some scholarly interest. Li et al. [1] studied the CO_2 miscible flooding process in a two-dimensional double-layered heterogeneous visualization model and found that the gas absorption capacity of the reservoir, the gravitational differentiation, and the miscible mass transfer were key factors affecting the migration of the oil–gas interface and distribution of the miscible zone. Song et al. [2] also investigated the CO_2–oil two-phase flow in pore-scale two-dimensional models using the phase field method and analyzed the effects of the capillary number, viscosity ratio, wettability, density, gravity, interfacial tension, and absolute permeability on the two-phase fluid flow characteristics. Qu et al. [3] determined the variations in rock microstructure, minerals, and crude oil properties (e.g., components, viscosity) in the CO_2 Huff-n-Puff in a low-permeability reservoir, and Tang et al. [4] tested the CO_2–brine relative permeability in the sandstone of Ordos basin. As can be seen, the pore-scale fluid transport mechanism was emphasized by many scholars. However, most studies on this topic focused on the immiscible flow of CO_2 liquids, neglecting the miscible gas-flooding mechanism which contributed significantly to enhancing oil recovery. The mathematical and numerical modeling of complex interactions between CO_2–liquids–grains remain substantial challenges for scholars, e.g., a dynamic miscible gas-flooding mechanism with a reaction between CO_2 with grains, etc.

Scientific efforts have also been devoted to the development of low-carbon energy, e.g., natural gas hydrate and coalbed methane. Song et al. [5] studied the hydrate decomposition process in porous sediments by means of numerical modeling using computational fluids dynamics (CFD) codes, including fluid heat and mass transfer, multiphase flow mechanics, and reaction kinetics with phase change. The effects of the gas saturation, outlet pressure, temperature, absolute permeability, and geo-stress on the decomposition of natural gas hydrate were studied. Wang et al. [6] determined the mineral composition and parametric characteristics of the microstructure of coal in the Ordos basin, as well as its relationship

Citation: Song, R.; Liu, J. Porous Flow of Energy and CO_2 Transformation and Storage in Deep Formations: An Overview. *Energies* **2024**, *17*, 2597. https://doi.org/10.3390/en17112597

Received: 17 May 2024
Accepted: 20 May 2024
Published: 28 May 2024

with the adsorption capacity. However, the porous flow mechanism considering phase change with a reaction in the complex and disordered microstructure of rock remained difficult to track using experiments or numerical modeling [7], which requires further scientific efforts in the future.

The mechanical response of rock during fluid flows in the pores was also emphasized by scholars focusing on underground energy and CO_2 transformation and storage. Zheng et al. [8] tested the mechanical properties and failure characteristics of layered rock using uniaxial compression tests. Song et al. [9] proposed a scheme for calculating the critical differential pressure of sand production coupled with laboratory tests and inversed analysis with well logging data and numerical simulations, which were validated using the engineering benchmark data. The effects of moisture contents and the cycling times of gas injection and withdrawal on the critical differential pressure were predicted. Tan et al. [10] studied the mechanical (deformation, damage, or failure) and acoustic responses under cyclic loading–unloading processes in the high-rate injection and production of underground gas storage. They found that mixed tensile–shear cracks are continuously generated in low-permeability sandstone during the cyclic loading process, and the shear cracks are more obviously developed. Wang et al. [11] studied the effects of grain size and layer thickness on the physical and mechanical properties of 3D-printed rock analogs, which provided references for preparing samples with more controllable properties and printing schemes for laboratory tests. Although plenty of scientific efforts were devoted to the manufacturing of rock or rock-like samples, the parallel tests on the samples with the same pore structure and mineral grains as the natural rock samples were still challenging [12], which requires a deep understanding in cementation and diagenesis processes.

The papers published in this Special Issue cover some important aspects of energy and CO_2 transformation and storage in deep formations. We believe that the presented studies will contribute to the development of theoretical, experimental, and numerical modeling methods, as well as providing guidance for engineering applications in this area.

Funding: This research received no external funding.

Acknowledgments: The Guest Editors would like to thank the reviewers for their work, which helped the authors improve their manuscripts.

Conflicts of Interest: The authors declare no conflicts of interest.

References

1. Li, W.; Yu, H.; Yang, Z.; Li, J.; Chen, X.; Ma, L. Experimental Study on the Sweep Law of CO_2 Miscible Flooding in Heterogeneous Reservoir in Jilin. *Energies* **2022**, *15*, 5755. [CrossRef]
2. Song, R.; Tang, Y.; Wang, Y.; Xie, R.; Liu, J. Pore-Scale Numerical Simulation of CO_2–Oil Two-Phase Flow: A Multiple-Parameter Analysis Based on Phase-Field Method. *Energies* **2023**, *16*, 82. [CrossRef]
3. Qu, G.; Tian, X.; Liu, Y.; Li, B.; Li, X. Effects of Changes in Physical Properties of Porous Media and Fluid under Supercritical CO_2 Huff-n-Puff in Low-Permeability Reservoir. *Energies* **2023**, *16*, 6813. [CrossRef]
4. Tang, L.; Ding, G.; Song, S.; Wang, H.; Xie, W.; Zhou, Y.; Song, Z.; Xie, C.; Song, H. Effect of Confining Pressure on CO_2-Brine Relative Permeability Characteristics of Sandstone in Ordos Basin. *Water* **2023**, *15*, 4235. [CrossRef]
5. Song, R.; Duan, Y.; Liu, J.; Song, Y. Numerical Modeling on Dissociation and Transportation of Natural Gas Hydrate Considering the Effects of the Geo-Stress. *Energies* **2022**, *15*, 9311. [CrossRef]
6. Wang, T.; Tian, F.; Deng, Z.; Hu, H. The Characteristic Development of Micropores in Deep Coal and Its Relationship with Adsorption Capacity on the Eastern Margin of the Ordos Basin, China. *Minerals* **2023**, *13*, 302. [CrossRef]
7. Song, R.; Liu, J.; Yang, C.; Sun, S. Study on the multiphase heat and mass transfer mechanism in the dissociation of methane hydrate in reconstructed real-shape porous sediments. *Energy* **2022**, *254*, 124421. [CrossRef]
8. Zheng, Y.; Zhang, T.; Yang, H.; Wang, W.; Niu, Q.; Wei, H. An Experimental Investigation on Mechanical Properties and Failure Characteristics of Layered Rock Mass. *Appl. Sci.* **2023**, *13*, 7537. [CrossRef]
9. Song, R.; Zhang, P.; Tian, X.; Huang, F.; Li, Z.; Liu, J. Study on Critical Drawdown Pressure of Sanding for Wellbore of Underground Gas Storage in a Depleted Gas Reservoir. *Energies* **2022**, *15*, 5913. [CrossRef]
10. Tan, H.; Liu, H.; Shi, X.; Ma, H.; Qiu, X.; Guo, Y.; Ban, S. Mechanical and Acoustic Response of Low-Permeability Sandstone under Multilevel Cyclic Loading-Unloading Stress Paths. *Energies* **2023**, *16*, 6821. [CrossRef]

11. Wang, Y.; Li, S.; Song, R.; Liu, J.; Ye, M.; Peng, S.; Deng, Y. Effects of Grain Size and Layer Thickness on the Physical and Mechanical Properties of 3D-Printed Rock Analogs. *Energies* **2022**, *15*, 7641. [CrossRef]
12. Song, R.; Wang, Y.; Tang, Y.; Peng, J.; Liu, J.; Yang, C. 3D Printing of natural sandstone at pore scale and comparative analysis on micro-structure and single/two-phase flow properties. *Energy* **2022**, *261*, 125226. [CrossRef]

energies

MDPI

Article

Experimental Study on the Sweep Law of CO_2 Miscible Flooding in Heterogeneous Reservoir in Jilin

Wen Li [1,2,3,*], Hongwei Yu [4], Zhengming Yang [2,3], Jinlong Li [5], Xinliang Chen [1,2,3] and Longfei Ma [1,2,3]

[1] College of Engineering Science, University of Chinese Academy of Sciences, Beijing 100049, China
[2] Institute of Porous Flow and Fluid Mechanics, Chinese Academy of Sciences, Langfang 065007, China
[3] Research Institute of Petroleum Exploration & Development, Beijing 100083, China
[4] State Key Laboratory of Enhanced Oil Recovery, PetroChina Research Institute of Petroleum Exploration and Development, Beijing 100083, China
[5] PetroChina Jilin Oilfield Company, Songyuan 138099, China
* Correspondence: liwen20@mails.ucas.ac.cn

Abstract: It is very important to effectively describe the sweep characteristics of CO_2 miscible flooding based on physical models for actual reservoir development. In this study, based on the geological characteristics of the Jilin ultra-low permeability reservoir, which has significant vertical heterogeneity, a two-dimensional double-layer heterogeneous visualization model with a permeability contrast of 10 and thickness contrast of 2 was designed to perform experimental research on the sweep law of CO_2 miscible flooding with an injection-production mode of "united injection and single production". With the goal of determining the obvious differences in the gas absorption capacity and displacement power of the two layers, the CO_2 dynamic miscible flooding characteristics were comprehensively analyzed, and the sweep law of CO_2 miscible flooding, including the oil and gas flow trend, migration direction of the oil–gas interface, and distribution characteristics of the miscible zone, was further studied in combination with the oil displacement effect. In this experiment, the gas absorption capacity was the key factor affecting the sweep efficiency of the CO_2 miscible flooding. Under the combined influence of the internal and external control factors of the reservoir thickness, permeability, and injection-production mode, the gas absorption capacity of the high-permeability layer was much greater than that of the low-permeability layer, resulting in the retention of a large amount of remaining oil in the low-permeability layer, which effectively displaced and swept the oil in the high-permeability layer. The gas absorption capacity of the reservoir, gravitational differentiation, and miscible mass transfer were key factors affecting the migration of the oil–gas interface and distribution of the miscible zone. The entire displacement process could be divided into three stages: ① The gas-free rapid oil production stage, which was dominated by the displacement; ② the low gas–oil ratio stable oil production stage, which was jointly affected by the displacement and miscible mass transfer; and ③ the high gas–oil ratio slow oil production stage, which was dominated by the effect of CO_2 carrying.

Keywords: CO_2 miscible flooding; vertical heterogeneity; sweep law; 2D visual model; gas absorption capacity

Citation: Li, W.; Yu, H.; Yang, Z.; Li, J.; Chen, X.; Ma, L. Experimental Study on the Sweep Law of CO_2 Miscible Flooding in Heterogeneous Reservoir in Jilin. *Energies* **2022**, *15*, 5755. https://doi.org/10.3390/en15155755

Academic Editor: Antonio Zuorro

Received: 23 June 2022
Accepted: 5 August 2022
Published: 8 August 2022

1. Introduction

By the end of 2019, the confirmed reserves of the Jilin ultra-low permeability reservoir reached 460 million tons, accounting for 36% of the total verified reserves. It is extremely important to adopt effective methods for the stable and long-term development of the Jilin oilfield [1]. This reservoir has poor physical properties and significant vertical heterogeneity, and it is difficult to form an effective displacement environment through waterflood development [2,3]. In 2006, an investigation began at the Jilin oilfield on the use of CO_2 flooding technology. This is a type of miscible flooding in which the injection pressure is higher than the minimum miscible pressure [4]. Field practice and laboratory research have shown that CO_2 miscible flooding can significantly improve the development effect for the ultra-low permeability reservoir in Jilin [5,6]; however, the reservoir heterogeneity considerably affects the sweep area of CO_2 miscible flooding. Moreover, it is difficult to predict and describe the sweep characteristics of CO_2 miscible flooding during dynamic displacement. Therefore, it is extremely important to study the sweep law of CO_2 miscible flooding in relation to the heterogeneous effects of the Jilin reservoir.

At present, most physical simulation experiments on CO_2 miscible flooding performed by researchers use one-dimensional long cores or short cores. For example, to study the influence of water content on the CO_2 flooding effect in ultra-low permeability reservoirs, Yu et al. [7] conducted two sets of physical simulation experiments on long-core flooding in the low-water-cut and high-water-cut stages, analyzed the displacement law at the different water cut stages, and evaluated the oil displacement effect using two main parameters: the gas–oil ratio and oil recovery factor. Liu et al. [8] conducted two sets of comparative long-core CO_2 flooding experiments. In these experiments, the oil displacement effects of the CO_2 miscible and non-miscible floodings of ultra-low permeability reservoirs were evaluated using parameters such as the oil recovery factor and gas–oil ratio. Qian et al. and Wang et al. [9,10] conducted short-core CO_2 physical simulation experiments based on nuclear magnetic resonance technology to explore the microscopic flooding mechanism of CO_2 miscible flooding under different injection methods. They clarified the relationship between the pore-size structure and movable-oil distribution, comprehensively evaluated the CO_2 flooding effect under different injection methods, and optimized the injection methods. It was observed that this type of experiment could only evaluate the effect of CO_2 miscible flooding using parameters such as the oil recovery factor, gas–oil ratio, and oil saturation, but could not describe the sweep characteristics of CO_2 miscible flooding owing to the limitation of the one-dimensional physical model. With the development of experimental technology, two-dimensional (2D) models with relatively large sizes and visual characteristics have been widely used in indoor experiments. For example, Wang et al. [11] conducted a 2D visual physical simulation experiment on a bottom-water reservoir exploited with a horizontal well and analyzed the variation characteristics and mechanism of water coning with horizontal sections with different lengths. Qian et al. [12] simulated the water cresting process and changes in crest configurations using a 2D visual model to predict the dynamic change trend of water cresting. Huang et al. [13] established a horizontal 2D visual physical model to study the development process for the water cresting of horizontal wells and analyzed the water breakthrough characteristics of bottom-water reservoirs. Li et al. [14] designed a 2D visual model, studied the dynamic process of foam flooding in bottom-water reservoir development based on this model, and analyzed the migration characteristics of the foam fluid in the anti-water coning process. To solve the problem of ineffective development caused by injected water migrating along the high-permeability zones in thick reservoirs with a positive rhythm, based on a 2D visual heterogeneous sand-packing model, Liu et al. [15] designed a physical simulation water-flooding experiment by injecting glue into horizontal wells to form a "gel dam", which could change the direction of water flooding and expand the production range. On the basis of previous studies, to further solve the problem of the uneven sweep area caused by injected water tending to migrate in the dominant channel in heterogeneous reservoirs, Xu et al. [16] proposed the "gel dam profile" technology, and verified the effectiveness of this technology using a 2D visual plane sand filling model. It can be observed that most scholars focus on the use of 2D visible models for experimental research on the use of horizontal wells for bottom-water reservoirs and mainly solve the problem of crude oil plane exploitation. In terms of gas flooding experiments, most scholars mainly use 2D microscopic visual models to deeply study the mechanism of miscible mass transfer between oil and gas in different pore throat distributions and displacement stages. However, due to the limitation of model size, it is impossible to deeply study the sweep characteristics of macroscopic miscible gas flooding. For example, Qing et al. [17] designed a plane glass etching model and carried out a high temperature-pressure CO_2 miscible flooding experiment, and observed the miscible mass transfer characteristics of crude oil and CO_2 in the local microscopic pore size distribution. Guo [18] carried out CO_2 miscible flooding experiments by using microscopic 2D visual experimental simulation system to restore the actual temperature and pressure conditions of the reservoir, and studied the miscible microscopic migration characteristics between oil and gas in different pore size distributions. Wang et al. [6] designed two microscopic visual models of pore-throat scales, and carried out CO_2 flooding experiments under different injection modes, among which the miscible mechanism at the corner was deeply studied. In 2021, Yu et al. [19] designed a variety of 2D visual models with the size of $150 \times 170 \times 20$ mm based on the characteristics of sandstone reservoirs with developed interlayers and fractures. They carried out miscible hydrocarbon gas gravity drainage experiments in both the homogeneous model and the model with interlayers, and for the first time observed the distribution of the large-area miscible zone in the experiments, and its sweep characteristics were described and analyzed. This lays a foundation for further development of miscible gas flooding sweep experiments. However, at present, there is still a lack of systematic research on CO_2 flooding sweep experiment based on large-scale 2D visual sand-filling model. Few scholars have conducted in-depth gas flooding experiments based on such models or have effectively used visual research methods to accurately describe the characteristics of CO_2 miscible flooding in different displacement stages to further study the sweep law of CO_2 miscible flooding.

Based on the characteristics of the Jilin ultra-low permeability reservoir, which has significant vertical heterogeneity, this study designed a 2D double-layer heterogeneous visualization model and performed a sweep law experiment on CO_2 miscible flooding to study its dynamic sweep characteristics, including the oil and gas flow trend, migration direction of the oil–gas interface, and distribution characteristics of the miscible zone.

2. Experimental Equipment and Methods

2.1. Model Design

In order to deeply study the sweep law of CO_2 miscible flooding under the heterogeneous reservoir in Jilin, this paper takes a certain block of Jilin ultra-low permeability reservoir as the research background. The top structure of the block is a fault nose structure blocked by reverse normal fault, and the type of reservoir is a lithologic structure. The average effective thickness of oil layer in this block is 9.5 m, the average porosity is 13.0%, and the average permeability is 4.5×10^{-3} μm^2.The block is mainly rich in two thin layers: No. 11 and No. 12, the No. 11 thin layer has a single effective thickness of 2 m, an average porosity of 10.6%, and an average permeability of 1.7×10^{-3} μm^2; the No. 12 has a thickness of 4 m, an average porosity of 15.1%, and an average permeability of 8.0×10^{-3} μm^2. In addition, the fractures in this block are relatively developed. The fractures are mainly in the east-west direction, and there is no filler on the fracture surface. They are closed underground and are mainly located between two thin layers.

According to the geological characteristics of the above-mentioned target block, based on the similarity principle, a 2D double-layer heterogeneous visualization model is designed, as shown in Figure 1. The model consists of a set of stainless steel frames, an organic glass plate and a sand-filled core. The outer frame is pressurized sealed with screws, the upper limit of the working pressure is 22 MPa, and the upper limit of the working temperature is 110 °C. The model size is 20 cm × 15 cm × 2 cm, the average porosity is 13.2%. The core is mainly made of 120–500 mesh quartz sand and glass beads, mixed and poured with epoxy resin, and an impermeable resin plate located at 2/3 of the model height is built to simulate the interlayer. The length of the interlayer is 10 cm and the thickness is 4 mm. With the interlayer as the boundary, the upper part simulates a low-permeability layer with relatively low permeability, with a thickness of 5 cm and a permeability of 1 mD; the lower part simulates a high-permeability layer with relatively high permeability, with a thickness of 10 cm and a permeability of 10 mD. It satisfies the condition of reservoir permeability contrast and reflects the vertical heterogeneity of the reservoir.

In addition, the inlet and outlet valves can be set around the model. Through system regulation, valve control and pipeline connection, various combinations of injection-production modes can be formed, and experimental studies under different injection-production modes can be carried out.

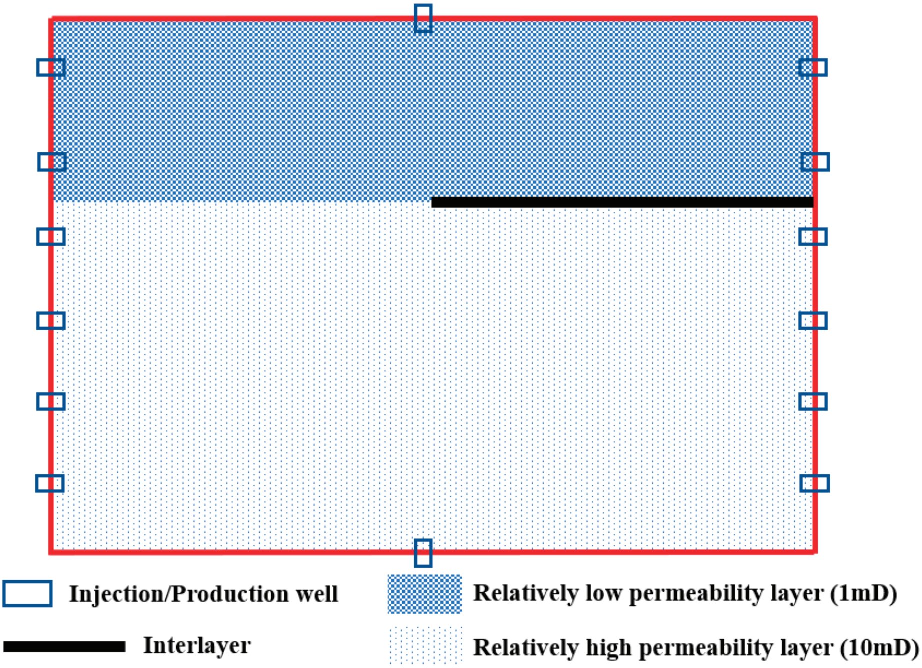

Figure 1. Design diagram of the 2D double-layer heterogeneous visualization model.

2.2. Experimental System

The experimental system mainly includes four parts: displacement system, 2D model, image monitoring capture system, and produced fluid measurement system, as shown in Figure 2. Among them, the displacement system uses two sets of Quizix qx5210 high-pressure precision displacement pumps and two piston intermediate containers to work together for core saturation and displacement. The 2D model has the characteristics of visualization, which can further study the displacement and sweep law. The image monitoring capture system is composed of a high-speed camera and a computer operating terminal, which is used to monitor, capture, and record the complete dynamic miscible flooding process. The produced liquid measurement system is composed of an output liquid metering device, a separation bottle and a real-time gas flow meter, which is used for precise measurement of the produced liquid. In addition to the water bath, the intermediate containers and pipelines are wrapped with heating sleeves to ensure the experimental temperature.

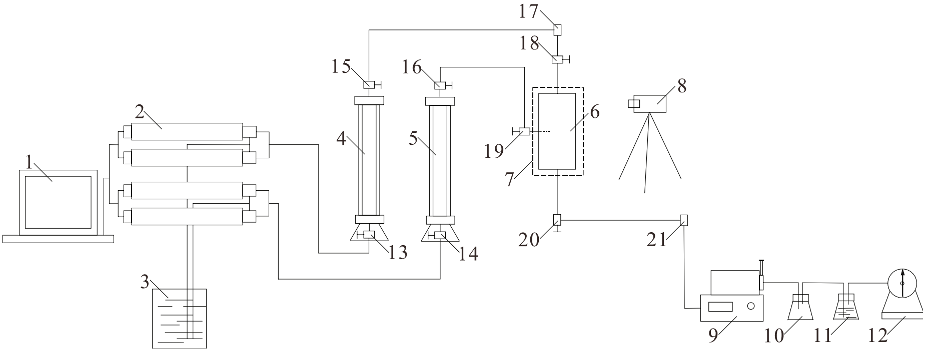

Figure 2. Experimental flow chart.1: computer operating terminal; 2: Quizix qx5210 high-pressure precision displacement pump; 3: distilled water; 4: simulated oil intermediate container; 5: gas intermediate container; 6: 2D double-layer heterogeneous visualization model; 7: constant temperature water bath equipment; 8: high-speed camera; 9: back-pressure controller; 10: output liquid flow device; 11: separation bottle; 12: gas flow meter; 13–21: stop valve.

2.3. Experimental Scheme

According to the combination of various injection-production modes selected for the actual production and development of the target block, the injection-production mode in this experiment is designed as “united injection and single production”, that is, it is injected uniformly at the top of the double layers of the right side of the reservoir, and produced at the bottom of the high-permeability layer at the left side, as shown in Figure 3. Uniform injection from the top position, both high and low permeability layers can effectively utilize the gravitational differentiation caused by the difference in oil and gas densities. Single production from the bottom of the high-permeability layer, the layer contradiction caused by the heterogeneity of the ultra-low permeability reservoir can be highlighted, and the obvious difference in the gas absorption capacity and displacement power of the high and low permeability layers can be exposed. Therefore, by adopting the injection-production mode of “united injection and single production”, an in-depth study can be carried out on the control effects of gas absorption capacity of reservoir, gravitational differentiation, miscible mass transfer on the oil and gas flow trend, the migration direction of oil–gas interface and the distribution characteristics of miscible zone, and the dynamic sweep law of CO_2 miscible flooding is obtained.

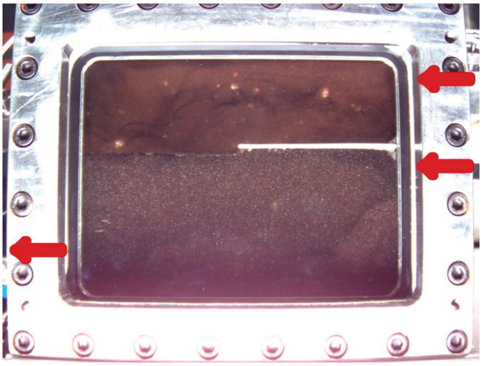

Figure 3. Schematic diagram of the injection-production mode of the 2D double-layer heterogeneous visualization model. (The arrow at the right side is the injection end; the arrow at the left side is the production end).

2.4. Experimental Materials and Procedures

The experimental temperature is 50 °C, the back pressure is 8.5 MPa, and the displacement pressure is 9.5 MPa. The experimental gas is CO_2 with a purity of 99.99%. The experimental oil sample is prepared from aviation kerosene, a certain content of C_2–C_5 components and ground gas-free crude oil of the target block, and the density is 0.78 g/cm^3. Under the experimental conditions, the simulated oil can be miscible with CO_2 (Figure 4), with a viscosity of 2.08 mPa·s, which is equivalent to the viscosity of the formation oil in the target block under miscible conditions (temperature of 96.7 °C and pressure of 23.9 MPa).

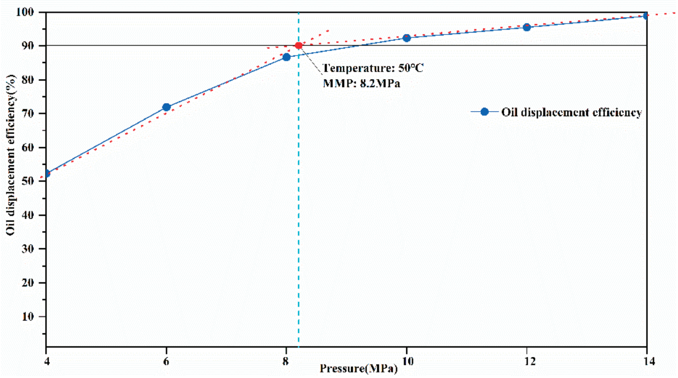

Figure 4. Diagram of minimum miscible pressure measured by slim tube experiment.

The experimental procedures are as follows:

(1) The model was vacuumized for more than 6 h.

(2) The simulated oil was injected from the bottom of the model. The oil was saturated at a constant speed and then at a constant pressure, and the saturation time was more than 24 h.

(3) Control the back pressure to 8.5 MPa, inject CO_2 at a constant pressure of 9.5 MPa from the injection side of the model, control the pressure difference to be about 1 MPa, and carry out oil at the production side.

(4) During the entire displacement process, the displacement process was photographed and recorded at a non-uniform time interval of every 5–120 s. Measure the produced volume of simulated oil and CO_2 at certain time intervals.

(5) By visualizing the dynamic displacement process and the degree of oil and gas recovery, it was judged that when the gas–oil ratio was maintained at a high level or no more oil was produced, the experiment was terminated.

3. Experimental Results and Analysis

3.1. CO_2 Dynamic Miscible Flooding

The darker area shown in Figure 5 indicates the oil-layer area, and the relatively lighter area denotes the sweep area of the CO_2 miscible flooding. It is established that the thickness and permeability of a reservoir are the intrinsic control factors affecting its gas absorption capacity [20]. In this experiment, both layers were ultra-low permeability reservoirs with a permeability contrast of 10 and thickness contrast of 2. Thus, they were positive-rhythm reservoirs with significant vertical heterogeneity. In addition, the injection-production mode of “united injection and single production” directly led to an obvious difference in the displacement power of the high- and low-permeability layers. Therefore, under the combined influence of internal and external control factors that included the reservoir thickness, permeability, and injection-production mode, the gas absorption capacity of the high-permeability layer was much greater than that of the low-permeability layer.

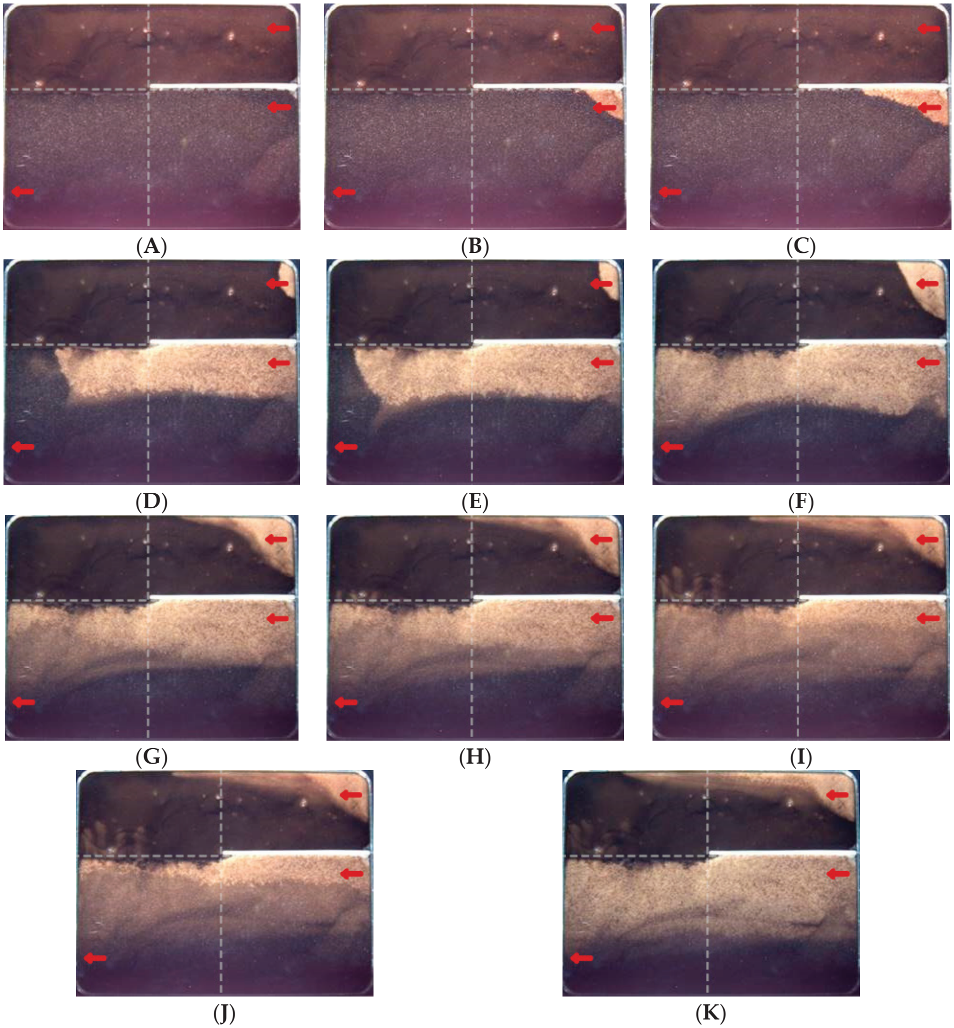

Figure 5. State diagram of CO_2 miscible flooding at different production time. (**A**) 0 min; (**B**) 1 min; (**C**) 2 min; (**D**) 20 min; (**E**) 24 min; (gas breakthrough); (**F**) 34 min; (**G**) 74 min; (**H**) 164 min; (**I**) 344 min; (**J**) 358 min (increasing oil production rate); (**K**) 468 min (end of experiment). (The arrow at the right side is the injection end; the arrow at the left side is the production end).

In the early stage of displacement, as shown in Figure 5A–D, because of the difference in the gas absorption capacities of the layers, CO_2 was first injected into the high-permeability layer. Simultaneously, under the gravitational differentiation and shielding effect of the interlayer on the vertical oil and gas migration, the oil–gas interface in the high-permeability layer changed rapidly, the gravity override phenomenon was obvious, and the crude-oil utilization degree was good. In contrast, the low-permeability layer exhibited a smaller gas absorption capacity, resulting in a weak displacement power, slow oil and gas migration speeds, and slow interface changes.

As shown in Figure 5D–F, the gravity override of the high-permeability layer was continuously enhanced, and gas breakthrough was rapidly achieved. After the gas breakthrough, the displacement power of the overall reservoir was enhanced, the gravity override continued to expand the sweep area, and the oil and gas migration speeds improved. However, because of the fundamental influence of the gas absorption capacity, when the gas preferential pathway was formed, more than half of the oil layer in the high-permeability layer was effectively completely displaced, and there was only a certain area where the remaining oil was distributed in the non-displacement area at the bottom (Figure 6). In comparison, a large amount of the remaining oil was retained in the low-permeability layer. But, under the advantage of miscible flooding, the bottom oil layer on the left side of the low-permeability layer that was not shielded by the interlayer could come into contact with the CO_2 in the high-permeability layer, which led to mutual dissolution and mass transfer, allowing it to migrate to the high-permeability layer and be carried and produced by the CO_2 (Figure 7).

As shown in Figure 5F–I, after the formation of the gas preferential pathway, a large amount of CO_2 occupied the pores of the reservoir, resulting in the weakening of the overall displacement power, and the displacement mode was dominated by miscible mass transfer. The remaining oil in the high- and low-permeability layers was fully in contact with the CO_2, which led to mutual dissolution and mass transfer, forming a miscible zone with obvious miscible characteristics and a gradually expanding distribution range (Figure 8). In addition, owing to the large difference in oil and gas densities, a fingering phenomenon could easily form inside the reservoir during the miscible mass transfer (Figure 9).

In the late stage of miscible flooding, as shown in Figure 5J,K, in order to observe the overall migration trend after the formation of the large-area miscible zone, the outlet valve was adjusted by increasing the oil production rate. The miscible zone in the high-permeability layer was rapidly carried and produced by the CO_2, the migration of the oil–gas interface in the low-permeability layer changed, and the fingering phenomenon at the bottom was interrupted. Finally, there was a small amount of remaining oil distributed at the bottom of the high-permeability layer, whereas almost all of the oil in the low-permeability layer was not effectively displaced. In addition, a comparison of Figure 5F,K clearly shows that under the action of the miscible mass transfer, the sweep efficiency of the remaining oil in the high-permeability layer was significantly improved. Therefore, for the high-permeability layer, miscible mass transfer could be used to mobilize the remaining oil in the bottom layer to form a large-area miscible zone and expand the sweep area. For the low-permeability layer, owing to its smaller gas absorption capacity and insufficient displacement power, the remaining oil was difficult to displace and produce. It could only come into full contact with the CO_2 in the high-permeability layer for mass transfer and slowly migrate to the high-permeability layer to be carried and produced by the CO_2; however, this process requires a long production time. Therefore, it was difficult to achieve efficient production of the remaining oil in the low-permeability layer under the injection-production mode of “united injection and single recovery”.

In addition, by estimating the size of the lighter-colored sweep area in Figure 5, the proportions of the gas absorption ranges for the high- and low-permeability layers in the total reservoir space could be roughly determined, as listed in Table 1. In the different displacement stages, there was a large difference in the inspiratory volume proportions of the two layers.

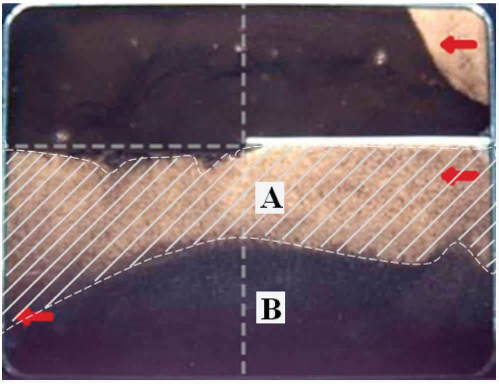

Figure 6. Distribution of remaining oil in high-permeability layer when gas preferential pathway is formed. (A—Displacement area channel; B—remaining oil distribution area). (The arrow at the right side is the injection end; the arrow at the left side is the production end).

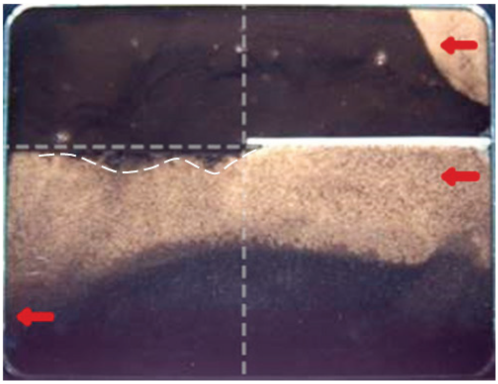

Figure 7. Distribution of miscible mass transfer between the bottom oil layer on the left side of the low-permeability layer and the CO_2 in the high-permeability layer. (The arrow at the right side is the injection end; the arrow at the left side is the production end).

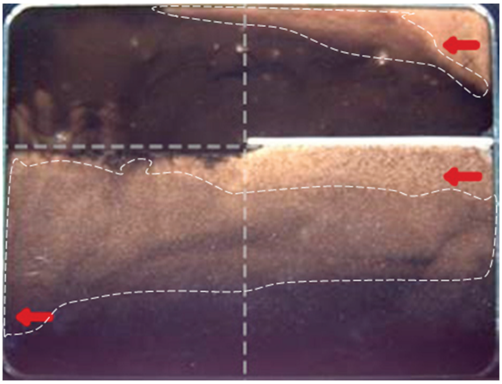

Figure 8. Distribution of miscible zone formed by contact between remaining oil and CO_2 in two layers. (The arrow at the right side is the injection end; the arrow at the left side is the production end).

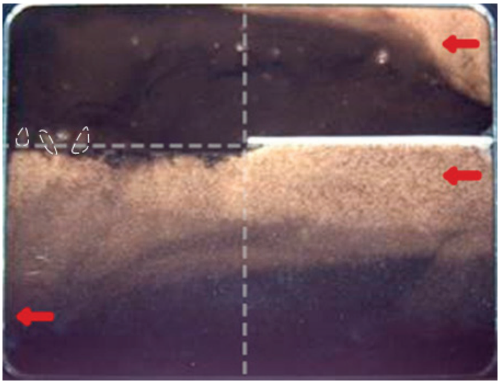

Figure 9. Development diagram of fingering phenomenon at the bottom of low-permeability layer. (The arrow at the right side is the injection end; the arrow at the left side is the production end).

Table 1. Data table of the proportion of gas absorption range of high and low permeability layers in total reservoir space at different production time.

State	0 min	1 min	2 min	20 min	24 min	34 min	74 min	164 min	344 min	358 min	468 min
The proportion of the sweep area in the high-permeability	0%	1.0%	2.3%	19.2%	22.9%	33.0%	34.5%	35.7%	38.4%	39.6%	40.9%
The proportion of the sweep area in the low-permeability	0%	0%	0%	0.7%	0.8%	2.8%	4.5%	5.3%	6.4%	7.0%	9.0%

3.1.1. Migration Characteristics of Oil–Gas Interface

By comparing and observing the characteristics of oil–gas interface migration in high- and low-permeability layers, it could be judged that the gas absorption capacity of the reservoir and gravitational differentiation were the key factors affecting the migration and change of oil–gas interface. With the CO_2 injection, a semicircular gas cap would be formed first. After the gas cap was formed, the oil–gas interface migrated stably under the actions of gas cap expansion and gravitational differentiation (Figure 10A,B). When shielded by the interlayer or wall, the oil–gas interface developed into a tongue-shaped slope, and continued to migrate in the form of slope expansion under the effect of gravitational differentiation (Figure 10C,E). Subsequently, the change of oil–gas interface was mainly controlled by the gas absorption capacity of the reservoir. When the gas absorption capacity of the reservoir was greater, the oil–gas interface rapidly developed from a tongue-shaped slope to a long column with a slightly inclined front interface and a tip, where the tip pointed to the outlet (Figure 10E,F). On the contrary, the oil–gas interface slowly developed from a small tongue-shaped slope to a large slope with a finger-like front (Figure 10G,H). This was due to the poor gas absorption capacity, weak gravitational differentiation, and large difference in oil and gas viscosities, resulting in slow migration speed of oil and gas and slow change of oil–gas interface, and it was easy to form the fingering phenomenon that developed in the horizontal direction at the front end of oil and gas contact.

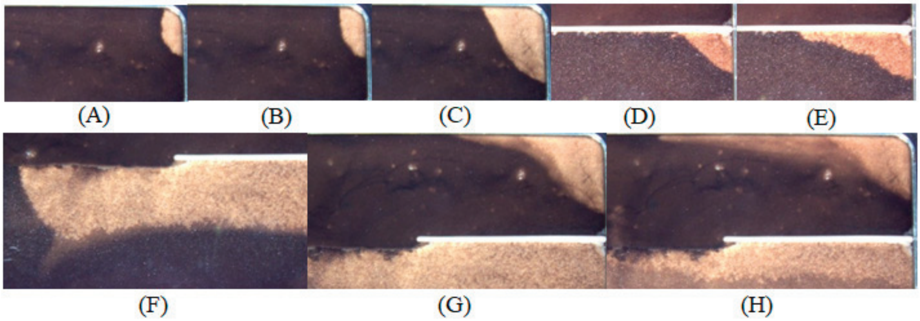

Figure 10. Migration diagram of oil–gas interface.

3.1.2. Distribution Characteristics of Miscible Zone

The formation and distribution characteristics of the miscible zone were mainly related to the miscible mass transfer and displacement power. From the whole process of CO_2 miscible flooding, it could be found that there was a miscible zone with a lighter color than the oil layer at the contact position of oil and gas, and the oil–gas interface was no longer obvious with the expansion of the miscible zone. The color of the miscible zone also became darker with the enhancement of the miscible mass transfer between oil and gas (Figure 11A,B). Among them, when the displacement power was greater, the displacement was the main. The effect of miscible mass transfer was weaker at this stage, resulting in a slow formation speed of the miscible zone with a small distribution range, and only existed in contact parts of the oil and gas. As the displacement progressed, it was rapidly displaced by CO_2. When the displacement power was weaker, the mutually soluble mass transfer between oil and gas could be fully exerted in the miscible state, the remaining oil efficiently produced, the sweep efficiency improved, and the distribution characteristics of the miscible zone developing in multiple directions could be formed, as shown in Figure 11C,D).

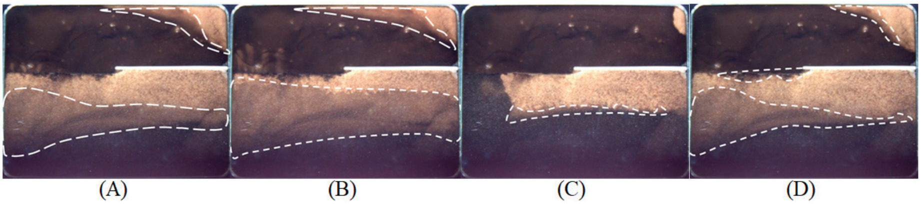

Figure 11. Distribution diagram of miscible zone formation.

3.2. Oil Displacement Effect of CO_2 Miscible Flooding

The oil displacement effect of CO_2 miscible flooding in this experiment were comprehensively analyzed based on the sweep characteristics of dynamic CO_2 flooding, combined with the changes in the oil recovery factor, gas–oil ratio, and oil production rate. As shown in Figures 12 and 13, the entire displacement process could be divided into three stages: the gas-free rapid oil production, low gas–oil ratio stable oil production, and high gas–oil ratio slow oil production stages.

The process from CO_2 injection to gas breakthrough involved rapid oil production without the gas, which was dominated by the displacement. As shown in Figures 12 and 13, the oil production rate in this process was relatively high, and the oil recovery factor showed a rapid growth trend. When gas breakthrough occurred, the oil recovery factor was 23.1%, while the total gas injection volume was 0.23 HCPV, the growth amplitude was 100.4%/HCPV, and the oil displacement effect was better. Combined with Figure 5A–E, it can be observed that this process was affected by the difference in the gas absorption capacity of the reservoir, and the displacement range of the high-permeability layer with its significant gas absorption capacity expanded rapidly, which was consistent with the curve change characteristics.

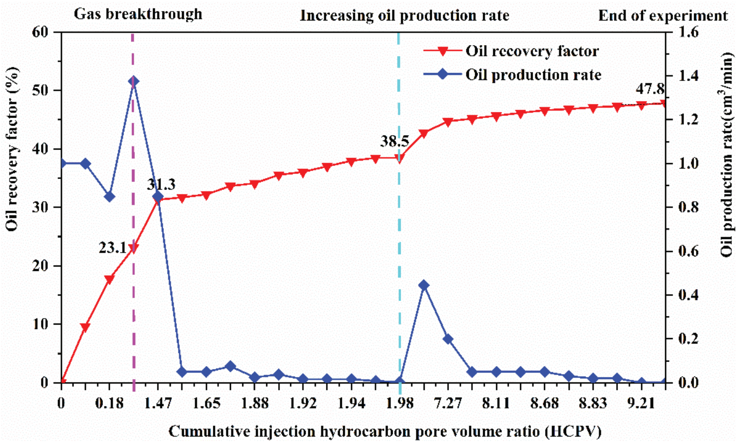

Figure 12. Relationship between cumulative injection hydrocarbon pore volume ratio (HCPV), oil recovery factor, and oil production rate.

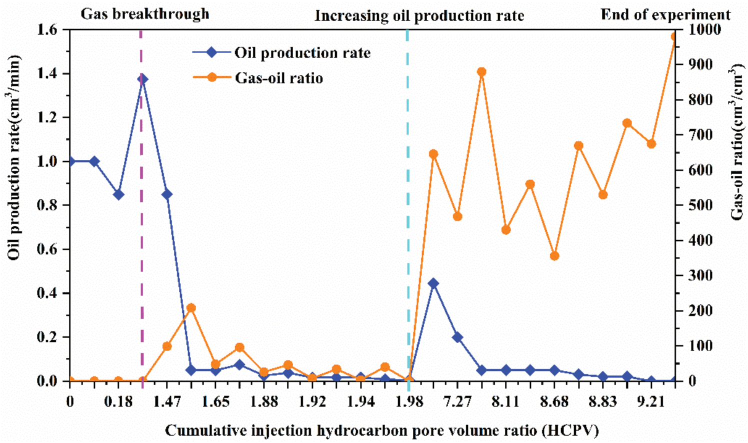

Figure 13. Relationship between cumulative injection hydrocarbon pore volume ratio (HCPV), gas-oil ratio, and oil production rate.

The stage of stable oil production with a low gas–oil ratio occurred from the gas breakthrough to before the increase of oil production rate. It was caused by the combined actions of the displacement and miscible mass transfer. As shown in Figures 12 and 13, after the gas breakthrough, there was an obvious turning point in the curve of the oil recovery factor when the injection volume was 1.47 HCPV and the oil recovery factor was 31.3%. Combined with Figure 5E–G, it can be observed that after the gas breakthrough to the formation of the gas preferential pathway, the displacement range of the entire reservoir further expanded, and the change in the sweep range of the entire reservoir obviously slowed down after the formation of the channel. Therefore, it could be determined that the turning point was the point where the gas preferential pathway formed. From this turning point to before the increase of oil production rate, the oil production rate and gas-oil ratio fluctuated and decreased, the growth amplitude of the oil recovery factor was

14.1%/HCPV, and the oil displacement efficiency decreased significantly. Combined with Figure 5G–J, it can be concluded that this was caused by the miscible mass transfer. After the formation of the gas preferential pathway, a large amount of CO_2 occupied the pores of the reservoir, the displacement power weakened, and the displacement mode changed, with the miscible mass transfer as the main factor and displacement as a supplementary factor. The miscible zone began to form, and its range gradually expanded.

After the oil production rate increased, it is the stage of slow oil production with high gas–oil ratio, which is dominated by the effect of CO_2 carrying. As shown in Figures 12 and 13, after the increase of oil production rate, the gas–oil ratio and oil recovery factor increased sharply, and the amount of CO_2 injected also increased to approximately 7 HCPV. It could be determined that once the oil production rate increased, the miscible zone would be rapidly carried out by a large amount of CO_2. Subsequently, owing to the lower amount of remaining oil, the overall gas–oil ratio increased, mass transfer became weaker, and exchange scale between the oil and gas became smaller. The remaining oil was carried and produced only by high-speed CO_2, and the oil production rate decreased to zero. The final recovery factor was 47.8%, and the total injection volume at this stage was 7.47 HCPV, with a growth amplitude of 1.3%/HCPV. The oil displacement effect was poorer.

In addition, as shown in Figure 5K, there was a large amount of remaining oil distributed in the low-permeability layer and a small amount at the bottom of the high-permeability layer, but the final recovery factor was 47.8%. Thus, high-efficiency displacement and a sweep of the oil layer in the high-permeability layer were achieved, giving full play to the advantages of CO_2 miscible flooding.

4. Conclusions

In this study, a 2D double-layer heterogeneous visualization model was designed. Based on this model, a physical simulation experiment involving CO_2 miscible flooding was conducted by adopting an injection-production mode of "united injection and single production", which highlighted the significant vertical heterogeneity of ultra-low permeability reservoirs. The characteristics of CO_2 dynamic miscible flooding were comprehensively analyzed, and combined with the oil displacement effect, the sweep law of CO_2 miscible flooding in the heterogeneous reservoir of Jilin was thoroughly studied. The main conclusions are summarized as follows.

(1) Under the combined influence of internal and external control factors, which included the reservoir thickness, permeability, and injection-production mode, the gas absorption capacity of the high-permeability layer was much greater than that of the low-permeability layer. This directly affected the sweep area and remaining oil distribution of the two layers.

(2) The gas absorption capacity of the reservoir and gravitational differentiation were the key factors affecting the migration and variation of the oil–gas interface, and the miscible mass transfer and displacement power were the main factors affecting the formation and distribution characteristics of miscible zone.

(3) The entire displacement process of the CO_2 miscible flooding could be divided into three stages: gas-free rapid oil production, low gas–oil ratio stable oil production, and high gas–oil ratio slow oil production. The process from the CO_2 injection to gas breakthrough was the stage of rapid oil production without gas, which was dominated by the displacement. The stage of stable oil production with a low gas–oil ratio occurred from the gas breakthrough to before the increase of oil production rate, it was jointly affected by the displacement and miscible mass transfer. After the oil production rate increased, the stage of slow oil production with a high gas–oil ratio was dominated by the effect of CO_2 carrying.

Author Contributions: Conceptualization and formal analysis, H.Y. and W.L.; methodology and supervision, H.Y.; investigation, W.L.; oilfield data, J.L.; writing—original draft, W.L.; writing—review and editing, Z.Y., H.Y. and W.L.; paper layout, W.L., X.C. and L.M. All authors have read and agreed to the published version of the manuscript.

Funding: This work was supported by the major Science and Technology Projects of China National Petroleum Corporation (2021ZZ01-03).

Institutional Review Board Statement: Not applicable.

Informed Consent Statement: Not applicable.

Data Availability Statement: Not applicable.

Conflicts of Interest: The authors declare no conflict of interest.

References

1. *China Mineral Resources Report. 2021: Ministry of Natural Resources, PRC*; Geology Press: Beijing, China, 2021; ISBN 978-7-116-12858-3.
2. Zhang, X.; Kou, G.; Wang, Z.; Zhang, H.; Zhang, G.S. Technical Discussion on Development Effects of CO_2 Flooding in Jilin Extra-Low Permeability Reservoir. *Drill. Prod. Technol.* **2019**, *42*, 64–67.
3. Qi, Y.D.; Lei, Q.; Yu, R.Z.; Yan, J.; Liu, X.W.; Zhan, J.F. Analysis on factors influencing development effect of extra-ultra low permeability sandstone reservoirs. *J. China Univ. Pet. (Ed. Nat. Ence)* **2013**, *37*, 89–94.
4. Lou, Y.; Yang, S.; Zhang, X.; Yu, Y.; Yin, D.; Li, M.; Wen, B. Experimental research on CO_2 miscible flooding by advanced gas injection in low permeability reservoir-case of H79 block, Jilin oilfield. *Pet. Geol. Recovery Effic.* **2012**, *19*, 78–80. [CrossRef]
5. Li, Y. Technical advancement and prospect for CO_2 flooding enhanced oil recovery in low permeability reservoirs. *Pet. Geol. Recovery Effic.* **2020**, *27*, 1–10. [CrossRef]
6. Wang, S.-T.; Tan, J.-L.; Lei, X.-H.; Shi, H.-X.; Tang, Z.-W. CO_2 flooding technology for low pereability sandstone reservoir of Changqing oilfield. *Int. Field Explor. Dev. Conf.* **2018**, *2018*, 2542–2553.
7. Yu, H.-W.; Yang, S.-Y.; Li, S.; Yang, Y.Z. Rules of Water Cut Variation in Low Permeability Oil Reservoir CO_2 Flooding Process. *J. Jilin Univ. (Earth Sci. Ed.)* **2011**, *41*, 1028–1032. [CrossRef]
8. Liu, F.; Yue, P.; Wang, Q.; Yu, G.; Zhou, J.; Wang, X.; Fang, Q.; Li, X. Experimental Study of Oil Displacement and Gas Channeling during CO_2 Flooding in Ultra—Low Permeability Oil Reservoir. *Energies* **2022**, *15*, 5119. [CrossRef]
9. Qian, K.; Yang, S.L.; Dou, H.; Zhang, J. Microscopic Characteristics of Oil Displacement with Different CO_2 Injection Modes in Extra-Low Permeability Reservoirs. *Xinjiang Pet. Geol.* **2020**, *41*, 204–208.
10. Wang, X.; Wang, L.; Xia, Z.; Shi, F. Microscopic mechanism of oil displacement under different CO_2 injection modes in tight oil reservoirs. *China Encepaper* **2018**, *13*, 1754–1758.
11. Wang, J.; Liu, Y.; Jiang, R.; Guan, C. 2-D physical modeling of water coning of horizontal well production in bottom water driving reservoirs. *Pet. Explor. Dev.* **2007**, *5*, 590–593.
12. Qian, C.; Liu, Y.; Chi, X.; Zhou, X.; Luo, F. Physical Simulation Researches on the Water Cresting Constraint of the Horizontal Wells in Bottom-Water-Driven Oil Reservoir. *Pet. Geol. Oilfield Dev. Daqing* **2012**, *31*, 5.
13. Huang, S.; Zeng, B.; Zhao, F.; Cheng, L.; Du, B. Water Breakthrough Shape Description of Horizontal Wells in Bottom-Water Reservoir. *Math. Probl. Eng.* **2014**, *2014*, 460896. [CrossRef]
14. Li, B.; Liu, K. Visualization Study of Anti-water Coning Using Foam. *Int. Field Explor. Dev. Conf.* **2017**, *2017*, 1508–1514.
15. Liu, Y.; Lu, J.; Wang, J.; Gao, J.; Li, Y. Physical modeling of in-depth fluid diversion by "gel dam" placed with a horizontal well. *Pet. Explor. Dev.* **2011**, *38*, 332–335.
16. Xu, K.; Liu, W.; Guo, Y.; Yan, W.; Luo, L.; Gou, F.; Zhang, C. Experimental Study of Profile Control with Gel-dam. *Sci. Technol. Eng.* **2015**, *15*, 187–190.
17. Qin, J.; Zhang, K.; Chen, X. Mechanism of the CO_2 flooding as reservoirs containing high water. *Acta Pet. Sin.* **2010**, *31*, 797–800.
18. Guo, X. Study on microscopic migration characteristics of heavy oil by CO_2 flooding at high temperature and high pressure. *Pet. Geol. Recovery Effic.* **2019**, *26*, 99–104. [CrossRef]
19. Yu, H.; Wang, L.; Zhou, D.; Wang, F.; Li, S.; Li, J.; Chen, X.; Cao, A.; Han, H. Experimental Study on Sweep Characteristics of Gas Gravity Drainage in the Interlayer Oil Reservoir. *Front. Energy Res.* **2021**, *9*, 660. [CrossRef]
20. Jian, G.; Yang, S.; Li, J.; Wang, H.; Zhou, T. Main Controlling Factors of the CO_2 Injectivity for Jilin Daqingzi Oilfifld. *Pet. Geol. Oilfield Dev. Daqing* **2016**, *35*, 128–131.

energies

Article

Study on Critical Drawdown Pressure of Sanding for Wellbore of Underground Gas Storage in a Depleted Gas Reservoir

Rui Song [1], Ping Zhang [2], Xiaomin Tian [2], Famu Huang [2], Zhiwen Li [2] and Jianjun Liu [1,*]

[1] State Key Laboratory of Geomechanics and Geotechnical Engineering, Institute of Rock and Soil Mechanics, Chinese Academy of Sciences, Wuhan 430071, China
[2] PipeChina West East Gas Pipeline Company, Shanghai 200120, China
* Correspondence: jjliu@whrsm.ac.cn

Abstract: Accurately predicting the critical differential pressure (CDP) of sand production contributes to improving the peak-shaving capacity and ensuring safe operation of underground gas storage (UGS). The CDP of sanding production in the target wells of the UGS was predicted coupling laboratory tests, inversed analysis with well logging data and numerical simulations. The in-situ mechanical properties of rock were estimated by coupling the laboratory test results and well-logging data. The in-situ stress field of the target formation was then deduced through inversed analysis coupled finite element method (FEM) and genetic algorithm (GA), based on the existing known stress data and the seismic data of the measured points. Using the critical strain limit (CSL) of 5‰ as the sanding criterion of the wellbore, the CDPs of the gas production in the UGS were predicted, which was 5.59 MPa, 3.98 MPa, and 4.01 MPa for well #1, well #2 and well #3, when the pressure of the gas storage was 30 MPa, respectively. The simulation results showed good agreements with the field-measured benchmark data of well #2 and well #3. The effects of moisture contents (ranging from 10 to ~40%), and cycling times of gas injection and withdrawal (ranging from 40 to ~200 cycling times) on the critical differential pressure were simulated and analyzed. The results indicated that the CDP decreased with an increase of the moisture content and the cycling times. This study provides a reliable tool for the sanding prediction of the wellbore in the UGS.

Keywords: sanding prediction; underground gas storage; depleted gas reservoir; inversed analysis; in-situ crustal stress; critical differential pressure

Citation: Song, R.; Zhang, P.; Tian, X.; Huang, F.; Li, Z.; Liu, J. Study on Critical Drawdown Pressure of Sanding for Wellbore of Underground Gas Storage in a Depleted Gas Reservoir. *Energies* **2022**, *15*, 5913. https://doi.org/10.3390/en15165913

Academic Editor: Reza Rezaee

Received: 25 July 2022
Accepted: 12 August 2022
Published: 15 August 2022

1. Introduction

In the past half year of 2022, the world witnessed a surge in energy prices due to geopolitical conflicts and the resulting energy crisis, which highlights the urgency of building national energy reserves. Fossil fuels, including coal, oil and natural gas, have been powering economies for over hundred years, and currently supply about 80 percent of the world's energy [1–3]. Currently, underground gas storage (UGS) has been regarded as the best potential tool for the storage and peak-regulation supply to meet the load variations of natural gas (NG) [4]. There are three main types of UGS, including depleted gas reservoirs, aquifer reservoirs and salt cavern reservoirs [5]. The depleted gas reservoirs are the most common for UGS, from which the economically favorable NG has previously been produced. The high-pressure NG is injected into the reservoir and stored in pore space between grains. Depleted gas reservoirs are regarded as the most economically attractive UGS, since they could re-use the extraction and distribution infrastructure of the gas field after suitable modification to reduce the construction costs [6]. Moreover, the geological and physical characteristics of the depleted gas reservoir have already been studied and are usually well known [7,8]. The most common factors used to evaluate the UGS facility are storage facility and injection–withdrawal capacity, both of which depend on the total amount of gas in the reservoir and the operational parameters [9,10].

A higher injection–withdrawal capacity means more NG will be stored and extracted in a short time and achieve the balance between supply and demand. However, the periodic injection and withdrawal of the gas make the pore pressure change significantly, resulting in alternating loads on the rock skeleton of the reservoir. When the differential pressure of the NG withdrawal is increased to meet for the peak shaving requirements, the effective pressure of the well bore may rise beyond the loading capacity of the rock and cause sand production. The sands in the high-speed gas will wear downhole pipe strings and production equipment, and cause failure of high-pressure processing equipment for surface gas production, plugging of the production wellbore and damage to the reservoir, and even disasters of borehole collapse and casing damage [11,12]. Thus, accurately predicting the critical differential pressure (CDP) of sand production is one of the key issues to improving the peak-shaving capacity and ensuring safe operation of UGS.

Experimental study on the sanding of the reservoir can be dated from the beginning of the petroleum industry. Many scholars studied the sanding production through the sand arching phenomenon. They used specially designed boxes filled with sands of different properties (e.g., grain size and shape [13,14], roughness [15], moisture content [16], minerals [17], compactness [17]) and investigated the evolution of the sand arching under different confining pressures [18] and different rates of fluid injection [19,20]. However, the laboratory tests were time-consuming and expensive, especially in samples preparation, and the boundary effects could not be neglected since the size of the testing sample was too small compared to engineering applications. In addition, the sand production of loosely consolidated rock was mainly studied by these experiments since it was hard to investigate the sanding phenomenon of rock with high strength, such as the rock of the UGS in a depleted gas reservoir.

The theoretical and numerical modelling of the sanding evaluations of the injection–withdrawal well in the reservoir have been studied for decades [21], and can be classified into three categories: a sanding risk evaluation index (e.g., rock properties, or operating conditions), analytical approaches, and numerical modelling of CDP [22]. The sanding risk evaluation indexes in the literature included porosity [23], acoustic log signature [24], mechanical properties (e.g., bulk modulus, shear modulus), density, or an empirical index combining some of these parameters [25–27], as listed in Table 1. These empirical indexes were simple and convenient for the estimation of the sanding risk of the target reservoir. However, these indexes were applied and validated in unconsolidated reservoirs, but usually failed in tight reservoirs. The unconsolidated reservoir is mainly composed of loose sandstone, which is characterized by weak cementation, high porosity and high permeability, low strength and strong plasticity [28]. The tight reservoir is defined using the in-situ gas permeability of 0.1 mD or less by the U.S. Federal Energy Regulatory Commission in 1970s [29]. Compared to the unconsolidated reservoir, the rock in the tight reservoir is characterized by stronger cementation, lower porosity, lower permeability, and higher strength. The critical value of indexes usually varied with the reservoir types.

Table 1. Index of sanding risk of reservoirs in the literature.

Sanding Index	Equation	Threshold
Porosity [23]	$\psi = Volume_{pore}/Volume_{total}$	Varying with the reservoir types; where $Volume_{pore}$ and $Volume_{total}$ are the volume of the pore and the rock, respectively.
Acoustic wave travel time [24]	$\Delta t_c = \frac{1}{V_P}$	where V_p is the velocity of the P-wave; 95 μs/ft $<\Delta t_c <$ 105 μs/ft, Slight sanding; $\Delta t_c \geq$ 105 μs/ft, Severe sanding
Combination modulus E_c [25]	$E_c = \frac{9.94\times10^8\rho_r}{\Delta t_c{}^2}$	where ρ_r is the rock density; $E_c \geq 2.0 \times 10^4$ MPa, No sanding; 2.0×10^4 MPa $\geq E_c \geq 1.5 \times 10^4$ MPa, Slight sanding; $E_c < 1.5 \times 10^4$ MPa, Severe sanding

Table 1. *Cont.*

Sanding Index	Equation	Threshold
Index B_i [26]	$B_i = K + \frac{4}{3}G$	where *K* and *G* are the volumetric modulus and shear modulus; B_i > 20 GPa, No sanding; 20 GPa > $B_i \geq 1.4 \times 10^4$ MPa, Slight sanding (but will sanding seriously after water breakthrough); B_i < 14 GPa, Severe sanding
Schlumberger's ratio [27]	$R = \frac{(1-2\mu)+(1+\mu)\rho^2}{6(1-\mu)\left(\Delta t_p\right)^4}$	where μ is the Poisson's ratio; $R \leq 5.9 \times 10^7$ MPa^2, *Sanding*

In addition, these indexes only reflected the influences of the intrinsic rock properties on the sanding risk estimation, without considering the production conditions in the well. Some scholars studied the stress distribution of the wellbore after drilling, and found the yielding zone near the well zone was the main reason for the sanding during the production of the reservoir. Through assuming that the wellbore zone was homogeneous, isotropic and met the plane strain condition, the stress distribution of the wellbore was derived. Coupling with different yield criterions of rock (e.g., compressional, shear, or tensile failure), the CDP of the wellbore could be predicted [30–34], some of which are listed in Table 2. However, the analytical models can only predict the onset of sanding production with limited accuracy due to all the assumptions and simplification, and fail in considering the complexity and heterogeneity of the formation and the dynamic crustal stress and operational conditions.

Table 2. Analytical equation of CDP for sanding production in the literature.

CDP Model	Equation	Nomenclature	Failure Mode
Unconfined compressive strength(UCS)/2 [30]	$\Delta P_w^{cr} = L \times \sigma_{UCS}$	*L* is the empirical constant of 0.3~0.5, σ_{UCS} is the uniaxial compressive strength	Compressional failure
Nordgren's model [31]	$\Delta P_w^{cr} = J_2 - c\bar{J}_1$ $\bar{J}_1 = (\sigma_1 + \sigma_2 + \sigma_3)/3 - p$ $J_2 = \left([\sigma_1 - \sigma_2]^2 + [\sigma_2 - \sigma_3]^2 + [\sigma_3 - \sigma_1]^2\right)/6$	*c* is the material constant for non-linearity	
Almisned's model [32]	$\Delta P_w^{cr} = \max\left\{\begin{array}{c} \frac{\frac{3\mu}{1-\mu}P_{ob}-\sigma_{UCS}S^a}{2B} \\ \frac{\left(3-\frac{3\mu}{1-\mu}\right)P_{ob}-\sigma_{UCS}S^a}{2B} \\ \frac{\frac{\mu}{1-\mu}P_{ob}-\sigma_{UCS}S^a}{B} \end{array}\right\}$	*B* is the Biot's constant, P_{ob} is the overburden pressure, *s* and *a* are Hoek Brown material constants	Shear failure
Morita et al.'s model [33]	$\Delta p_w^{cr} = \frac{1}{3-2\left(\frac{1-2\mu}{1-\mu}\right)} \left(\begin{array}{l} -3\overline{\sigma_H} - 2T_0 + \frac{2T_0(3+\alpha)}{\alpha} \times \\ \left\{\left[1 + \frac{B_0+2B_1T_0}{2T_0\frac{1-\mu}{E}\frac{3+\alpha}{3+2\alpha}\sqrt{\frac{1}{6}\left(\alpha^2+4\alpha+6\right)}}\right]^{\frac{\alpha}{(2\alpha+3)}} - 1\right\} \end{array}\right)$	$C_0 = \frac{3C}{\sqrt{9+12\tan^2\phi}}$, $C_1 = \frac{\tan\phi}{\sqrt{9+12\tan^2\phi}}$, $\alpha = \frac{6C_1}{\frac{1}{\sqrt{3}}-2C_1}$, $T_0 = \frac{C_0}{\frac{1}{\sqrt{3}}-2C_1}$	
Vaziri et al.'s model [34]	$\Delta P_w^{cr} \leq P_0 - \frac{2\sigma_v-\lambda\times TWC}{2-A} - P_0\frac{A}{2-A}$ $A = \frac{(1-2\mu)B}{1-\mu}$	σ_v is the vertical stress, λ is a factor depending on thick-wall cylinder strength (TWC) test,	
	$\Delta P_w^{cr} = (Ck + P_0) - \sqrt{(Ck + P_0)^2 - 2CkP_0}$; $k = \frac{4\cos\phi}{1-\sin\phi}$	*C* is the cohesive force, φ is the frictional angle, *P*P_0 is the pore pressure	Tensile Failure

Numerical simulations based on the Finite Element Method (FEM), Finite Difference Method (FDM), Boundary Element Method (BEM) and Discrete Element Method (DEM) were widely used for sanding prediction coupling with the geological modeling of the reservoir [35–37]. Nouri et al. [38] coupled laboratory experiments and numerical simulation to study the time-dependent stability of the wellbore, and sand production induced by depletion, drawdown, and water-cut. Volonté et al. [39] established an ideal 3D model of the wellbore and simulated the equivalent plastic strain around the perforations for sanding prediction. Gui et al. [40] acquired the plastic strain limits modelled from advanced TWC core tests and systematic triaxial compressive core tests. They coupled this rock failure criterion and numerical simulations for sanding evaluations. Zhang et al. [25] calculated the CDP of sanding onset for offshore depleted and water cut gas reservoirs coupling with the fully-polyaxial rock failure criterion Mogi–Coulomb and FEM. Lu et al. [41] predicted the CDP of sanding onset considering the influence of drag stress, formation water production, reservoir pressure depletion, and temperature difference in the perforated wellbore in ultra-deep reservoirs. More studies of the numerical simulations on the CDP of sanding production are included in [35–37]. However, the in-situ crustal stress of the reservoir was not considered in these studies. In addition, it was usually difficult to acquire the accurate distribution of the rock properties as the target formation size increased.

The present study took a depleted gas reservoir as a potential UGS site to study the CDP of sanding production in the wellbore. Laboratory tests on the rock samples drilled from three target wells were conducted to acquire the basic rock properties. The in-situ mechanical properties of rock were estimated by coupling the laboratory test results and well-logging data. The in-situ stress field of the target formation was then deduced through inversed analysis coupled with finite element method (FEM) and genetic algorithm (GA), based on the existing known stress data and the seismic data of the measured points. The CDPs for the onset sanding production of three target wells in the UGS were predicted. The effects of the moisture content and cycling times of gas injection and withdrawal on the CDP were analyzed.

2. Methodology

2.1. Experimental Test on Mechanical Properties of Reservoir Rock

Accurate estimation of the rock properties in the target reservoir is essential for the case study on geomechanical numerical simulation. The laboratory tests were conducted to acquire the static properties including the density, porosity, permeability and mechanical properties. A depleted gas reservoir in China was chosen as the potential UGS site. A total of 40 sandstone core samples from the wells (named #1, #2 and #3) in the target reservoir were drilled and used for laboratory tests, including the density, porosity, permeability, uniaxial compression strength, cohesive strength and friction angle. The density of the tested cores was in the range1.9 g/cm^3 to 2.4 g/cm^3, and the porosity range was 7.8% to 27.9%; the permeability range of from 0.65 to 973.37 mD. The mechanical properties tests were performed using the MTS 815 rock mechanics test system, as shown in Figure 1a. The acquired stress-strain curve and the core images before and after the test in well #1 are presented in Figure 1b. The results indicate that the triaxial compressive strength ranged from 55.9 MPa to 143.9 MPa, and the Poisson's ratio ranged from 0.07 to 0.19, while the Young's modulus ranged from 4.5 GPa to 9.4 GPa. As shown in Figure 1c, by fitting the maximum principal stress and confining pressure obtained by the experiment, the Mohr circle of the corresponding rock sample can be obtained, and then the friction angle and cohesion strength can be obtained.

The in-situ mechanical properties of rock were estimated by coupling the laboratory test results and well-logging data including the caliper (CAL), compressional sonic travel time (DTC), shear sonic travel time (DTS), gamma ray (GR), neutron porosity (NP), invaded zone resistivity (RI), flushed zone resistivity (RXO), true formation resistivity (RT) and the density logging data (DEN). The empirical correlations [42] were adopted to estimate the Poisson's Ratio, Young's Modulus, and Shear Modulus using DTS and DTC, as follows:

$$\mu = \frac{\Delta t_s^2 - 2\Delta t_p^2}{2\left(\Delta t_s^2 - \Delta t_p^2\right)} \tag{1}$$

$$E = \rho \frac{(1+\mu)(1-2\mu)}{\Delta t_p^2 (1-\mu)} \tag{2}$$

$$G = \frac{\rho}{\Delta t_s^2} \tag{3}$$

where E, μ, and G are the Young's Modulus (YM), the Poisson's Ratio (PR), and the Shear Modulus, respectively. Δt_p and Δt_s are the compressional sonic travel time and shear sonic travel time, respectively.

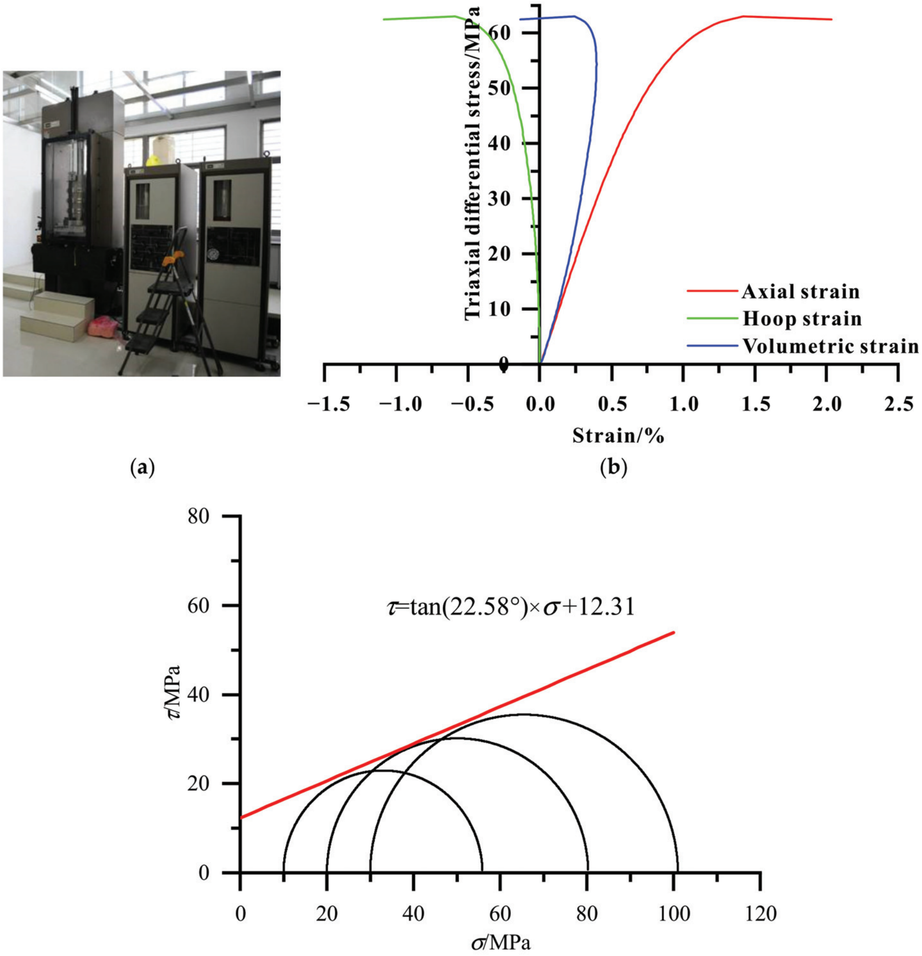

(**a**) (**b**)

(**c**)

Figure 1. Triaxial compression test on the drilled core from the target formation. (**a**) MTS 815 rock mechanics test system. (**b**) Stress-strain curve and images before and after the test of one core sample in well #1. (**c**) The fitted Mohr circle and the calculation of the friction angle and cohesion strength.

The well logging data of #1, #2 and #3 included the CAL, DTC, DTS, GR, NP, RI, RXO, RT and DEN. Then, the mechanical properties of the rock in the corresponding well were calculated using the linearly modified equations of Equations (1)–(3), as shown in Figure 2. Meanwhile, the crustal stress of the three wells (shown in Figure 3a), including the maximum horizontal principal stress (SH_{max}), the minimum horizontal principal stress (SH_{min}), and the vertical principal stress (SV), were estimated using the empirical equation proposed by [43]. The estimated crustal stress values of the three wells were adopted as the initial conditions for the inversed analysis of the in-situ crustal stress in the target formation in the next section, in order to improve the convergence efficiency.

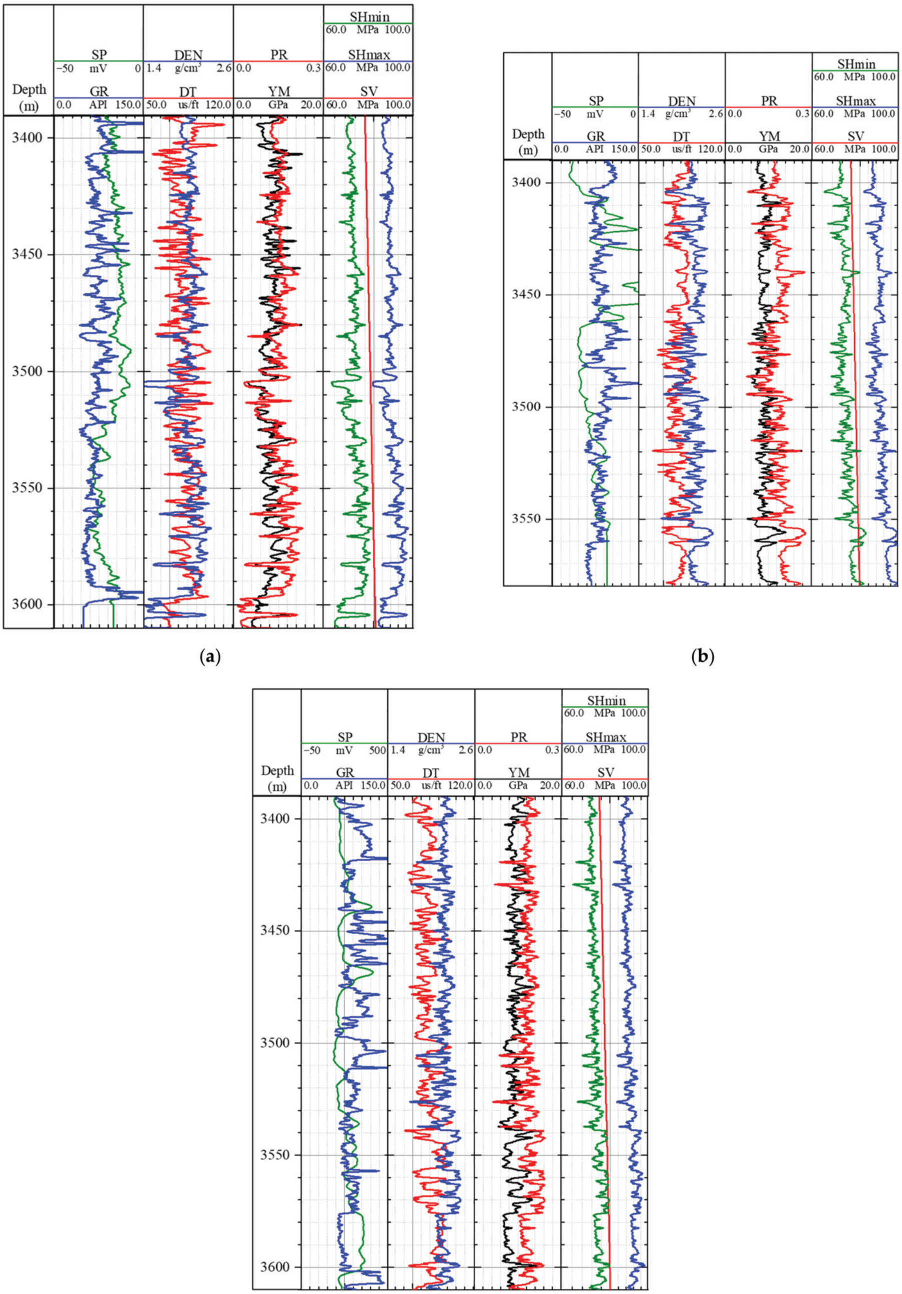

(**a**) (**b**)

(**c**)

Figure 2. Well logging and geomechanical properties profile of the target wells. (**a**) Well #1. (**b**) Well #2. (**c**) Well #3.

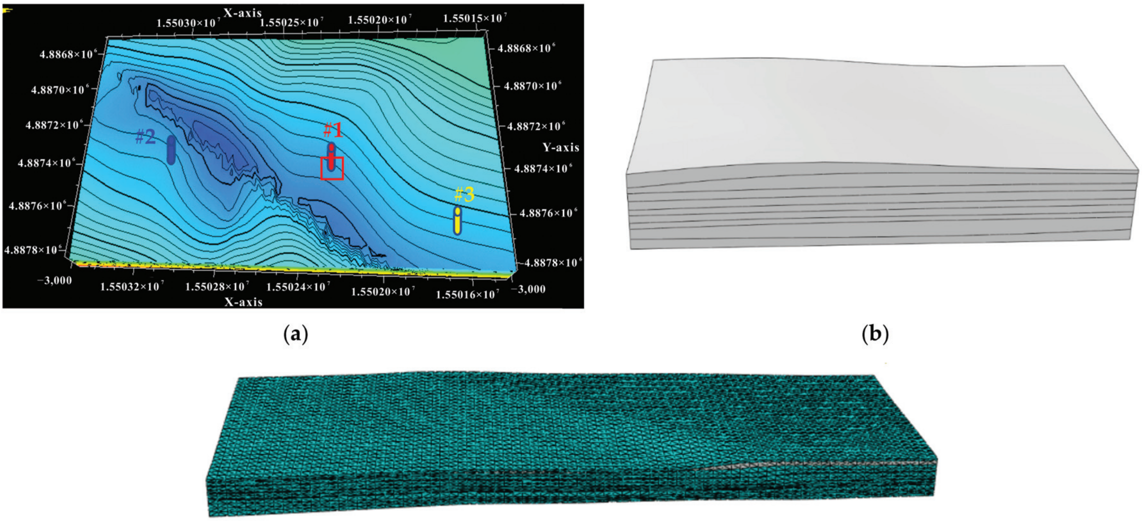

(**a**) (**b**)

(**c**)

Figure 3. FEM geomechanical modeling of the target reservoir. (**a**) Geological model and well location. (**b**) Geometry of FEM geomechanical model. (**c**) FEM geomechanical model mesh.

The geological model of the reservoir horizon in the target UGS site was extracted, which was 3800 m × 1740 m on the plane and divided into 9 layers, as shown in Figure 3a. The locations of the three target wells described in this article are also marked in Figure 3a. The geological model was converted into an FEM geomechanical model using 3DMAX and Abaqus software, as shown in Figure 3b,c. Based on the mechanical properties from the well logging data, the rock properties near the well zone were initialized in the geological model. Taking the rock properties of the three wells as the restrictions, the rock properties of reservoir (e.g., the density, YM and PR) could be mapped in the extracted 3D geological model by weighted interpolation analysis method based on the seismic data and the fine geological model, as shown in Figure 4a–c.

2.2. Mathematical Model of the Yield Criterion for Simulation

The Drucker–Prager yield criterion is adopted for the plastic deformation of rock [44],

$$\sqrt{J_2} = A + BI_1 \tag{4}$$

where I_1 is the first invariant of the Cauchy stress and J_2 is the second invariant of the deviatoric part of the Cauchy stress. The constants A, B are determined from experiments. If assuming that the Drucker–Prager yield surface circumscribes the Mohr–Coulomb yield surface, then the expressions for A and B are as follows [44]:

$$\begin{aligned} A &= \frac{6c\cos\phi}{\sqrt{3}(3-\sin\phi)} \\ B &= \frac{2\sin\phi}{\sqrt{3}(3-\sin\phi)} \end{aligned} \tag{5}$$

where c and ϕ are the cohesive strength and friction angle, respectively.

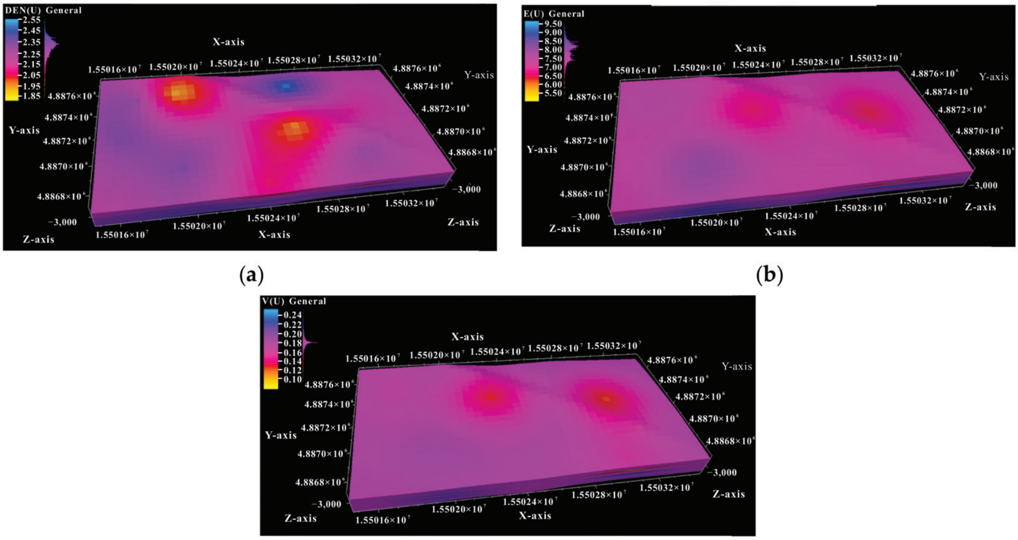

(**a**) (**b**) (**c**)

Figure 4. Mapped rock properties based on the FEM model of the target reservoir. (**a**) Density (unit: g/cm^3) distribution of the target formation. (**b**) Young's Modulus (unit: GPa) distribution of the target formation. (**c**) Poisson's Ratio distribution of the target formation.

The equivalent plastic strain (ε_p) is adopted as the failure criterion of the rock near the wellbore [44],

$$\varepsilon_p = \sqrt{\frac{2}{3}\left(\varepsilon_{px}^2 + \varepsilon_{py}^2 + \varepsilon_{pz}^2\right)} \tag{6}$$

where ε_{px}, ε_{py}, ε_{pz} and are the plastic strains in the three principal stress directions, dimensionless. According to the previous studies, the well is believed to be sanding when the equivalent plastic strain exceeds the critical strain limit (CSL), which was usually defined as from 3‰ to 8‰ [30,45,46]. In this study, the CSL of 5‰ is used.

3. Results and Discussion

3.1. Inversion of the In-Situ Stress Distribution

In this article, the in-situ stress field of the target formation was deduced through inversed analysis coupled FEM and genetic algorithm (GA), based on the existing known stress data and the seismic data of the measured points. The workflow of the inversed analysis on the in-situ stress is presented in Figure 5. In the inversed analysis, the displacement boundary variables were treated as the target parameters, and the in-situ stresses at the wellbore #1 as the objective function. The FEM geomechanical model was constructed on the ABAQUS software platform to calculate the in-situ stress state. The simulations on the stress equilibrium of FEM geomechanical model were conducted according to the initialization of the crustal stress in Section 2.1. Then, the ABAQUS software coupling the GA code via MATLAB software platform was employed to realize the reversion analysis of the in-situ crustal stress. The GA codes generated different boundary displacement loading variables and transferred them to ABAQUS for in-situ stress calculation, and then the errors were obtained by comparison with the objective function of the measured stress value of well #1. When the errors were beyond the threshold, the GA codes would generate new arrays of the inputted parameters and conduct new iterations. As shown in Figure 6, as genetic iterations increase, the error gradually decreases and it is tending towards stability when the iterations are more than 500. The inversed analysis process was regarded as being complete.

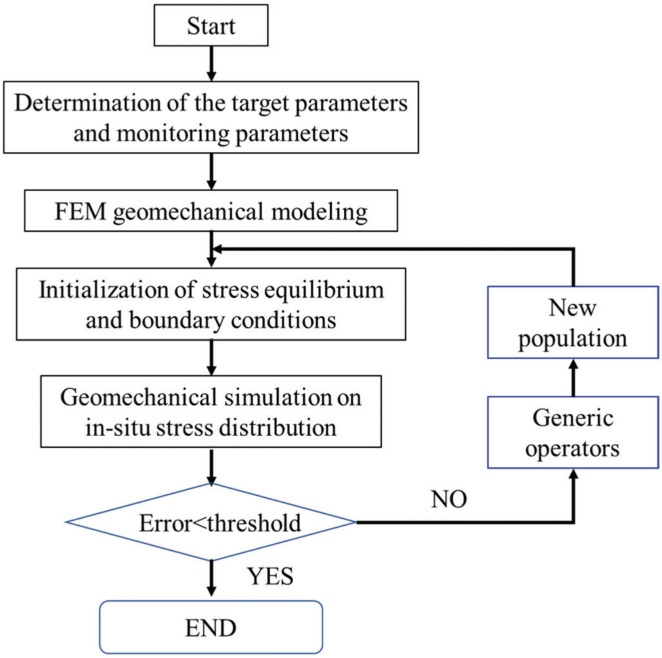

Figure 5. Reversion of in-situ geostress coupling FEM simulation with GA.

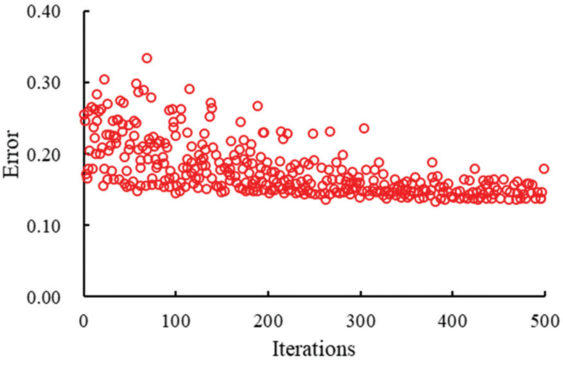

Figure 6. Calculation error vs. genetic iterations.

The distribution of the in-situ crustal stress after the inversion analysis is presented in Figure 7, including the vertical principal stress, maximum and minimum horizontal principal stress. The results follow the convention of elastic-plastic mechanics, that is, tensile stress is positive and compressive stress is negative. The maximum horizontal principal stress ranges from 92.6 MPa to 93.7 MPa, minimum horizontal principal stress is 67.9 MPa to 76.0 MPa and vertical principal stress is 79.4 MPa to 83.2 MPa. The direction of the maximum horizontal primary stress is in the *x* direction.

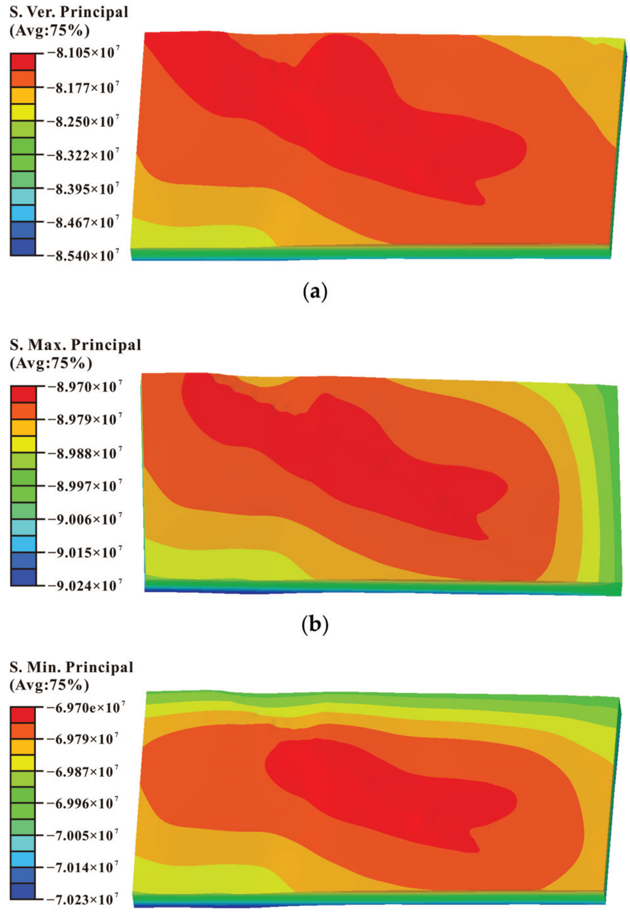

(**a**)

(**b**)

(**c**)

Figure 7. Simulation results of distribution of three principal stresses. (**a**) Vertical principal stress. (**b**) Maximum horizontal principal stress. (**c**) Minimum horizontal principal stress.

3.2. Simulation on Sanding Prediction of Well Failure in UGS

As shown in Figure 8a, three wells (named #1, #2, and #3) in the target reservoir were simulated for the sand onset prediction of well failure during the gas injection and withdrawal of the UGS. Based on the stress distribution obtained by inversed analysis, the sub model of the zone near the wellbore was established, as shown in Figure 8a. The diameter of the gas wellbore in the UGS is 99 mm, as shown in Figure 8b,c. The side length of the sub model is 2 m, about 20 times larger than the wellbore diameter, in order to reduce the boundary effect. The corresponding crustal stress distribution was extracted (as shown in Figure 8d), and then it was imposed on the sub model while the surrounding surfaces and the bottom surface were defined as fixed support. According to the Saint-Venant's principle, the equivalent treatment of the crustal stress will not change the stress distribution of the zone near a well. The stress distribution of the well #1, #2, and #3 after the equilibrium of the crustal stress was presented in Figure 9, including the equivalent stress and the stress along x, y, z directions. The results indicate that the maximum horizontal principal stress (in x direction) ranges from 84.6 to 91.2 MPa, the minimum horizontal principal stress (in y direction) ranges from 64.6 to 72.0 MPa, and the vertical Intermediate principal stress (in z direction) ranges from 77.8 to, 82.0 MPa. The three wells are in strike-slip stress state.

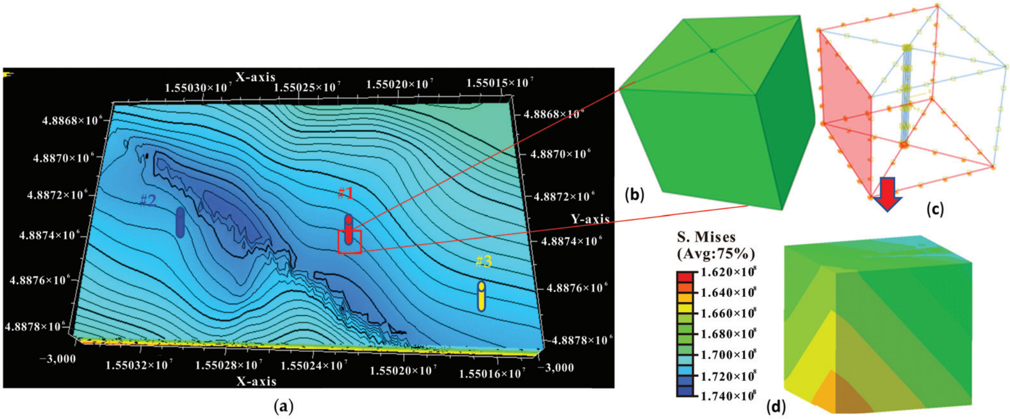

Figure 8. Extraction of the sub-model with stress field surrounding the target well. (**a**) Geological model of target formation. (**b**) Model of the zone near well. (**c**) Schematic of wellbore and boundary conditions. (**d**) Schematic of crustal stress for the sub.

The well drilling was simulated through deactivating the wellbore elements in ABAQUS. At the same time, the static fluid column pressure (equal to the static pressure of the mud column with density of 1.0 g/cm^3 at vertical height) was applied to the inner wall to ensure the stability of the wellbore and simulate the process of balanced drilling. Then the static fluid column pressure in the wellbore was decreased to simulate the gas production process. The amplitude function of the equivalent plastic strain around the wellbore was investigated. When the equivalent plastic strain exceeded the CSL, the wellbore was considered to be at high risk of sanding. The maximum principal stress and the equivalent plastic strain distribution of the wells when exceeding the CSL are presented in Figure 10. The maximum equivalent plastic strain distributed in the direction of maximum principal stress. As usual, compressive stress is negative. The corresponding differential pressures of the gas production are the critical pressure of the wellbore sanding, which are 5.59 MPa, 3.98 MPa and 4.01 MPa for well #1, well #2 and well #3 when the pressure of the gas storage is 30 MPa, respectively. During the gas injection and withdrawal of UGS, sand onset occurred at well #2 and #3 in the gas production when the differential pressure of the increased to 3.8 MPa and 4.1 MPa. The simulation results showed good agreements with the field-measured benchmark data.

3.3. Influencing Factors of the Critical Pressure Difference for Sanding in UGS

The rock strength is the intrinsic factor for the critical differential pressure (CDP) of sanding in the wellbore during gas production. The experimental results showed that with the increase of moisture contents, and cycling times of gas injection and withdrawal, the rock strength of the reservoir decreases, which affects the critical sand production pressure difference of gas wells. Taking well #1 as an example, the effects of water saturation (ranging from 10% to 40%), and cycling times of gas injection and withdrawal (ranging from 40 to 200 cycling times) on the critical differential pressure were simulated and analyzed. The maximum principal stress and the equivalent plastic strain distribution of the wells for different moisture contents and cycling times when exceeding the CSL are presented in Figures 11 and 12. The maximum equivalent plastic strain distributed in the direction of maximum principal stress. The CDP for different moisture contents are presented in Figures 13 and 14. The results indicated that the CDP decreased with increase of the moisture content and the cycling times. The functional relationship between the CDP and the moisture content and the cycling times were fitted and are presented in Figures 13 and 14.

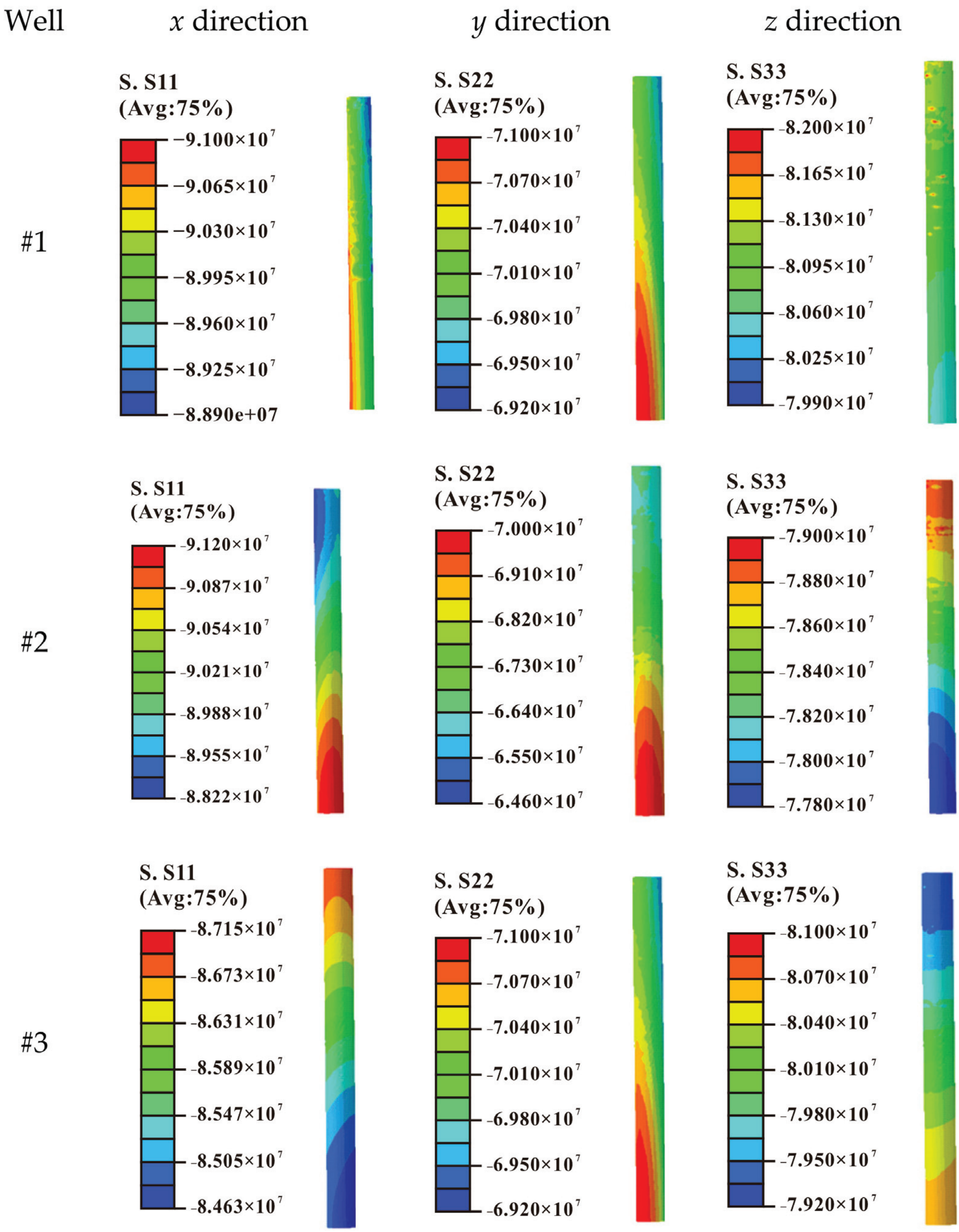

Figure 9. Stress distribution of the well zone after crustal stress initialization.

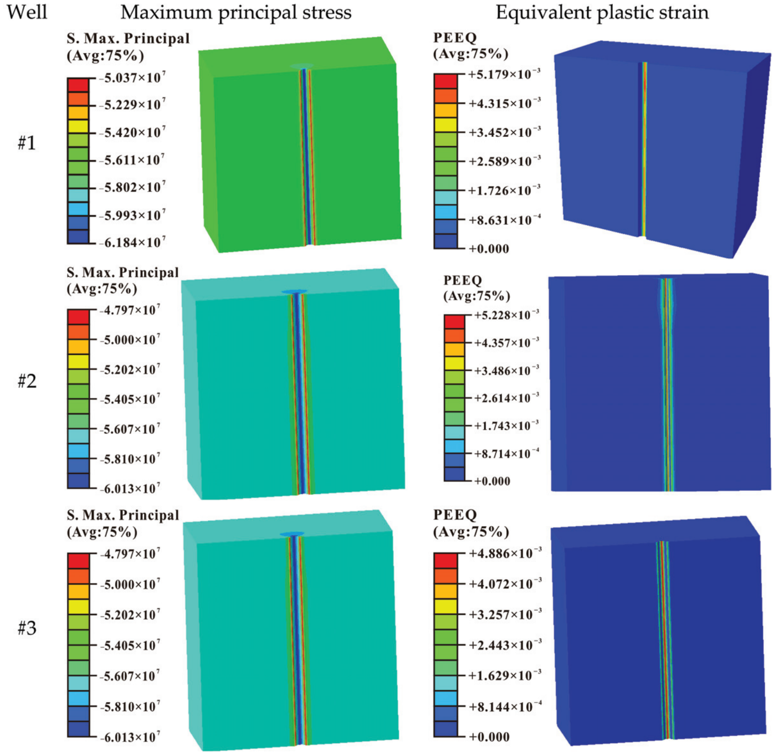

Figure 10. Maximum principal stress and the equivalent plastic strain distribution of the wells at the CSL.

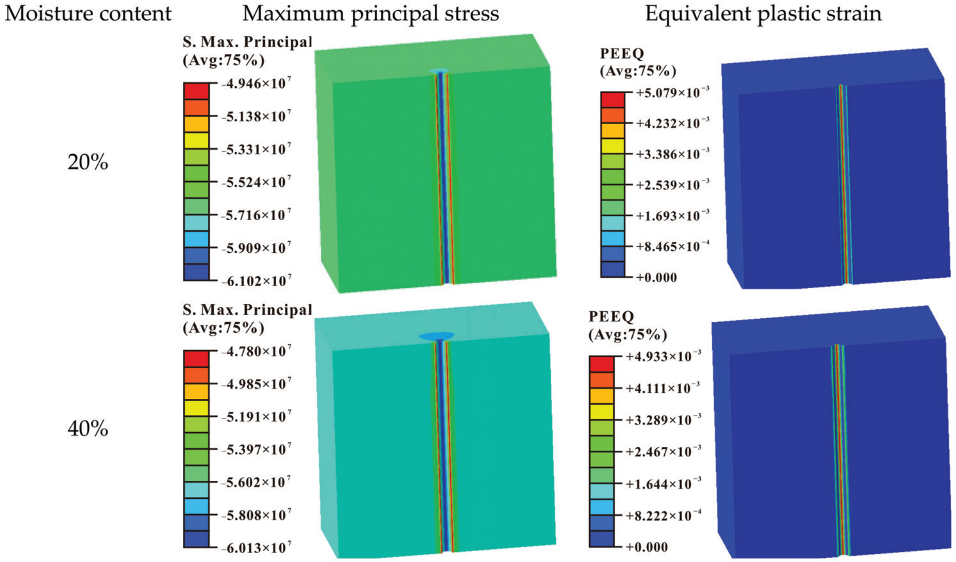

Figure 11. Maximum principal stress and the equivalent plastic strain distribution of the wells at CSL for different moisture contents.

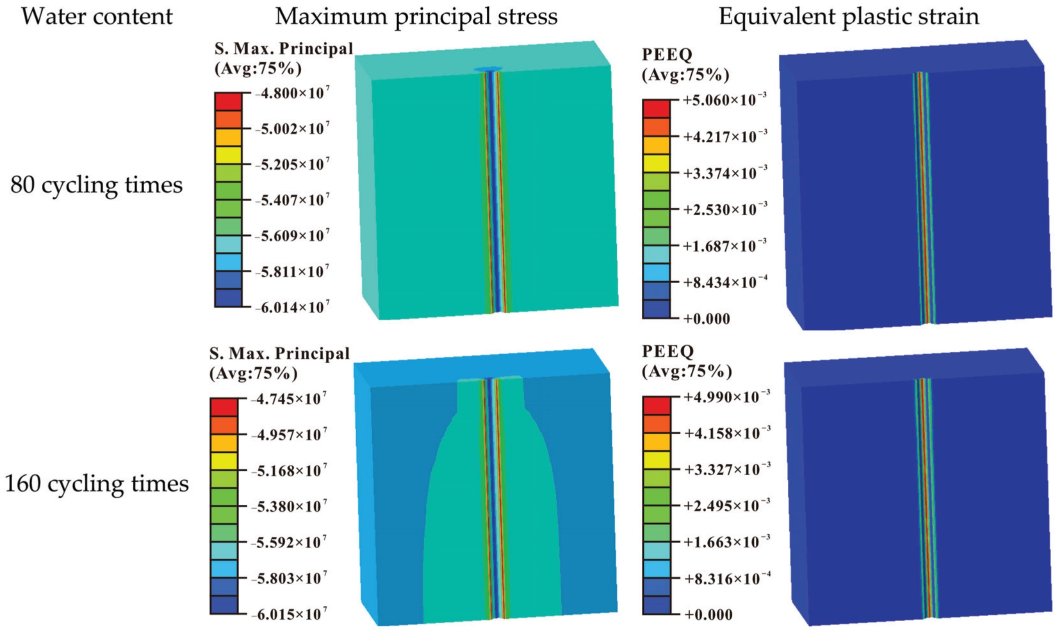

Figure 12. Maximum principal stress and the equivalent plastic strain distribution of the wells at CSL for different cycling times of gas injection and withdrawal.

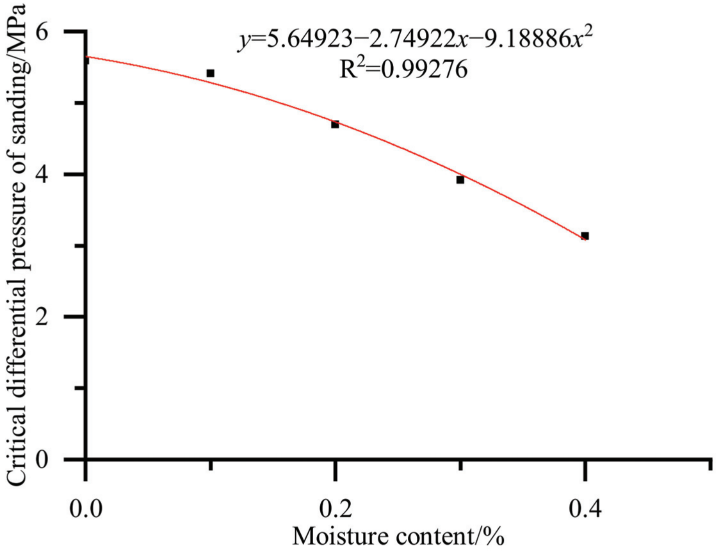

Figure 13. Critical differential pressure of gas production for different moisture content.

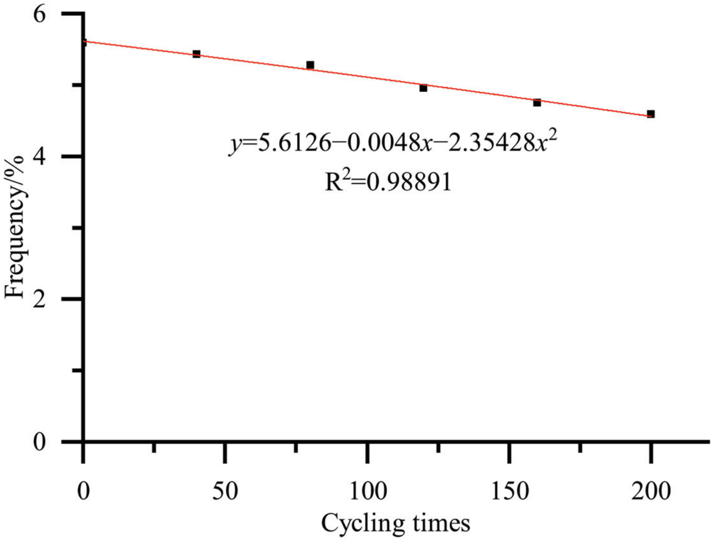

Figure 14. Critical differential pressure of gas production for different cycling times of gas injection and production.

4. Conclusions

A depleted gas reservoir was taken as the potential UGS site to investigate the CDP of sanding production in the wellbore in this study. Laboratory tests on the rock samples drilled from three target wells were conducted to acquire the basic rock properties. The in-situ mechanical properties of the rock were estimated by coupling the laboratory test results and well-logging data. The in-situ stress field of the target formation was then deduced through inversed analysis coupled finite element method (FEM) and genetic algorithm (GA), based on the existing known stress data and the seismic data of the measured points. The CDP of the wellbore in the UGS and the influencing factors were also predicted and analyzed. The following conclusions can be reached:

(1) Based on the experimental results, the functional relationship between key rock mechanics and rock density, such as compressive strength, elastic modulus, and Poisson's ratio, was established. Coupling with the well-logging curves, the mechanical properties of the rock in the coring well could be calculated accurately.

(2) The 3D geological model of the reservoir for UGS was transformed to a finite element geomechanics model, and was used as inputs for the inversed analysis of in-situ crustal stress. Adopting the measured in-situ stress in the samples of Well #1 as the target parameter, the crustal stress of the reservoir was determined coupling with the genetic algorithm and geomechanical simulation on Abaqus software.

(3) Based on the stress distribution obtained by inversed analysis, the sub model of the zone near the wellbore was established. Numerical simulations on the well drilling and the cycling of high-speed injection-withdrawal were conducted. Taking the CSL of 5‰ as the sanding criterion of the wellbore, the CDPs of the gas production in the UGS were predicted, which are 5.59 MPa, 3.98 MPa, and 4.01 MPa for well #1, well #2 and well #3 when the pressure of the gas storage is 30 MPa, respectively. The simulation results showed good agreement with the field-measured benchmark data of well #2 and well #3.

(4) The effects of moisture contents (ranging from 10% to 40%), and cycling times of gas injection and withdrawal (ranging from 40 to 200 cycling times) on the critical differential pressure were simulated and analyzed. The results indicated that the CDP decreased with increase of the moisture content and the cycling times.

This study provides a workflow of the sanding prediction coupling laboratory tests, inversed analysis with well logging data and numerical simulations, which requires plenty of drilled cores to acquire the accurate mechanical properties of the rock in the production wells of the UGS. Some testing technology based on the rock cuttings will decrease the coring and experimental costs. Meanwhile, more in-situ crustal stress data will contribute to the accuracy of the CDP prediction.

Author Contributions: Conceptualization, R.S.; Data curation, R.S., P.Z. and X.T.; Funding acquisition, R.S.; Investigation, J.L.; Software, F.H.; Validation, Z.L.; Visualization, Z.L.; Writing–original draft, J.L.; Writing–review & editing, J.L. All authors have read and agreed to the published version of the manuscript.

Funding: This research was funded by [Knowledge Innovation Program of Wuhan-Basic Research] grant number [2022010801010158]. The APC was funded by [Knowledge Innovation Program of Wuhan-Basic Research].

Institutional Review Board Statement: Not applicable.

Informed Consent Statement: Not applicable.

Data Availability Statement: All the data and materials used in this paper are available from the corresponding author upon request.

Acknowledgments: This work was financially supported by Knowledge Innovation Program of Wuhan-Basic Research (2022010801010158).

Conflicts of Interest: The authors declare that they have no known competing financial interest or personal relationships that could have appeared to influence the work reported in this paper.

Abbreviations

3D	Three dimensional
ATWC	Advanced thick-walled cylinder ()
BEM	Boundary Element Method
CSL	Critical strain limit
CDP	Critical differential pressure
DEM	Discrete Element Method
FDM	Finite Difference Method
FEM	Finite element method
GA	Genetic algorithm
NG	Natural gas
PR	Poisson's Ratio
TWC	Thick-wall cylinder strength
UCS	Unconfined compressive strength
UGS	Underground gas storage
YM	Young's Modulus

References

1. Song, R.; Cui, M.; Liu, J. Single and multiple objective optimization of a natural gas liquefaction process. *Energy* **2017**, *124*, 19–28. [CrossRef]
2. Song, R.; Sun, S.; Liu, J.; Yang, C. Pore scale modeling on dissociation and transportation of methane hydrate in porous sediments. *Energy* **2021**, *237*, 121630. [CrossRef]
3. Song, R.; Liu, J.; Yang, C.; Sun, S. Study on the multiphase heat and mass transfer mechanism in the dissociation of methane hydrate in reconstructed real-shape porous sediments. *Energy* **2022**, *254*, 124421. [CrossRef]
4. Ali, A. Data-driven based machine learning models for predicting the deliverability of underground natural gas storage in salt caverns. *Energy* **2021**, *229*, 120648. [CrossRef]
5. Gümrah, F.; Katircioglu, D.; Aykan, Y.; Okumus, S.; Kilincer, N. Modeling of gas demand using degree-day concept: Case study for Ankara. *Energy Sources* **2001**, *23*, 101–114.
6. Verga, F. What's conventional and what's special in a reservoir study for underground gas storage. *Energies* **2018**, *11*, 1245. [CrossRef]

7. Matos, C.R.; Carneiro, J.F.; Silva, P.P. Overview of large-scale underground energy storage technologies for integration of renewable energies and criteria for reservoir identification. *J. Energy Storage* **2019**, *21*, 241–258. [CrossRef]
8. Confort, M.J.F.; Mothe, C.G. Estimating the required underground natural gas storage capacity in Brazil from the gas industry characteristics of countries with gas storage facilities. *J. Nat. Gas Sci. Eng.* **2014**, *18*, 120–130. [CrossRef]
9. Arfaee, M.I.R.; Sola, B.S. Investigating the effect of fracture–matrix interaction in underground gas storage process at condensate naturally fractured reservoirs. *J. Nat. Gas Sci. Eng.* **2014**, *19*, 161–174. [CrossRef]
10. Vilarrasa, V.; De Simone, S.; Carrera, J.; Villaseñor, A. Unraveling the causes of the seismicity induced by underground gas storage at Castor, Spain. *Geophys. Res. Lett.* **2021**, *48*, e2020GL092038. [CrossRef]
11. Schultz, R.A.; Evans, D.J. Occurrence frequencies and uncertainties for US underground natural gas storage facilities by state. *J. Nat. Gas Sci. Eng.* **2020**, *84*, 103630. [CrossRef]
12. Zhang, S.; Yan, Y.; Sheng, Z.; Yan, X. Uncertainty failure risk quantitative assessments for underground gas storage near-wellbore area. *J. Energy Storage* **2021**, *36*, 102393. [CrossRef]
13. McNulty, J.W. *An Experimental Study of Arching in Sand (No. 1)*; Waterways Experiment Station: Vicksburg, MS, USA, 1965.
14. Clearly, M.P.; Melvan, J.J.; Kohlhaas, C.A. The Effect of Confining Stress and Fluid Properties on Arch Stability in Unconsolidated Sands. In Proceedings of the SPE Annual Technical Conference and Exhibition, Las Vegas, NV, USA, 23–26 September 1979.
15. Tippie, D.B.; Kohlhaas, C.A. Effect of Flow Rate on Stability of Unconsolidated Producing Sands. In Proceedings of the Fall Meeting of the Society of Petroleum Engineers of AIME, Las Vegas, NV, USA, 30 September–3 October 1973.
16. Ranjith, P.; Perera, M.; Perera, W.; Wu, B.; Choi, S. Effective parameters for sand production in unconsolidated formations: An experimental study. *J. Pet. Sci. Eng.* **2013**, *105*, 34–42. [CrossRef]
17. Hall, C.J.; Harrisberger, W.H. Stability of Sand Arches: A Key to Sand Control. *J. Pet. Technol.* **1970**, *22*, 821–829. [CrossRef]
18. Rahman, K.; Khaksar, A.; Kayes, T.J. Minimizing Sanding Risk by Optimizing Well and Perforation Trajectory Using an Integrated Geomechanical and Passive Sand-Control Approach. In Proceedings of the SPE Annual Technical Conference and Exhibition, Denver, CO, USA, 21–24 September 2008.
19. Cook, J.M.; Bradford, I.D.R.; Plumb, R.A. A study of the physical mechanisms of sanding and application to sand production prediction. In Proceedings of the European Petroleum Conference, London, UK, 25–27 October 1994.
20. Bianco, L.C.B.; Halleck, P.M. Mechanisms of arch instability and sand production in two-phase saturated poorly consolidated sandstones. In Proceedings of the SPE European Formation Damage Conference, The Hague, The Netherlands, 21–22 May 2001.
21. Honari, S.; Seyedi Hosseininia, E. Particulate Modeling of Sand Production Using Coupled DEM-LBM. *Energies* **2021**, *14*, 906. [CrossRef]
22. Al-Shaaibi, S.K.; Al-Ajmi, A.M.; Al-Wahaibi, Y. Three dimensional modeling for predicting sand production. *J. Pet. Sci. Eng.* **2013**, *109*, 348–363. [CrossRef]
23. Arbelaez-Londoño, A.; Osorio, G.; Alzate-Espinosa, G. The Wormholes Formation During the Cold Heavy Oil Production with Sand (CHOPS). In Proceedings of the ISRM 8th International Symposium Geomechanics, Bucaramanga, Colombia, 6–10 May 2019.
24. Veeken, C.A.M.; Davies, D.R.; Kenter, C.J.; Kooijman, A.P. Sand production prediction review: Developing an integrated approach. In Proceedings of the SPE Annual Technical Conference and Exhibition, Dallas, TX, USA, 6–9 October 1991.
25. Zhang, R.; Shi, X.; Zhu, R.; Zhang, C.; Fang, M.; Bo, K.; Feng, J. Critical drawdown pressure of sanding onset for offshore depleted and water cut gas reservoirs: Modeling and application. *J. Nat. Gas Sci. Eng.* **2016**, *34*, 159–169. [CrossRef]
26. Ou, Q.; Yang, J.; Zhang, Z.; Liu, L.; Qu, X.; Hong, Y. Prediction of high-temperature and high-pressure well sand production in the DF gas field. In Proceedings of the 55th US Rock Mechanics/Geomechanics Symposium, Virtual, 18–25 June 2021.
27. Zhou, S.; Sun, F. *Sand Production Management for Unconsolidated Sandstone Reservoirs*; Petroleum Industry Press: Beijing, China, 2016. [CrossRef]
28. Song, R.; Wang, Y.; Ishutov, S.; Zambrano-Narvaez, G.; Hodder, K.J.; Chalaturnyk, R.J.; Sun, S.; Liu, J.; Gamage, R.P. A Comprehensive Experimental Study on Mechanical Behavior, Microstructure and Transport Properties of 3D-printed Rock Analogs. *Rock Mech. Rock Eng.* **2020**, *53*, 5745–5765. [CrossRef]
29. Zuloaga, P.; Yu, W.; Miao, J.; Sepehrnoori, K. Performance evaluation of CO_2 Huff-n-Puff and continuous CO_2 injection in tight oil reservoirs. *Energy* **2017**, *134*, 181–192. [CrossRef]
30. Deng, J.; Wang, L.; Li, P.; Zhao, W. The Critical Pressure Difference Prediction of Sand Production in Deepwater Sandstone Gas Reservoirs. *Pet. Sci. Technol.* **2013**, *31*, 1925–1932. [CrossRef]
31. Nordgren, R.P. Strength of well completions. In Proceedings of the 18th US Symposium on Rock Mechanics (USRMS), Golden, CO, USA, 22–24 June 1977.
32. Almisned, O.A. A Model for Predicting Sand Production from Well Logging Data. Ph.D. Thesis, The University of Oklahoma, Norman, OK, USA, 1995.
33. Morita, N.; Whitfill, D.L.; Fedde, O.P.; Lovik, T.H. Parametric Study of Sand-Production Prediction: Analytical Approach. *SPE Prod. Eng.* **1989**, *4*, 25–33. [CrossRef]
34. Vaziri, H.; Barree, B.; Xiao, Y.; Palmer, I.; Kutas, M. What is the magic of water in producing sand? In Proceedings of the SPE Annual Technical Conference and Exhibition, San Antonio, TX, USA, 29 September–2 October 2002.
35. Rahmati, H.; Jafarpour, M.; Azadbakht, S.; Nouri, A.; Vaziri, H.; Chan, D.; Xiao, Y. Review of Sand Production Prediction Models. *J. Pet. Eng.* **2013**, *2013*, 864981. [CrossRef]

36. Ranjith, P.G.; Perera, M.S.A.; Perera, W.K.G.; Choi, S.K.; Yasar, E. Sand production during the extrusion of hydrocarbons from geological formations: A review. *J. Pet. Sci. Eng.* **2014**, *124*, 72–82. [CrossRef]
37. Subbiah, S.K.; Samsuri, A.; Mohamad-Hussein, A.; Jaafar, M.Z.; Chen, Y.R.; Kumar, R.R. Root cause of sand production and methodologies for prediction. *Petroleum* **2021**, *7*, 263–271. [CrossRef]
38. Nouri, A.; Vaziri, H.; Kuru, E.; Islam, R. A comparison of two sanding criteria in physical and numerical modeling of sand production. *J. Pet. Sci. Eng.* **2006**, *50*, 55–70. [CrossRef]
39. Volonté, G.; Scarfato, F.; Brignoli, M. Sand prediction: A practical finite-element 3D approach for real field applications. *SPE Prod. Oper.* **2013**, *28*, 95–108. [CrossRef]
40. Gui, F.; Khaksar, A.; Van Zee, W.; Cadogan, P. Improving the Sanding Evaluation Accuracy by Integrating Core Tests, Field Observations and Numerical Simulation. In Proceedings of the SPE Asia Pacific Oil & Gas Conference and Exhibition, Perth, Australia, 25–27 October 2016. [CrossRef]
41. Lu, Y.; Xue, C.; Liu, T.; Chi, M.; Yu, J.; Gao, H.; Xu, X.; Li, H.; Zhuo, Y. Predicting the critical drawdown pressure of sanding onset for perforated wells in ultra-deep reservoirs with high temperature and high pressure. *Energy Sci. Eng.* **2021**, *9*, 1517–1529. [CrossRef]
42. Cornelio, J.; Ershaghi, I. A Machine Learning Approach for Predicting Rock Brittleness from Conventional Well Logs. In Proceedings of the SPE Eastern Regional Meeting, Charleston, WV, USA, 15–17 October 2019. [CrossRef]
43. Jingen, D.; Kangping, W.; Rongzun, H. In-situ stress determination at great depth by using acoustic emission technique. In Proceedings of the 35th US Symposium on Rock Mechanics (USRMS), Reno, NV, USA, 5–7 June 1995.
44. Park, S.-H.; Bang, K.-H.; Cho, J.-R. Structural Integrity Evaluation of a Reactor Cavity during a Steam Explosion for External Reactor Vessel Cooling. *Energies* **2021**, *14*, 3605. [CrossRef]
45. Santana, C.; Likrama, F. Workflow on Incorporating Thick-Walled Cylinder Test Results in Finite Element Models of near Wellbore for Sanding Prediction Studies. In Proceedings of the 50th US Rock Mechanics/Geomechanics Symposium, Houston, TX, USA, 26–29 June 2016.
46. Deng, F.; Yan, C.; Jia, S.; Chen, S.; Wang, L.; He, L. Influence of Sand Production in an Unconsolidated Sandstone Reservoir in a Deepwater Gas Field. *J. Energy Resour. Technol.* **2019**, *141*, 092904. [CrossRef]

energies

MDPI

Article

Effects of Grain Size and Layer Thickness on the Physical and Mechanical Properties of 3D-Printed Rock Analogs

Yao Wang [1,2,*], Shengjun Li [1], Rui Song [3,*], Jianjun Liu [3], Min Ye [4], Shiqi Peng [5] and Yongjun Deng [1,2]

[1] School of Civil Engineering and Architecture, Southwest University of Science and Technology, Mianyang 621010, China
[2] Shock and Vibration of Engineering Materials and Structures Key Lab of Sichuan Province, Southwest University of Science and Technology, Mianyang 621010, China
[3] State Key Laboratory of Geomechanics and Geotechnical Engineering, Institute of Rock and Soil Mechanics, Chinese Academy of Sciences, Wuhan 430071, China
[4] School of Mathematics and Physics, Southwest University of Science and Technology, Mianyang 621010, China
[5] Nuclear Power Institute of China, Chengdu 610000, China
* Correspondence: wangyao0927@swust.edu.cn (Y.W.); rsong@whrsm.ac.cn (R.S.)

Abstract: Due to the complexity of the sedimentary and diagenetic processes, natural rocks generally exhibit strong heterogeneity in mineral composition, physicochemical properties, and pore structure. Currently, 3D printed (3DP) rock analogs fabricated from sandy materials (silica sand) are widely applied to study the petrophysical and geomechanical characteristics of reservoir rocks, which provides an alternative and novel approach for laboratory tests to calibrate the environmental uncertainties, resolve up-scaling issues, and manufacture customized rock specimens with consistent structure and controllable petrophysical properties in a repeatable fashion. In this paper, silica sand with various grain sizes (GS) and Furan resin were used to fabricate rock analogs with different layer thicknesses (LTs) using the binder-jetting 3DP technique. A comprehensive experimental study was conducted on 3DP rock analogs, including helium porosity measurement, micro-CT scanning, SEM, and uniaxial compression. The results indicate that the LT and GS have a great influence on the physical properties, compression strength, and failure behavior of 3DP rock analogs. The porosity decreases (the difference is 7.09%) with the decrease in the LT, while the density and peak strength increase (showing a difference of 0.12 g/cm^3 and 5.67 MPa). The specimens printed at the 200 and 300 μm LT mainly experience tensile shear destruction with brittle failure characteristics. The ductility of the 3DP rocks increases with the printing LT. The higher the content of the coarse grain (CG), the larger the density and the lower the porosity of the specimens (showing a difference of 0.16 g/cm^3 and 8.8%). The largest peak compression strength with a mean value of 8.53 MPa was recorded in the specimens printed with CG (i.e., 100% CG), and the peak strength experiences a decrease with the increment in the content percentage of the fine grain (FG) (showing a difference of 2.01 MPa). The presented work helps to clarify the controlling factors of the printing process and materials characteristics on the physical and mechanical properties of the 3DP rock analogs, and allows for providing customizable rock analogs with more controllable properties and printing schemes for laboratory tests.

Keywords: 3D printing; sandstone; porosity; compression strength; failure behavior

Citation: Wang, Y.; Li, S.; Song, R.; Liu, J.; Ye, M.; Peng, S.; Deng, Y. Effects of Grain Size and Layer Thickness on the Physical and Mechanical Properties of 3D-Printed Rock Analogs. *Energies* **2022**, *15*, 7641. https://doi.org/10.3390/en15207641

Academic Editor: Dong Chen

Received: 12 September 2022
Accepted: 11 October 2022
Published: 16 October 2022

1. Introduction

The physical tests based on natural rock specimens are essential to many rock mechanics-related engineering applications including oil/gas exploitation, geothermal extraction, and geotechnical engineering [1,2]. Due to the complexity and strong heterogeneity in mineral composition and pore/fracture system of the rock mass in the natural scenario, quantitative characterization and accurate prediction of the mechanical response and failure behavior of rock mass are still challenging [3]. With certain assumptions, researchers have established various types of analytical models to help predict the stress–strain relationship of rock mass under load, although those models are limited to quantifying the stress–strain distribution and structural evolution of inner rock mass [4,5]. Numerical approaches allow us to visualize the stress and strain fields of inner rock mass, as well as capture structure evolution locally and globally [6]. However, the limitation of the numerical simulation lies in that the accuracy is highly dependent on the selection of constitutive models, as well as the calibration of the material parameters [7]. Moreover, it is necessary to make appropriate simplifications on the numerical model of the complex rock mass to balance the computation cost and accuracy. In view of this, the laboratory tests performed on rock specimens are still regarded as the most valuable and effective way in rock mechanics and geoscience studies to capture the physical and mechanical properties of rock mass, as well as to calibrate and validate the analytical models and numerical simulations.

The heterogeneity of natural rock specimens and the destructive laboratory tests not only limit the parallel experiments of the multi-factor response of the same sample, but also increase the uncertainty of test results from sample to sample. Therefore, researchers have attempted to fabricate artificial cores by casting and sand-filling methods to resolve the aforementioned limitations in laboratory tests [8–10]. However, the artificial cores made by those traditional methods failed to mimic the sedimentation process of the natural rocks, and they cannot yet guarantee a consistent inner structure from sample to sample. What is more, since those methods were very manually intensive and environmentally sensitive, the physical and mechanical properties can be varied from sample to sample, which may cause a large deviation in the test results [11,12]. Recent developments in 3D printing, also known as additive manufacturing (AM), in rock mechanics, and geosciences provide an alternative scheme for fabricating rock analogs with consistent structure and controllable properties in a more cost-effective and time-saving way [13–16]. Compared to traditional artificial cores, 3DP rock analogs fabricated from digital rock models can mimic rock texture accurately from the perspective of pore morphology and topological property [17]. Moreover, thousands of materials have been used for 3D printing to fabricate rock analogs to date. For that reason, 3D printing has been widely adopted to explore potential applications in the rock mechanics and geoscience engineering fields. Researchers have attempted to 3D print rock analogs with various types of polymer materials including photosensitive resin, plastic, and nylon [18–21]. However, those resin-based 3DP rock analogs were proved to be too ductile to simulate the brittleness of the natural rocks [22,23]. On the plus side, resin-based 3D printing techniques, such as the PolyJet and stereolithography (SLA), generally achieved a high printing resolution. Thus, those types of 3D printing techniques were very suitable to capture and characterize the pore morphology and pore-throat connectivity of natural rocks. Various studies have reported on the 3D printing of rock pore structure from 2D to 3D at microscale [24,25]. Among the resin-based 3DP rock analogs, transparent resin was the most widely used material for mimicking rock structure. Due to its transparent property, the internal stress field and fluids flow process could be visualized and dynamically monitored with the help of visualization techniques such as the photoelastic stress freeze method, digital image correlation (DIC), particle image velocimetry (PIV), and in situ CT scanning [26–28]. Several research teams have attempted to resolve the pore features of natural rocks at original dimensions without upscaling, which is essential for understanding the effect of pore morphology on fluids flow process [22,25]. In addition, complex fracture networks can be easily fabricated via 3D printing with controlled parameters including aperture, surface roughness, and orientation. On the basis of the 3DP fractured rock mass, the hydraulic characteristics are comprehensively investigated to validate those classical empirical equations and analytical model [29,30]. Although the super high resolution (~2 μm in theory) of the resin-based 3D printing allowed the printing of the pore/fracture structure at its original dimensions, the inherent physicochemical properties of the resin materials failed to mimic the surface roughness and fluid–solid interaction of the natural rocks. In view of this, those natural powder materials, such as silica sand, gypsum, and ceramic, were used to 3D-print rock analogs.

The powder-based 3D printing, such as binder jetting, utilizes a print head to jet "cement" onto the printing bed to bond the discrete grains [31]. Natural sandstones are mainly composed of mineral grains (quartz) and corresponding cementing agents, which makes the aforementioned powder-based 3D printing technique very suitable for fabricating sandstone analogs [32]. Compared to resin materials, 3DP rock analogs printed with natural powder materials have shown remarkable advantages in mimicking the surface physicochemical properties of natural rock, as well as the mechanical and deformation behaviors [33]. Researchers have attempted to 3D print rock analogs with ceramic and gypsum powders, and the ceramic powder-based specimens showed an abnormal brittleness property compared to the natural rocks, while the gypsum powder-based specimens showed good ductile strength. Various types of post-processing techniques have been utilized to improve the physical and mechanical properties of the 3DP rock analogs, which made the 3DP rock analogs suitable for mimicking many types of natural rocks, including brittle rocks and highly-stressed soft rocks [34–36]. With the powder-based 3DP rock analogs, researchers have explored the similarity of mechanical, transport, acoustic, and electrical properties in comparison to the natural rocks for potential applications in laboratory tests [37–40]. Flaws, i.e., single fracture or fracture networks, were embedded into the 3DP specimens to simulate the effect of the fracture system on the mechanical and transport properties of rock mass, as well as the fracture propagation evolution property by using acoustic emission (AE) and DIC measurements [41,42]. With the help of 3D printing, the defective rock specimens could be fabricated in a more customized fashion with various types of fracture length, aperture, number, orientation, spacing, and even the intersection angle of fracture networks [43,44]. Limited by the inherent properties of gypsum and ceramic powder, the pore geometry and morphology differed from the natural sandstone, which has a great influence on modeling transport properties in laboratory tests. Thus, silica sand (~98% quartz) was used to 3D print the rock analogs. Compared to ceramic and gypsum powder, the "sandstone" 3D printed with silica sand exhibits superior properties to mimic natural rocks both in macroscopic physical–mechanical properties and microstructural characteristics (e.g., mineral composition, grain cementing mode, and pore structure) [45,46]. Although the matrix material has a great influence on the properties of the 3DP specimens, the influence of the printing process (including printing orientation, LT, binder saturation, and drying time) on the specimens cannot be ignored. Previous studies have investigated the effect of different matrix materials and printing processes on the macroscopic properties of 3DP rock analogs individually. However, they failed to explore the effect of the GS on the 3DP rock analogs, which is a great influence factor on natural sandstone properties according to the corresponding studies on grain sorting during the sedimentary process [47,48]. In addition, corresponding studies related to the synergetic influence mechanism on the 3DP rock analogs between the GS of the matrix material and printing LT are still rare.

The main motivation of this study was to reveal the influencing mechanism of the sand GS and printing LT on the physical and mechanical properties of silica sand-based 3DP rock analogs. To this end, five types of matrix material combinations with different GS and three types of printing LT were designed to fabricate 3DP sandstones. The physical and mechanical properties of the 3DP sandstones were comprehensively investigated and the effect of the GS and printing LT on the 3DP sandstones was discussed in an integrated way. The present work might aid in clarifying the main controlling factors affecting the macroscopic properties of the 3DP rock analogs, and provides a recommended printing scheme for 3DP rock fabrication for various application scenarios and purposes in the rock mechanics and geoscience engineering fields.

2. Materials and Methods

2.1. 3D Printing of Rock Analogs

Prior to 3D printing, the corresponding digital model should be designed and processed first to meet the requirements of the 3D printer. Generally, the printing procedures differ from other 3D printing techniques, and the main printing process can be divided into four parts: digital data acquisition, model discretization, printing layer by layer, and post-processing [49]. The VX-2000 3D printer (VoxelJet, Suzhou Branch, China) was adopted to fabricate the silica sand-based 3DP rock analogs used in this study, which uses the binder jetting (BJ) technique for bonding silica sand with an organic binder, as shown in Figure 1a. According to the manufacturer's datasheets, the printer used in this study has a large printing volume of 2000 L with a high printing resolution (plane) of up to 300 dpi and a low printing LT of ~200 μm.

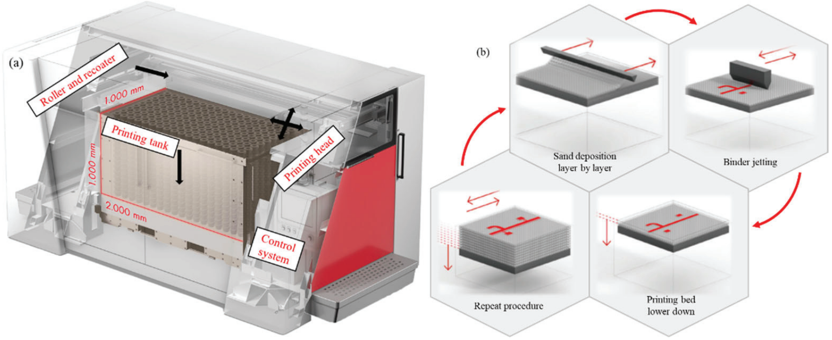

Figure 1. Schematic of the internal structure (**a**) and the main printing procedure (**b**) of the VX-2000 3D printer (the black arrows show the working orientation of different components).

The main manufacturing process of the 3D printer is as follows: Prior to printing, the silica sand is pre-mixed with acid activator (p-toluene sulfonic acid) with a certain ratio and loaded into the recoater. Then, the recoater moves from left to right above the printing bed in the job box to deposit the sands, followed by the rotating roller behind the recoater to spread the sands. After that, the print head passes over the printing bed to jet binder on the sand layer to form the bonding neck at the designed location controlled by the digital model. Afterwards, the heater travels over the printing bed to accelerate the curing process between layers. The printing bed is then lowered by one layer with a designed LT, and the aforementioned procedures are repeated until the objective is complete, as shown in Figure 1b. After the printing process, the job box is removed from the printer. No waiting times are required since an adequate level of unpacking strength of the printing objective already forms during the printing process. To facilitate the curing of the binder, as well as to remove the extra moisture to achieve designed strength, the job box is placed into a furnace to dry the specimens at 80 °C [16]. After the drying process, the rock analogs are removed from the job box, and rough cleaning is conducted manually using brushes to remove the unbound sands. More intensive cleaning can be carried out by compressed air.

2.2. Matrix Material and Printing Parameters

The silica sands with different GS were utilized as printing matrix material in this study (Figure 2). The CS (GS 19 type) and FS (GS 12 type) purchased from the VoxelJet, Suzhou Branch, China, have a medium grain size of 190 and 120 μm, respectively, and according to vendor datasheets, both silica sands are composed of ~98% quartz. Five types of blends of sand mixture were designed with coarse and fine sands, i.e., 100% CS (Type I), 70% CS and 30% FS (Type II), 50% CS and 50% FS (Type III), 30% CS and 70% FS (Type IV), and 100% FS (Type V), and the ratios of the different sands were determined by weight. The furan resin (the active ingredients consist of 70–90% α-furfuryl alcohol, 5–15% bisphenol A, 1–10% resorcinol, and 0.1–0.2% 3-aminopropyltriethoxysilane) purchased from the ASK (Zhejiang) New Materials Technology Co., Ltd. was chosen as the binder. The default setting of binder saturation was 10% for all the 3DP rock analogs in this study.

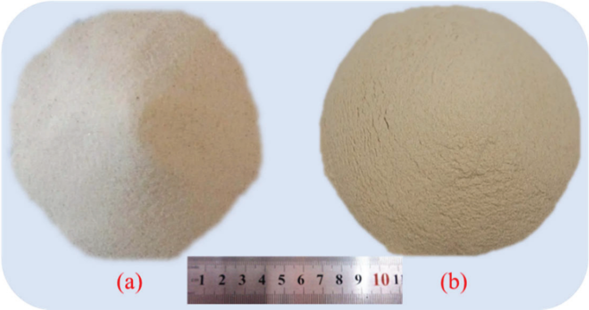

Figure 2. Silica sand used in this study with different grain sizes (**a**) coarse; (**b**) fine.

The printing resolution was set to 300 dpi on the plane, and the printing direction was along the *z* direction. For different types of sand mixtures, 200 μm LT was set to print rock analogs to investigate the effect of the GS on 3DP rocks. Type I sand mixture was used to print rock analogs with various LTs of 200 μm, 300 μm, and 400 μm to investigate the effect of LT on 3DP rocks. The designed schemes of the sand mixtures and printing parameters for 3DP rock fabricating used in this study are shown in Table 1. In this study, the 3DP rock specimens were fabricated in cylindrical shape with two types of dimensions, i.e., 50 mm × 100 mm for UCS testing, and 25 mm × 50 mm for microscopic structure characterization followed by the ASTM D4543-19 [50], as shown in Figure 3.

Table 1. Printing schemes of 3DP rocks.

	Sand Mixture	LT/μm		Sand Mixture	LT/μm
Group I	Type I	200	**Group II**	Type I	200
	Type II				300
	Type III				400
	Type IV				
	Type V				

Note that the default settings of binder saturation, printing resolution, and orientation are the same for the two groups.

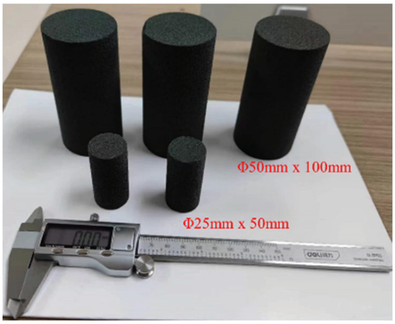

Figure 3. 3DP rock specimens of different sizes (The large cores and small cores are used for mechanical testing and microscopic structure characterization, respectively).

2.3. Uniaxial Compression Testing

The unconfined compressive strength (UCS) of the 3DP rock analogs was tested following ASTM D7012-14e1 [51] on an ETM105D universal material testing system (Figure 4) located in the Experimental Center for Structure and Mechanics, at Southwest University of Science and Technology. Two copies of each type of 3DP rock were used for UCS testing to reduce the testing deviation. The testing system has a maximum operating load of up to 100 KN, and the measurement accuracy of the force and deformation control rate can achieve 0.005~5% and 0.02~5% FS/s, respectively. During the compression, the sample was pre-loaded at a rate of 0.5 kN/s to establish contact between the rock sample and the loading plate. Afterward, the force control mode was utilized to initiate the loading procedure with a rate of 0.05 KN/s until failure.

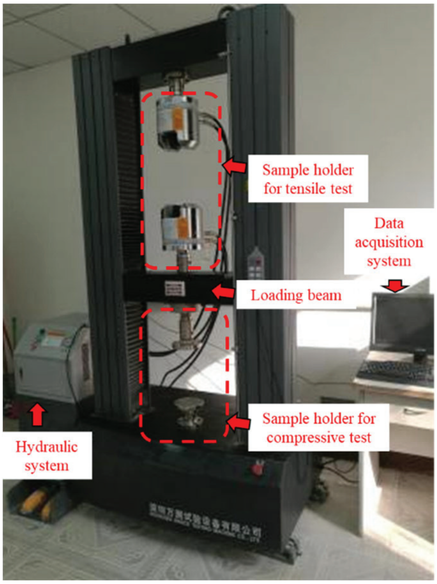

Figure 4. ETM105D universal material testing system.

2.4. Physical Properties Measurements

The physical dimensions and weight of the 3DP rocks were measured by vernier caliper and electronic balance manually prior to other tests to calculate the bulk density. The porosity was determined by measuring the grain phase volume of the 3DP rocks by using helium pycnometry under laboratory conditions. A QYK-II helium porosimeter was utilized to measure the grain phase volume located at the Material Testing Center at Southwest University of Science and Technology. The details of the test processes can be referred to in our previous study [49]. Prior to measuring the porosity of the 3DP rocks, five intact steel blocks with standard dimensions were used to calibrate the testing system and establish the fitting curve between the equilibrium pressure and the bulk volume of the sample chamber for porosity calculation, as shown in Figure 5. The grain phase volume of the 3DP rocks could be calculated by introducing the corresponding equilibrium pressure value from the test into the aforementioned fitting equation [52]. Afterward, pore phase volume can be acquired by subtracting the grain phase volume from the apparent volume [53].

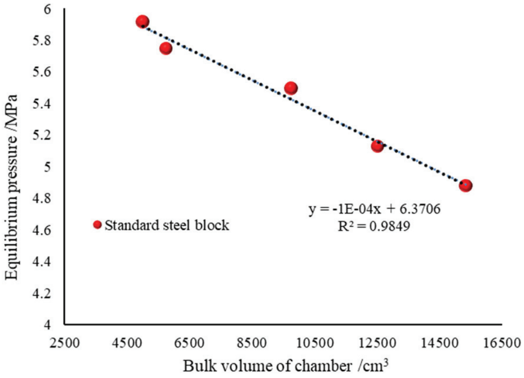

Figure 5. The fitting curve between the bulk volume of the chamber and equilibrium pressure.

2.5. Microscopic Structure Characterization

SEM scanning was carried out to capture the grain distribution and pore geometry of the 3DP rocks using the Phenom ProX scanner located at the Fundamental Science on Nuclear Waste and Environmental Safety Laboratory at Southwest University of Science and Technology. The SEM scanner is equipped with a highsensitivity quadrate backscattered electron detector which can provide 20,000× magnification and better than 1 μm resolution. In addition, the grain cementing mode and binder distribution can be determined with the help of the Energy Dispersive Spectrum (EDS) analysis on the same area captured in the backscattering mode simultaneously with the SEM scanning. Prior to scanning, small discs measuring 5 mm in length were cut off from the 3DP rock core plugs, as shown in Figure 6.

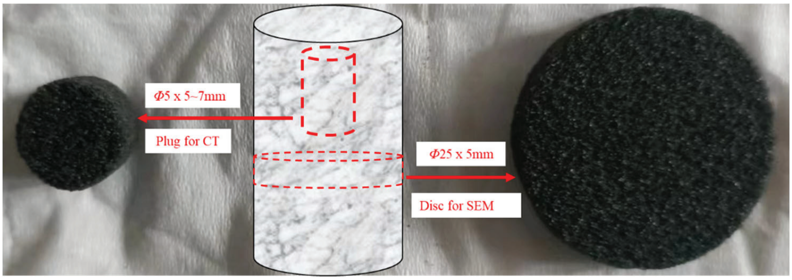

Figure 6. Sample preparation for SEM and CT scanning.

CT scanning was conducted using the nano Voxel 2000 micro-CT scanner (Tianjin Sanying Precision Instrument Co., Ltd., Tianjin, China) to investigate the spatial topology of the pore structure of the 3DP rocks. The CT scanner is equipped with various lenses to achieve multiple magnification (4×, 10×, and 20×). The high-resolution CCD camera can achieve an image resolution larger than 4096 × 4096/pixels with a high pixel spatial resolution of 1 μm. To achieve ideal imaging quality, a mini core plug was drilled from the whole specimen with a dimension of 5mm in diameter and 5–7 mm in length, as shown in Figure 6.

3. Results and Discussion

3.1. Porosity and Density

The porosity and density of the 3DP rock analogs were calculated with the physical measurements, as listed in Table 2. The 3DP rock analogs in group I printed with various sand mixtures with a 200 μm LT show a rapid increase and decrease in porosity and density with the increase in the content percentages of the CG respectively. The results indicate that the porosity and density show a difference of 8.8% and 0.16, respectively. The unit mass of the 3DP rocks printed with coarser sands is heavier than the rock analogs printed with finer sands with the same dimension. Hence the density is larger. What is more, according to random packing theory (RPT) [54], the size distribution of the sand mixtures has a great influence on the sand packing mode, which directly determines the porosity and density of the 3DP rock analogs. The RPT suggests the grain size ratio of the sand mixtures has a great influence on the porosity and density of the granular medium. It means that the density increases with the grain size ratio, while the porosity decreases since the pore space between the coarse sands can be filled by extra-fine sands. According to the vendor datasheets, the coarse sands and the fine sands used in this study exhibit the bi-modal and mono-modal GS distribution, respectively. Therefore, the 3DP rock analogs with a higher percentage of the coarse sands can achieve denser packing since the grain size ratio between the smallest and the largest grains is higher. However, with the increment in fine sand percentage, the grain size ratio decreases rapidly, and the GS distribution tends to the mono-modal. The effect of the grain size ratio on the porosity and density of 3DP rocks printed with different blends of sand mixtures is shown in Figure 7. An empirical relation between the porosity and density of the 3DP rocks printed with different blends of sand mixtures was fitted and the correlation coefficient of the linear trend shows an R^2 value of 0.993. It can help to estimate and validate the physical properties of the 3DP rocks with controllable dimensions and matrix materials prior to printing. According to previous studies [55,56], increasing the size ratio between the largest and smallest grains in the sand mixtures can effectively improve the packing ability, which means the size of the CG should be seven times larger than the FG. However, the size of the FG cannot be deduced without limit; on the one hand, the manufacturing of FG is a challenge, on the other hand, the extremely small size of the FG can strongly affect the flowability during the sand deposition and recoating process during 3D printing.

Table 2. Porosity and density of the 3DP rocks.

Rock Type	Sand Mixture	LT /μm	Weight /g	Porosity /%	Density /g/cm^3
Group I	Type I	200	281.5	40.56	1.43
	Type II		272.5	43.24	1.38
	Type III		261.5	46.31	1.33
	Type IV		258.0	47.2	1.30
	Type V		252.5	49.36	1.27
Group II	Type I	200	279.5	41.23	1.42
		300	268.4	44.56	1.36
		400	258.5	48.32	1.30

Note that the default settings of binder saturation, printing resolution, and orientation are the same for the two groups.

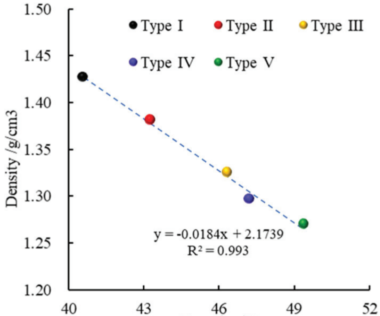

Figure 7. Comparison of porosity and density of the 3DP rocks printed with different blends of sand mixtures.

As shown in Figure 8, the 3DP rocks in group II printed with different LTs with Type I sand mixture show an increase and decrease in porosity and density with the increment in LT, respectively. There is a difference of 7.09% and 0.12 g/cm^3 in porosity and density, respectively. Since the default setting of binder saturation is invariable for all specimens printed with different printing parameters, the dosage of the binder jetted onto the sand at each layer is the same. However, with the increment in the LT, the amount of the total sand at each layer increases rapidly, which means a reduction in the binder-to-sand ratio. On the one hand, with the reduction in the binder-to-sand ratio, the amount of unbonded sand at each layer increases, which means the sand packing is not efficient, with more voids between the sands. On the other hand, the interface effect of printing layer amplified with the increase in printing LT, which has a great influence on the physical and mechanical properties of the 3DP rocks.

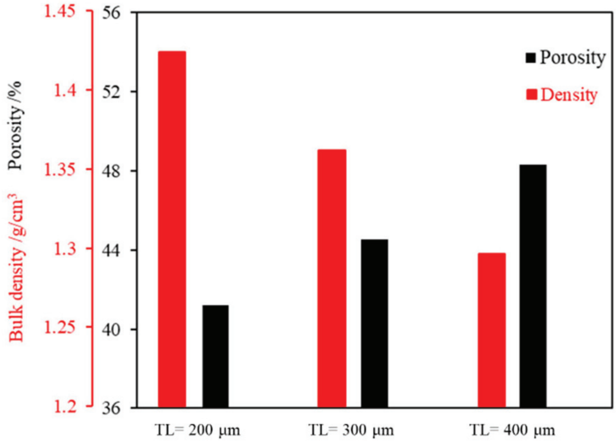

Figure 8. Comparison of porosity and density of the 3DP rocks printed with different LTs.

3.2. Unconfined Compressive Strength and Failure Behavior

The UCS and failure behavior of the 3DP rock analogs were investigated by unconfined compression testing. To avoid the test error, three specimens of each type of 3DP rock analogs were tested and used to calculate the mean value of the peak strength of the UCS. The test results are listed in Table 3. The axial stress–strain curves of the 3DP rock analogs printed with different blends of sand mixtures are recorded and shown in Figure 9. For the 3DP rocks printed with different blends of sand mixtures (group I), the largest peak strength of the UCS was recorded in type I (100% CG) with a mean value of 8.53 MPa. Moreover, the UCS decreases with the increment in the percentage of the FG in the sand mixtures. As mentioned above, the higher the percentage of the FG in the sand mixtures, the looser the structure of the 3DP rocks, with higher porosity and lower density. Hence, the stage of the pore space compaction is more obvious. The GS tends to the mono-modal distribution with the increment in the FG. Since the pore space between the large grains cannot be filled by the small grains, it limits the efficient compaction of the sand layer during printing. According to our previous study [15], the strength of the 3DP rocks is mainly provided by the "binder neck" bonding between the sand grains. In addition, the engaging force between the sand grains during the post-compression stage also contributes to the full strength of the 3DP rocks. In view of these points, the strength of the 3DP rocks printed with a higher percentage of the FG decreases rapidly since the "binder neck" bonding between the sand grains is relatively sparse and can provide limited strength.

Table 3. Results of the UCS test on the 3DP rock analogs.

Rock Type	Sand Mixture	LT /µm	Peak Strength /MPa
Group I	Type I	200	8.53
	Type II		8.22
	Type III		7.92
	Type IV		7.45
	Type V		6.52
Group II	Type I	200	8.49
		300	6.12
		400	2.82

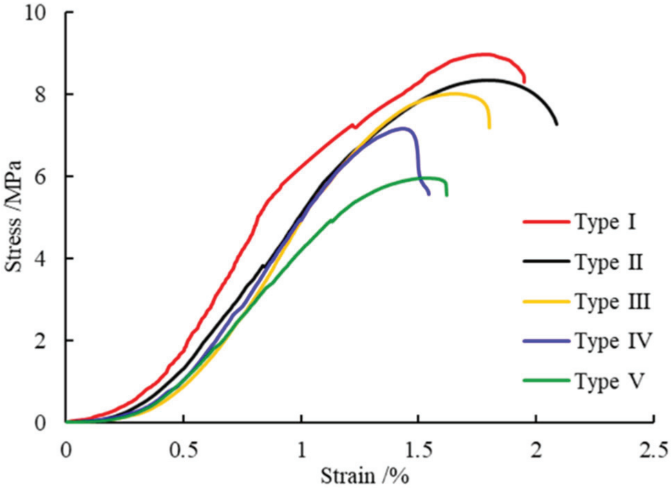

Figure 9. Stress–strain curves of the 3DP rock analogs printed with different blends of sand mixtures.

The failure patterns of the 3DP rocks printed with different blends of sand mixtures are plotted and re-drawn in Figure 10. For the specimens with a higher percentage of CG, the tensile failures with shear cracks at the end of the cores are the main failure mode (Type I~III). These phenomena are also named as the “end cap” cone, which has been reported in a previous study, i.e., a failure zone with a cone shape at the end of the core [39]. There are multiple crack planes and many sand grains fall down from the crack planes during compression. Finally, the specimen breaks into several fragments. With the increment in the FG, the specimens mainly experience compression shear damage with a main shear crack plane through the core, which exists at a certain inclination angle with the loading direction (Type IV~V).

The various types of macroscopic failure behaviors of the 3DP sandstones are mainly caused by the different microscopic failure modes of the binder neck and the grain-to-grain interaction. The failure modes observed in the different types of the 3DP rocks agree well with some weak-cemented sandstones in a natural scenario, which proves the suitability of using the 3DP rocks printed with different blends of sand mixtures to simulate different types of natural sandstones.

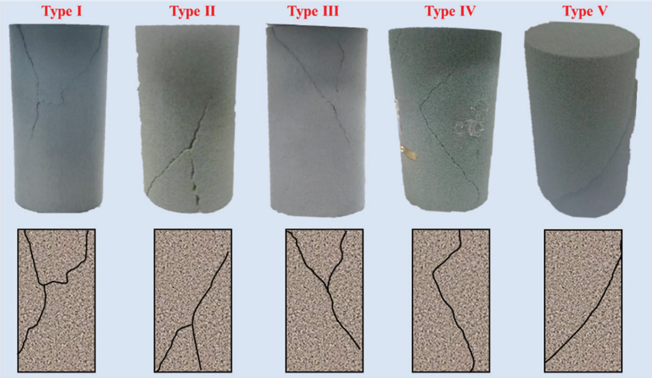

Figure 10. Pictures and re-drawn schematic of the failure pattern of the 3DP rock analogs printed with different blends of sand mixtures.

The axial stress–strain curves of the 3DP rocks printed with different LTs are shown in Figure 11. The figure shows that the specimens printed with the same LT are very similar, whereas the specimens printed with different LTs show a large difference with various mechanical and deformation properties. The calculated mean values of the peak strength of the UCS are 8.49 MPa, 6.12 MPa, and 2.82 MPa for the 3DP rocks printed with 200 µm, 300 µm, and 400 µm LT, respectively. The peak strength decreases rapidly with the increment in LT. In addition, the reduction trend is much larger than the specimens printed with different blends of sand mixtures. To distinguish the difference between mechanical and failure behaviors, the typical stress–strain curves and destructive specimens of the 3DP rocks printed with different LTs are selected for comparison, as shown in Figure 12. The specimens printed with 200 µm and 300 µm LT exhibit similar deformation behavior after the pore compaction stage. Since the gaps are larger between the layers, the specimen (LT = 300 µm) has a longer pore compaction period than the one (LT = 200 µm). After that, both specimens experience the elastic deformation stage, the plastic deformation stage, and the crack stage. Finally, the specimen (LT = 200µm) experiences tensile shear failure with a "Y-shape" crack through the core (highlighted by a black line), while the specimen (LT = 300 µm) undergoes compressive shear damage with a single shear plane (highlighted by a red line). Compared to the aforementioned specimens, the specimen (LT = 400 µm) exhibits strong ductility with a lower USC of 2.82 MPa. The pore compaction stage is much longer than for the other two types of specimens, and the stress increases slowly with large deformation in the loading direction. The specimen reaches the peak stress under a small axial loading force, but the peak strain is relatively larger than for the other two types of specimens, with a value approaching 2%. Finally, the failure mainly occurred in the middle region of the specimen with multiple irregular cracks. As mentioned above, the binder saturation was the default for all types of 3DP sandstones, which means the binder-to-sand ratio will reduce with the increment in the LT both at each layer level and the entire specimen level. The reduction in the binder-to-sand ratio can significantly influence the effective packing, which is the main cause of abnormal mechanical responses and failure behaviors. The test results indicate that the printing LT has a great influence on the mechanical and deformation behaviors of the 3DP rocks. A small printing LT contributes to a higher UCS value, and the deformation process and failure mode are more similar to the natural rocks.

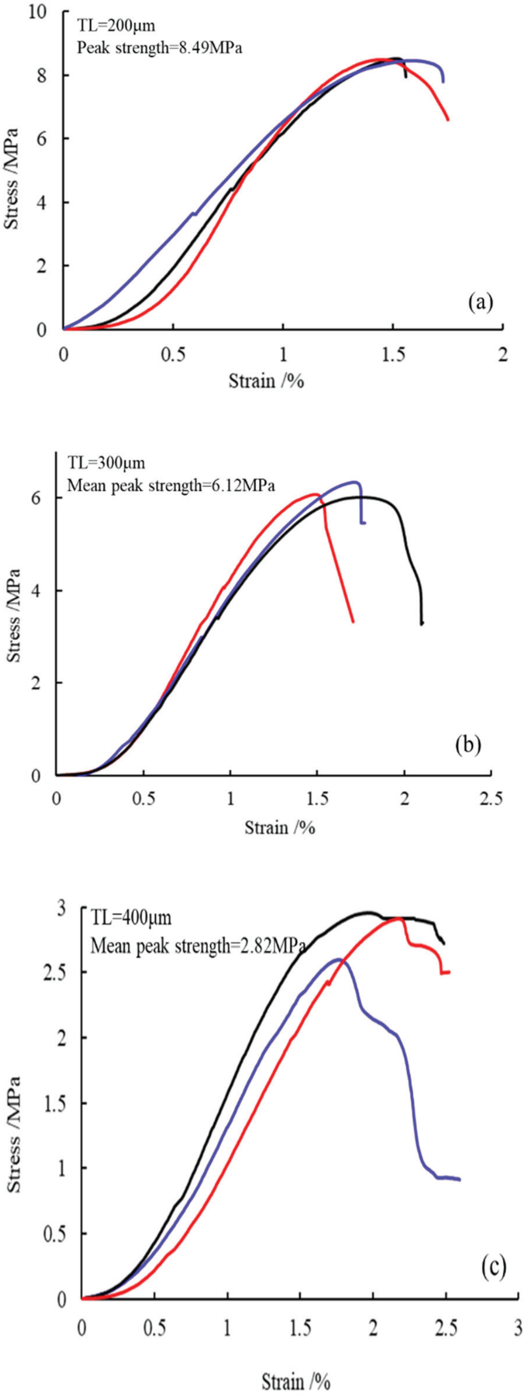

Figure 11. Stress–strain curves of the 3DP rock analogs printed with different LTs: (**a**) 200 μm, (**b**) 300 μm, (**c**) 400 μm.

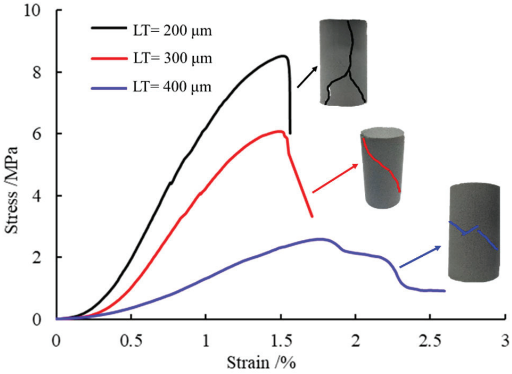

Figure 12. Comparison of stress–strain curves and failure patterns of the 3DP rocks printed with different LTs.

3.3. Sand Grain Packing and Pore Morphology

To reveal the mechanism behind the variations of the physical and mechanical properties of the 3DP rocks fabricated with different blends of sand mixtures and printing LTs, visualization equipment was utilized to extract the microstructure for quantitative characterization of the sand grain packing and pore morphology. SEM and EDS were used to investigate the sand grain packing, pore morphology, and the binder bonding mode in an integrated way.

As shown in Figure 13, the compositions of the 3DP rocks were determined using an integrated SEM–EDS test. Two test points were selected, and the silica sand (point 1) and binder (point 2) were identified and highlighted in blue and yellow circles, respectively. Since the main active ingredients of the silica sand and binder are quartz (SiO_2) and organic matter, the element distribution of the test points are main silicon (oxygen) and carbon for point 1 and point 2, respectively. The test results indicated that the binder was mainly distributed in the gap between the sand grains and formed the bond in a "binder neck" shape with a point (or line) contact. Based on the results of the binder distribution, the binder bonding mode of the sand grain and the pore type of the 3DP rocks were investigated in the selected region of a part of the SEM image, as shown in Figure 14.

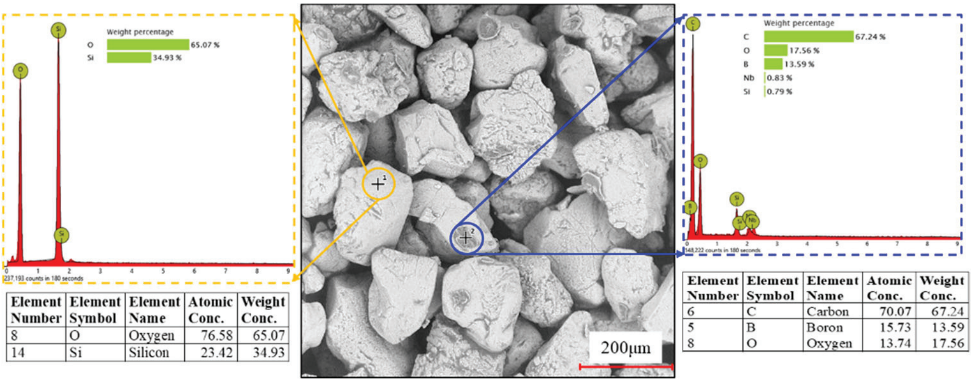

Element Number	Element Symbol	Element Name	Atomic Conc.	Weight Conc.
8	O	Oxygen	76.58	65.07
14	Si	Silicon	23.42	34.93

Element Number	Element Symbol	Element Name	Atomic Conc.	Weight Conc.
6	C	Carbon	70.07	67.24
5	B	Boron	15.73	13.59
8	O	Oxygen	13.74	17.56

Figure 13. SEM–EDS test of sand grain and binder distribution (Type I sand mixture is used as an example).

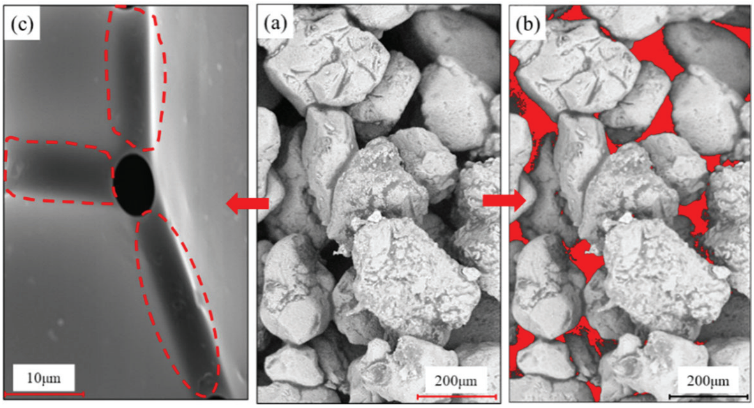

Figure 14. Binder bonding form between sand grains (**a**) ("binder neck" is highlighted by red dashed lines (**c**)) and (**b**) pore space extraction of the 3DP rocks (highlighted in red) (Type I sand mixture is used as an example).

Part of the SEM image is selected to identify the grain bonding shape and perform the pore space extraction, as shown in Figure 14a. The cementation between the grains is observed in a "binder neck" shape, which is marked by the red dashed lines (Figure 14c). The "binder neck" bonding form has a great influence not only on the mechanical properties of the 3DP rocks, but also on the microstructure. It can be noted from the extracted pore space, as shown in Figure 14b highlighted in red, the pore type of the 3DP rocks is mainly intergranular pore. The phenomenon of pore filling by the binder is not occurring. The SEM images of the 3DP rocks printed with different blends of sand mixtures are shown in Figure 15. It can be noted from the SEM images that the porosity of the 3DP rocks increases with the increment in the percentage of the FG in the sand mixtures. The sand grain size distribution of the coarse sand exhibits is bi-modal, and the pore space between the coarse sands is filled by the fine sand. The phenomenon is similar to some natural sandstone with poor grain sorting, which can lead to low porosity [57,58]. What is more, the larger the size ratio between the largest and the smallest grains, the worse the grain sorting of the sand mixtures (i.e., the better the gradation of the sand grains), and this can result in a denser structure with more effective compaction. Further, the effective compaction of the 3DP rocks means more "binder necks" (i.e., bonding points) between the coarse and fine grains, which can provide an extra cohesive force to the full strength of the 3DP rocks.

Furthermore, the micro-CT is performed on the 3DP rocks to capture the spatial morphology and topological characteristics of the pore structure, as shown in Figure 16. The 3DP specimen printed with Type I sand mixtures at 200 μm LT is used as an example for micro-CT imaging. At first, the large view mode is utilized to capture the sand grain distribution of the whole 3DP rock with a resolution of 31.65 μm, as shown in Figure 16a. The dimensions of the scanned region are 800 × 800 × 960. From the image, it can be noted that the sand grain shows a relatively homogeneous distribution and effective compaction. The 3D view of the grain phase exhibits excellent morphology in the cylindrical shape (Figure 16c). Tiny deficiencies occur in the edge area in both diametric directions, which may be caused by the shifting of the sand grains during recoating and binder jetting at every individual layer. For a more intensive visualization of the internal structure of the 3DP rocks, a mini core plug (shown in Figure 6 and highlighted by the red circle in Figure 16a) is drilled from the original core sample for micro-CT imaging with a higher resolution of 3.61 μm. The dimensions of the scanned region are 1430 × 1430 × 1130, as shown in Figure 16b. The sand grain and pore phase are shown in light gray and blue, respectively. It can be noted from the image that the pore structure shows a relatively homogeneous distribution, and the intergranular pore is the main type as mentioned above. The compaction of the sand grains is also denser than in the specimens fabricated in our previous study [15]. What is more, it can be noted from the image that the sand grains experience more effective compaction near the edge area than the center area. This phenomenon is believed to be caused by the uneven distribution of the packing pressure provided by the roller pressure during the recoating process at every individual layer. A sub-domain with a dimension of 600 × 600 × 600 voxels is extracted to visualize the morphology of the pore structure, as shown in Figure 16d. Based on the extracted pore phase, the image porosity is calculated by counting the pore phase volume. The calculated image porosity (41.32%) agrees well with the corresponding helium-measured porosity (40.56%). Compared to our previous study, there are no significant morphological variations in the topology and connectivity properties of the pore structure. Investigations of the binder bonding mode and the microstructural properties of the 3DP rocks can strengthen the understanding of the influencing mechanism on the variations of the macroscopic characteristics of the 3DP rocks, and help design the fabrication scheme of the 3DP rocks (models) with more controllable properties.

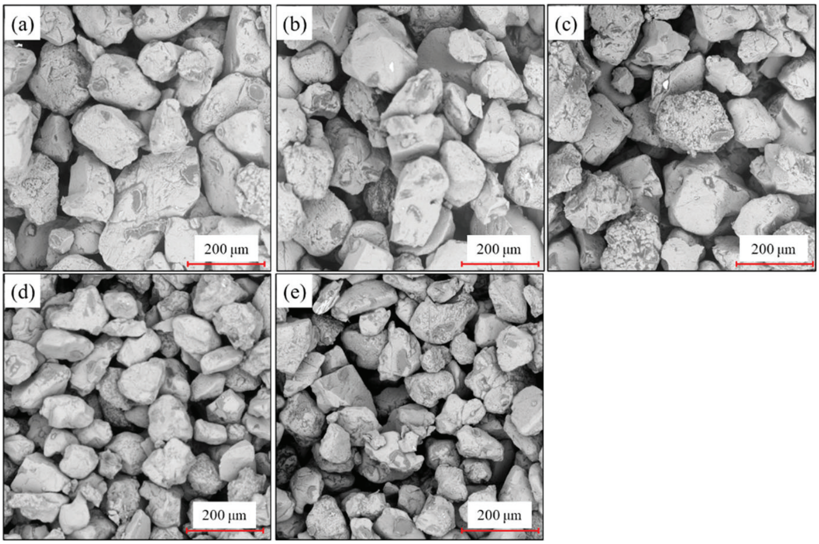

Figure 15. Collage of the SEM images of the 3DP rocks printed with different blends of sand mixtures: (**a**) Type I, (**b**) Type II, (**c**) Type III, (**d**) Type IV, (**e**) Type V.

3.4. Current Challenges and Prospects of the 3DP Sandstones

Considering the physical and mechanical properties of the 3DP sandstones fabricated with different blends of sand mixtures and printing LTs, the 3DP sandstones are very suitable to mimic weak-cemented natural sandstones. Despite the low strength of the conventional 3DP sandstones, they can contribute to meeting the load requirements between the physical model and the engineering prototype when a similar theory is considered. Besides, the physical strength of the 3DP sandstones can be improved rapidly with certain post-processing operations, such as the epoxy resin penetration in a vacuum condition, which makes it suitable to model those highly stressed rocks. However, the microstructure of the 3DP sandstone could be changed significantly since the pore space will be clogged, which has a great influence on the hydraulic property. The deformation and failure behaviors of the 3DP sandstones also vary based on the used sand grains and printing settings, as well as the post-processing operations.

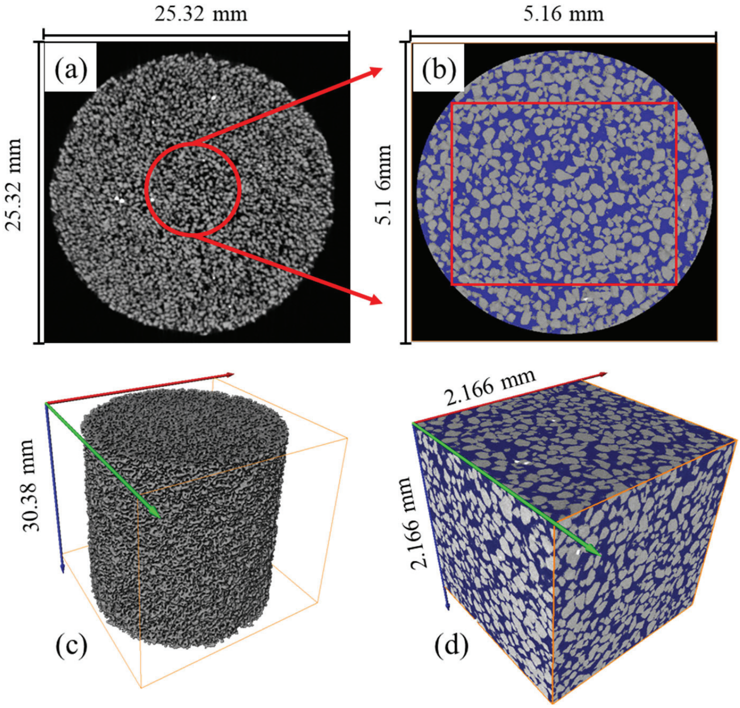

Figure 16. Pore structure characterization of the 3DP rocks via micro-CT imaging under large view mode (**a**,**c**) and high-resolution mode (**b**,**d**); the sand grain and pore phase are shown in gray and blue color, respectively.

Nowadays, despite the research on the 3DP sandstones, especially in combination with digital rock physics, the state-of-the-art approaches in rock mechanics and geosciences, the applications of the 3DP sandstones are still at an early stage. There are several challenging issues in completely replacing natural rocks with 3DP sandstones in rock mechanics research, in view of the inherent limitations of the 3DP sandstones involving material issues, fabrication, and post-processing operations. One of the biggest challenges lies in the limited printing LT of the 3DP sandstones. Limited by the smallest size of the sand grains and the mechanical capacity of the 3D printers, the sedimentary property (bedding thickness) of the natural sandstones cannot be mimicked well by the current 3D printer. Once the GS of the sand grains is determined, the printing LT cannot be lower than the GS of the sand grain. On the other hand, with the decrease in the sand grain size, the flowability decreases rapidly, which has a great influence on the deposition and spreading of the sand grains on the printing bed. To resolve the aforementioned limitations, an effective way is to rely on the further development of the 3D printer and the design and control techniques of the printing materials. The surface physicochemical properties of the 3DP sandstones can be adjusted via the appropriate post-processing operations, such as coating technology, to better simulate the interface characteristics, such as non-uniform wettability, so as to better mimic the fluid flow process in natural scenarios.

4. Conclusions

The aim of this paper was to reveal the effect of the different printing parameters and blends of sand mixtures on the physical and mechanical properties of the 3DP sandstones. To this end, 3DP sandstones were fabricated with various types of sand mixtures and printing LTs in this study. Then, a comprehensive experimental investigation was conducted to investigate the bulk properties (i.e., porosity and density), microstructural characteristics (i.e., sand grain packing and bonding mode, pore morphology), and mechanical and failure behaviors of the 3DP sandstones. The results confirm that both the sand mixtures and printing LT contribute to the variation in the physical and mechanical properties of the 3DP sandstones, and the following conclusions can be reached:

(1) The porosity of the 3DP sandstones increases with the increment in the percentage of the FG in the sand mixtures, while the density decreases. With the increment in the printing LT, the same trend is also observed in the evolution of porosity and density of the 3DP sandstones. Based on that, an empirical relation between the porosity and density of the 3DP sandstones is fitted, which can help estimate and validate the physical properties of the 3DP sandstones with designed dimensions and controllable matrix materials prior to printing.

(2) The UCS of the 3DP sandstones decreases with the increment in the percentage of the FG in the sand mixtures, as well as the printing LT. Various failure patterns occurred in the 3DP sandstones printed with different blends of sand mixtures and printing LTs, which agree well with some weak-cemented sandstones in a natural scenario and prove the suitability of using the 3DP sandstones to simulate different types of natural sandstones. What is more, the 3DP sandstones printed with a smaller LT and a higher percentage of CG contribute to a higher UCS value, and the deformation process and failure mode are also more similar to the natural rocks.

(3) The 3DP sandstones have a much more homogeneous pore structure and looser compaction of sand grain compared to the natural sandstones. The cementation between the sand grains of the 3DP sandstones is observed in a “binder neck” shape, which has a great influence not only on the mechanical properties, but also on the microstructure. Benefiting from the sand grain bonding form, the pore type of the 3DP rocks is mainly an intergranular pore.

Based on the findings in this paper, we attempt to establish a customized workflow for fabricating 3DP rock analogs with designed properties and structures in a more controllable way for various applications and purposes in the rock mechanics and geoscience engineering fields. Finally, there are still challenges to overcome in future work on 3DP rock analogs, including multitype components printing with various types of minerals, the non-uniform wettability design, and the accurate control of the brittle–ductile conversion.

Author Contributions: Conceptualization, Y.W.; Formal analysis, M.Y. and S.P.; Funding acquisition, Y.W.; Investigation, Y.W.; Writing—original draft, Y.W. and S.L.; Writing—review and editing, R.S., J.L. and Y.D. All authors have read and agreed to the published version of the manuscript.

Funding: This research was funded by National Natural Science Foundation of China grant number [51909225]; Natural Science Foundation of Sichuan, grant number [2022NSFSC1161], and Doctoral Foundation of SWUST, grant number [20zx7129]. And The APC was funded by [2022NSFC1161 and 20zx7129].

Institutional Review Board Statement: Not applicable.

Informed Consent Statement: Not applicable.

Data Availability Statement: All the data and materials used in this paper are available from the corresponding authors upon request.

Acknowledgments: Hao Zhou and Xiaoyu Li are acknowledged for providing the assistance on the CT and SEM test.

Conflicts of Interest: The authors declare that there are no competing financial interests with any other people or groups regarding the publication of this manuscript.

References

1. Liu, L.; Deisman, N.; Chalaturnyk, R. Elastic stiffness modelling of opalinus clay based on laboratory measurements with implications for in-situ testing. *Rock Mech. Rock Eng.* **2022**, *55*, 1832–1842. [CrossRef]
2. Almetwally, A.; Jabbari, H. Experimental investigation of 3D printed rock samples replicas. *J. Nat. Gas Sci. Eng.* **2020**, *76*, 103192. [CrossRef]
3. Zheng, Y.; Liu, J.; Zhang, B. An investigation into the effects of weak interfaces on fracture height containment in hydraulic fracturing. *Energies* **2019**, *12*, 3245. [CrossRef]
4. Patsoukis, D.; Menke, H.; Maes, J. Benchmarking the viability of 3D printed micromodels for single phase flow using particle image velocimetry and direct numerical simulations. *Transp. Porous Media* **2022**, *141*, 279–294. [CrossRef]
5. You, M.; Hua, A. The failure mode and decrease of compressive strength of rock under uniaxial compression condition. *Chin. J. Rock Mech. Eng.* **1998**, *17*, 292–296.
6. Ju, Y.; Wang, H.; Yang, Y.; Hu, Q.; Peng, R. Numerical simulation of mechanisms of deformation, failure and energy dissipation in porous rock media subjected to wave stresses. *Sci. China Tech. Sci.* **2010**, *53*, 1098–1113. [CrossRef]
7. Wang, Y.; Song, R.; Liu, J.; Cui, M.; Ranjith, P. Pore scale investigation on scaling-up micro-macro capillary number and wettability on trapping and mobilization of residual fluid. *J Contam. Hydrol.* **2019**, *225*, 103499. [CrossRef]
8. Shi, D.; Li, L.; Liu, J.; Wu, M.; Pan, Y.; Tang, J. Effect of discrete fractures with or without roughness on seepage characteristics of fractured rocks. *Phys. Fluids* **2022**, *34*, 073611. [CrossRef]
9. Gell, E.; Walley, S.; Braithwaite, C. Review of the validity of the use of artificial specimens for characterizing the mechanical properties of rocks. *Rock Mech. Rock Eng.* **2019**, *52*, 2946–2961. [CrossRef]
10. Li, W.; Yu, H.; Yang, Z.; Li, J.; Chen, X.; Ma, L. Experimental study on the sweep law of CO_2 miscible flooding in heterogeneous reservoir in Jilin. *Energies* **2022**, *15*, 5755. [CrossRef]
11. Charalampos, K.; Giovanna, B.; Jiang, N.; Kenichi, S. Application of microbially induced carbonate precipitation to form bio-cemented artificial sandstone. *J. Rock Mech. Geotech. Eng.* **2021**, *13*, 579–592.
12. Zhou, T.; Zhu, J.; Ju, Y.; Xie, H. Volumetric fracturing behavior of 3D printed artificial rocks containing single and double 3D internal flaws under static uniaxial compression. *Eng. Fract. Mech.* **2019**, *205*, 190–204. [CrossRef]
13. Wang, H.; Shao, J.; Zhang, J.; Zou, D.; Sun, X. Bond shear performances and constitutive model of interfaces between vertical and horizontal filaments of 3D printed concrete. *Constr. Build. Mater.* **2022**, *316*, 125819. [CrossRef]
14. Ren, Z.; Zhang, Q.; Ju, Y.; Xie, H. Determination of the full-field stress and displacement using photoelasticity and sampling moiré method in a 3D-printed model. *Theor. Appl. Mech. Lett.* **2022**, 100380. [CrossRef]
15. Song, R.; Wang, Y.; Ishutov, S.; Narvaez, G.; Hodder, K.; Chalaturnyk, R.; Sun, S.; Liu, J.; Ranjith, P. A comprehensive experimental study on mechanical behavior, microstructure and transport properties of 3D-printed rock analogs. *Rock Mech. Rock Eng.* **2020**, *53*, 5745–5765. [CrossRef]
16. Primkulov, B.; Chalaturnyk, J.; Chalaturnyk, R.; Narvaez, G. 3D printed sandstone strength: Curing of furfuryl alcohol resin-based sandstones. *3D Print Addit. Manuf.* **2017**, *4*, 149–155. [CrossRef]
17. Ishutov, S.; Hasiuk, F. 3D printing Berea sandstone: Testing a new tool for petrophysical analysis of reservoirs. *Petrophysics* **2017**, *58*, 592–602.
18. Ishutov, S.; Hasiuk, F.; Harding, C.; Gray, J. 3D printing sandstone porosity models. *Interpretation* **2015**, *3*, SX49–SX61. [CrossRef]
19. Ishutov, S.; Hasiuk, F.; Fullmer, S.; Buono, A.; Gray, J.; Harding, C. Resurrection of a reservoir sandstone from tomographic data using three-dimensional printing. *AAPG Bull.* **2017**, *101*, 1425–1443. [CrossRef]
20. Jiang, C.; Zhao, G. A preliminary study of 3D printing on rock mechanics. *Rock Mech. Rock Eng.* **2015**, *48*, 1041–1050. [CrossRef]
21. Ma, G.; Wang, L.; Ju, Y. State-of-the-art of 3D printing technology of cementitious material-An emerging technique for construction. *Sci. China Technol. Sci.* **2018**, *61*, 475–495. [CrossRef]
22. Song, R.; Wang, Y.; Tang, Y.; Peng, J.; Liu, J.; Yang, C. 3D Printing of natural sandstone at pore scale and comparative analysis on micro-structure and single/two-phase flow properties. *Energy* **2022**, *261*, 125226. [CrossRef]
23. Ngo, T.; Kashani, A.; Imbalzano, G.; Nguyen, K.; Hui, D. Additive manufacturing (3D printing): A review of materials, methods, applications and challenges. *Compos. Part B-Eng.* **2018**, *143*, 172–196. [CrossRef]
24. Kofi, O.; Paul, G.; Nima, S. Investigation of foam flow in a 3D printed porous medium in the presence of oil. *J. Colloid Interf. Sci.* **2017**, *490*, 850–858.
25. Ishutov, S.; Hodder, K.; Chalaturnyk, R.; Narvaez, G. Replication of carbonate reservoir pores at the original size using 3D printing. *Petrophysics* **2021**, *62*, 477–485. [CrossRef]
26. Liu, P.; Ju, Y.; Ranjith, P.; Zheng, Z.; Wang, L.; Wanniarachchi, A. Visual representation and characterization of three-dimensional hydrofracturing cracks within heterogeneous rock through 3D printing and transparent models. *Int. J. Coal Sci. Technol.* **2016**, *3*, 284–294. [CrossRef]
27. Ahkami, M.; Roesgen, T.; Saar, M.; Kong, X. High-resolution temporo-ensemble PIV to resolve pore-scale flow in 3D-printed fractured porous media. *Transp. Porous Media* **2019**, *129*, 467–483. [CrossRef]
28. Sharafisafa, M.; Shen, L.; Xu, Q. Characterisation of mechanical behaviour of 3D printed rock-like material with digital image correlation. *Int. J. Rock Mech. Min. Sci.* **2018**, *112*, 122–138. [CrossRef]
29. Suzuki, A.; Minto, J.; Watanabe, N.; Li, K.; Horne, R. Contributions of 3D printed fracture networks to development of flow and transport models. *Transp. Porous Media* **2019**, *129*, 485–500. [CrossRef]

30. Zhang, Y.; Ye, J.; Li, P. Flow characteristics in a 3D-printed rough fracture. *Rock Mech. Rock Eng.* **2022**, *55*, 4329–4349. [CrossRef]
31. Hodder, K.; Nychka, J. Silane treatment of 3D-printed sandstone models for improved spontaneous imbibition of water. *Transp. Porous Media* **2019**, *129*, 583–598. [CrossRef]
32. Kong, L.; Ostadhassan, M.; Li, C. Can 3-D printed gypsum samples replicate natural rocks? An experimental study. *Rock Mech. Rock Eng.* **2018**, *51*, 3061–3074. [CrossRef]
33. Kong, L.; Ostadhassan, M.; Hou, X.; Mann, M.; Li, C. Microstructure characteristics and fractal analysis of 3D-printed sandstone using micro-CT and SEM-EDS. *J. Petro. Sci. Eng.* **2019**, *175*, 1039–1048. [CrossRef]
34. Song, L.; Jiang, Q.; Shi, Y.; Feng, X.; Li, Y.; Su, F.; Liu, C. Feasibility investigation of 3D printing technology for geotechnical physical models: Study of tunnels. *Rock Mech. Rock Eng.* **2018**, *51*, 2617–2637. [CrossRef]
35. Hodder, K.; Craplewe, K.; Ishutov, S.; Chalaturnyk, R. Binder saturation as a controlling factor for porosity variation in 3D-printed sandstone. *Petrophysics* **2021**, *62*, 450–462. [CrossRef]
36. Wu, Z.; Zhang, B.; Weng, L.; Liu, Q.; Wong, L. A new way to replicate the highly stressed soft rock: 3D printing exploration. *Rock Mech. Rock Eng.* **2020**, *53*, 467–476. [CrossRef]
37. Li, Y.; Zhou, H.; Zhang, L.; Zhu, W.; Li, S.; Liu, J. Experimental and numerical investigations on mechanical property and reinforcement effect of bolted jointed rock mass. *Constr. Build. Mater.* **2016**, *126*, 843–856. [CrossRef]
38. Kong, L.; Ostadhassan, M.; Li, C.; Tamimi, N. Pore characterization of 3D-printed gypsum rocks: A comprehensive approach. *J. Mat. Sci.* **2018**, *53*, 5063–5078. [CrossRef]
39. Hodder, K.; Nychka, J.; Chalaturnyk, R. Improvement of the unconfined compressive strength of 3D-printed model rock via silica sand functionalization using silane coupling agents. *Int. J. Adhes. Adhes.* **2018**, *85*, 274–280. [CrossRef]
40. Gomez, J.; Chalaturnyk, R.; Navaez, G. Experimental investigation of the mechanical behavior and permeability of 3D printed sandstone analogs under triaxial conditions. *Transp. Porous Media* **2019**, *129*, 541–557. [CrossRef]
41. Ardila, N.; Narvaez, G.; Chalaturnyk, R. Wettability measurements on 3D printed sandstone analogues and its implications for fluid transport phenomena. *Transp. Porous Media* **2019**, *129*, 521–539. [CrossRef]
42. Kong, L.; Ishutov, S.; Hasiuk, F.; Xu, C. 3D Printing for experiments in petrophysics, rock physics, and rock mechanics: A review. *SPE Reserv. Eval. Eng.* **2021**, *24*, 721–732. [CrossRef]
43. Alyafei, N.; Al, M.; Bautista, J.; Idris, M.; Seers, T. Enhanced learning of fundamental petrophysical concepts through image processing and 3D printing. *Petrophysics* **2021**, *62*, 463–476. [CrossRef]
44. Zhou, T.; Zhu, J. Identification of a suiTable 3D printing material for mimicking brittle and hard rocks and its brittleness enhancements. *Rock Mech. Rock Eng.* **2018**, *51*, 765–777. [CrossRef]
45. Zhu, J.; Zhou, T.; Liao, Z.; Sun, L.; Li, X.; Chen, R. Replication of internal defects and investigation of mechanical and fracture behavior of rock using 3D printing and 3D numerical methods in combination with x-ray computerized tomography. *Int. J. Rock Mech. Min. Sci.* **2018**, *106*, 198–212. [CrossRef]
46. Hodder, K.; Sanchez, A.; Ishutov, S.; Narvaez, Z.; Chalaturnyk, R. Increasing density of 3D-printed sandstone through compaction. *Energies* **2022**, *15*, 1813. [CrossRef]
47. Xu, Q.; Jiang, L.; Ma, C.; Niu, Q.; Wang, X. Effect of layer thickness on the physical and mechanical properties of sand powder 3D printing specimens. *Front. Earth Sci.* **2021**, *9*, 763202. [CrossRef]
48. Mostafaei, A.; Rodriguez De Vecchis, P.; Nettleship, P.; Chmielus, M. Effect of powder size distribution on densification and microstructural evolution of Binder-Jet 3D printed alloy 625. *Mater. Des.* **2019**, *162*, 375–383. [CrossRef]
49. Song, R.; Wang, Y.; Sun, S.; Liu, J. Characterization and microfabrication of natural porous rocks: From micro-CT imaging and digital rock modelling to micro-3D-printed rock analogs. *J. Petro. Sci. Eng.* **2021**, *205*, 108827. [CrossRef]
50. ASTM International. *D4543-19 Standard Practices for Preparing Rock Core As Cylindrical Test Specimens and Verifying Conformance to Dimensional and Shape Tolerances*; ASTM International: West Conshohocken, PA, USA, 2019.
51. ASTM International. *D7012-14e1 Standard Test Methods for Compressive Strength and Elastic Moduli of Intact Rock Core Specimens Under Varying States of Stress and Temperatures*; ASTM International: West Conshohocken, PA, USA, 2014.
52. Xiao, B.; Wang, W.; Zhang, X.; Long, G.; Fan, J.; Chen, H.; Deng, L. A novel fractal solution for permeability and Kozeny-Carman constant of fibrous porous media made up of solid particles and porous fibers. *Powder Technol.* **2019**, *349*, 92–98. [CrossRef]
53. Liang, M.; Fu, G.; Xiao, B.; Luo, L.; Wang, Z. A fractal study for the effective electrolyte diffusion through charged porous media. *Int. J. Heat Mass Transf.* **2019**, *137*, 365–371. [CrossRef]
54. Bertei, A.; Nicolella, C. A comparative study and an extended theory of percolation for random packings of rigid spheres. *Powder Technol.* **2011**, *213*, 100–108. [CrossRef]
55. Gregorski, S. High Green Density Metal Parts by Vibrational Compaction of Dry Powder in the Three-Dimensional Printing Process. Ph.D. Thesis, Massachusetts Institute of Technology MIT, Cambridge, MA, USA, 1996.
56. Real, D.; Orzan, L.; Leonardi, D.; Salomon, C. Improving the dissolution of triclabendazole from stable crystalline solid dispersions formulated for oral delivery. *AAPS PharmSciTech* **2020**, *21*, 16. [CrossRef] [PubMed]
57. Song, R.; Liu, J.; Yang, C.; Sun, S. Study on the multiphase heat and mass transfer mechanism in the dissociation of methane hydrate in reconstructed real-shape porous sediments. *Energy* **2022**, *254*, 124421. [CrossRef]
58. Wang, Y.; Song, R.; Liu, J.; Qin, M.; Zheng, Z.; Qin, Y. Comprehensive investigation of the petrophysical and two-phase flow properties of the tight sandstone in Yanchang formation, Ordos Basin, China insights from computed tomography imaging and pore scale modelling. *Lithosphere* **2022**, *12*, 8766247. [CrossRef]

energies

Article

Numerical Modeling on Dissociation and Transportation of Natural Gas Hydrate Considering the Effects of the Geo-Stress

Rui Song [1,2,3], Yaojiang Duan [1,*], Jianjun Liu [2,3,*] and Yujia Song [2,3]

[1] School of Geoscience and Technology, Southwest Petroleum University, Chengdu 610500, China
[2] State Key Laboratory of Geomechanics and Geotechnical Engineering, Institute of Rock and Soil Mechanics, Chinese Academy of Sciences, Wuhan 430071, China
[3] University of Chinese Academy of Sciences, Beijing 100049, China
* Correspondence: duanyaojiangswpu@163.com (Y.D.); jjliu@whrsm.ac.cn (J.L.)

Abstract: A deep understanding of the dissociation and transportation mechanism of natural gas hydrate (NGH), taking into account the effects of geo-stress, contributes to optimizing the development strategy and increases the exploitation efficiency of NGH. In this paper, the mathematical model, coupled with fluid heat and mass transfer, multiphase flow mechanics, and reaction kinetics with phase change in the process of hydrate decomposition was established. An axisymmetric two-dimensional model was developed to simulate the depressurization decomposition process of natural gas hydrate in the Berea sandstones. FLUENT software was used to solve the fundamental governing equations of the multi-phase flow, and UDF programming was employed to program the hydrate decomposition model and the modified permeability model in the dissociation and transportation of NGH. The simulation results were then validated by Masuda's experimental data. The effects of gas saturation, outlet pressure, temperature, absolute permeability and geo-stress on the decomposition of natural gas hydrate were studied. The results indicated that a higher absolute permeability, higher initial gas saturation, lower outlet pressure, and higher initial temperature advance the decomposition rate of hydrate. Thus, an optimized production plan is essential to promote the extraction efficiency of the NGH. The geo-stress causes a decrease in the porosity and permeability of the porous rock, which restricts the efficiency of the heat and mass transfer by the fluid flow, leading to a slower dissociation and transportation rate of the NGH. Thus, it is important to take geo-stress into consideration and balance the extracting efficiency and the well pressure, especially when the NGH is developed by depressurization.

Keywords: natural gas hydrate; heat and mass transfer; reaction kinetics; geo-stress

Citation: Song, R.; Duan, Y.; Liu, J.; Song, Y. Numerical Modeling on Dissociation and Transportation of Natural Gas Hydrate Considering the Effects of the Geo-Stress. *Energies* **2022**, *15*, 9311. https://doi.org/10.3390/en15249311

Academic Editor: Hossein Hamidi

Received: 28 October 2022
Accepted: 26 November 2022
Published: 8 December 2022

1. Introduction

The increasing global demands for energy and environmental protection urge governments and scientists to exploit unconventional oil and gas resources, but with tremendous reservation, such as coalbed methane, shale gas, tight sandstone gas, and natural gas hydrate, among others [1,2]. Natural gas hydrate (NGH), which accounts for the largest proportion of unconventional natural gas resources, is a kind of high-quality, efficient, and clean energy with great potential [3]. NGH is a non-fixed stoichiometric cage-like crystalline compound formed by the reaction of one or several small molecular gases with water at a certain temperature and pressure [4]. One cubic meter of NGH can release 164 cubic meters of methane in standard conditions, which is 10 times the energy density of other unconventional gas source rocks (such as coalbed methane), and 2~5 times the energy density of conventional natural gas [5]. Therefore, the commercial exploitation of NGH is crucial to worldwide energy supply and economic development.

NGH requires low temperature and high-pressure conditions to maintain a stable state, and is generally distributed in deep sea or continental permafrost. Up to now, the short-term field tests of hydrate exploitation in the world have been carried out in sandy (or partially sandy) sediments [6]. The exploitation methods of NGH mainly include the thermal stimulation method, depressurization method, chemical reagent injection method and CO_2 replacement method [7–9]. Current thermal stimulation methods in mining technology are inefficient and can only achieve local heating [10]. The chemical reagents huff-n-puff method is high-cost and low-efficiency, and has a potential risk of environmental pollution [11]. The efficiency of the carbon dioxide replacement method is also low [12]. Consequently, the depressurization method is regarded as the most economical and environmentally friendly way for NGH exploitation [13–15]. By depressurization, the solid NGH decomposes into gas and water, and, then, gas escapes from the reservoir. Stable NGH serves as the cementing material for the mineral grains of rocks and improves the strength of the rock mass. The dissociation of the NGH may cause potential geo-hazards. Thus, a study on the dissociation and transportation mechanism of NGH, considering the effects of the geo-stress, contributes to the economic and safe development of NGH.

To date, extensive studies have been performed to investigate the dissociation and transportation process of NGH in porous media by numerical modeling. Zhao et al. [16] simulated the distribution of temperature, pressure, and hydrate saturation as natural gas hydrate decomposed in a two-dimensional axisymmetric model. Deng et al. [17] established a coupling model of two-phase flow and heat transfer for hydrate dissociation. Zhang et al. [18] adopted the dynamic grid algorithm to analyze the effects of permeability, lithology, and reservoir compression modulus on the recovery efficiency of natural gas hydrate in the core. Based on the implicit pressure–explicit saturation (IMPES) method, Liang et al. [19] created a two-dimensional axisymmetric model and analyzed the effects of outlet pressure, initial hydrate saturation and other parameters on hydrate decomposition and gas production rate in porous media. Ruan et al. [20] investigated the responses of hydrate dissociation to permeability and hydrate saturation of the reservoir. Two-dimensional axisymmetric models were established in FLUENT software to investigate the impact of temperature, permeability, pressure, phase distribution and other factors on the rate of NGH dissociation [21–28]. However, the geo-stress was not considered in these studies. The effective pressure is believed to be one of the key factors for efficiency and stability in the formation of NGH [29]. White et al. [30] integrated the geomechanical calculation into the existing thermal and hydrological coupling model framework to simulate the process of NGH exploitation by using IGHCCS2 codes. Cheng et al. [31] developed a gas–water two-phase fluid mechanics coupling model to investigate the effects of the interaction of the fluid and solid on the gas production of NGH. Lee et al. [32] developed a 3D geological model to investigate the geo-stress on gas production of NGH by using the cyclic depressurization method. Liu et al. [33] utilized the thermal-hydrological-mechanical-chemical (THCM) coupling model to study the geomechanical issues during the exploitation of NGH. Wu et al. [34] investigated the effects of the effective stresses on the permeability and porosity of natural gas hydrate reservoirs with different NGH saturations. Sun et al. [35] developed a fully coupled thermal-hydrological-mechanical-chemical (THCM) model. The impacts of compressibility on the rate of gas production, pore pressure, temperature, permeability, and other parameters were investigated. Jang et al. [36] studied the effects of geo-stress on fluid flow in NGH reservoirs. Kimoto et al. [37] conducted a numerical simulation based on a chemical-thermal-mechanical coupling model and an updated Lagrangian equation, and investigated the influencing factors of ground deformation caused by NGH dissociation. Sun et al. [38,39] used COMSOL to simulate the mechanical behavior of NGH by integrating the Mohr–Coulomb model into the fully coupled thermal-water-mechanics model. Cheng et al. [40] proposed a thermal-hydro-mechanical (THM) coupling model and studied the distribution of pressure, saturation of each phase, temperature, and mechanical parameters around the wellbore. Wan et al. [41] proposed a thermal-water-mechanical-chemical (THMC) coupling model based on the CVFEM framework, which was then validated by Masuda's triaxial compression experiment [42] and sandstone core experiment [43]. However, the mechanical parameters used in most of these studies were estimated empirically, which limited the validation and applicability in engineering applications.

In this paper, a mathematical model, considering fluid heat and mass transfer, multiphase flow mechanics, and reaction kinetics with phase change in the process of hydrate decomposition, was established. In this model, the mechanical properties of the Berea sandstone and its stress sensitivity were adopted. The THMC codes were programmed in C language and used as a subroutine in FLUENT software. The Masuda's experiments on the Berea sandstone were simulated and used as benchmark data for model verification. The effects of initial gas saturation, outlet pressure, initial temperature, absolute permeability and geo-stress on the decomposition of natural gas hydrate were studied.

2. Methods

2.1. Computer Model

This work employed Masuda's experimental benchmark data [43] to validate the numerical model, and, on that basis, addressed and investigated the effect of effective stress on hydrate decomposition and gas production in sandy sediments. Masuda's experiment involved distributing a specified volume of water, methane gas, and hydrate in the core of a cylindrical sandstone. The core had a cross-sectional size of 20.3 cm^2. The gas phase followed the Peng–Robinson equations. The Euler model was adopted to simulate the multiphase flow in the porous rock containing NGH. This study turned the original three-dimensional model into a two-dimensional axisymmetric model for processing using ICEM software, as in Figure 1. The symmetry axis was chosen to be the bottom edge, and the calculation area was divided into 120 × 20 grids. FLUENT was then used to import the mesh model. In Masuda's experiment, the left side was the outlet, while the surrounding and right side were the non-slip and free convection walls with external heat flow through the rubber casing around the sandstone. In this study, the casing thickness in the experiment was 10 mm, and the appropriate range of h was 1.90–272.7 W/(m^2·K), and 50 W/(m^2·K) was employed. The temperature monitoring points were P1 (7.5, 2.5), P2 (15, 2.5), and P3 (22.5, 2.5) in Figure 1. The initial conditions, and boundary conditions used in this simulation followed the experiment of Masuda et al. [43], as shown in Table 1 The properties of the fluids in the simulation referred to the standard database at the same temperature and pressure conditions as the experiment. The material properties of the porous sandstone referred to average values of the Berea sandstones in literature [44], as shown in Table 2.

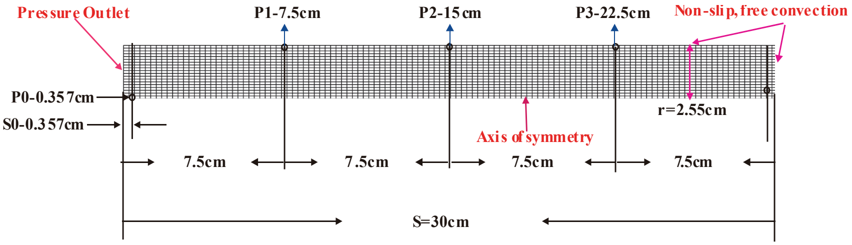

Figure 1. Mesh model and boundary conditions for Masuda's experiment.

Table 1. Initial conditions, boundary conditions and properties of sandstone cores in Masuda's experiment.

Properties	Value	Properties	Value
Average saturation of initial hydrate	0.501	Initial permeability of sandstone core	97.98 mD
Average saturation of initial water	0.199	Sandstone core porosity	0.182
Average saturation of initial methane gas	0.3	Joule-Thomson throttling coefficient	-1.5×10^{-4}
initial temperature	275.45 K	Critical pressure of methane	4.599 MPa
initial pressure	3.75 MPa	Critical temperature of methane	190.56 K
outlet pressure	2.84 MPa	ambient temperature	274.15 K

Table 2. Material properties in the simulation.

	Density (kg/m$^{3)}$	Fluid Viscosity (cP)	Thermal Conductivity ($\mathrm{w{\cdot}m^{-1}{\cdot}k^{-1}}$)	Thermal Capacity ($\mathrm{J{\cdot}kg^{-1}{\cdot}k^{-1}}$)
water	1001.5	1	0.6	4180
hydrate	913	-	0.393	2010
methane	PR equation	0.01	0.00332	2190
Berea sandstone	2030	-	5	800

2.2. Mathematical Model

Mathematical models of the multiphase flow and heat transfer include mass balance equations, heat balance equations, additional source terms of mass and energy, and initial and boundary conditions. The basic governing equations for the multiphase flow in the porous rock and the reaction kinetics of the NGH dissociation are presented in Table 3.

The effects of the geo-stress are also coupled with the transportation and dissociation process of the NGH in the porous media. Based on the assumptions of stress and strain linearity and the reversibility of medium deformation, Biot et al. [45] proposed the pore elastic constitutive equation of fluid saturated porous media. Detournay et al. [46] proposed the pore elastic constitutive equation illustrated in Equation (1), and defined volumetric strain as follows, under isotropic compressive stress:

$$\varepsilon_V = \frac{\sigma}{2G} - (\frac{1}{6G} - \frac{1}{9K_T})\delta\sigma + \frac{1}{3H'}\delta P_T \tag{1}$$

$$\varepsilon_V = 3\varepsilon = \frac{1}{K}(\sigma - \alpha P_T) \tag{2}$$

where ε_v is volumetric strain, G is the shear modulus, K_T is bulk modulus, δ is a unit matrix, H' is the constitutive constant (stress-strain coupling of fluid), σ is confining pressure, and P_T is pore pressure.

Usually, the effective stress is calculated, based on the test results of variable confining pressure experiments. There are various forms of effective stress. In 1923, Terzaghi proposed the calculation formula of effective stress:

$$\sigma' = \sigma - p \tag{3}$$

In this study, the influence of effective stress in sandstone core was studied, and the effective stress coefficient was set to 1 in this study.

$$\sigma' = \sigma - \alpha p \tag{4}$$

where α is the effective stress coefficient. Fatt et al. [47,48] suggested that α could be set between 0.75 and 1. Knaap et al. [49], Hubbert et al. [50] and Zimmerman et al. [51] believed that the effective stress coefficient was set to 1 through the experimental results. In this study, $\alpha = 1$.

When the stress and pore pressure are known, the volumetric strain can be obtained by using the linear isotropic theory of pore elasticity. For the case of nonlinear volumetric deformation in porous rock, it was found that the fitting equation of stress–strain data collected in the Berea experiment was as follows (meeting the initial conditions $\sigma' = 0$, $\varepsilon_v = 0$) [52]:

$$\varepsilon_V = A'\sigma' - B'e^{-\sigma'/C'} + B'C' \tag{5}$$

where A', B', C' are the fitting constants [53], ε_V is volumetric strain.

Table 3. Different models of porous media methane hydrate dissociation flow.

	Sun et al. (2005)	Nazridoust and Ahmadi. (2007)	Ruan et al. (2012)	Chen et al. (2016)	This Study	
Modle	1-D	2-D	2-D	2-D	2-D	
Flow model	Darcy's law	Darcy's law	Darcy's law	Darcy's law	Darcy's law	
Relative perme-ability	Corey's model (1954)	Corey's model (1954)	Corey's model (1954)	Corey's model (1954)	Adapted Corey's model (1954)	
Permeability model	$k_{rw} = k\left(\frac{\frac{s_w}{s_w+s_g} - s_{wr}}{1-s_{wr}-s_{gr}}\right)^{nw}$, $k_{rg} = \left(\frac{\frac{s_g}{s_w+s_g} - s_{gr}}{1-s_{wr}-s_{gr}}\right)^{ng}$ $n_w = 4, n_g = 2, s_{wr} = 0.2, s_{gr} = 0.3;$ $k_D = \begin{cases} 5.51721 \times (\varphi_e)^{0.86}, \varphi_e < 0.11 \\ 4.84653 \times 10^8 \times (\varphi_e)^{9.13}, \varphi_e \geq 0.11 \end{cases}$	$k_D = k_{D0}(1-s_h)^N$ $N = 15$	$k_D = k_{D0}(1-s_h)^N$ $N = 11$	$k_D = k_{D0}(1-s_h)^N$ $N = 15$	$k_{rw} = \left(\frac{s_w - s_{wr}}{1-s_{wr}}\right)^{nw}, k_{rg} = \left(\frac{s_g}{1-s_{wr}}\right)^{ng}$ $n_w = 0.6, n_g = 1.42;$ $k_D = \begin{cases} 5.51721 \times \left(\frac{\varphi_0-\varepsilon_V}{1-\varepsilon_V}(1-s_h)\right)^{0.86}, \frac{\varphi_0-\varepsilon_V}{1-\varepsilon_V}(1-s_h) \geq 0.11 \\ k_{DO}\left(\frac{\varphi_0-\varepsilon_V}{1-\varepsilon_V}(1-s_h)\right)^{1.2}, \frac{\varphi_0-\varepsilon_V}{1-\varepsilon_V}(1-s_h) \geq 0.11 \end{cases}$	where K_{rw} and k_{rg} are the relative permeability of water and gas, S_{wr} is the irreducible saturation of water. where φ_O is absolute porosity, ε_v is volumetric strain, k_{DO} absolute permeability of the sandstone without contains hydrate, mD S_h is saturation of hydrate.
	Kim et al. (1987)	**Kim et al. (1987)**	**Kim et al. (1987)**	**Kim et al. (1987)**	**Kim et al. (1987)**	
Dissociation rate (k_d, A_d)	$\dot{m}_g = k_d A_S(fe - f), k_d = 4.4 \times 10^{-16}$				$\dot{m}_g = k_d M_g A_d\left(p_{eh} - p_g\right) = k_d^o e^{-\frac{\Delta E}{RT}} M_g A_d\left(P_{eg} - P_g\right)$	where P_{eh} is the equilibrium pressure, P_g is the methane pressure, A_d is reacting surface of hydrate, K_d^0 is the intrinsic constant, R is the universal gas constant, ΔE is an activation energy.
Dissociation constant k_d (kmol/Pa.s.m^2)	$k_d^0 = 2.75 \times 10^{-12}$	$k_d^0 = 8.06$ $\Delta E = 77.33 \times 10^3$ J	$k_d^0 = 36$ $\Delta E = 81.08 \times 10^3$ J	$k_d^0 = 124$ $\Delta E = 78.15 \times 10^3$ J	$k_d^0 = 36$ $\Delta E = 81.08 \times 10^3$ J	
Surface area of hydrate per unit volume A_d	$A_d = \sqrt{\frac{\varphi_e^3}{2K_D}}$	$A_d = \varphi_0 S_h A_{geo}, 2r = 16\ \mu\text{m}$ $A_{geo} = 3.75 \times 10^5\ \text{m}^2/\text{m}^3$	$A_d = \sqrt{\frac{\varphi_e^3}{2K_D}}$	$A_d = \varphi_0 S_h A_{geo}, 2r = 16\ \mu\text{m}$ $A_{geo} = 3.75 \times 10^5\ \text{m}^2/\text{m}^3$	$A_d = \sqrt{\frac{\varphi_e^3}{2K_D}}$	$\varphi_e = \varphi_o(1-s_h)$ where φ_e is the effective porosity of porous media.
The heat transfer Enthalpy, internal energy (J/Kg)	$\Delta H_d = 446.12 \times 10^3 - 132.638T$	$\Delta H_d = 473.63 \times 10^3 - 140.117T$	Sun et al. (2005)	$\Delta H_d = 473.63 \times 10^3 - 140.117T$	$\dot{m}_w = M_W N_H \dot{m}_g / M_g, -\dot{m}_h = M_h \dot{m}_g / M_g$ $q = \lambda_b(T_o - T)$ $\Delta H_d = \left[\begin{array}{l} 215.59 \times 10^3 - 394.945T, 248K < T < 273K \\ 446.12 \times 10^3 - 132.638T, 273K < T < 298K \end{array}\right.$	where M_w and M_h are molecular weights of water and hydrate. where q is boundary heat flux, T_o is air temperature, λ_b is the boundary heat transfer coefficient determined by the heat transfer coefficient of the rubber sleeve and the ambient convection intensity.

Table 3. *Cont.*

	Sun et al. (2005)	**Nazridoust and Ahmadi. (2007)**	**Ruan et al. (2012)**	**Chen et al. (2016)**	**This Study**
Continuity equation of different fluid phases are: Momentum equation	$\frac{\partial}{\partial t}\left(\varphi_0\rho_k S_k\right)+\frac{\partial}{\partial x}\left(\rho_k S_k\right)=\dot{m}_k$ $(k=h,g,w)$	$-\nabla.\rho_k\overrightarrow{u_k}+\dot{m}_k=\frac{\partial}{\partial t}\left(\varphi_0\rho_k S_k\right)$ $(k=h,g,w,i)$	$-\frac{1}{r}\frac{\partial}{\partial r}\left(r\rho_k v_{kr}\right)+\frac{\partial}{\partial x}\left(\rho_k v_{kx}\right)+\dot{q}_k$ $+\dot{m}_k=\frac{\partial}{\partial t}\left(\varphi_0\rho_k S_k\right)(k=g,w)$ $\dot{m}_h=\frac{\partial}{\partial t}\left(\varphi_0\rho_h S_h\right)$	Nazridoust and Ahmadi. (2007)	$-\nabla.\rho_k\overrightarrow{u_k}+\dot{m}_k=\frac{\partial}{\partial t}\left(\varphi_0\rho_k S_k\right)$ $(k=h,g,w)$ where ρ is the density, m_k is the mass rate of dissociation formation substance, φ_0 is the porosity, S is the saturation, μ_k is the fluid velocity. The subscripts h, g, w corresponds to hydrate, gas and water in multiphase systems, respectively. $u_k=-\frac{k_D k_{rk}}{\mu_k}\nabla p_{k,}(k=g,w)p$ where u_k is the relative permeability of phase k, K_D is the absolute permeability of hydrated sandstone, K_{rk} is the relative permeability of phase k, and P is fluid pressure
Energy equation	$\frac{\partial}{\partial_t}\begin{bmatrix}(1-\varphi_o)\rho_R H_R+\varphi_O S_h\rho_h H_h\\+\varphi_O S_w\rho_w H_w+\varphi_O S_g\rho_g H_g\end{bmatrix}$ $+\frac{\partial}{\partial_x}\left(\rho_w v_w H_w+\rho_g v_g H_g\right)$ $=\frac{\partial}{\partial x}\left(\lambda\frac{\partial T}{\partial x}\right)+q$	$\frac{\partial}{\partial_t}\begin{bmatrix}(1-\varphi_o)\rho_R C_R T+\varphi_O S_h\rho_h C_h T\\+\varphi_O S_w\rho_w C_w T+\varphi_O S_g\rho_g C_g T\end{bmatrix}C_K$ $+\nabla T.(\rho_w C_w\overrightarrow{u}w+\rho_g C_g\overrightarrow{u}g)-\nabla.(\lambda_e\nabla T)=\dot{Q}_h$ $\dot{Q}_h=\frac{-\dot{m}_H(c+dT)}{M_H}$ $C=56.599\text{J/mol}, d=-16.744\text{J/mol K}$	$\frac{1}{r}\frac{\partial}{\partial r}\left(rk_c\frac{\partial T}{\partial r}\right)+\frac{\partial}{\partial x}\left(k_c\frac{\partial T}{\partial x}\right)$ $-\frac{1}{r}\frac{\partial}{\partial r}\left(r\rho_g v_{gr}h_g+r\rho_w v_{wr}h_w\right)$ $-\frac{\partial}{\partial x}\left(\rho_g v_{gr}h_g+\rho_w v_{wr}h_w\right)$ $+\frac{\partial}{\partial x}\left(\rho_k v_{kx}\right)+\dot{q}_g h_g+\dot{q}_w h_w+\dot{q}_h+\dot{q}_{in}$ $=\frac{\partial}{\partial t}\left[(1-\varphi)\rho_r h_r+\varphi\left(h_h\rho_h S_h+h_g\rho_g S_g+h_w\rho_w S_w\right)\right]$	Nazridoust and Ahmadi. (2007)	$\frac{\partial}{\partial_t}\begin{bmatrix}(1-\varphi_o)\rho_R C_R T+\varphi_O S_h\rho_h C_h T\\+\varphi_O S_w\rho_w C_w T+\varphi_O S_g\rho_g C_g T\end{bmatrix}C_K$ $+\nabla T.\left(\rho_w C_w\overrightarrow{u}w+\rho_g C_g\overrightarrow{u}g\right)-\nabla.(\lambda_e\nabla T)=\dot{Q}_h$ where C is the heat capacity, T is the temperature, $\overrightarrow{u}$ is the internal energy, Subscript R represents rock, h is the enthalpy. λ_e is the effective thermal conductivity, $\dot{Q}_h$ is the source term of endothermic reaction based on hydrate dissociation. $\dot{Q}_h=-\dot{m}_h\Delta H_d-\phi\rho_g S_g\sigma_g\frac{\partial p_g}{\partial t}-\rho_g u_g\nabla p_g$ where $\dot{m}_h$ is the mass dissociation rate for methane hydrate, ΔH_d is the latent heat of hydrate during the dissociation of methane hydrate, σ_g is the Joule-Thomson throttling coefficient, $\sigma_g=-1.5\times 10^{-4}$ $\lambda_e=(1-\varphi_0)\lambda_R+\varphi_0\left(s_h\lambda_h+s_w\lambda_w+s_g\lambda_g\right)$ where $\lambda_R,\lambda_h,\lambda_w,\lambda_g$ are thermal conductivity of rock, hydrate, water, gas, respectively.

Haghi et al. [54] derived the calculation equation of stress-dependent porosity of intact rock without considering the differences between particle compressibility and pore compressibility:

$$\varphi_t = \frac{\varphi_0 - \varepsilon_V}{1 - \varepsilon_V} \tag{6}$$

Then the effective porosity under the condition of different geo-stresses is:

$$\varphi_e = \frac{\varphi_0 - \varepsilon_V}{1 - \varepsilon_V}(1 - s_h) \tag{7}$$

A new permeability formula under effective stress can be obtained as follows:

$$k_D = \begin{cases} 5.51721 \times \left(\frac{\varphi_0 - \varepsilon_V}{1 - \varepsilon_V}(1 - s_h) \right)^{0.86}, \frac{\varphi_0 - \varepsilon_V}{1 - \varepsilon_V}(1 - s_h) < 0.11 \\ k_{DO}\left(\frac{\varphi_0 - \varepsilon_V}{1 - \varepsilon_V}(1 - s_h) \right)^{1.2}, \frac{\varphi_0 - \varepsilon_V}{1 - \varepsilon_V}(1 - s_h) \geq 0.11 \end{cases} \tag{8}$$

3. Results and Discussions

3.1. Model Validation

The gas production vs. time in the simulation and Masuda's experiment are presented in Figure 2. The simulation results showed the generation of methane gas in this study was slightly delayed, compared to experimental results. The temperature of the inspecting points (P1, P2, P3) vs. time in the simulation and Masuda's experiment are presented in Figure 3. It can be seen that when the time *t* was in the range of 0–100 min, closer to the outlet, the faster the temperature dropped, which was generally consistent with Masuda's experimental results. The minimum temperature of the three monitoring points in the simulation was lower than that of the Masuda experiment. The R-square values of the three temperature monitoring points were 0.882, 0.799, and 0.852, respectively. The pore pressure at the far-field boundary vs. time is presented in Figure 4. The overall trend of the pressure drop at the far end in the simulation experiment was consistent with the results of the Masuda experiment. The R-square of the far end boundary pressure was 0.890. The variations between the simulation and experimental results were caused by the heterogeneous distribution of the different phases, as well as the heterogeneous pore structure in the Berea sandstone. Considering the influence of pore structure, hydrate heterogeneity, and the application of the mathematical model on the experiment, the simulation results were believed to be in good agreement with the Masuda experiment.

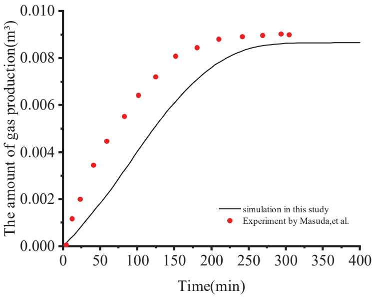

Figure 2. Gas production vs. time in the simulation experiment and Masuda's experiment [43].

As shown in Appendix A, the gas production of methane vs. time varies in literatures and in this study. The reasons lie in the fact that the initial hydrate saturation in some literature [19–25,43] was 0.443, while it was 0.501 in some others [17,18,26,28,41] and in this study. Zhang et al. [18] and Ruan's [20] gas production curves were in good agreement with the trials; however, Zhang only simulated gas production. The far-field boundary pressure was not simulated by Ruan et al. Chen et al. [23] simulated the pressure and temperature at the monitoring point without the gas generation. Additionally, the findings in this study and the literature [17,21–25,27] demonstrated that the early-stage gas generation rate was lower. The gas production rate was relatively higher, according to modeling results from Song et al. [44]. Overall, the simulation results in this study agreed well with the experimental benchmark data in far-field boundary pressure, temperature, and gas production, by assuming a homogenous initial distribution of the hydrate, water and methane in Berea sandstone.

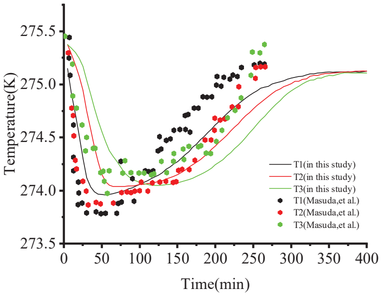

Figure 3. Temperature (T1, T2, T3) vs. time in the simulation experiment and Masuda's experiment [43].

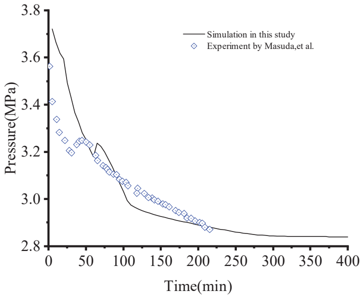

Figure 4. Pore pressure vs. time in the simulation experiment and Masuda's experiment [43].

As shown in Appendix B, Nazridoust et al. [21] the distal pressure did not significantly change at the start of the simulation, and the distal pressure of Chen et al. [23] was at its lowest point after 125 min of reaction time. Furthermore, Wan et al. [41] found that although the downward pressure trend throughout the earlier time was consistent, the downward pressure trend between 50 and 200 min was rather sluggish, and none of their results included small peaks. Small peaks were visible in the simulation findings from this work. The small peak predicted by Song et al. [44] and the trials were essentially in agreement; however, the pressure value remained high after the small peak arrived. The trials 'small peak fluctuated as the pressure lowered to roughly 3.2 MPa, and the small peak anticipated in this work exhibited the same behavior, but it occurred about 20 min later. Overall, the simulation results in this study agreed well with the experimental benchmark data in far-field boundary pressure.

Theoretically, the closer to the outlet, the lower the temperature and the earlier the dissociation of the hydrate. However, as shown in Appendix C, Chen et al.'s findings [23] did not support this conclusion. In terms of the temperatures at each monitoring point in the sandstone core during hydrate dissociation, the findings in this study and the literature [17–22,24–26,41] basically predicted the correct result. That is, the temperature at T1 decreased earlier than that at T2, and the temperature at T2 decreased earlier than that at T3. In this study and in [17,21,26,27,41], the monitoring point temperature was even lower, while in [19,20,23,24] it was higher. Since their boundary heat transfer coefficients were (50, 41.8, 16.6, 45.4, 45, 50) W/(m^{2}K), this study holds that the result was mostly caused by the boundary's uneven heat transmission. Considering the gas production at the outlet, the far-field boundary pressure and the temperature at the monitoring point, the curve fits of this study were good, compared with most previous research.

3.2. Effect of Initial Gas Saturation

The effects of initial gas saturation (0.1, 0.2, 0.25, 0.3, 0.4) on hydrate dissociation were investigated in this section. Other simulation conditions, except the initial gas saturation, were maintained. As shown in Figure 5, natural gas production with different initial gas saturations fluctuated over time. When the outlet valve was opened, gas production first increased sharply and then dropped steadily to zero over time. The fundamental cause for the first peak was that the gas tended to flow out when the outlet valve opened, due to the pressure difference between the inside and outside of the core. When the hydrate gradually decomposed, the difference between gas fugacity and equilibrium fugacity grew, promoting hydrate decomposition and increasing the gas production rate to the second peak. The value, $t_{90\%}$ (referring to the required time of 90% NGH dissociating in the core), decreased with increase of the initial gas saturation, as shown in Figure 6, which also showed that the higher the initial gas saturation, the faster the NGH decomposed.

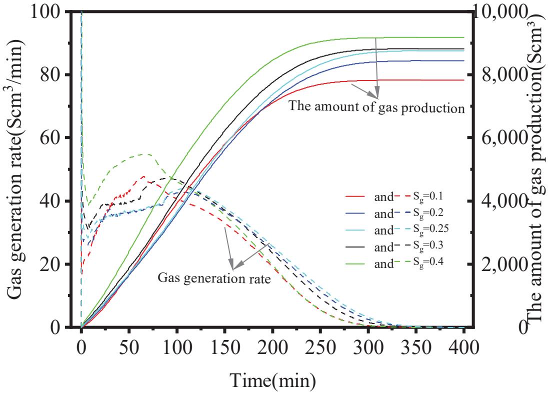

Figure 5. Gas production rate and cumulative gas production vs. time under different initial gas saturations.

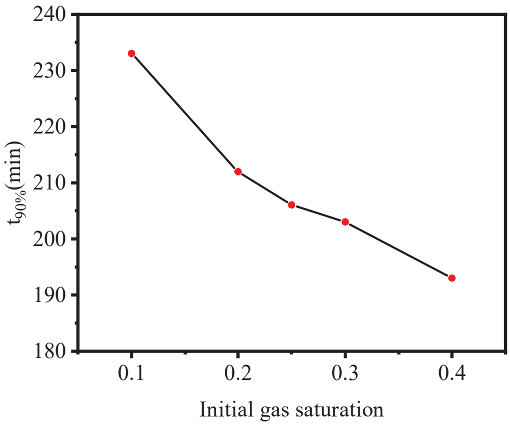

Figure 6. The value $t_{90\%}$ vs. initial gas saturation.

3.3. Effect of Outlet Pressure

The effects of outlet pressure (2.52 MPa, 2.68 MPa, 2.84 MPa, 3.00 MPa, 3.16 MPa) on hydrate dissociation were investigated in this section. Other simulation conditions, except the outlet pressure, were maintained. As shown in Figure 7, gas production and cumulative production fluctuated over time as the outlet pressure changed. The study found that natural gas production had four stages and two peaks, which were basically the same characteristics as mentioned earlier. The NGH in the core did not entirely dissociate in the first 400 min when the outlet pressure exceeded 3.16 MPa. Additionally, it was evident that when outlet pressure fell, a greater overall amount of gas was generated. The residual gas in the core varied under various pressure differences, which led to different cumulative gas production. The value,$t_{90\%}$, decreased with a decrease in the outlet pressure, as shown in Figure 8, which also showed that the lower the outlet pressure, the faster the natural gas hydrate decomposed.

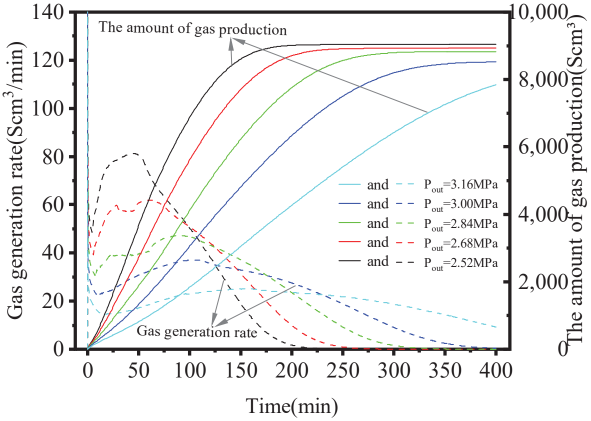

Figure 7. Gas production rate and cumulative gas production vs. time under different outlet pressure.

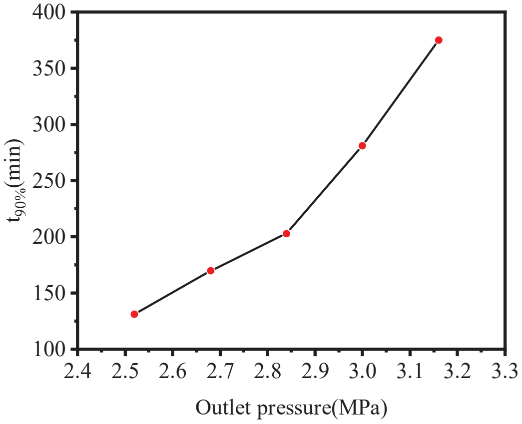

Figure 8. The value $t_{90\%}$ vs. outlet pressure.

3.4. Effect of Initial Temperature

The effects of initial temperatures (273.45 K, 274.45 K, 275.45 K, 276.45 K, 277.45 K) on hydrate dissociation were investigated in this section. Other simulation conditions, except the initial temperatures, were maintained. As shown in Figure 9, at higher initial temperatures, natural gas production and cumulative natural gas production fluctuated over time as the initial temperature changed, and as the initial temperature increased, the rate of natural gas hydrate dissociation accelerated. The total production of gas did not change much, though. The value, $t_{90\%}$, decreased with increasing initial temperatures, as shown in Figure 10, which also showed that the higher the initial temperatures, the faster the natural gas hydrate decomposed. As shown in Figure 11, it was discovered that, under adiabatic conditions, the gas generation rate rose instantly in the beginning and then gradually fell until it reached zero. As the final cumulative gas production was 2800 Scm^3, no new gas was generated, so it could be concluded that the hydrate would not decompose under adiabatic conditions (insufficient energy).

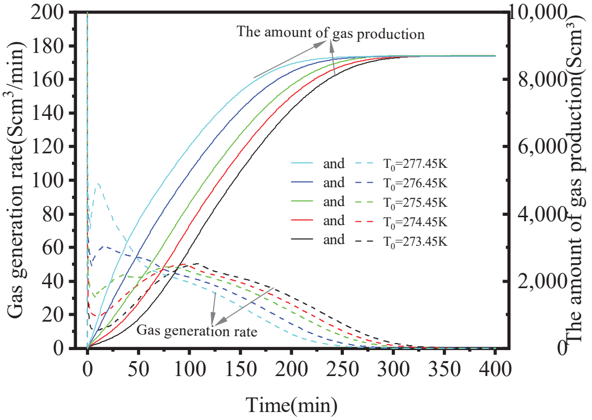

Figure 9. Gas production rate and cumulative gas production vs. time at different initial temperature.

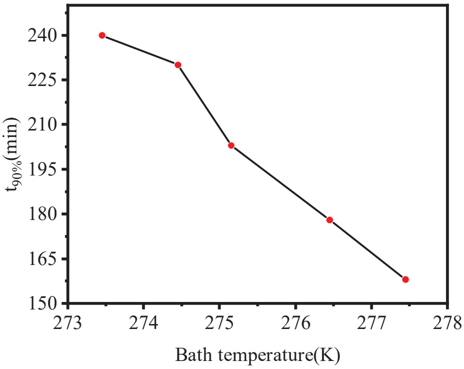

Figure 10. The value $t_{90\%}$ vs. initial temperature.

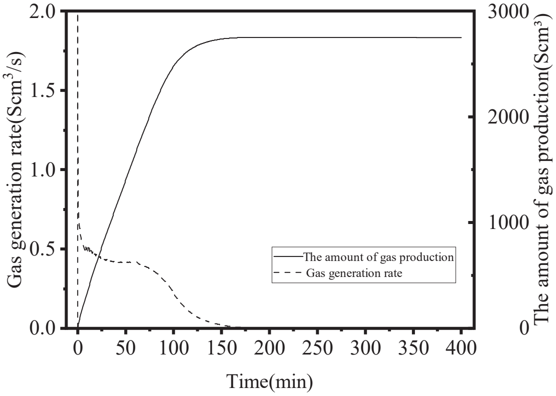

Figure 11. Gas production rate and cumulative gas production vs. time under adiabatic boundary conditions.

3.5. Effect of Absolute Permeability

The effects of absolute permeability (10 mD, 50 mD, 98.97 mD, 150 mD, 200 mD) on hydrate dissociation were investigated in this section. Other simulation conditions, except the absolute permeability, were maintained. As shown in Figure 12, variation of absolute permeability caused gas production rate and cumulative gas production to fluctuate with time. The gas production rate and cumulative gas production for 10 mD absolute permeability were different from the other four data, and the gas production rate was very low. This was because reduced absolute permeability limited fluid flowability and decreased the pressure driving force of hydrate dissociation, resulting in a lengthier hydrate dissociation process. The value, $t_{90\%}$, decreased with an increase in the absolute permeability, as shown in Figure 13, which also showed that the higher the absolute permeability, the faster the natural gas hydrate decomposed.

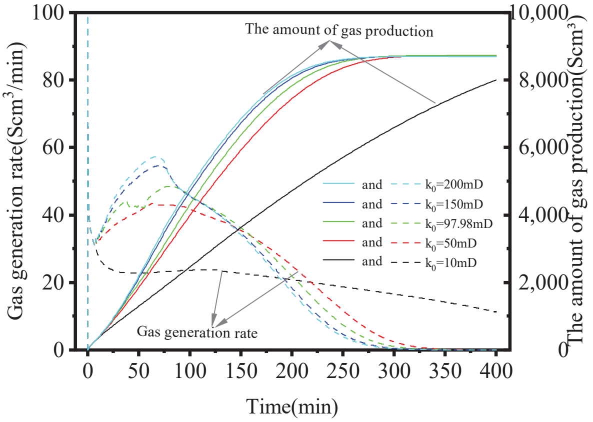

Figure 12. Gas production rate and cumulative gas production vs. time under different absolute.

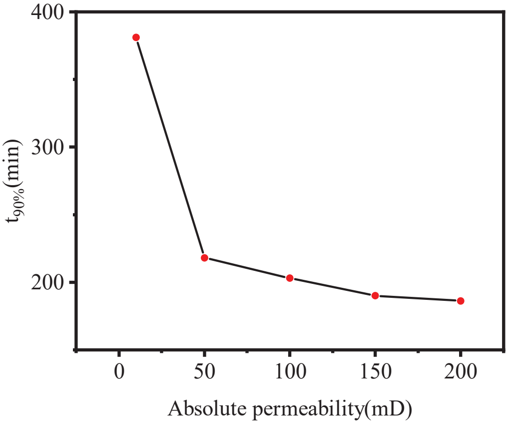

Figure 13. The value $t_{90\%}$ vs. absolute permeability.

3.6. Effect of Geo-Stress

As early as the 1940s, some researchers in other countries began to investigate the fluctuation of porosity and permeability with confining pressure. Fatt et al. [47,48], Gray et al. [53], and Mclatchie et al. [55] investigated the effect of reservoir stress fluctuations on rock permeability and porosity, and the researchers confirmed that porosity and permeability steadily declined as effective stress increased. In the late 1980s, China conducted a substantial study on reservoir stress sensitivity. Research [47,48,51–56] showed that the porosity and permeability of the reservoir decreased when effective stress increased. Furthermore, the stress sensitivity effect was particularly noticeable in low permeability reservoirs.

Zhu and Wang et al. [56] reported the stress-related porosity data of five different sandstones under isotropic effective stress conditions. As shown in Figure 14, the effective stress range of 0–30 MPa appeared in the data and the fitting curves of volumetric strain and stress-related porosity of Equations (5) and (6) to assess the validity of the aforesaid fitting correlation equation for Berea sandstone. The certain value of the fitting constants are displyed in Table 4.

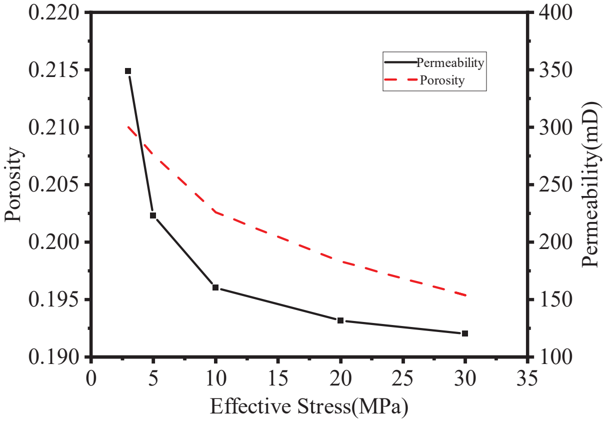

Figure 14. Fitted curves of porosity and permeability of Berea sandstone vs. effective stress in Zhu and Wang's experimental data [56].

Table 4. Fitting constants in Zhu and Wang experiments.

Rock	A'	B'	C'
Berea sandstone	0.183	0.01859	9.842

Based on Masuda's hydrate core decomposition experiment, the effective stress (5 MPa, 15 MPa, and 25 MPa) was changed by varying the confining pressure of the sandstone core, and numerical models were built for the evolution of physical properties of hydrate sandstone cores under different stresses.

Figure 15a,b show the volume of gas hydrate in the cores considering, or not considering, the effect of ground stress. The average volume fraction in the core, considering the geo-stress, was higher than that without considering the geo-stress at the same time point, which indicated that the effect of geo-stress reduced the decomposition rate of natural gas hydrate in sandstone core. The volume fraction of methane in the core without considering, or considering, the effect of geo-stress is shown in Figure 16a,b. The average volume fraction in the core, considering the geo-stress, was lower than that without considering the geo-stress at the same time, which indicated that the effect of geo-stress reduced the gas production rate in sandstone core. Figure 17 also illustrates this point. The temperature in the core without considering, or considering, the effect of geo-stress is shown in Figure 18a,b. In the process of the temperature dropping, caused by endothermic reaction, the average core temperature considering geo-stress effect was higher than that without considering geo-stress. In the process of the temperature rising, caused by heat transfer, the average core temperature considering geo-stress was lower than that without considering geo-stress, which indicated that the effect of geo-stress slowed down the efficiency of the heat and mass transfer in the sandstone core, leading to slower dissociation and transportation rates of the NGH.

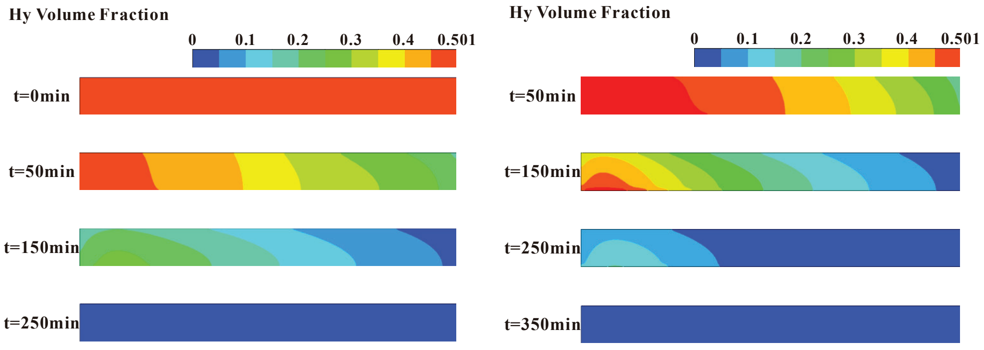

(a)The volume fraction of NGH in core without considering the effect of geo-stress

(b)The volume fraction of NGH in core considering the effect of geo-stress

Figure 15. Hydrate volume fraction in the core at different times.

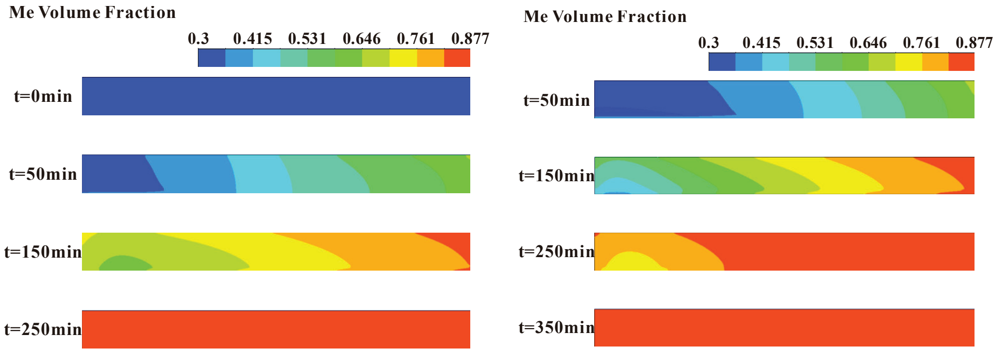

(a)The volume fraction of Methane in core without considering the effect of geo-stress

(b)The volume fraction of Methane in core considering the effect of geo-stress

Figure 16. Methane volume fraction in the core at different times.

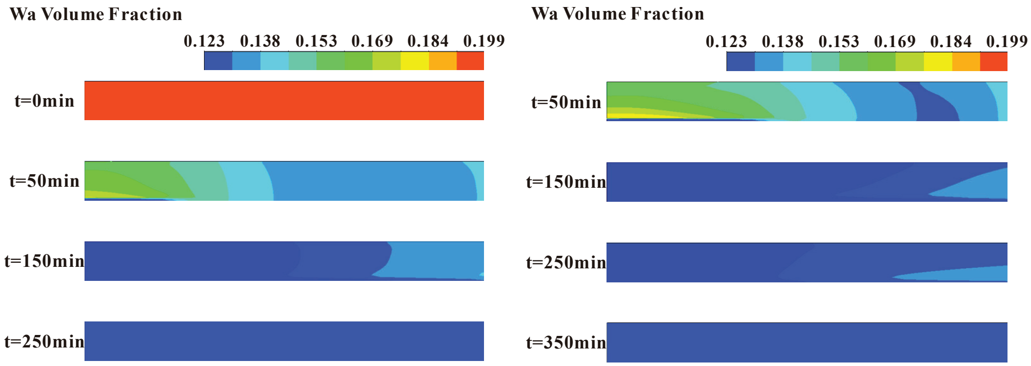

(a)The volume fraction of Water in core without considering the effect of geo-stress

(b)The volume fraction of Water in core considering the effect of geo-stress

Figure 17. Water volume fraction in the core at different times.

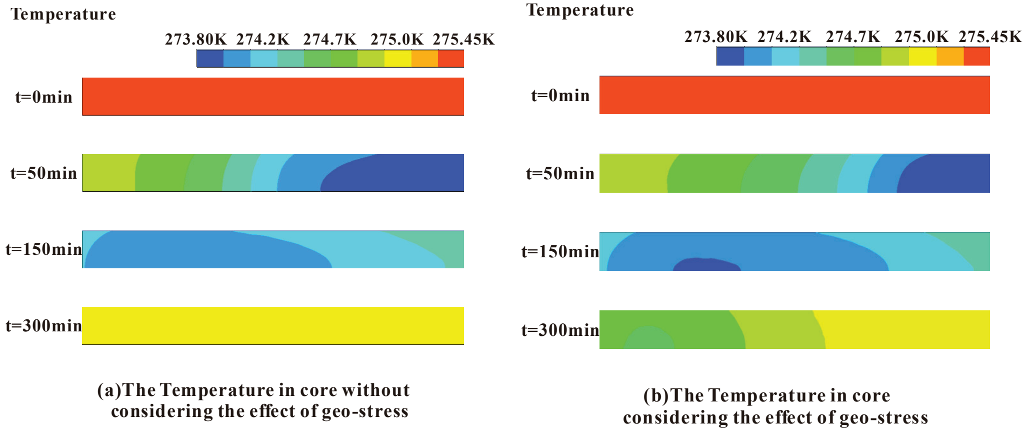

Figure 18. Temperature distribution in the core at different times.

As shown in Figure 19, natural gas production and cumulative natural gas production fluctuated with time under different effective stresses. The gas production rate graph shows that, at 125 min, before the reaction, the instantaneous gas production rate, without taking the effect of effective stress into account, was higher than that under the effect of effective stress. The rate of gas production decreased as effective stress increased. In addition, as the effective stress increased, the time to drop to zero for the corresponding gas production rate increased, which also meant that the time for the hydrate dissociation increased. This was because the effective stress decreased the amount of pore space, which lowered the core's permeability and porosity. The permeability and porosity in the core decreased as the effective stress increased. The slower the heat convection, the lower the mass transfer efficiency, and the longer it took for the hydrate to dissociate, the smaller the permeability, so, consequently, the longer the completion date for gas production from the use of natural gas hydrates. The cumulative gas output showed that, under various effective stress levels, the final cumulative gas output was equal. The time it took to reach the final cumulative gas output increased with the effective stress. This indicated that the effective stress decreased the permeability of the core, hence decreasing the rate of hydrate decomposition and mining efficiency. However, it had no impact on the hydrate decomposition's overall cumulative gas generation. As shown in Figure 20, $t_{90\%}$ rose as effective stress increased. This was because the increase of effective stress led to the volume shrinkage of pore space, thus reducing the permeability and porosity of sediments. Low permeability slowed thermal convection, which slowed down the pressure drop from one end of the core to the outlet and reduced mass transfer efficiency. This slowed down hydrate decomposition, which increased the time it took to produce gas from natural gas hydrates and reduced their exploitation efficiency. Therefore, the natural gas hydrate production would be less effective as effective stress rose, under various effective stresses.

Under various effective stress levels, pore pressure at the far-field boundary varied over time as shown in Figure 21. The diagram shows that when the effective stress was low, the duration and size of the small peak were close and the pore pressure test curve was more like the experimental results of Masuda. The pore pressure test curve was significantly different from the experimental data of Masuda. With a rise in effective stress, the small peak value also gradually declined, and the small peak value's appearance time arrived later and later. Additionally, there was a small peak in several conditions, and this small peak in the pore pressure curve at the far-field boundary was not a coincidence; rather, it was one of the characteristics of the two-phase flow in porous media that was brought on by hydrate dissociation. In the case of hydrate dissociation, for instance, the inability of the gas to spread quickly led to an increase in local pore pressure. This demonstrated that the impact of effective stress caused a reduction in pore space volume, which caused a reduction in the core's porosity and permeability. As a result, the gas produced by hydrate decomposition could not be discharged quickly and accumulated in the core, increasing core pressure and further impeding hydrate decomposition. Additionally, hydrate breakdown was slowed down by increasing effective stress.

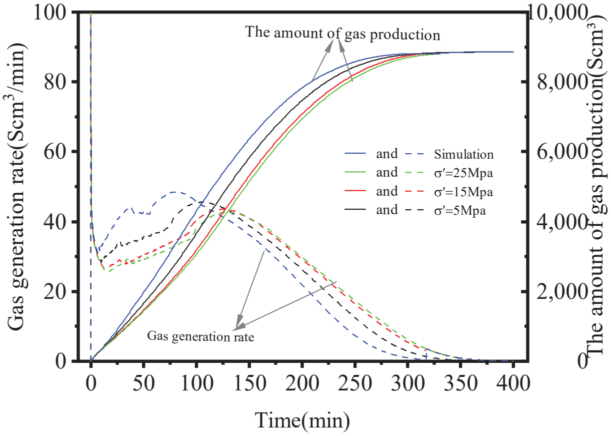

Figure 19. Gas production rate and cumulative gas production vs. time under different effective stresses.

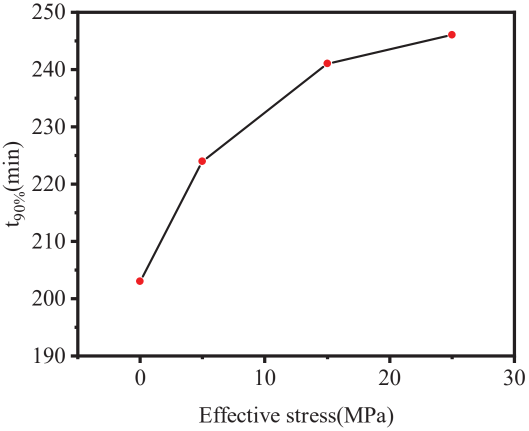

Figure 20. The value $t_{90\%}$ vs. confining pressure.

Three monitoring points' temperatures over time, and under various effective stress levels, are shown in Figure 22. The minimum temperature considering effective stress was higher than it was without considering effective stress 125 min before decompression, as shown in Figure 22. The increasing rate of temperature recovery (the heat transfer-induced temperature recovery process) was lower than it would be without taking effective stress into account. This was due to the decrease in effective stress, which lowered the core's porosity and permeability, and, moreover, slowing down the pace of hydrate dissociation to achieve a late minimum temperature. Additionally, it can be seen from a comparison of Figure 22a–c that the greater the effective stress, the later the minimum temperature appeared. This was because the core's porosity and permeability decreased as the effective stress increased. The low permeability restricted the efficiency of the heat and mass transfer by the fluid flow, leading to a slow dissociation and transportation rate of the NGH.

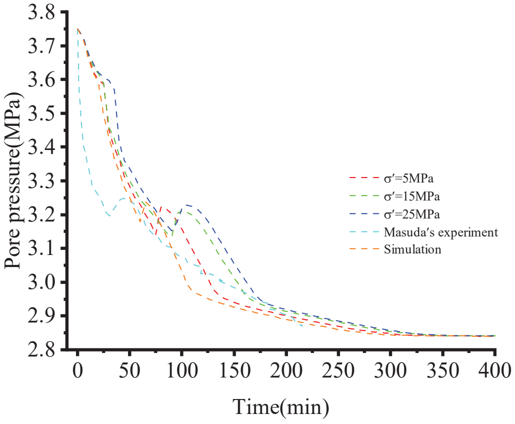

Figure 21. Far field pressure vs. time of the core for different effective stresses.

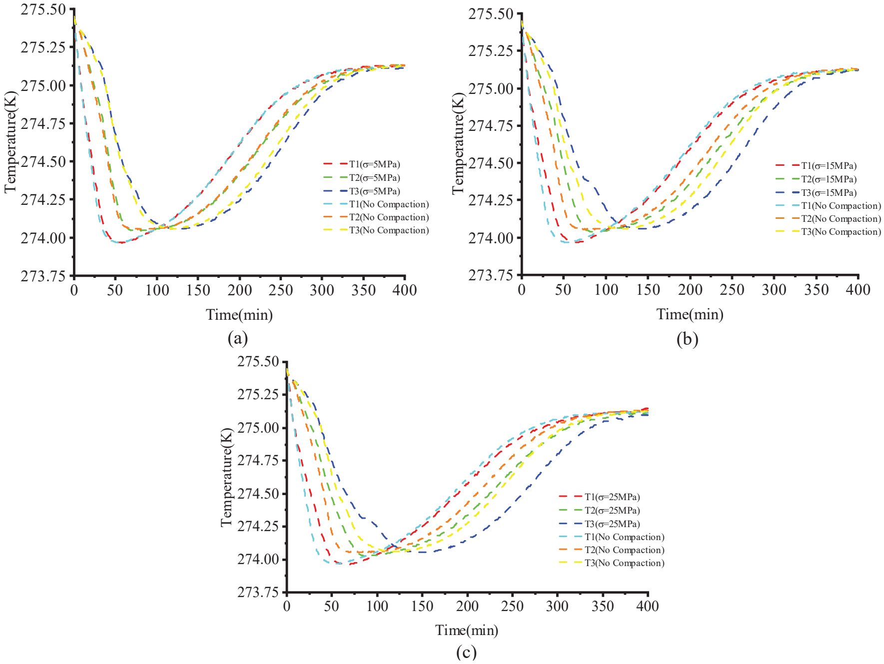

Figure 22. Temperature of monitoring points vs. time under different effective stress conditions and without considering stress. Subgraph (**a**–**c**) show that the temperature of monitoring points vs. time under the effective stress of 5 MPa, 15 MPa, 25 MPa and without considering stress.

4. Conclusions

In this study, an axisymmetric two-dimensional model was developed to simulate the depressurization decomposition process of natural gas hydrate in Berea sandstones. A mathematical model that considered fluid heat, mass transport, multiphase flow mechanics, and the kinetics of hydrate decomposition, was established. FLUENT was employed to solve the basic governing equations of multi-phase flow and UDF was used to program the hydrate dissociation model and modified permeability model during NGH dissociation and transport. The simulation results were then validated by Masuda's experimental data, and multi-parametric analysis was performed. The following conclusions could be achieved:

- The established mathematical model and the simulation scheme were validated by historical matching with the experimental benchmark data.
- The sensitivity analysis of the parameters revealed that a higher absolute permeability, higher initial gas saturation, lower outlet pressure, and higher initial temperature advanced the decomposition rate of hydrate. Thus, an optimized production plan is essential to promote the extraction efficiency of the NGH.
- Geo-stress caused a decrease of the porosity and permeability in the porous rock, which restricted the efficiency of the heat and mass transfer by the fluid flow, leading to a slow dissociation and transportation rate of the NGH. Thus, it is essential to take geo-stress into consideration and balance the extracting efficiency and the well pressure, especially when the NGH is developed by depressurization.

In this paper, the numerical modeling on the core scale dissociation and transportation of NGH was conducted. Future study will focus on the development of NGH in its formation.

Author Contributions: Conceptualization, R.S.; Methodology, J.L.; Investigation, R.S.; Data curation, Y.D.; Writing—original draft, Y.D.; Writing—review & editing, J.L. and Y.S.; Funding acquisition, R.S. All authors have read and agreed to the published version of the manuscript.

Funding: This research was funded by the National Natural Science Foundation of China (Grant Number 51909225), and the Knowledge Innovation Program of Wuhan-Basic Research (Grant Number 2022010801010158).

Data Availability Statement: All the data and materials used in this paper are available from the corresponding author upon request.

Conflicts of Interest: The authors declare that they have no known competing financial interests or personal relationships that could have appeared to influence the work reported in this paper.

Appendix A

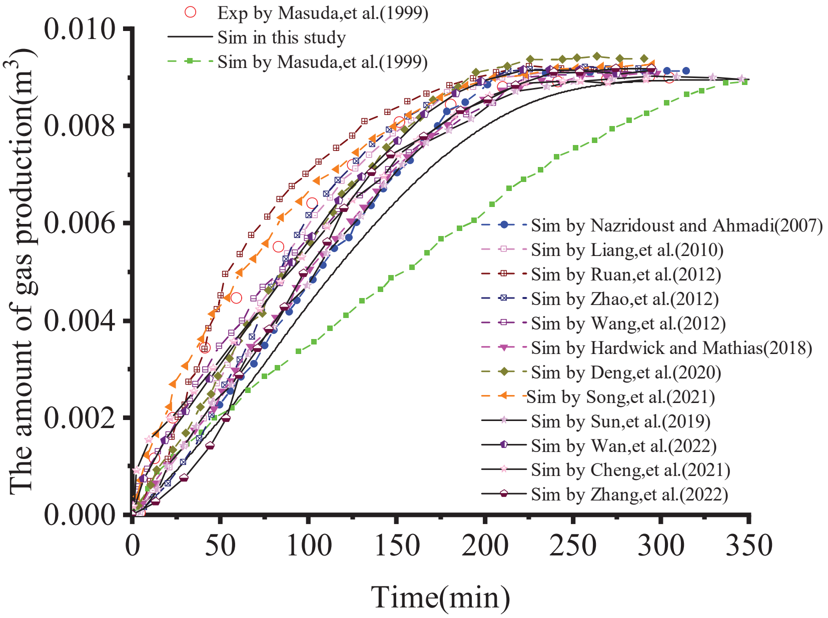

Figure A1. Gas production vs. time in this study and previous studies [17–28,41,43,44].

Appendix B

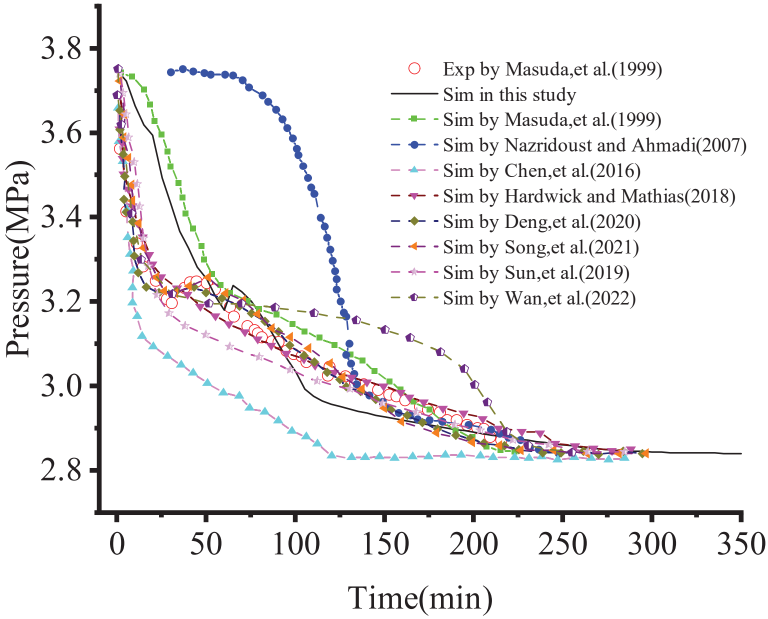

Figure A2. Far field pressure vs. time of this study and previous studies [17,20–22,27,41,43,44].

Appendix C

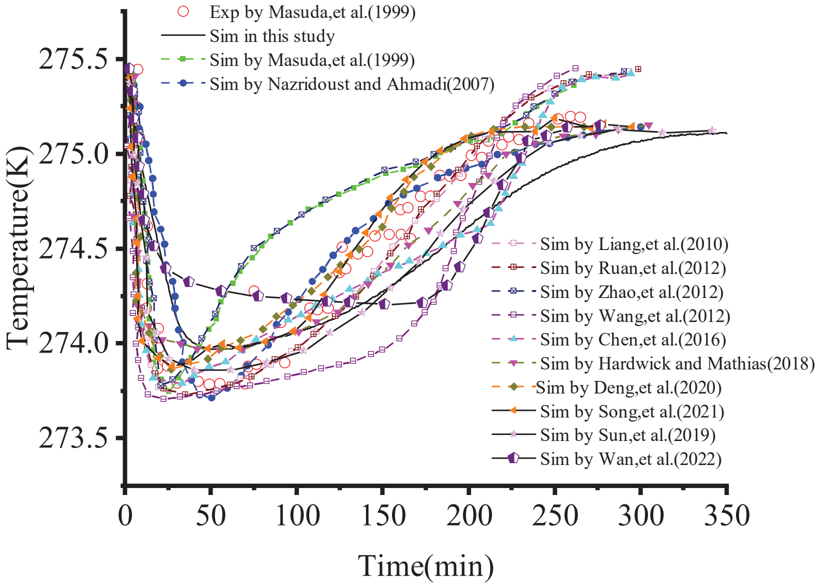

(**a**) Temperature at T1

Figure A3. *Cont.*

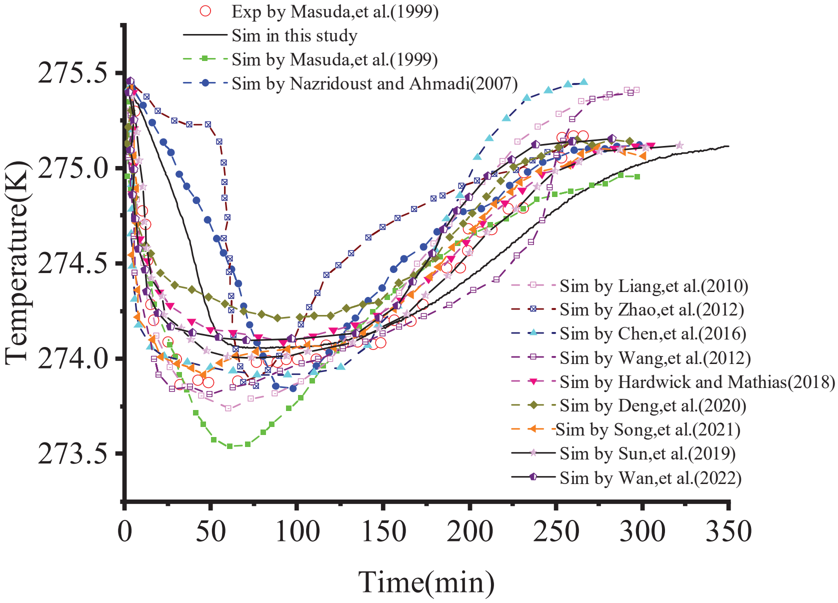

(**b**) Temperature at T2

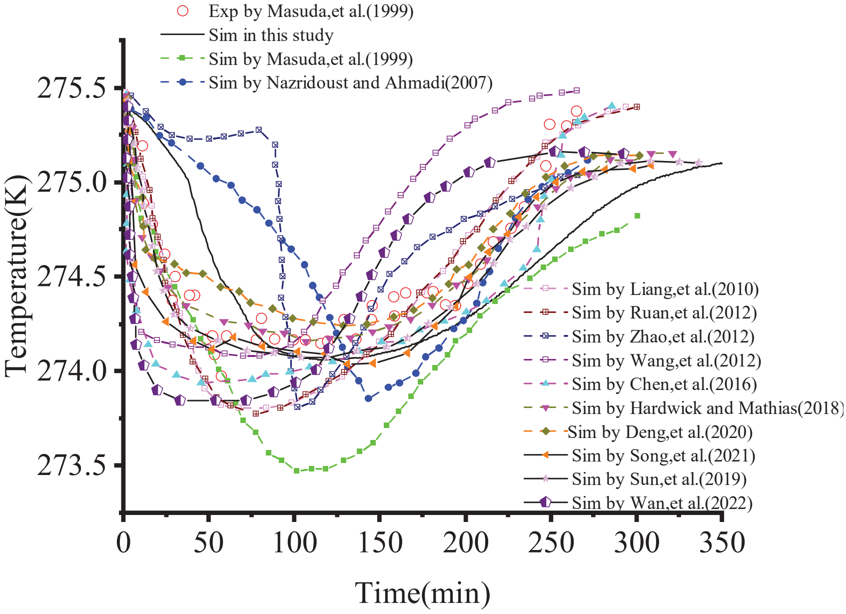

(**c**) Temperature at T3

Figure A3. Temperature at monitoring points vs. time of this study and previous studies [17,21–27,41,43].

References

1. Song, R.; Wang, Y.; Tang, Y.; Liu, J.; Yang, C. 3D Printing of natural sandstone at pore scale and comparative analysis on micro-structure and single/two-phase flow properties. *Energy* **2022**, *261*, 125226. [CrossRef]
2. Song, R.; Liu, J.; Yang, C.; Sun, S. Study on the multiphase heat and mass transfer mechanism in the dissociation of methane hydrate in reconstructed real-shape porous sediments. *Energy* **2022**, *254*, 124421. [CrossRef]
3. Song, R.; Sun, S.; Liu, J.; Yang, C. Pore scale modeling on dissociation and transportation of methane hydrate in porous sediments. *Energy* **2021**, *237*, 121630. [CrossRef]
4. Song, R.; Sun, S.; Liu, J.; Feng, X. Numerical modeling on hydrate formation and evaluating the influencing factors of its heterogeneity in core-scale sandy sediment. *J. Nat. Gas Sci. Eng.* **2021**, *90*, 103945. [CrossRef]
5. Yin, Z.; Linga, P. Methane hydrates: A future clean energy resource. *Chin. J. Chem. Eng.* **2019**, *27*, 2026–2036. [CrossRef]
6. Song, R.; Wang, Y.; Ishutov, S.; Zambrano-Narvaez, G.; Hodder, K.J.; Chalaturnyk, R.J.; Sun, S.; Liu, J.; Gamage, R.P. A comprehensive experimental study on mechanical behavior, microstructure and transport properties of 3D-printed rock analogs. *Rock Mech. Rock Eng.* **2020**, *53*, 5745–5765. [CrossRef]
7. Li, B.; Li, X.S.; Li, G.; Chen, Z.Y. Evaluation of gas production from Qilian Mountain permafrost hydrate deposits in two-spot horizontal well system. *Cold Reg. Sci. Technol.* **2015**, *109*, 87–98. [CrossRef]
8. Li, G.; Moridis, G.J.; Zhang, K.; Li, X.S. Evaluation of the gas production potential of marine hydrate deposits in the Shenhu Area of the South China Sea. In *Offshore Technology Conference*; OnePetro: Houston, TX, USA, 2010.
9. Feng, J.C.; Wang, Y.; Li, X.S.; Li, G.; Chen, Z.Y. Production behaviors and heat transfer characteristics of methane hydrate dissociation by depressurization in conjunction with warm water stimulation with dual horizontal wells. *Energy* **2015**, *79*, 315–324. [CrossRef]
10. Chong, Z.R.; Pujar, G.A.; Yang, M.; Linga, P. Methane hydrate formation in excess water simulating marine locations and the impact of thermal stimulation on energy recovery. *Appl. Energy* **2016**, *177*, 409–421. [CrossRef]
11. Chong, Z.R.; Yang, S.H.B.; Babu, P.; Linga, P.; Li, X.S. Review of natural gas hydrates as an energy resource: Prospects and challenges. *Appl. Energy* **2016**, *162*, 1633–1652. [CrossRef]
12. Wang, Y.; Lang, X.; Fan, S.; Wang, S.; Yu, C.; Li, G. Review on enhanced technology of natural gas hydrate recovery by carbon dioxide replacement. *Energy Fuels* **2021**, *35*, 3659–3674. [CrossRef]
13. Cai, J.; Xia, Y.; Lu, C.; Bian, H.; Zou, S. Creeping microstructure and fractal permeability model of natural gas hydrate reservoir. *Mar. Pet. Geol.* **2020**, *115*, 104282. [CrossRef]
14. Wang, X.; Dong, B.; Li, W.; Yu, M.; Song, Y. Microscale effects on methane hydrate dissociation at low temperature in the micro porous media channels by depressurization. *Int. J. Heat Mass Transf.* **2018**, *122*, 1182–1197. [CrossRef]
15. Makogon, Y.F. Natural gas hydrates–A promising source of energy. *J. Nat. Gas Sci. Eng.* **2010**, *2*, 49–59. [CrossRef]
16. Zhao, J.; Liu, D.; Yang, M.; Song, Y. Analysis of heat transfer effects on gas production from methane hydrate by depressurization. *Int. J. Heat Mass Transf.* **2014**, *77*, 529–541. [CrossRef]
17. Deng, X.; Feng, J.; Pan, S.; Wang, Z.; Zhang, J.; Chen, W. An improved model for the migration of fluids caused by hydrate dissociation in porous media. *J. Pet. Sci. Eng.* **2020**, *188*, 106876. [CrossRef]
18. Zhang, P.; Liu, B.; Hu, L.; Meegoda, J.N. Coupled multiphase flow and pore compression computational model for extraction of offshore gas hydrates. *Comput. Geotech.* **2022**, *145*, 104671. [CrossRef]
19. Liang, H.; Song, Y.; Chen, Y. Numerical simulation for laboratory-scale methane hydrate dissociation by depressurization. *Energy Convers. Manag.* **2010**, *51*, 1883–1890. [CrossRef]
20. Ruan, X.; Song, Y.; Liang, H.; Yang, M.; Dou, B. Numerical simulation of the gas production behavior of hydrate dissociation by depressurization in hydrate-bearing porous medium. *Energy Fuels* **2012**, *26*, 1681–1694. [CrossRef]
21. Nazridoust, K.; Ahmadi, G. Computational modeling of methane hydrate dissociation in a sandstone core. *Chem. Eng. Sci.* **2007**, *62*, 6155–6177. [CrossRef]
22. Zhao, E.; Hou, J.; Liu, Y.; Ji, Y.; Liu, W.; Lu, N.; Bai, Y. Enhanced gas production by forming artificial impermeable barriers from unconfined hydrate deposits in Shenhu area of South China sea. *Energy* **2020**, *213*, 118826. [CrossRef]
23. Chen, L.; Yamada, H.; Kanda, Y.; Lacaille, G.; Shoji, E.; Okajima, J.; Komiya, A.; Maruyama, S. Numerical analysis of core-scale methane hydrate dissociation dynamics and multiphase flow in porous media. *Chem. Eng. Sci.* **2016**, *153*, 221–235. [CrossRef]
24. Wang, B.; Fan, Z.; Zhao, J.; Lv, X.; Pang, W.; Li, Q. Influence of intrinsic permeability of reservoir rocks on gas recovery from hydrate deposits via a combined depressurization and thermal stimulation approach. *Appl. Energy* **2018**, *229*, 858–871. [CrossRef]
25. Zhao, J.; Fan, Z.; Dong, H.; Yang, Z.; Song, Y. Influence of reservoir permeability on methane hydrate dissociation by depressurization. *Int. J. Heat Mass Transf.* **2016**, *103*, 265–276. [CrossRef]
26. Hardwick, J.S.; Mathias, S.A. Masuda's sandstone core hydrate dissociation experiment revisited. *Chem. Eng. Sci.* **2018**, *175*, 98–109. [CrossRef]
27. Deng, X.; Pan, S.; Zhang, J.; Wang, Z.; Jiang, Z. Numerical investigation on abnormally elevated pressure in laboratory-scale porous media caused by depressurized hydrate dissociation. *Fuel* **2020**, *271*, 117679. [CrossRef]
28. Li, Q.P.; Lv, X.; Pang, W.X.; Yao, H.Y.; Ge, Y.; Wang, J.A. Numerical Simulation of the Effect of Porous Media Permeability on the Decomposition Characteristics of Natural Gas Hydrate at the Core Scale. *Energy Fuels* **2021**, *35*, 5843–5852. [CrossRef]
29. Dai, S.; Santamarina, J.C.; Waite, W.F.; Kneafsey, T.J. Hydrate morphology: Physical properties of sands with patchy hydrate saturation. *J. Geophys. Res. Solid Earth* **2012**, *117*, B11205. [CrossRef]

30. White, M.D.; Kneafsey, T.J.; Seol, Y.; Waite, W.F.; Uchida, S.; Lin, J.S.; Myshakin, E.M.; Gai, X.; Gupta, S.; Reagan, M.T.; et al. An international code comparison study on coupled thermal, hydrologic and geomechanical processes of natural gas hydrate-bearing sediments. *Mar. Pet. Geol.* **2020**, *120*, 104566. [CrossRef]
31. Cheng, Y.; Li, L.; Yuan, Z.; Wu, L.; Mahmood, S. Finite element simulation for fluid–solid coupling effect on depressurization-induced gas production from gas hydrate reservoirs. *J. Nat. Gas Sci. Eng.* **2013**, *10*, 1–7. [CrossRef]
32. Lee, T.; Son, H.; Lee, J.; Ahn, T.; Kang, N. Geomechanically Sustainable Gas Hydrate Production Using a 3D Geological Model in the Ulleung Basin of the Korean East Sea. *Energies* **2022**, *15*, 2569. [CrossRef]
33. Liu, Z.; Lu, Y.; Cheng, J.; Han, Q.; Hu, Z.; Wang, L. Geomechanics involved in gas hydrate recovery. *Chin. J. Chem. Eng.* **2019**, *27*, 2099–2106. [CrossRef]
34. Wu, Z.; Yang, S.; Liu, W.; Li, Y. Permeability analysis of gas hydrate-bearing sand/clay mixed sediments using effective stress laws. *J. Nat. Gas Sci. Eng.* **2022**, *97*, 104376. [CrossRef]
35. Sun, X.; Li, Y.; Liu, Y.; Song, Y. The effects of compressibility of natural gas hydrate-bearing sediments on gas production using depressurization. *Energy* **2019**, *185*, 837–846. [CrossRef]
36. Jang, J.; Dai, S.; Yoneda, J.; Waite, W.F.; Stern, L.A.; Boze, L.G.; Collett, T.S.; Kumar, P. Pressure core analysis of geomechanical and fluid flow properties of seals associated with gas hydrate-bearing reservoirs in the Krishna-Godavari Basin, offshore India. *Mar. Pet. Geol.* **2019**, *108*, 537–550. [CrossRef]
37. Kimoto, S.; Oka, F.; Fushita, T.; Fujiwaki, M. A chemo-thermo-mechanically coupled numerical simulation of the subsurface ground deformations due to methane hydrate dissociation. *Comput. Geotech.* **2007**, *34*, 216–228. [CrossRef]
38. Sun, X.; Luo, H.; Soga, K. A coupled thermal–hydraulic–mechanical–chemical (THMC) model for methane hydrate bearing sediments using COMSOL Multiphysics. *J. Zhejiang Univ.-Sci. A* **2018**, *19*, 600–623. [CrossRef]
39. Sun, X.; Luo, T.; Wang, L.; Wang, H.; Song, Y.; Li, Y. Numerical simulation of gas recovery from a low-permeability hydrate reservoir by depressurization. *Appl. Energy* **2019**, *250*, 7–18. [CrossRef]
40. Cheng, W.; Lu, C.; Ning, F.; Jia, M. A coupled thermal-hydraulic-mechanical model for the kinetic dissociation of methane hydrate in a depressurizing well. *J. Pet. Sci. Eng.* **2021**, *207*, 109021. [CrossRef]
41. Wan, Y.; Wu, N.; Chen, Q.; Li, W.; Hu, G.; Huang, L.; Ouyang, W. Coupled thermal-hydrodynamic-mechanical–chemical numerical simulation for gas production from hydrate-bearing sediments based on hybrid finite volume and finite element method. *Comput. Geotech.* **2022**, *145*, 104692. [CrossRef]
42. Yasuda, S.; Masuda, T.; Yoshida, N.; Nagase, H.; Kiku, H.; Itafuji, S.; Mine, K.; Sato, K. Torsional chear and triaxial compression tests on deformation characters of sands before and after liquefaction. In Proceedings of the Fifth US-Japan Workshop on Earthquake Resistant Design of Lifeline Facilities and Countermeasures against Soil Liquefaction, Snowbird, UT, USA, 29 September 1994; pp. 249–265.
43. Masuda, Y. Modeling and experimental studies on dissociation of methane gas hydrates in Berea sandstone cores. In Proceedings of the Third International Gas Hydrate Conference, Salt Lake City, UT, USA, 18–22 July 1999.
44. Song, R.; Feng, X.; Wang, Y.; Sun, S.; Liu, J. Dissociation and transport modeling of methane hydrate in core-scale sandy sediments: A comparative study. *Energy* **2021**, *221*, 119890. [CrossRef]
45. Biot, M.A. General theory of three-dimensional consolidation. *J. Appl. Phys.* **1941**, *12*, 155–164. [CrossRef]
46. Detournay, E.; Cheng, A.H.D. Fundamentals of poroelasticity. In *Analysis and Design Methods*; Pergamon: Oxford, UK, 1993; pp. 113–171.
47. Fatt, I.; Davis, D.H. Reduction in permeability with overburden pressure. *J. Pet. Technol.* **1952**, *4*, 16-16. [CrossRef]
48. Fatt, I. The effect of overburden pressure on relative permeability. *J. Pet. Technol.* **1953**, *5*, 15–16. [CrossRef]
49. Van der Knaap, W. Nonlinear behavior of elastic porous media. *Trans. AIME* **1959**, *216*, 179–187. [CrossRef]
50. Hubbert, M.K.; Rubey, W.W. Role of fluid pressure in mechanics of overthrust faultingi. mechanics of fluid-filled porous solids and its application to overthrust faulting. *GSA Bull.* **1959**, *70*, 115–166. [CrossRef]
51. Zimmerman, R.W.; Somerton, W.H.; King, M.S. Compressibility of porous rocks. *J. Geophys. Res. Solid Earth* **1986**, *91*, 12765–12777. [CrossRef]
52. Schutjens, P.M.T.M.; Hanssen, T.H.; Hettema, M.H.H.; Merour, J.; De Bree, P.; Coremans, J.W.A.; Helliesen, G. Compaction-induced porosity/permeability reduction in sandstone reservoirs: Data and model for elasticity-dominated deformation. *SPE Reserv. Eval. Eng.* **2004**, *7*, 202–216. [CrossRef]
53. Gray, D.H.; Fatt, I. The effect of stress on permeability of sandstone cores. *Soc. Pet. Eng. J.* **1963**, *3*, 95–100. [CrossRef]
54. Haghi, A.H.; Chalaturnyk, R.; Ghobadi, H. The state of stress in SW Iran and implications for hydraulic fracturing of a naturally fractured carbonate reservoir. *Int. J. Rock Mech. Min. Sci.* **2018**, *105*, 28–43. [CrossRef]
55. McLatchie, A.S.; Hemstock, R.A.; Young, J.W. The effective compressibility of reservoir rock and its effects on permeability. *J. Pet. Technol.* **1958**, *10*, 49–51. [CrossRef]
56. Zhu, W.; Wong, T.F. The transition from brittle faulting to cataclastic flow: Permeability evolution. *J. Geophys. Res. Solid Earth* **1997**, *102*, 3027–3041. [CrossRef]

energies

MDPI

Article

Pore-Scale Numerical Simulation of CO_2–Oil Two-Phase Flow: A Multiple-Parameter Analysis Based on Phase-Field Method

Rui Song [1,2], Yu Tang [1,*], Yao Wang [3,*], Ruiyang Xie [4] and Jianjun Liu [2]

[1] School of Geoscience and Technology, Southwest Petroleum University, Chengdu 610500, China
[2] State Key Laboratory of Geomechanics and Geotechnical Engineering, Institute of Rock and Soil Mechanics, Chinese Academy of Sciences, Wuhan 430071, China
[3] School of Civil Engineering and Architecture, Southwest University of Science and Technology, Mianyang 621010, China
[4] School of Civil Engineering and Geomatics, Southwest Petroleum University, Chengdu 610500, China
* Correspondence: 202022000604@stu.swpu.edu.cn (Y.T.); wangyao0927@swust.edu.cn (Y.W.)

Abstract: A deep understanding of the pore-scale fluid flow mechanism during the CO_2 flooding process is essential to enhanced oil recovery (EOR) and subsurface CO_2 sequestration. Two-phase flow simulations were performed to simulate the CO_2 flooding process based on the phase-field method in this study. Two-dimensional models with random positions and sizes of grains of circular shape were constructed to reproduce the topology of porous media with heterogeneous pore size distributions in the reservoir rock. A multiple-parameter analysis was performed to investigate the effects of capillary number, viscosity ratio, wettability, density, gravity, interfacial tension, and absolute permeability on the two-phase fluid flow characteristics. The results indicated that when the capillary number and viscosity ratio were large enough, i.e., $\log Ca = -3.62$ and $\log M = -1.00$, the fingering phenomenon was not obvious, which could be regarded as a stable displacement process. CO_2 saturation increased with the increase in the PV value of the injected CO_2. Once the injected CO_2 broke through at the outlet, the oil recovery efficiency approached stability. Two types of broken behaviors of the fluids were observed during the wettability alternation, i.e., snap-off and viscous breakup. Snap-off occurred when capillary forces dominated the fluid flow process, while viscous breakup occurred with a low viscosity ratio. With a low capillary number, the flooding process of the injected CO_2 was mainly controlled by the capillary force and gravity. With the decrease in the interfacial tension between the fluids and the increase in the permeability of the porous media, the recovery of the displaced phase could be enhanced effectively. In the mixed-wet model, with the increase in the percentage of the nonoil-wetted grains, the intersecting point of the relative permeability curve moved to the right and led to a higher oil recovery.

Keywords: CO_2 flooding; two-phase flow; phase-field method; wettability; capillary number

Citation: Song, R.; Tang, Y.; Wang, Y.; Xie, R.; Liu, J. Pore-Scale Numerical Simulation of CO_2–Oil Two-Phase Flow: A Multiple-Parameter Analysis Based on Phase-Field Method. *Energies* **2023**, *16*, 82. https://doi.org/10.3390/en16010082

Academic Editor: Rouhi Farajzadeh

Received: 2 November 2022
Revised: 11 December 2022
Accepted: 17 December 2022
Published: 21 December 2022

1. Introduction

Carbon dioxide (CO_2) capture, utilization, and storage (CCUS) technology is regarded as the most effective approach to deal with the greenhouse effect in recent years [1,2]. As one of the most effective and promising utilization methods, CO_2 flooding can not only achieve geological storage, but also greatly enhance the oil recovery of low-permeability reservoirs [3–5]. The aforementioned CO_2-EOR technology is a win-win approach which not only considers the economic benefits, but also the social benefits [6–8]. In 1972, the CO_2-EOR application was used for the first time in Texas, which utilized CO_2 to enhance oil recovery in a crude oil reservoir [9]. Since then, the CO_2-EOR technology has attracted more and more attention both in academic and industrial fields.

Varying based on the injected pressure and temperature conditions, the CO_2 flooding can be divided into three categories: CO_2-miscible flooding, CO_2-immiscible flooding, and CO_2-near-miscible flooding [10,11]. The difference among these three flooding forms lies in whether the injected pressure of CO_2 reaches the minimum miscible pressure. When the injected pressure is greater than the minimum miscible pressure, CO_2-miscible flooding can be achieved; in the absence of these pressure conditions, immiscible or near-miscible flooding is obtained instead. Miscible CO_2 flooding contributes to EOR, benefiting from two aspects. On the one hand, with the CO_2 injected, parts of the oil and water are dissolved, which increases the driving force and improves the flooding efficiency. On the other hand, the injected CO_2 can form a miscible oil zone with crude oil [12]. In the miscible oil zone, the viscosity and density of crude oil are reduced significantly, and the interfacial tension decreases as well, which effectively favors the improvement of the flow capacity of the crude oil [13].

In pursuit of the desirable double carbon policy and the great potential of CO_2-EOR technology, research on the mechanism of CO_2 flooding has attracted more and more attention in recent years. Desch et al. [14] conducted a CO_2-miscible flooding experiment at the core scale, and the results showed that parts of the crude oil and water were dissolved by CO_2 during the alternate water–gas flooding process, which resulted in the phenomenon of dissolved gas flooding and improved the oil–water flow ratio at the same time. During the miscible flooding process, the interfacial tension between the CO_2 and the oil was significantly reduced. Xiao et al. [15] conducted water flooding and CO_2-miscible flooding experiments using low-permeability cores, and the results showed that the recovery ratio of CO_2-miscible flooding was higher than water flooding. Feng et al. [16] obtained similar conclusions from the field experiments. Zhu et al. [17] studied the effect of the injection rate on CO_2-miscible flooding performance through a core-scale experiment. Ding et al. [18] studied the influence of core-scale fracture density and miscibility on CO_2 flooding recovery in fractured reservoirs. Gao et al. [19] conducted supercritical CO_2 ($scCO_2$) and non-supercritical CO_2 huff-puff simulations under the reservoir conditions of tight conglomerate formation (formation pressure 37 MPa, temperature 362.15 K). The results indicated that $scCO_2$ was helpful for improving the recovery of the crude oil of a tight conglomerate reservoir. Li et al. [20] conducted $scCO_2$ flooding experiments through core-scale experiments, and the results showed that increasing the displacement pressure or the interaction time between crude oil and CO_2 could effectively improve oil recovery. Li et al. [21] used three cores with different permeability to conduct CO_2 flooding experiments and investigated the effect of the pore structure and injection pressure on the recovery ratio of tight oil reservoirs. The results showed that both the total surface recovery efficiency and recovery efficiency of small pores increased with the increase in injection pressure.

Due to the complex structure and opacity of the reservoir rocks, the mechanism and influencing factors of CO_2 flooding contributing to the enhancement of the oil recovery ratio remain unclear. With the help of experimental high-resolution visualization technologies (e.g., micro-CT and NMR), researchers investigated the pore-scale mechanism of fluid interactions during CO_2 flooding. Kun et al. [22] used NMR technology to study the effect of different CO_2 injection methods on residual oil distribution and found that CO_2 injection after water flooding has a significant effect on improving the recovery efficiency of low-permeability reservoirs. Al-bayati et al. [23] conducted CO_2-miscible flooding experiments at the core scale and evaluated the influence of heterogeneity on CO_2-miscible flooding performance with the help of micro-CT scanning. The results showed that higher heterogeneity leads to lower recovery, and the CO_2 flooding effect was better in the miscible secondary recovery mode, which promoted the effective contact between CO_2 and oil. Pu et al. [24] used NMR technology to analyze the pore-scale CO_2 displacement mechanism of low-permeability reservoirs from different dimensions, and the results showed that the miscibility of CO_2 and crude oil formed a stable displacement front, in which case the crude oil could be effectively displaced, especially in large and medium pores. Wei et al. [25] carried out a comprehensive visualization study on the CO_2 dissolution and miscibility process by using a high-pressure temperature unit. The results showed that the CO_2 solubility would decrease with the increase in temperature and oil density.

During the mixing process, the components of the CO_2 phase and oil phase were quite close. Yang et al. [26] used micro-CT imaging technology to scan porous media with high water content and classified the patterns of residual oil in pores using shape factor and Eulerian number. It was found that the distribution of the remaining oil was constantly changing in the process of water flooding. Zhang et al. [27] studied the pore throat heterogeneity of tight sandstone using NMR technology, and the results showed that the complexity of pore structure and surface roughness hindered the migration of two-phase fluid and the swept area of single-phase fluid. Chung et al. [28], combined with micro-CT imaging technology, used a new method to quickly estimate absolute permeability from micro-CT images of rocks. Cao et al. [29] conducted a series of pore-scale simulations of gas reservoirs with increasing injection pressure using tight sandstone cores and studied the fluid phase distribution, gas mass characteristics, and gas reservoir change rules of gas reservoirs using micro-CT technology. The results showed that with the increase in gas injection pressure, the gas saturation was increased, the number and volume of gas reservoirs increased, the shape deviated from the spherical shape, and the connectivity improved. Wang et al. [30] used micro-CT imaging technology to scan and image four kinds of rocks and used these CT images to generate a grid structure model to conduct a two-phase flow numerical simulation, studying the immiscible oil displacement process in the oilfield development process. The results show that wettability has an important impact on recovery efficiency. The existing high-resolution visualization experiment system is expensive and time-consuming. Due to the strong heterogeneity of natural cores and the destructive nature of most fluid displacement experiments, it is difficult to carry out parallel experiments under the same pore structure and physical properties.

Therefore, the pore-scale numerical simulation of CO_2 flooding in porous media is very important as an important supplement to laboratory experiments. Zhang et al. [31] numerically simulated the process of liquid CO_2 flooding through two heterogeneous pore network models with different permeation zones. The study found that at a low injection rate, displacement changed from capillary fingering to viscous fingering with the increase in injection flow rate. Liu et al. [32] carried out the numerical simulation of liquid CO_2 flooding in the dual-permeability pore network model using the Lattice Boltzmann method (LBM). The results indicated that the preferential flow channel and flow behavior of liquid CO_2 depended on the number of capillaries. Amiri et al. [33] studied the immiscible water flooding process through a homogeneous model. The results show that the pore-scale displacement mechanisms that affect the displacement efficiency are different under water-wet and oil-wet conditions. Shi et al. [34] studied the factors affecting the flow behavior of non-Newtonian fluids in porous media using LBM. These factors include capillary number, viscosity, wettability, and gravity. Zhu et al. [35] used the phase-field method to numerically simulate the immiscible CO_2 oil displacement process through a homogeneous porous media model. The research found that after CO_2 broke through the outlet, the pressure on the CO_2 main channel decreased significantly, and the oil phase began to flow back into the pores previously occupied by CO_2. Basirat et al. [36] used the phase-field method to simulate the two-phase flow of CO_2 brine in the real pore structure through a two-dimensional core real pore model and studied the factors affecting the geological storage of CO_2 in the deep saline aquifer. The study showed that the saturation of the saturated phase and the normalized interface area increased with the decrease in the contact angle. Rokhforouz et al. [37] studied the effect of pore structure approximation on water flooding by using the phase-field method through the real core pore model and its simplified model. The results show that the change in small particle size can lead to different displacement profiles, especially under low capillary numbers and oil moisture conditions. Ma et al. [38] studied the mechanism of CO_2 flooding to enhance oil recovery through a heterogeneous porous media model and immiscible flooding and near-miscible flooding. The results show that, compared with immiscible flooding, near-miscible flooding increases the CO_2 sweep area to a certain extent, but the oil displacement efficiency is still low in the small hole throat.

In the process of CO_2 displacement of crude oil, there are often pore-scale displacement phenomena such as fingering, preferential flow channel, swept range, oil phase trap, and jamming; the existence of these phenomena is unfavorable for improving oil recovery [2,31,32], and the numerical simulation study provides a very convenient condition for observing the formation process of the pore-scale displacement phenomenon during CO_2 flooding. To study the two-phase flow phenomenon during CO_2 displacement of crude oil, a currently available and better method is the pore-scale visual numerical simulation [33–38]. At present, there are mainly two kinds of porous media models used in pore-scale visualization of numerical simulation: one is an artificially created pore network model [31–35,38], and another one is 2D or 3D images of the rock core made by using various scanning techniques to scan the real rock core [30,36,37,39]. The method for obtaining these images is not easy, as it is limited by experimental conditions. Therefore, based on the artificial pore-scale models, the numerical solution of the N-S equation to obtain the fluid flow state in porous media provides a new research method for the simulation of CO_2 flooding [40–45]. However, the mechanism of CO_2 displacement of crude oil in the pore-scale models with heterogeneous and mixed wettability conditions has rarely been investigated. Zhang [31], Liu [32], and Basirat et al. [36] carried out numerical simulation research on the process of CO_2 displacement of water. Therefore, further research on the process of CO_2 displacing oil is needed. Amiri [33] and Shi et al. [34] studied the effects of capillary number, viscosity, wettability, and gravity on fluid flow but did not consider the effects of interfacial tension, absolute permeability, and mixed wettability on fluid flow in heterogeneous porous media. Zhu et al. [35] conducted a numerical simulation study on the process of CO_2 displacing oil using the phase-field method in a homogeneous porous medium model, which cannot truly reflect the heterogeneity of natural rocks. Rokhforouz et al. [37] studied the influence of pore structure on water flooding by using the phase-field method in the simplified model of natural rock. Ma et al. [38] conducted a simulation of CO_2 flooding in the heterogenous pore model and analyzed oil recovery using immiscible flooding, near-miscible flooding, and miscible flooding, without considering the impact of mixed wettability. However, most natural rocks are mixed-wetted, which was rarely studied in these studies. This paper presents a comprehensive study on the CO_2 flooding process in the heterogeneous and mixed-wetted pore models based on phase-field method.

In this paper, 2D grain (of circular shape) models with random position and size distribution were constructed to reproduce the topology and morphology characteristics of the pore structure with heterogeneous wettability in the reservoir rocks. Pore-scale two-phase flow simulations were carried out to simulate the CO_2 flooding process considering multiple influencing factors, and the phase-field method was used to capture the phase interface during the two-phase flow simulations. The effects of capillary number, viscosity ratio, wettability, density, gravity, interfacial tension, absolute permeability, and other factors on the performance of CO_2 flooding were investigated comprehensively, and the two-phase flow mechanism was studied and analyzed.

2. Theory and Mathematical Model

2.1. Two-Phase Flow Model

In porous media, the fluid flow process can be described by the Navier–Stokes (N-S) equation. The momentum equation and mass conservation equation are listed as follows [40,46–48]:

Momentum equation:

$$\rho\frac{\partial\mathbf{u}}{\partial t}+\rho(\mathbf{u}\cdot\nabla)\mathbf{u}=\nabla\cdot\left[-p\mathbf{I}+\mu\left(\nabla\mathbf{u}+(\nabla\mathbf{u})^T\right)\right]+\boldsymbol{F_{st}} \tag{1}$$

Mass conservation equation:

$$\nabla\cdot\mathbf{u}=0 \tag{2}$$

where ρ represents the density of the fluid (kg/m^3), $\mathbf{u}$ is the velocity (m/s), $\mathbf{I}$ is the unit vector, t is the time (s), μ is the viscosity of the fluid (Pa·s), $\boldsymbol{F_{st}}$ is the term representing interfacial tension force (N/m).

For an incompressible fluid, the equations of motion and continuity of CO$_2$/oil two-phase fluid flow in porous media are Equations (1) and (2), respectively.

2.2. Phase-Field Model

The phase-field method is used to capture the interface of two different fluids. Describing the generation and dynamic changes of physical properties such as density and viscosity at the phase interface between two fluids is the most critical point in this method. The auxiliary functions are generally used to describe the interface of two fluids on a fixed grid. This method considers not only the difference in density and viscosity between fluids, but also the influence of interfacial tension and gravity. The diffusion interface separating two phases is realized by the convection–diffusion equation (Cahn–Hilliard equation) [40,43,49,50]. The phase-field method is suitable to simulate the interface broken, coalescence, and contact line dynamics.

(1) Representation of a two-phase flow interface

On the interface of two-phase fluid, the Cahn–Hilliard equation is generally used to describe the generation and dynamic change of the interface. The Cahn–Hilliard equation is used to calculate the convection and diffusion at the phase interface. In the process of solving, it is decomposed into two equations to participate in the calculation:

$$\frac{\partial \varphi}{\partial t} + \mathbf{u} \cdot \nabla \varphi = \nabla \cdot \frac{\gamma \lambda}{\varepsilon^2} \nabla \psi \tag{3}$$

$$\psi = -\nabla \cdot \varepsilon^2 \nabla \varphi + \left(\varphi^2 - 1\right) \varphi \tag{4}$$

where γ is the mobility, which denotes the moving velocity of the interface under a unit driving force (m^3·s/kg), λ is the magnitude of the mixing energy (N), ε is the interface thickness (m), and φ is the phase-field variable, used to distinguish phases and the interface.

(2) Interfacial tension

Convection and diffusion in the phase interface region of two-phase fluid will cause the change of interface free energy. Therefore, with the help of the diffusion interface representation, the interfacial tension can be calculated by the following expression:

$$\boldsymbol{F_{st}} = G \nabla \varphi \tag{5}$$

where G is the chemical potential (J/m^3). The chemical potential is calculated as follows:

$$G = \lambda \left(-\nabla^2 \varphi + \frac{\varphi\left(\varphi^2 - 1\right)}{\varepsilon^2} \right) = \frac{\lambda}{\varepsilon^2} \psi \tag{6}$$

In the phase-field method, the interfacial tension is calculated by the phase-field variable gradient and the phase-field auxiliary variable (ψ), and the interfacial tension is continuously distributed on the phase interface. The hybrid energy density parameter (λ) and the interface thickness control parameter (ε) are related to the interfacial tension (σ) coefficient, and they are connected by Equation (7). When the phase interface is in equilibrium, the hybrid free energy of the phase interface region is minimum, and the interfacial tension is obtained by integrating the energy on the interface curve per unit length [41,49,51].

$$\sigma = \frac{2\sqrt{2}}{3} \frac{\lambda}{\varepsilon} \tag{7}$$

In general, the interface thickness control parameter (ε = $h_c/2$) h_c represents the size of the feature grid. During the calculation, mobility parameters (γ) are obtained by the interface thickness (ε); $\gamma = \varepsilon^2$ is generally considered the most appropriate value. The mobility parameter determines the diffusion coefficient of the phase field to some extent. It must consider two aspects: keeping the interface thickness constant and not excessively suppressing the convection term [52].

(3) Wetting angle

The fluid–rock interface is defined as the non-slip boundary, and there is a certain wetting angle [42,53,54].

$$u = u_w \tag{8}$$

$$n \cdot \frac{\gamma\lambda}{\varepsilon^2}\nabla\psi = 0 \tag{9}$$

$$n \cdot \varepsilon^2\nabla\varphi = -\varepsilon^2\cos(\theta)|\nabla\varphi| \tag{10}$$

where u_w represents the slip velocity of the particle surface (m/s); Equation (9) indicates that the normal flow rate of the phase-field variable is 0, and n indicates the unit vector perpendicular to the particle wall; Equation (10) represents the wetting angle of the particle surface, which can be given by the phase-field variable.

(4) Density and viscosity

During the CO_2 flooding process, fluid 1 and fluid 2 are defined as CO_2 and oil, respectively. At the same time, under the condition of multi-physical field coupling, the density and viscosity of a two-phase fluid are defined as functions related to the phase-field variables, expressed, respectively, as:

$$\rho = \rho_c\frac{1+\varphi}{2} + \rho_o\frac{1-\varphi}{2} \tag{11}$$

$$\mu = \mu_c\frac{1+\varphi}{2} + \mu_o\frac{1-\varphi}{2} \tag{12}$$

where the subscripts c and o denote the CO_2 phase and the oil phase, respectively.

Equations (1)–(4) constitute the governing equations in the numerical simulation of micro-scale CO_2 flooding.

3. Results and Discussion

At first, the model is verified by a single-phase flow simulation of CO_2. At the pore scale, the influencing factors of CO_2 flooding are discussed through a heterogeneous porous medium model.

3.1. Validation of the Numerical Model

A uniform porous medium model was reconstructed to verify the reliability of the numerical model proposed in this study, and the related parameters used in the validation model are shown in Table 1.

Table 1. Basic parameters of the pore-scale model.

Parameter	Numerical Value
Length of fluids domain (μm)	10,030.65
Height of fluids domain (μm)	4876.80
Particle diameter (μm)	508.00
P (MPa)	5.00
T(K)	293.15
$\rho CO_2 (kg/m^3)$	140.65
μCO_2 (Pa·s)	1.648×10^{-5}

The schematic diagram of the verification model and its boundary conditions are shown in Figure 1; the white circle represents the simplified solid particles inside the rock.

The left side of the model is the velocity inlet, and CO_2 is injected from the left side, with an injection velocity of 0.01 m/s; the right side is the pressure outlet, the outlet pressure is 0 Pa, and the grain surface and the upper and lower boundaries of the model are defined as non-slip boundaries.

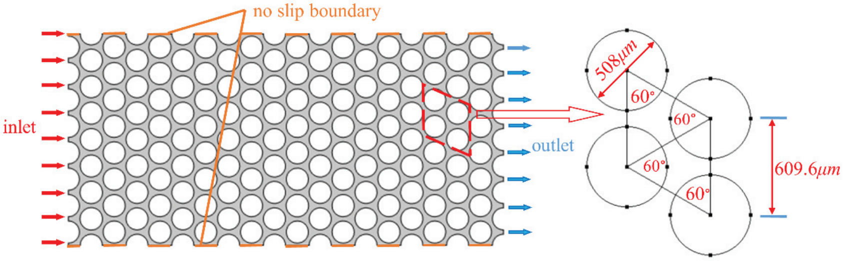

Figure 1. Schematic diagram of the pore-scale model and its boundary conditions.

The obtained velocity and pressure fields are shown in Figure 2, in which the white indicates the solid particles. Since the single-phase flow simulation ignores the influence of gravity, the velocity and pressure fields are symmetrically distributed, which verifies the numerical models.

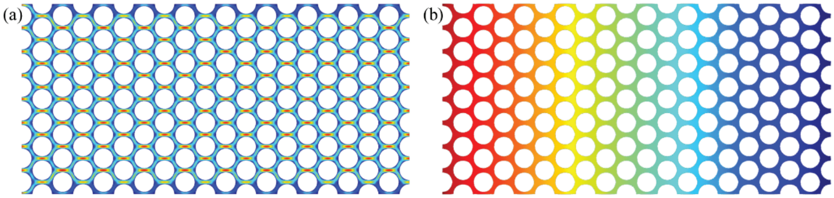

Figure 2. Simulation results of single-phase flow. (**a**) Velocity distribution; (**b**) Pressure distribution.

3.2. Geometry Setup of the 2D Heterogeneous Model and Input Parameters of the Two-Phase Flow

To study the microscopic displacement mechanism of CO_2 flooding, a two-dimensional heterogeneous porous media model was constructed, as shown in Figure 3a. This model is in a rectangular shape 10,030.65 μm in length and 4876.80 μm in width. The circles of various sizes are arranged randomly in the 2D heterogeneous model. The maximum and minimum diameters of the circles are 609.60 μm and 152.40 μm, respectively. The grey areas indicate pores, and the porosity of the two-dimensional model is 36.36%.

The schematic diagram of the grid model is shown in Figure 3b. The number of elements included in the grid in the two-dimensional model is 83,771, the maximum and minimum grid cell sizes are 63.50 μm and 0.73 μm, respectively. The maximum unit growth rate is 1.08 and the curvature factor is 0.25.

The boundary conditions of the model are set as: (1) The inlet on the left side of the model is the velocity inlet, and CO_2 is injected from the left side; (2) The outlet on the right side of the model is a pressure outlet with a size level of 0 Pa; (3) The surface of circular solid particles is a neutral wetting boundary, contact angle = 90° (the solid particle surface is neither oil-wetted state nor nonoil-wetted state); (4) The upper and lower boundaries of the model and the circular particle surface are non-slip boundaries; (5) CO_2 and oil are considered incompressible Newtonian fluids due to the small scale of the model and the small variation in fluid pressure; (6) Without taking into account the effects of gravity and temperature. The initial state of the model is saturated with oil, and the simulation is terminated after injecting 2 PV of CO_2 into the inlet. The basic physical parameters of oil and CO_2 are shown in Table 2. In the process of simulation calculation, the size of the time step is controlled by a numerical solver, the initial time step is set to 10^{-9} s, the discretization of the equations is in backward differential format, and the solver is PARDISO.

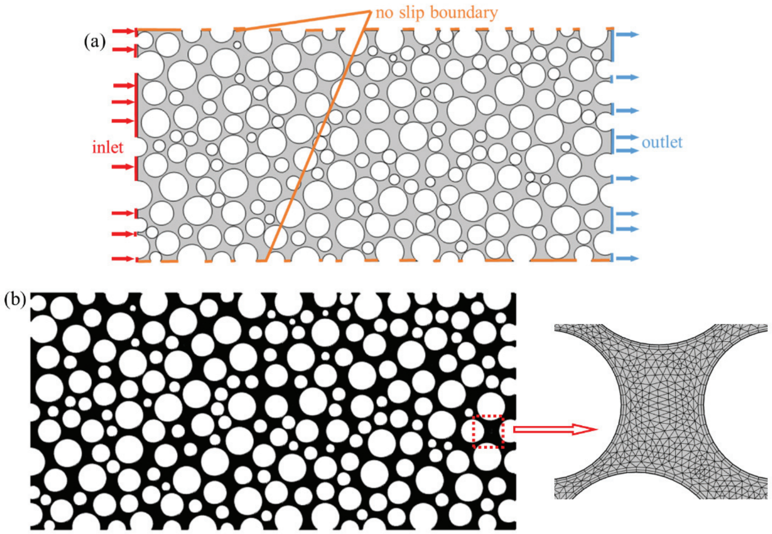

Figure 3. Schematic diagram of the 2D geometric model and its mesh model. (**a**) Schematic diagram of the geometric model and initial and boundary conditions for numerical simulations; (**b**) Schematic diagram of mesh model.

Table 2. Parameters of oil and CO_2.

Parameter	Numerical Value
T (K)	293.15
P (MPa)	5.00
ρCO_2 (kg/m^3)	140.65
ρoil (kg/m^3)	900.00
σ (N/m)	0.025
Contact angles (θ)	90°

3.3. Multiple-Parameter Analysis

3.3.1. Effect of Capillary Number and Viscosity Ratio on Fluid Flow

When CO_2 is used to displace oil, CO_2 will displace the oil in the pores in a gaseous or liquid state under the influence of temperature and pressure. In the process of CO_2 flooding, the different injection velocities will lead to different dominant forces of displacement, which may be a viscous force or capillary force. It is precisely because of the different dominant forces that the state and distribution of fluid flow in pores are different. Capillary number and viscosity ratio are the two most important factors, and their variations lead to changes in the fingering state during displacement. Next, the effect of capillary number and viscosity ratio on the CO_2 flooding effect is studied by numerical simulation. The capillary number is a dimensionless value which represents the ratio of the viscous force to the capillary force of the fluid; the mathematical expression is as follows [55,56]:

$$\mathrm{Ca} = \frac{u_{inj}\mu_c}{\sigma} \tag{13}$$

where u_{inj} is the average injection velocity at the inlet (m/s), μ_c is the viscosity of CO_2 (Pa·s), and σ is the interfacial tension coefficient (N/m).

The viscosity ratio is also dimensionless and represents the ratio of the viscosity of CO_2 to the viscosity of the oil. The mathematical expression is [55,56]:

$$\mathrm{M} = \frac{\mu_c}{\mu_o} \tag{14}$$

where the subscripts *c* and *o* denote the CO_2 phase and the oil phase, respectively.

The physical parameters of CO_2 are kept constant, while the physical parameters of the oil are changed so that the number of capillaries and the viscosity ratio change. According to different capillary numbers and viscosity ratios, six groups of control models are set up to study the effect of the change in capillary number and viscosity ratio on CO_2 flooding. The specific parameter settings of each simulation group are shown in Table 3.

Table 3. Capillary number and viscosity ratio used in the simulation.

Model	Log M	Log Ca	Contact Angle (θ)
a	−3.00	−5.62	90°
b	−3.00	−4.62	90°
c	−3.00	−3.62	90°
d	−1.00	−5.62	90°
e	−1.00	−4.62	90°
f	−1.00	−3.62	90°

Under the conditions of different capillary numbers and viscosity ratios, the distribution of CO_2 saturation corresponding to CO_2 breaking through the outlet is shown in Figure 4; the red and blue areas represent CO_2 and oil, respectively. Figure 4 shows that the injected CO_2 forms a continuous flow channel throughout the porous medium model regardless of the conditions, due to the injected CO_2 overcoming the inlet pressure. In the CO_2 flooding process, the fingering phenomenon can be observed in most models. Only in the case of a large capillary number (log Ca = −3.62) and large viscosity ratio (log M = −1.00) (Figure 4f) is there no obvious fingering phenomenon in the displacement process, so it can be regarded as a stable displacement process.

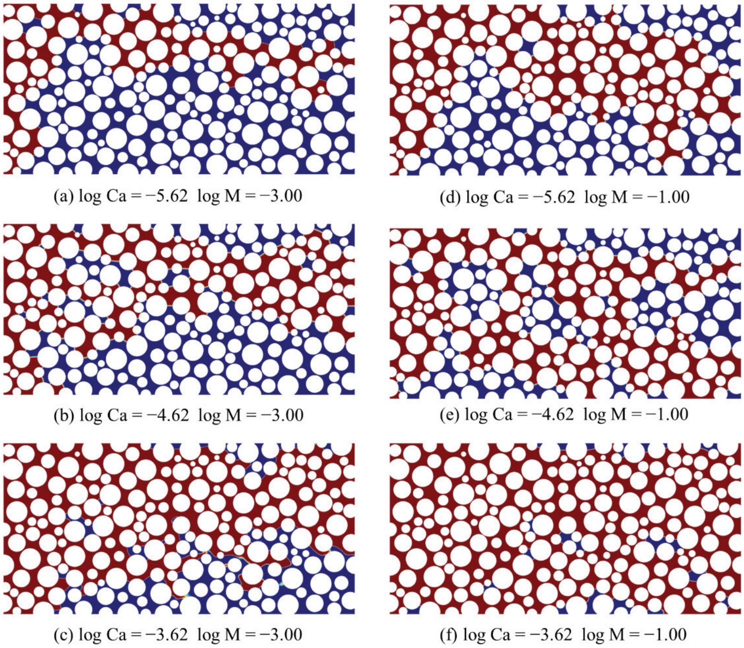
(a) log Ca = −5.62 log M = −3.00

(d) log Ca = −5.62 log M = −1.00

(b) log Ca = −4.62 log M = −3.00

(e) log Ca = −4.62 log M = −1.00

(c) log Ca = −3.62 log M = −3.00

(f) log Ca = −3.62 log M = −1.00

Figure 4. CO_2 saturation distribution during CO_2 breakthrough for different capillary number and viscosity ratio (red and blue regions represent CO_2 and oil, respectively).

At a low capillary number (log Ca = −5.62) and a low viscosity ratio (log M = −3.00), the CO_2 saturation distribution is shown in Figure 4a. It shows a thin and long CO_2 main channel, which shows an obvious fingering phenomenon. This phenomenon is a capillary fingering phenomenon, which is an unstable displacement situation. In this case, the influence of viscous force can be ignored due to the small injection speed, and the dominant force of displacement is the capillary force.

At a low capillary number (log Ca = −5.62) and a high viscosity ratio (log M = −1.00), the CO_2 saturation distribution is shown in Figure 4d. It shows a larger CO_2 main channel compared with the CO_2 saturation distribution in Figure 4a, and the distribution of CO_2 is also increased significantly when it breaks through the outlet, which is also recognized as a capillary fingering phenomenon and an unstable displacement. By comparing Figure 4a with Figure 4d, it can be seen that under the low capillary number condition, a higher viscosity ratio contributes to displacement and oil extraction.

In this heterogeneous two-dimensional porous medium model, the CO_2 saturation (*Sc*) in the pores can reflect the oil recovery ratio. In the simulation, CO_2 of two pore volume (PV) is injected, and the relationship between the final CO_2 saturation (*Sc*) and the capillary number and viscosity ratio is shown in Figure 5. It can be seen from Figure 5a that CO_2 saturation increases with the increase in capillary number when the viscosity ratio is the same. It can be seen from Figure 5b that CO_2 saturation increases with the increase in viscosity ratio when the capillary number is constant.

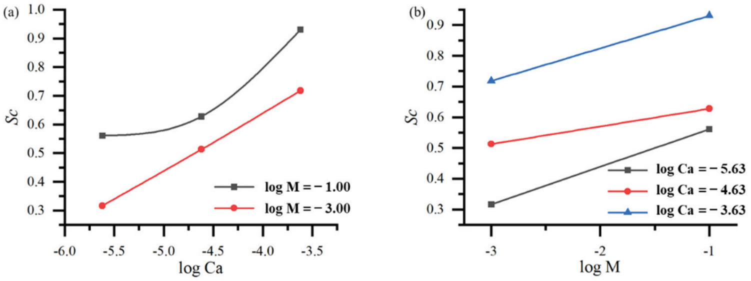

Figure 5. Relationship between CO_2 saturation (S_C) and log Ca and log M. (**a**) CO_2 saturation (S_C) as a function of log Ca; (**b**) CO_2 saturation (S_C) as a function of log M.

A total of 2 PV of CO_2 is injected into the model; the relationship between the CO_2 saturation and the PV number of the injected CO_2 is shown in Figure 6. It can be seen that the CO_2 saturation increased sharply during the period when 1 PV of CO_2 was injected into the pore. However, with the injection volume's continuous increase, the increase rate of CO_2 saturation decreased rapidly. At the early stages of CO_2 flooding, the injected CO_2 broke through along the highly permeable zone with lower resistance. Once the CO_2 breaks through, it is difficult to sweep other regions, which results in a lower increase in recovery.

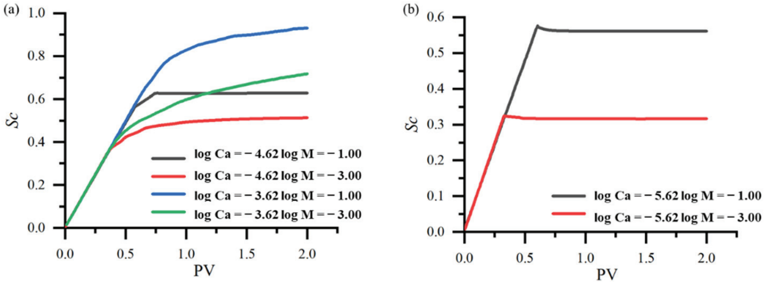

Figure 6. CO_2 saturation (S_C) vs. PV number for different Ca and M (**a**) CO_2 saturation (S_C) as a function of PV (log Ca = −3.62 and −4.62); (**b**) CO_2 saturation (S_C) as a function of PV (log Ca = −5.62).

It can be seen from Figure 6b that at a low capillary number (log Ca = −5.62) and a high viscosity ratio (log M = −1.00), once the CO_2 breaks through the outlet, there is a slight decrease in the CO_2 saturation, and then it reaches a stable value.

Figure 7 shows the typical change in the CO_2 main channel during CO_2 flooding. Around the yellow grain, the interface of the CO_2 main channel shrinks after CO_2 breaks through the outlet (0.77 s). Figure 8 shows the pressure changes at point P near the outlet, which steadily increases until the frontier of CO_2 flooding reaches point P. When the CO_2 passes through point P (t = 0.66 s), the pressure noticeably increases, and the maximum pressure appears at 0.67 s. We denote the pressure in the CO_2 plume as p_c, the pressure in the oil phase as p_o, and the capillary pressure as p. When CO_2 displaces crude oil in pores (0.61−0.67 s), the pressure in the CO_2 plume is greater than the sum of the pressure in the oil phase and the capillary pressure ($p_c > p_o + p$). After the CO_2 flooding front passes point P, the pressure (p_c) of the main channel drops rapidly, as shown in Figure 8. At this time, the pressure in the CO_2 plume is significantly less than the sum of the pressure in the oil phase and the capillary pressure ($p_c < p_o + p$). After the CO_2 plume breaks through the outlet (0.77 s), the pressure at point P decreases to a minimum and then remains almost constant, and oil begins to flow back into the pores previously occupied by CO_2. The oil reflow process leads to the contraction of the CO_2 main channel, as shown in Figure 7. When the pressure reaches equilibrium ($p_c = p_o + p$), the flow state becomes stable, as shown in Figure 7d. It can be seen that the CO_2 saturation curve decreases in the opposite direction during the CO_2 injection, which is caused by the oil flows back into the previously occupied pores, and the oil reflux process is caused by the outlet effect; this phenomenon also appeared in the study of Zhu et al. [35].

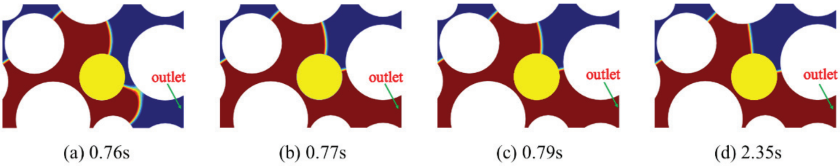

(a) 0.76s (b) 0.77s (c) 0.79s (d) 2.35s

Figure 7. Variations of the CO_2 main channel at different times (log Ca = −5.62, log M = −3.00; red and blue regions represent CO_2 and oil, respectively).

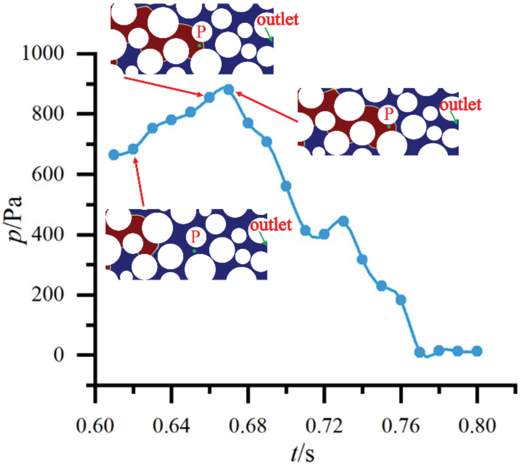

Figure 8. Pressure vs. time at point P near the outlet.

The breakups of non-wetting fluids are generally caused by the mechanisms of snap-off and viscous breakup. The snap-off occurs when the capillary force dominates the fluid flow behavior, which is an interface instability phenomenon. According to the previous description, there is no breakup of the CO_2 plume to be observed (in Figure 4a,d, log Ca = −5.62) when the capillary force dominates the flow behavior. This indicates that although the dominant force of displacement is the capillary force, the capillary force is not large enough, which is consistent with the study of Zhu et al. [35]. When the capillary force is relatively weak (log Ca= −4.62), there is no snap-off. Therefore, the fracture of the CO_2 plume in Figure 9 belongs to viscous breakup. At the same time, it is shown that the effect of low-viscosity CO_2 to displace high-viscosity oil is not satisfactory in the case of too small a viscosity ratio, and the low-viscosity CO_2 cannot sweep the high-viscosity oil. Viscous breakup indicates that the viscous force plays an important role in the CO_2 displacement of oil, which is detrimental to oil recovery.

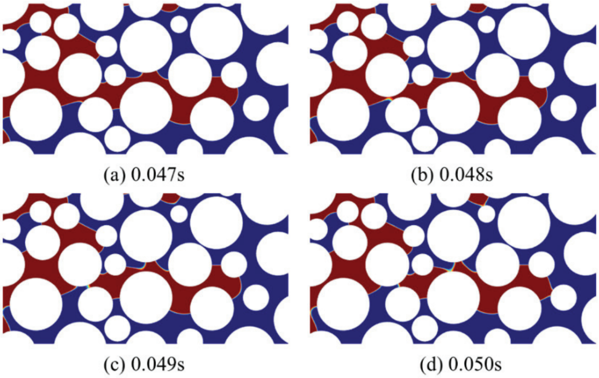
(a) 0.047s
(b) 0.048s
(c) 0.049s
(d) 0.050s

Figure 9. Fracture of the CO_2 plume during the displacement process (log Ca = −4.62, log M = −3.00; red and blue regions represent CO_2 and oil, respectively).

3.3.2. Effect of Wettability on Fluid Distribution

The wettability of a rock wall is one of the important factors affecting the fluid flow in pores, the residual oil saturation, and the capillary force. In the simulation, the contact angle is defined for the oil phase. Thus, the rock surface is oil-wetted if $\theta < \pi/2$ and nonoil-wetted if $\theta > \pi/2$.Under the conditions of log Ca = −4.25 and log M = −3.00, the effect of wall wettability on CO_2 flooding is studied. When the medium is oil-wetted ($\theta < \pi/2$), CO_2 injection is a drainage process; otherwise, it is an imbibition process when the medium is nonoil-wetted ($\theta > \pi/2$).

The pore-scale displacement mechanisms in the strong nonoil- and oil-wetted models were investigated in our previous study [57]. Therefore, the contact angle parameters adopted in this section are shown in Table 4, corresponding to strong oil-wetted, relatively strong oil-wetted, middle wettability, weak nonoil-wetted, and strong nonoil-wetted, respectively.

Table 4. Simulation parameters of different contact angles.

Model	Numerical Value
a	60°
b	75°
c	90°
d	105°
e	120°

When the contact angles are 60°, 75°, 90°, 105°, and 120°, the distribution of CO_2 saturation after stable displacement is shown in Figure 10. It can be seen that with the increase in oil phase contact angle, the wettability of the circular particle surfaces gradually becomes strong nonoil-wetted, and the distribution range of CO_2 in porous media increases significantly. When the surfaces of circular particles in the porous medium are strong oil-wetted (Figure 10a, contact angle = 60°) in the process of CO_2 flooding, the CO_2 plume will bypass a large area of oil saturation, so there is significantly more residual oil in the pores, and the recovery efficiency is obviously low. When the surfaces of circular particles are strongly nonoil-wetted (Figure 10e, contact angle = 120°) in the process of CO_2 flooding, the CO_2 plume can occupy more oil-saturated areas, and the recovery efficiency is improved compared with Figure 10a.

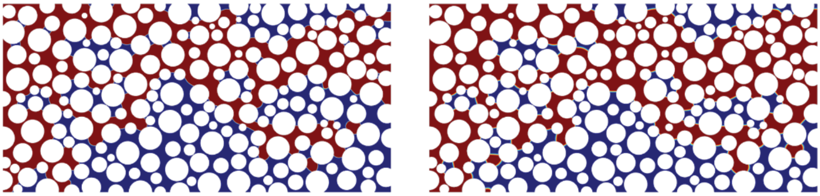

(a) contact angle=60°

(b) contact angle=75°

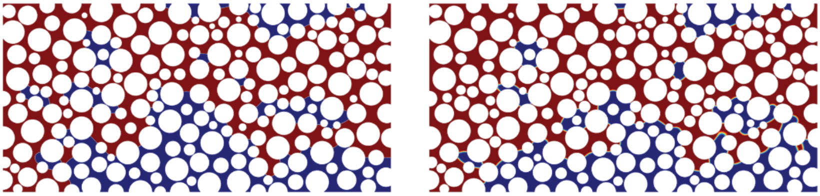

(c) contact angle=90°

(d) contact angle=105°

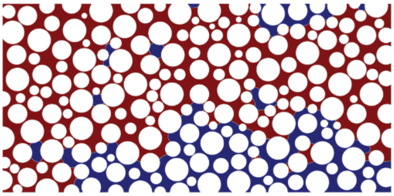

(e) contact angle=120°

Figure 10. CO_2 saturation distribution after CO_2 flooding for different contact angles (Red and blue regions represent CO_2 and oil, respectively).

According to the equation $P_c = 2\sigma \cdot \cos\theta / r$, when $\theta < \pi/2$, the wall is in an oil-wetted state, and the capillary force increases with the decrease in the contact angle; CO_2 is a non-wetting phase, and the capillary force increases with the same displacement force, which leads to the decrease in displacement force and a lower recovery efficiency.

The relationship between contact angle, PV number of CO_2 injection, and CO_2 saturation is shown in Figure 11. As can be seen from Figure 11a, when the wettability of the surface of circular particles in the porous medium changes from strong oil-wetted (contact angle = 60°) to strong nonoil-wetted (contact angle = 120°), the CO_2 saturation in the porous medium increases significantly; the CO_2 saturation increases from about 0.56 for strong oil-wetted (contact angle = 60°) to about 0.70 for strong nonoil-wetted (contact angle = 120°), an increase of nearly 25%. It should be noted that with the increase in the wetting degree of the circular oil particles in porous media, the CO_2 breakthrough will occur earlier. For example, when the wetting angle is 60° and 120°, the CO_2 breakthrough time is 0.357 PV and 0.377 PV, respectively. As can be seen in Figure 11b, the CO_2 saturation generally increases with the increase in the number of PV injected by CO_2, regardless of the wettability conditions of the medium. It can also be seen from Figure 11b that CO_2 saturation is at a maximum when the wettability of the medium is strong nonoil-wetted (contact angle = 120°).

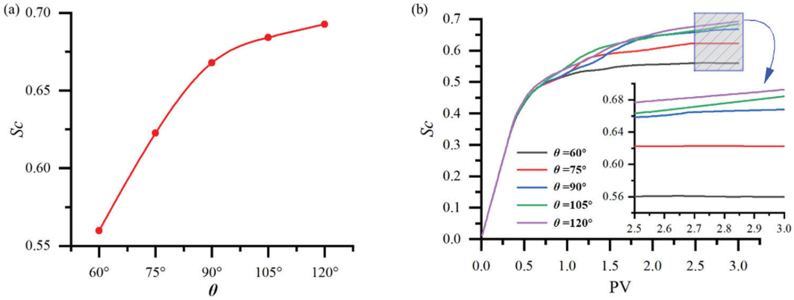

Figure 11. CO_2 saturation (S_C) vs. contact angle (**a**) and PV number of CO_2 injection (**b**).

Figures 12 and 13 show four amplified instantaneous fluid profiles during CO_2 flooding in strong oil-wetted (contact angle = 60°) and strong nonoil-wetted (contact angle = 120°) media, respectively. Under the condition of strong oil-wetted (contact angle = 60°), the remaining oil in the pores mainly exists in three forms: cluster-like heterogeneous residual oil occupying multiple pore bodies, pore throat residual oil, and blind-end residual oil. The thinning of the CO_2 plume and the trapping of the CO_2 plume are found in strong oil-wetted media. As shown in Figure 12, at contact angle = 60°, the CO_2 plume on the right side of the green-marked circular particle narrows in the pores due to the growth of the oil film around the particle (Figure 12a), the CO_2 plume is divided into several parts (Figure 12b,c), and the CO_2 plume splits to form two CO_2 gas masses trapped in the pore body (Figure 12d). This phenomenon is also observed below the yellow-marked particles. In an oil-wetted medium, the thinning and fracturing of the CO_2 plume and the trapping of the CO_2 plume reduce the oil displacement efficiency.

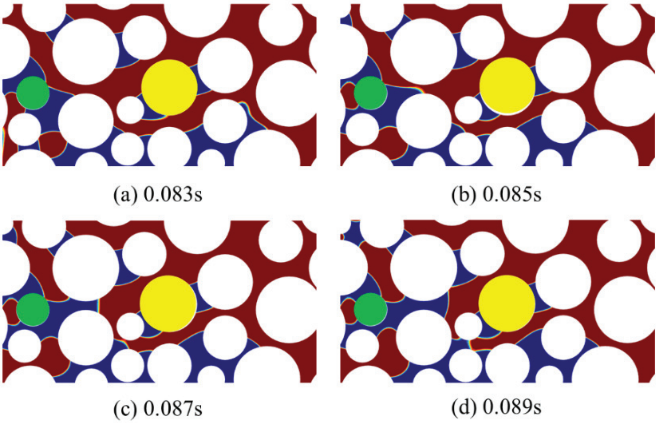
(a) 0.083s
(b) 0.085s
(c) 0.087s
(d) 0.089s

Figure 12. Under strong oil-wetted conditions, snapshots of fluid distributions in an enlarged section of the medium at four instants (contact angle = 60°, log Ca = −4.25, log M = −3.00). Red and blue regions represent CO_2 and oil, respectively.

Three mechanisms of oil film thinning and fracture, including CO_2 oil contact line movement and oil droplet formation and detachment, are observed under strong nonoil-wetted conditions. It can be seen from Figure 13a,b that when CO_2 approaches the green-labeled particles, the oil film on the surface of the labeled particles gradually thins until it breaks. After forming the CO_2–oil particle contact line, the oil droplets move on the particle surface (Figure 13c,d). The wetting phase adsorbs into the porous medium and invades the pore network. Thus, the oil displacement efficiency under strong nonoil-wetted conditions is significantly higher than that under strong oil-wetted conditions.

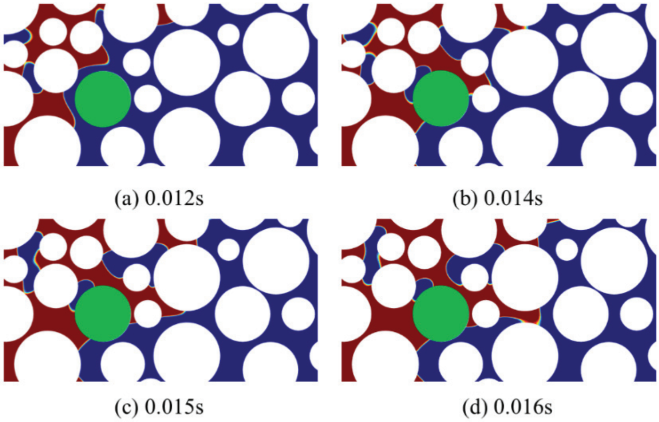
(a) 0.012s (b) 0.014s (c) 0.015s (d) 0.016s

Figure 13. Under strong nonoil-wetted conditions, snapshots of fluid distributions in an enlarged section of the medium at four instants (contact angle = 120°, log Ca = −4.25, log M = −3.00). Red and blue regions represent CO_2 and oil, respectively.

3.3.3. Effect of Density Ratio on Fluid Flow

Due to the influence of formation temperature and pressure, CO_2 may be in a gaseous, liquid, or supercritical state, and the density of CO_2 will change greatly. This section studies the effect of density ratio on CO_2 flooding by numerical simulation. The density ratio, which is defined as the density of CO_2 compared with the density of the oil phase, is dimensionless. The expression of the density ratio is as follows:

$$\beta = \frac{\rho_c}{\rho_o} \tag{15}$$

where the subscripts c and o denote the CO_2 phase and the oil phase, respectively.

From the expression of the density ratio, it can be seen that the density ratio is determined by the density of CO_2 and the density of oil. Since the density of oil is less affected by temperature and pressure, the change in density ratio is mainly caused by the CO_2 density. This section is still based on the previous model, in order to study the effect of density ratio on CO_2 flooding. In the case of log M = −3.00, the density ratio is set to 0.156 and 0.778, respectively. Based on the above model, a series of numerical simulation studies were carried out by changing the density of CO_2 and maintaining the same density of the oil phase.

After CO_2 flooding is stable, the relationship between CO_2 saturation and density ratio is shown in Figure 14. It can be seen from Figure 14 that the CO_2 saturation obtained under the condition of a high-density ratio is greater than that of a low-density ratio with the same capillary number; this shows that under the same viscosity ratio and capillary number, CO_2 flooding with high density can achieve better oil recovery efficiency. With the increase in the capillary number, the oil recovery increases significantly. According to Equation (13) ($\mathrm{Ca} = u \cdot \mu / \sigma$), Ca refers to the ratio of the viscous force to the capillary force of the fluids. Thus, a higher injection rate and viscosity of the CO_2 will contribute to EOR.

3.3.4. Effect of Gravity on Fluid Flow

Gravity is an important factor affecting multiphase flow in porous media. The effect of gravity on CO_2 flooding is studied under the condition of low capillary number and the same viscosity ratio in this section. The boundary conditions of the model are set as: (1) The inlet on the left side of the model is the speed inlet; (2) The outlet on the right side of the model is a pressure outlet with a size of 0 Pa; (3) The surfaces of circular solid particles are oil-wetted with a contact angle of 60°; (4) The upper and lower boundaries of the model and the circular particle surfaces are no-slip boundaries; (5) The initial state of the model is saturated with oil at a constant temperature.

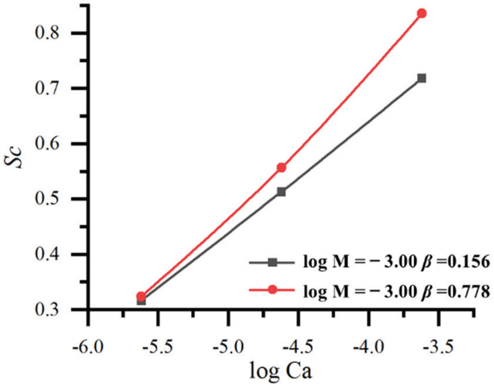

Figure 14. CO_2 saturation (*Sc*) vs. log Ca for same log M.

Figure 15 shows the effect of gravity on the final CO_2 saturation. When the capillary number is log Ca = −4.25, the CO_2 saturation of the model considering the gravity factor is significantly higher than that without considering the gravity factor; this shows that gravity improves the sweep range of CO_2. When the capillary number is log Ca = −4.10, the CO_2 saturation of the model considering the gravity factor is also higher than that without considering the gravity factor. In general, under the condition of low capillary number, the flow behavior of the injected CO_2 is mainly controlled by capillary force and gravity; when the viscosity ratios are the same, the gravity increases the final saturation in pores of CO_2, which indicates that gravity has a positive effect on oil displacement efficiency. Since gravity is set along the Y direction of the model, CO_2 will migrate upward by buoyancy in the Y direction of the model, which increases the sweeping efficiency as well as the oil recovery efficiency.

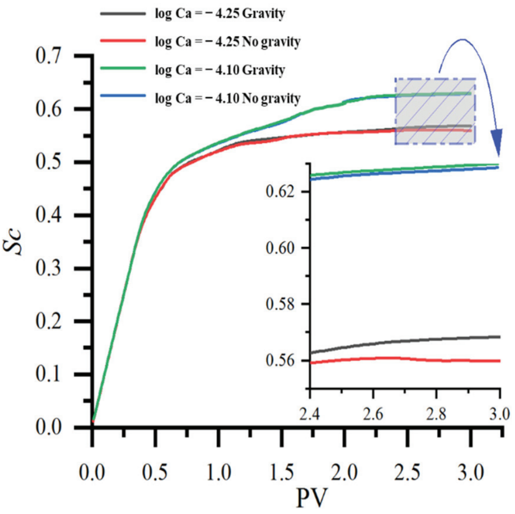

Figure 15. Influence of gravity on final CO_2 saturation (*Sc*) after CO_2 flooding.

3.3.5. Effect of Interfacial Tension on Fluid Flow

Reducing the interfacial tension between oil and CO_2 by adding surfactants is another way to improve the oil recovery ratio. With log M = −3.00, by reducing the interfacial tension between oil and CO_2 from 0.025 N/m to 0.01 N/m with the same injection rate, the CO_2 saturation profile after stabilization of CO_2 flooding is observed. As can be seen from Figure 16, the CO_2 distribution range is significantly larger at low interfacial tension. The capillary force is reduced at low interfacial tension when the same volume of CO_2 is injected. Figure 17 shows the relationship between the PV number of CO_2 injection and CO_2 saturation under different interfacial tension; as can be seen from the figure, the CO_2 saturation is 63.20% when the interfacial tension is 0.01 N/m, while the CO_2 saturation is only 51.80% when the interfacial tension is 0.025 N/m. The final CO_2 saturation also shows that low interfacial tension is more conducive to oil recovery. In practice, compared to water flooding, the injection of CO_2 or chemical reagents is usually adopted to decrease the interfacial tension between the displacing fluids and oil for EOR.

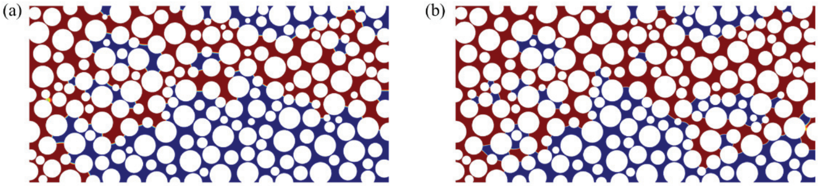

Figure 16. CO_2 saturation distribution under different interfacial tension. Red and blue regions represent CO_2 and oil, respectively. (**a**) σ = 0.025 N/m; (**b**) σ = 0.01 N/m.

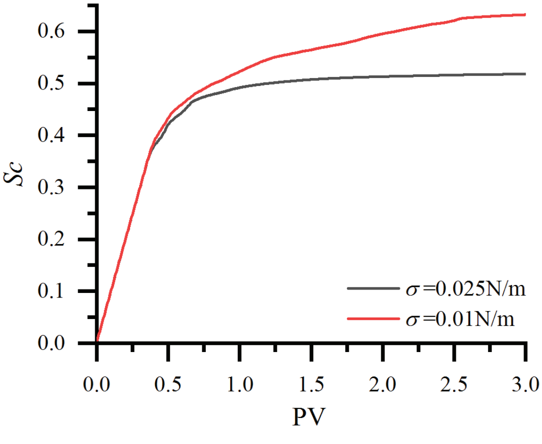

Figure 17. Saturation (S_C) vs. PV for different interfacial tension.

3.3.6. Effect of Absolute Permeability on Fluid Flow

The absolute permeability is an important physical parameter that affects the two-phase flow in porous media. A two-dimensional model with larger absolute permeability is set up based on the aforementioned model of circular random distribution, which keeps the same porosity as the previous model, as shown in Figure 18. The inlet, outlet, and upper and lower boundaries of the model adopt the same circular particle distribution as the previous model, except that the inner circles are arranged in a relatively uniform way.

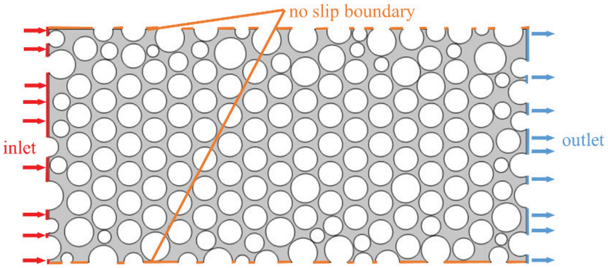

Figure 18. Schematic diagram of the 2D model with larger absolute permeability.

In this two-dimensional model, porosity is the ratio of the pore area to the two-dimensional rectangular area. The expression is as follows:

$$\varphi = \frac{A_p}{A_b} \times 100\% = \frac{A_p}{A_p + A_s} \times 100\% \tag{16}$$

where φ is the porosity (%); A_b is the rectangular area in the two-dimensional model (m^2); A_p is the pore area (m^2); A_s is the area of round particles (m^2).

The absolute permeability is obtained using numerical calculation software with Darcy's law in the case of single-phase flow:

$$u = -\frac{K}{\mu}\nabla p \tag{17}$$

where u is the Darcy speed (m/s); K is the permeability(m^2); μ is the viscosity of the fluid (Pa·s); ∇p is the pressure gradient. According to the above equation, the specific parameters of porosity and absolute permeability obtained are shown in Table 5.

Table 5. Porosity and absolute permeability parameters.

Model	Porosity (%)	Absolute Permeability (m^2)
a	36.36	7.7192×10^{-11}
b	36.36	1.5487×10^{-10}

The boundary conditions of the model are set up as: (1) The inlet on the left side of the model is the velocity inlet with a size of 0.03 m/s; (2) The outlet on the right side of the model is a pressure outlet with a size of 0 Pa; (3) The surface of circular solid particles is oil-wetted, and the contact angle is 60°; (4) The upper and lower boundaries of the model and the circular particle surface are non-slip boundaries; (5) CO_2 and oil are considered to be incompressible Newtonian fluids due to the small scale of the model and small change in fluid pressure. Regardless of the influence of temperature and gravity, the initial state of the model is saturated with oil.

In Figure 19, the CO_2 distribution range in the two-dimensional model with large absolute permeability (Figure 19b) is significantly larger; after CO_2 flooding is stable, the CO_2 saturation in pores corresponding to Figure 19a,b is 38.23% and 45.15%, respectively. Figure 20 shows the velocity field cloud diagram corresponding to the injected CO_2 of 3 PV number. The velocity cloud diagram shown in Figure 20 is in good correspondence with Figure 19, which shows that the two-dimensional model with larger absolute permeability has a better oil recovery efficiency under the same porosity.

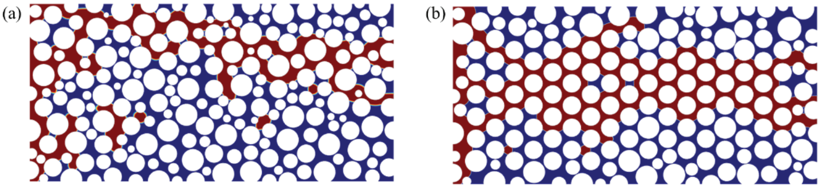

Figure 19. CO_2 saturation distribution after 2 PV CO_2 injection (red and blue regions represent CO_2 and oil, respectively). (**a**) $K = 7.7192 \times 10^{-11} m^2$; (**b**) $K = 1.5487 \times 10^{-10}$ m^2.

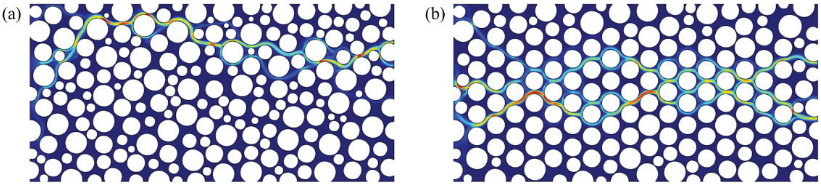

Figure 20. Under different absolute permeability conditions, cloud diagram of velocity field corresponding to injected 2 PV CO_2. (**a**) $K = 7.7192 \times 10^{-11}$ m^2; (**b**) $K = 1.5487 \times 10^{-10}$ m^2.

3.3.7. Effect of Mixed Wettability on Fluid Flow

The wettability of the natural rocks is often mixed. In other words, there are both oil-wetted and nonoil-wetted substances on the surface of rock particles, rather than a single case. This section adopts the model in Section 3.3.2. At log Ca = −4.25 and log M = −3.00, three groups of experimental models are set up by changing the wetting angle distribution of the circular particle wall, which are as follows: (1) The oil-wetted particles account for 70% of all particles (Figure 21a), the nonoil-wetted particles account for 70% (Figure 21b), and the particles are selected randomly in this process; (2) Particles with a diameter greater than or equal to 508 μm are set as oil-wetted, accounting for 47.62% (Figure 21c), and particles with a diameter greater than or equal to 508 μm are set as nonoil-wetted, accounting for 47.62% (Figure 21d); (3) The porous media model is divided equally into three areas in the vertical direction. The wettability of round particles in the three areas is set as oil-wetted, nonoil-wetted, and oil-wetted (the oil-wetted area accounts for 66.67%; Figure 21e) and nonoil-wetted, oil-wetted, and nonoil-wetted (the nonoil-wetted area accounts for 66.67%; Figure 21f), respectively. The contact angle is set to 60° (the oil-wetted particles account for 100%; Figure 21g) and 120° (the nonoil-wetted particles account for 100%; Figure 21h); these models, in Section 3.3.2, are set as the control model.

Figure 21 shows that under mixed wettability conditions, the final CO_2 saturation profiles are significantly different after injecting 3 PV of CO_2, which indicates that mixed wettability is an important factor for the oil recovery. It can be seen that the distribution of CO_2 in Figure 21b is more than that in Figure 21a (the same situation exists in Figure 21c–h), indicating that the more nonoil-wetted particles, the more conducive to CO_2 flooding. This is because the more nonoil-wetted particles, the more likely it is for the capillary force to be in the same direction as the driving force of displacement. By comparing Figure 21c,d, it can be seen that CO_2 flooding is more favorable when the walls of large particles are in the nonoil-wetted state, which is due to the wider distribution and influence of large particles. By comparing Figure 21e,f, it can be seen that the CO_2 distribution in the middle region of Figure 21e is significantly larger than that in Figure 21f. This is because, in the middle region of the model, Figure 21e is set as a nonoil-wetted region, while Figure 21f is an oil-wetted region. The result indicates that under the same injection condition, the occurrence of the nonoil-wetted region is conducive to expanding the sweep efficiency of CO_2 flooding.

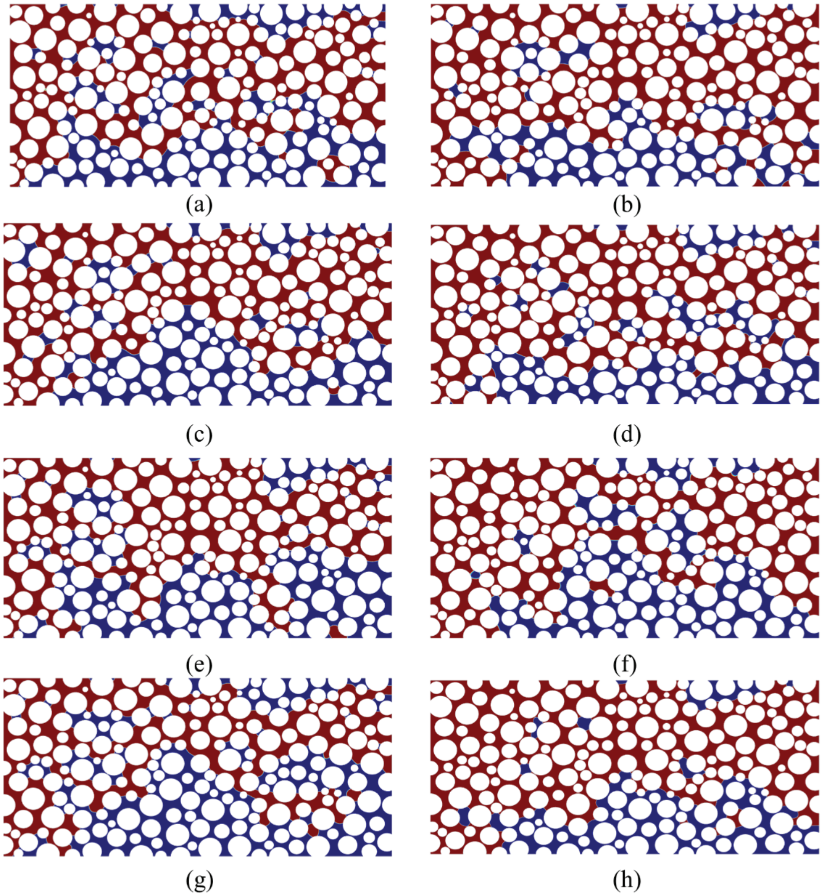

Figure 21. CO_2 saturation distribution corresponding to 3 PV number of CO_2 injected under mixed wettability conditions. (**a**) Oil-wetted particles account for 70%; (**b**) Nonoil-wetted particles account for 70%; (**c**) Large particles, oil-wetted, account for 47.62%; (**d**) Large particles, nonoil-wetted, account for 47.62%; (**e**) Oil-wetted area accounts for 66.67%; (**f**) Nonoil-wetted area accounts for 66.67%; (**g**) Oil-wetted particles account for 100%; (**h**) Nonoil-wetted particles account for 100%; red and blue regions represent CO_2 and oil, respectively.

As shown in Figure 22, the relationship between the number of PV and CO_2 saturation is presented. At the later stage of CO_2 flooding (2.5–3.0 PV), the CO_2 saturation curves of the model in Figure 21g,h are located at the top and bottom. When the particles are completely oil-wetted, the CO_2 saturation is 55.99%, while when the particles are completely nonoil-wetted, the CO_2 saturation is 69.26%, and the CO_2 saturation curves of other numerical models fall in the range of the above two saturation curves. In the same group of experimental models, after injecting 3 PV CO_2, the data represented by dotted lines in the figure are larger than those represented by solid lines, while the dotted line represents that the state of the model is that the nonoil-wetted area is larger.

Figure 23 shows the curve of oil/CO_2 relative permeability during CO_2 flooding in mixed-wetted models. It can be seen from Figure 23b–d that the isotonic point of the model is larger when the nonoil-wetted region is larger. However, Figure 23a shows the opposite situation, which is caused by the wettability setting of 70% of particles randomly selected in the process of setting the wettability of this group of model particles. As can be seen from Figure 23d, as the wettability of the model changes from strong oil-wetted to strong nonoil-wetted, the intersection points of the curve between the oil phase and CO_2 phase move to the right. When the model is strong oil-wetted, the CO_2 saturation at the intersection point is less than 0.45, while when the model is strong nonoil-wetted, it is greater than 0.45. The mixed wettability can better reflect the real situation of the oil reservoir, so the numerical simulation results are closer to the real situation under the mixed wettability condition. With the rising of the nonoil-wetted area in the pores, CO_2 can occupy a larger volume of the pores, which will improve the oil recovery.

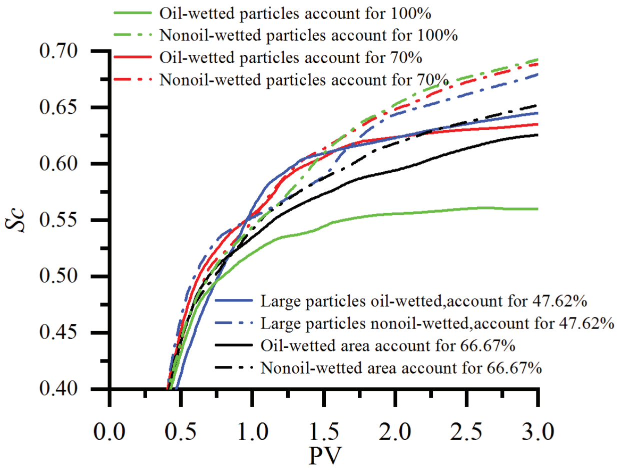

Figure 22. Relationship between PV number and CO_2 saturation (S_C) under the condition of mixed wettability.

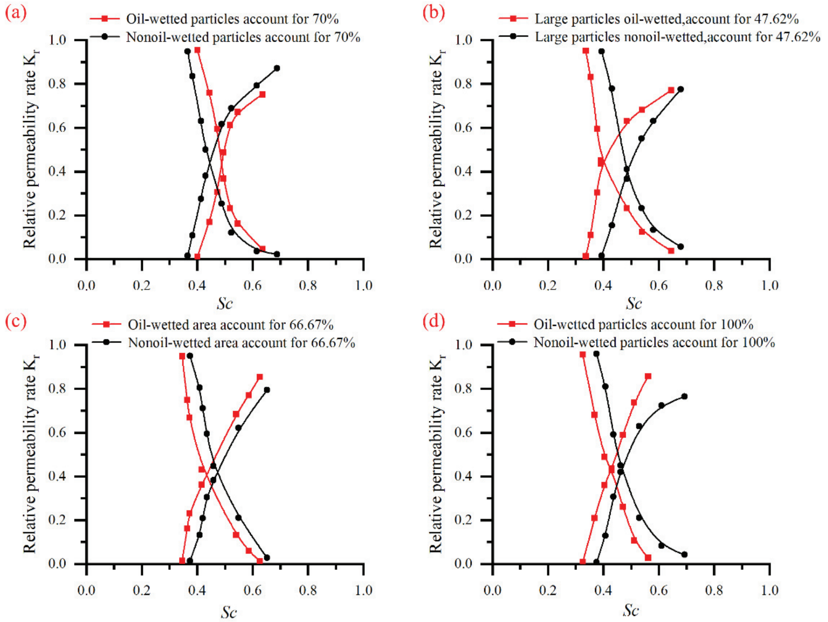

Figure 23. Oil/CO_2 relative permeability curve during CO_2 flooding under mixed wettability. (**a**) Random distribution of mixed wettability; (**b**) Large particles, oil-wetted/nonoil-wetted; (**c**) Oil-wetted/nonoil-wetted area account for 66.67%; (**d**) All particles are oil-wetted/nonoil-wetted.

4. Conclusions

In this study, the two-phase flow of CO_2 flooding was simulated by the phase-field method in a 2D heterogeneous model with random distribution and sizes of grains. A multiple-parameter analysis was performed to investigate the effects of capillary number, viscosity ratio, wettability, density, gravity, interfacial tension, and absolute permeability on the pore-scale mechanism of the CO_2 flooding. The trapping and mobilization mechanisms of the residual oil were also analyzed. The following conclusions can be drawn:

(1) A higher capillary number and viscosity ratio contribute to EOR. Furthermore, with the increase in the capillary number and viscosity ratio, the fingering phenomenon becomes less obvious and shows a stable displacement process. Viscosity fingering is the main pattern that occurred in the CO_2 flooding.

(2) When the wettability alternates from strong oil-wetted to nonoil-wetted, the recovery efficiency keeps constant at the initial stage and then increases slightly. For the mixed wettability scenario, the higher the proportions of the nonoil-wetted area in the model, the higher the oil recovery will be achieved. The patterns of residual fluids trapped after CO_2 breaks through are mainly oil film, oil cluster, and blind-end types in oil-wetted pores, while they are mainly pore-cluster and blind-end types in nonoil-wetted pores.

(3) The model of larger absolute permeability has a better oil recovery efficiency by CO_2 flooding under the same porosity.

(4) A higher density ratio and lower interfacial tension contribute to a higher oil recovery efficiency, which indicates that the scCO_2 injection combined with surfactant flooding is an effective way to enhance the oil recovery. The gravity contributes to increase the sweeping efficiency by enhancing the CO_2 migration in the vertical direction and enhancing the ultimate oil recovery efficiency.

Author Contributions: Conceptualization, R.S.; Formal analysis, Y.T. and R.X.; Funding acquisition, R.S. and Y.W.; Investigation, Y.T.; Writing—original draft, Y.T.; Writing—review and editing, R.S., Y.W., and J.L. All authors have read and agreed to the published version of the manuscript.

Funding: This work was financially funded by National Natural Science Foundation of China, grant number [51909225]; Knowledge Innovation Program of Wuhan-Basic Research, grant number [2022010801010158]; and Natural Science Foundation of Sichuan, grant number [2022NSFSC1161]. The APC was funded by [51909225].

Data Availability Statement: All the data and materials used in this paper are available from the corresponding authors upon request.

Conflicts of Interest: The authors declare that there are no competing financial interest with any other people or groups regarding the publication of this manuscript.

References

1. Hoegh-Guldberg, O.; Bruno, J. The impact of climate change on the world's marine ecosystems. *Science* **2010**, *328*, 1523–1528. [CrossRef] [PubMed]
2. Song, R.; Wang, Y.; Tang, Y.; Liu, J.; Yang, C. 3D Printing of natural sandstone at pore scale and comparative analysis on micro-structure and single/two-phase flow properties. *Energy* **2022**, *261*, 125226. [CrossRef]
3. Song, R.; Liu, J.; Cui, M. A new method to reconstruct structured mesh model from micro-computed tomography images of porous media and its application. *Int. J. Heat. Mass Trans.* **2017**, *109*, 705–715. [CrossRef]
4. Bode, S.; Jung, M. Carbon dioxide capture and storage—liability for non-permanence under the UNFCCC. *Int. Environ. Agreem. Politics Law Econ.* **2006**, *6*, 173–186. [CrossRef]
5. Cao, S.; Dai, S.; Jung, J. Supercritical CO_2 and brine displacement in geological carbon sequestration: Micromodel and pore network simulation studies. *Int. J. Green. Gas Control.* **2016**, *44*, 104–114. [CrossRef]
6. Song, R.; Liu, J.; Yang, C.; Sun, S. Study on the multiphase heat and mass transfer mechanism in the dissociation of methane hydrate in reconstructed real-shape porous sediments. *Energy* **2022**, *254*, 124421. [CrossRef]
7. Blunt, M.; Fayers, F.J.; Orr, F.M., Jr. Carbon dioxide in enhanced oil recovery. *Energy Convers. Manag.* **1993**, *34*, 1197–1204. [CrossRef]
8. Alvarado, V.; Manrique, E. Enhanced oil recovery: An update review. *Energies* **2010**, *3*, 1529–1575. [CrossRef]

9. Parker, M.E.; Meyer, J.P.; Meadows, S.R. Carbon dioxide enhanced oil recovery injection operations technologies. *Energy Procedia* **2009**, *1*, 3141–3148. [CrossRef]
10. Wang, X.Q.; Gu, Y.A. Oil recovery and permeability reduction of a tight sandstone reservoir in immiscible and miscible CO_2 flooding processes. *Ind. Eng. Chem. Res.* **2011**, *50*, 2388–2399. [CrossRef]
11. Song, R.; Sun, S.; Liu, J.; Yang, C. Pore scale modeling on dissociation and transportation of methane hydrate in porous sediments. *Energy* **2021**, *237*, 121630. [CrossRef]
12. Song, R.; Wang, Y.; Liu, J.; Cui, M.; Lei, Y. Comparative analysis on pore-scale permeability prediction on micro-CT images of rock using numerical and empirical approaches. *Energy Sci. Eng.* **2019**, *7*, 2842–2854. [CrossRef]
13. Peng, X.; Wang, Y.; Diao, Y.; Zhang, L.; Yazid, I.M.; Ren, S. Experimental investigation on the operation parameters of carbon dioxide huff-n-puff process in ultralow permeability oil reservoirs. *J. Pet. Sci. Eng.* **2019**, *174*, 903–912. [CrossRef]
14. Desch, J.B.; Larsen, W.K.; Lindsay, R.F.; Nettle, R.L. Enhanced oil recovery by CO_2 miscible displacement in the Little Knife field, Billings County, North Dakota. *J. Pet. Technol.* **1984**, *36*, 1592–1602. [CrossRef]
15. Xiao, P.; Yang, Z.; Wang, X.; Xiao, H.; Wang, X. Experimental investigation on CO_2 injection in the Daqing extra/ultra-low permeability reservoir. *J. Pet. Sci. Eng.* **2017**, *149*, 765–771. [CrossRef]
16. Feng, H.; Haidong, H.; Yanqing, W.; Liang, Z.; Bo, R. Assessment of miscibility effect for CO_2 flooding EOR in a low permeability reservoir. *J. Pet. Sci. Eng.* **2016**, *145*, 328–335. [CrossRef]
17. Zhu, C.; Li, Y.; Zhao, Q.; Gong, H.; Sang, Q.; Zou, H. Experimental study and simulation of CO_2 transfer processes in shale oil reservoir. *Int. J. Coal Geol.* **2018**, *191*, 24–36. [CrossRef]
18. Ding, M.; Gao, M.; Wang, Y.; Qu, Z.; Chen, X. Experimental study on CO_2-EOR in fractured reservoirs: Influence of fracture density, miscibility and production scheme. *J. Pet. Sci. Eng.* **2019**, *174*, 476–485. [CrossRef]
19. Gao, H.; Pu, W. Experimental Study on Supercritical CO_2 Huff and Puff in Tight Conglomerate Reservoirs. *ACS Omega* **2021**, *6*, 24545–24552. [CrossRef]
20. Li, H.; Yang, Z.; Li, R. Mechanism of CO_2 enhanced oil recovery in shale reservoirs. *Petro. Sci.* **2021**, *18*, 1788–1796. [CrossRef]
21. Li, X.; Xue, J.; Wang, Y.; Yang, W.; Lu, J. Experimental study of oil recovery from pore of different sizes in tight sandstone reservoirs during CO_2 flooding. *J. Pet. Sci. Eng.* **2022**, *208*, 109740. [CrossRef]
22. Kun, Q.; Sheng, L.; Hong, E. Microscopic characteristics of oil displacement with different CO_2 injection modes in extra-low permeability reservoirs. *Xinjiang Pet. Geol.* **2020**, *41*, 204.
23. Al-Bayati, D.; Saeedi, A.; Xie, Q.; Myers, M.B.; White, C. Influence of permeability heterogeneity on miscible CO_2 flooding efficiency in sandstone reservoirs: An experimental investigation. *Transp. Porous Med.* **2018**, *125*, 341–356. [CrossRef]
24. Pu, W.; Gao, H.; Zhao, S.; Gao, X. Microscopic Oil Displacement Mechanism of CO_2 in Low-Permeability Heterogeneous Glutenite Reservoirs in the Junggar Basin. *ACS Omega* **2022**, *7*, 4420–4428. [CrossRef]
25. Wei, B.; Gao, H.; Pu, W.; Zhao, F.; Li, Y. Interactions and phase behaviors between oleic phase and CO_2 from swelling to miscibility in CO_2-based enhanced oil recovery (EOR) process: A comprehensive visualization study. *J. Mol. Liquids.* **2017**, *232*, 277–284. [CrossRef]
26. Yang, Y.; Yang, H.; Tao, L. Microscopic determination of remaining oil distribution in sandstones with different permeability scales using computed tomography scanning. *J. Energy Resour. Technol.* **2019**, *141*, 092903. [CrossRef]
27. Zhang, F.; Jiang, Z.; Sun, W. Effect of microscopic pore-throat heterogeneity on gas-phase percolation capacity of tight sandstone reservoirs. *Energy Fuels* **2020**, *34*, 12399–12416. [CrossRef]
28. Chung, T.; Da, W.; Armstrong, R.; Mostaghimi, P. Voxel agglomeration for accelerated estimation of permeability from micro-CT images. *J. Pet. Sci. Eng.* **2020**, *184*, 106577. [CrossRef]
29. Cao, Q.; Gong, Y.; Fan, T. Pore-scale simulations of gas storage in tight sandstone reservoirs for a sequence of increasing injection pressure based on micro-CT. *J. Nat. Gas Sci. Eng.* **2019**, *64*, 15–27. [CrossRef]
30. Wang, Y.; Song, R.; Liu, J.; Cui, M.; Ranjith, P. Pore scale investigation on scaling-up micro-macro capillary number and wettability on trapping and mobilization of residual fluid. *J. Contam. Hydrol.* **2019**, *225*, 103499. [CrossRef]
31. Zhang, C.; Oostrom, M.; Grate, J. Liquid CO_2 displacement of water in a dual-permeability pore network micromodel. *Environ. Sci. Technol.* **2011**, *45*, 7581–7588. [CrossRef] [PubMed]
32. Liu, H.; Valocchi, A.; Werth, C.; Kang, Q.; Oostrom, M. Pore-scale simulation of liquid CO_2 displacement of water using a two-phase lattice Boltzmann model. *Adv. Water Resour.* **2014**, *73*, 144–158. [CrossRef]
33. Amiri, H.; Hamouda, A. Pore-scale modeling of non-isothermal two phase flow in 2D porous media: Influences of viscosity, capillarity, wettability and heterogeneity. *Int. J. Multiphase Flow.* **2014**, *61*, 14–27. [CrossRef]
34. Shi, Y.; Tang, G. Non-Newtonian rheology property for two-phase flow on fingering phenomenon in porous media using the lattice Boltzmann method. *J. Non-Newtonian Fluid Mech.* **2016**, *229*, 86–95. [CrossRef]
35. Zhu, G.P.; Yao, J.; Li, A.E.; Sun, H.; Zhang, L. Pore-scale investigation of carbon dioxide-enhanced oil recovery. *Energy Fuel* **2017**, *31*, 5324–5332. [CrossRef]
36. Basirat, F.; Yang, Z.; Niemi, A. Pore-scale modeling of wettability effects on CO_2–brine displacement during geological storage. *Adv. Water Resour.* **2017**, *109*, 181–195. [CrossRef]
37. Rokhforouz, M.R.; Amiri, H.A. Effects of grain size and shape distribution on pore-scale numerical simulation of two-phase flow in a heterogeneous porous medium. *Adv. Water Resour.* **2019**, *124*, 84–95. [CrossRef]

38. Ma, Q.; Zheng, Z.; Fan, J.; Jia, J.; Bi, j. Pore-scale simulations of CO_2/oil flow behavior in heterogeneous porous media under various conditions. *Energies* **2021**, *14*, 533. [CrossRef]
39. Zhang, L.; Kang, Q.; Yao, J.; Gao, Y.; Sun, Z. Pore scale simulation of liquid and gas two-phase flow based on digital core technology. *Sci. China Technol. Sci.* **2015**, *58*, 1375–1384. [CrossRef]
40. Yue, P.T.; Feng, J.J.; Liu, C.; Shen, J. A diffuse-interface method for simulating two-phase flows of complex fluids. *J. Fluid Mech* **2004**, *515*, 293–317. [CrossRef]
41. Yue, P.T.; Zhou, C.F.; Feng, J.J.; Olliveier-Gooch, C.E.; Hu, H.H. Phase-field simulations of interfacial dynamics in viscoelastic fluids using finite elements with adaptive meshing. *J. Comput. Phys.* **2006**, *219*, 47–67. [CrossRef]
42. Shen, J.; Yang, X. Decoupled, energy stable schemes for phase-field models of two-phase incompressible flows. *SIAM J. Numer. Anal.* **2015**, *53*, 279–296. [CrossRef]
43. Jacqmin, D. Calculation of two-phase Navier–Stokes flows using phase-field modeling. *J. Comput. Phys.* **1999**, *155*, 96–127. [CrossRef]
44. Chaudhary, K.; Bayani, C.; Wolfe, W. Pore-scale trapping of supercritical CO_2 and the role of grain wettability and shape. *Geophys. Res. Lett.* **2013**, *40*, 3878–3882. [CrossRef]
45. Chen, H.; Li, B.; Duncan, I.; Elkhider, M.; Liu, X. Empirical correlations for prediction of minimum miscible pressure and near-miscible pressure interval for oil and CO_2 systems. *Fuel* **2020**, *278*, 118272. [CrossRef]
46. Tryggvason, G.; Bunner, B.; Esmaeeli, A. A front-tracking method for the computations of multiphase flow. *J. Comput Phys.* **2001**, *169*, 708–759. [CrossRef]
47. Gunde, A.C.; Bera, B.; Mitra, S.K. Investigation of water and CO_2 (carbon dioxide) flooding using micro-CT (micro-computed tomography) images of Berea sandstone core using finite element simulations. *Energy* **2010**, *35*, 5209–5216. [CrossRef]
48. Liu, P.; Yao, J.; Couples, G.D.; Ma, J.; Huang, Z.; Sun, H. Modeling and simulation of wormhole formation during acidization of fractured carbonate rocks. *J. Pet. Sci. Eng.* **2017**, *154*, 284–301. [CrossRef]
49. Villanueva, W.; Amberg, G. Some generic capillary-driven flows. *Int. J. Multiphase Flow.* **2006**, *32*, 1072–1086. [CrossRef]
50. Zhu, G.; Yao, J.; Zhang, L.; Sun, H.; Li, A.; Shams, B. Investigation of the dynamic contact angle using a direct numerical simulation method. *Langmuir* **2016**, *32*, 11736–11744. [CrossRef]
51. Boyer, F.; Lapuerta, C.; Minjeaud, S.; Piar, B.; Quintard, M. Cahn–Hilliard/Navier–Stokes model for the simulation of three-phase flows. *Transp. Porous Med.* **2010**, *82*, 463–483. [CrossRef]
52. COMSOL, A. *CFD Module User's Guide*; COMSOL Inc.: Stockholm, Sweden, 2020.
53. Zhou, C.; Yue, P.; Feng, J.J.; Ollivier-Gooch, C.F.; Hu, H.H. 3D phase-field simulations of interfacial dynamics in Newtonian and viscoelastic fluids. *J. Comput. Phys.* **2010**, *229*, 498–511. [CrossRef]
54. Shen, J. Modeling and numerical approximation of two-phase incompressible flows by a phase-field approach. *Multiscale Modeling Anal. Mater. Simul.* **2012**, *9*, 147–195.
55. Or, D. Scaling of capillary, gravity and viscous forces affecting flow morphology in unsaturated porous media. *Adv. Water Resour.* **2008**, *31*, 1129–1136. [CrossRef]
56. Hizir, F.E.; Hardt, D.E. Phase-field modeling of liquids splitting between separating surfaces and its application to high-resolution roll-based printing technologies. *Phys. Fluids* **2017**, *29*, 052007. [CrossRef]
57. Peng, J.; Song, R.; Wang, Y.; Xiao, H. Comparative study of VOF, LS, and VOSET on pore-scale immiscible waterflooding modeling. *Petroleum* **2021**, *7*, 314–324. [CrossRef]

minerals

MDPI

Article

The Characteristic Development of Micropores in Deep Coal and Its Relationship with Adsorption Capacity on the Eastern Margin of the Ordos Basin, China

Tao Wang [1,2,3], Fenghua Tian [4], Ze Deng [2,3,*] and Haiyan Hu [5,*]

[1] School of Geosciences, Yangtze University, Wuhan 430100, China
[2] PetroChina Exploration and Development Research Institute, Beijing 100083, China
[3] CNPC Unconventional Key Laboratory, Beijing 100083, China
[4] PetroChina Coal Bed Methane Co., Ltd., Beijing 100028, China
[5] School of Resource and Environment, Yangtze University, Wuhan 430100, China
[*] Correspondence: dengze@petrochina.com.cn (Z.D.); hyhucom@163.com (H.H.)

Abstract: The accurate description of micro-/nanopores in deep coal reservoirs plays an important role in evaluating the reservoir properties and gas production capacity of coalbed methane (CBM). This work studies nine continuous samples of high–rank coal from the Daning–Jixian area of the Ordos Basin. Maceral analysis, proximate analysis, field emission scanning electron microscopy (FE-SEM), low-pressure CO_2 adsorption (LPA), low-temperature N_2 adsorption (LTA) and high-pressure methane adsorption (HPMA) experiments were conducted for each sample. The fractal dimension (D) of the LPA data was calculated by using the micropore fractal model. The characteristics of the deep coal reservoir pore structure, proximate analysis, relationship between maceral and fractal dimensions, and gas adsorption capacity of the micropores are discussed. The results showed that the combination of LPA with nonlocalized density functional theory (NLDFT) models and LTA with NLDFT models can more accurately determine the pore size distribution of the micropores. The pore volume (PV) and specific surface area (SSA) of the coals were distributed in the ranges of 0.059~0.086 cm^3/g and 204.38~282.42 m^2/g, respectively. Although the degree of micropore development varies greatly among different coal samples, the pore distribution characteristics are basically the same, and the PV and SSA are the most developed in the pore size range of 0.4–0.7 nm. Ash content (A_d) and mineral composition are two major factors affecting micropore structure, but they have different impacts on the fractal dimension. The higher the vitrinite content, moisture content (M_{ad}) and Ad are, the larger the micropore fractal dimension (D) and the stronger the heterogeneity of the pore structure. Micropores account for 99% of the total SSA in coal, and most methane can be adsorbed in micropores. The fractal dimension of micropores can be used to evaluate the pore structure characteristics. The larger the fractal dimension, the smaller the micro-SSA and micro-PV of the coal sample. Fractal analysis is helpful to better understand the pore structure and adsorption capacity of CBM reservoirs.

Keywords: coalbed methane; gas adsorption; micropores; pore structure distribution; eastern Ordos Basin

Citation: Wang, T.; Tian, F.; Deng, Z.; Hu, H. The Characteristic Development of Micropores in Deep Coal and Its Relationship with Adsorption Capacity on the Eastern Margin of the Ordos Basin, China. *Minerals* **2023**, *13*, 302. https://doi.org/10.3390/min13030302

Academic Editors: Jianjun Liu, Yuewu Liu, Zhengming Yang, Yiqiang Li, Fuquan Song, Rui Song, Yun Yang and Saiied Aminossadati

Received: 13 December 2022
Revised: 21 January 2023
Accepted: 16 February 2023
Published: 21 February 2023

1. Introduction

Coal, as a strong heterogeneous porous medium, has a complex pore structure and has been widely studied [1,2]. According to the International Union of Pure and Applied Chemistry (IUPAC) classification of pores in porous materials, pores can be divided into micropores (<2 nm), mesopores (2–50 nm) and macropores (>50 nm) [3]. Some researchers had speculated that most gas in coal may be adsorbed in the micropores [4–6]. CBM mainly exists on the surfaces of micropores in the adsorbed state and connected pore and fracture systems as gas migration and transmission channels [7–9]. CBM is produced continuously through desorption, diffusion and seepage, and the diffusion and seepage that occur in micropores are the initial stages of gas desorption and migration. In the development of CBM, more attention is drawn to the influence of the development scale and connectivity of larger fractures (macroscopic fractures) on reservoir permeability, but the development characteristics and connectivity of micropores may restrict and potentially affect CBM desorption and migration [9–12].

The pore-related characteristics of coal include the porosity, specific surface area (SSA), pore volume (PV), pore size distribution (PSD) and pore connectivity. The development scale and distribution characteristics of pore fissure in coal reservoir determine the adsorption and seepage capacity of CBM. The fine characterization of the development scale, structure and distribution characteristics of pore in coal is the premise of studying the desorption and migration of CBM at micro scale [3,13,14]. The existing characterization methods of pore structure in coal mostly apply the characterization techniques of porous solid materials, which can be roughly divided into three categories: fluid injection, image analysis and nonfluid injection methods. The image analysis method identifies and analyses pores in coal by using micro-observation techniques, such as scanning electron microscopy (SEM), transmission electron microscopy (TEM) and atomic force microscopy (AFM), which can visualize the shape, size and distribution of pores [13,15–18]. In addition, quantitative information, such as porosity and PSD, can be further obtained by combining statistical methods; however, its accuracy depends on sample characteristics, instrument performance and human factors. The fluid injection method adopts the injection of nonwettable fluid (mercury, for example) or gas (usually N_2, CO_2 and Ar) into the sample under different pressures and then obtains the PSD, PV and SSA by applying a corresponding theoretical calculation model via the fluid injection volume [19–23]. This method is easy to operate and can obtain detailed pore information of coal rock, so it is widely used in the pore characterization of coal reservoirs. However, the fluid injection method also has some limitations, and this method is suitable for studying only open pores, not closed pores. Nonfluid injection methods mainly include nuclear magnetic resonance (NMR), small angle scattering (SAS) and computed tomography (CT); these methods are advanced and accurate, but the cost of analysis is high [10,13,24–26].

Among these experimental methods, low-pressure CO_2 adsorption (LPA) and low-temperature N_2 adsorption (LTA) are the most basic and widely used [9,27]; however, the PV and SSA of coal micropores determined by the LTA method and LPA method and different models may be contradictory and lack accurate verification [9]. For example, the PV of micropores (micro-PV) and SSA of micropores (micro-SSA) determined by the LPA method are much higher than those determined by the LTA method. The SSA and PV calculated by the Dubinin–Astakhov (DA) model are usually smaller than those calculated by the density functional theory (DFT) model, and the average pore size calculated by the DA model is slightly larger than that calculated by the DFT model [19,28–32]. Although many studies have focused on the PV and SSA of pores of different scales in coal, few studies have investigated the characteristics of pores with sizes of 0.35~2.0 nm [9,20]. In this paper, nine coal samples from the Daning–Jixian block on the eastern margin of the Ordos Basin were selected as research objects. Through LPA and LTA experiments, the micropore structure of deep coal reservoirs in the research area was analysed, and the fractal dimension of the micropores in the coal samples was calculated by using LPA data. High-pressure methane adsorption (HPMA) experiments were carried out to measure the CH4 adsorption capacity of the coal samples. The specific objectives were (1) to analyse and compare the accuracy of the calculation results of different models (including the DA, Dubinin—Radushkevich (DR), grand canonical Monte Carlo (GCMC) and nonlocal density functional theory (NLDFT) models); (2) to explore the ratios of the PVs and SSAs of micropores and mesopores in deep coal reservoirs; (3) to discuss the factors influencing micropore fractal dimensions in deep coal reservoirs; and (4) to determine whether there is a strict correlation between the micro-SSA, micro-PV and adsorption capacity of deep coal reservoirs.

2. Geological Setting

The Ordos Basin is one of the main oil-bearing basins in China and has an area of approximately 37 × 10^4 km^2 [33,34]. According to the tectonic morphology, the basin can be subdivided into 6 secondary tectonic units [8,33,35]. The study area is located in the eastern margin of the Ordos Basin, spanning Shanxi and Shaanxi provinces, in Daning County and Ji County (Figure 1a) [8]. As a part of the Ordos Basin, the study area experienced a palaeogeographic evolution process in the late Carboniferous–middle Permian, which was dominated by marine sedimentary surface continental marine facies, transitional facies and fluvial clastic sedimentary facies, during which several transgression events occurred. The study area can be divided into the Permian Shanxi Formation, Taiyuan Formation and Carboniferous Benxi Formation [34,36,37]. The lithology of the top of the Taiyuan Formation is micritic bioclastic limestone, indicating that the sedimentary water was clear seawater with normal salinity, corresponding to a typical shallow marine shelf sedimentary environment. The lower Benxi Formation was formed in coastal and shallow shelf environments, and mudstone, grey and black mudstone interbedded with thin sandstone, limestone and black coal were deposited from bottom to top. The Shanxi Formation is characterized by rapid sedimentary phase transformation and complex lithologic assemblages, and the Shanxi Formation can be divided into the lower Shan2 member and the upper Shan1 member (Figure 1b) [33,34]. The main target strata are the No. 5 coal of the Shanxi Formation, No. 8 coal of the Taiyuan Formation and No. 9 coal of the Benxi Formation, with the main body buried 2000–2400 m deep; the No. 5 coal seam has thicknesses of 1~3 m, and the No. 9 coal seam has thicknesses of 5~12 m. This seam is the main exploration target layer of deep CBM.

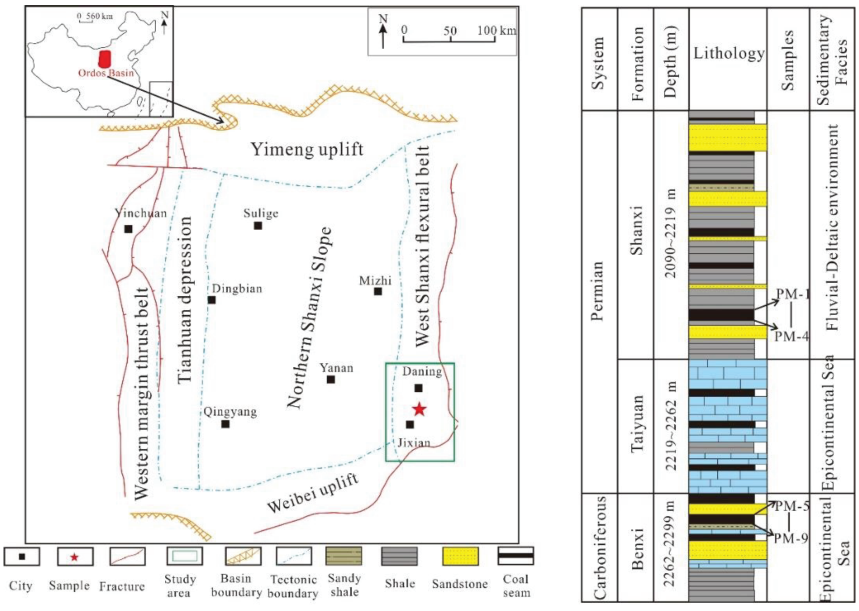

(a) (b)

Figure 1. (**a**) Location of the study area. (**b**) Stratigraphic columns of the coal-bearing strata.

3. Samples and Experimental Methods

Nine fresh coal samples from recently drilled wells in the Daning–Jixian area on the eastern margin of the Ordos Basin were selected; the coal-bearing strata, including the Shanxi Formation and Benxi Formation, were formed in a transitional environment between land and sea. All 9 coal samples are black semi-dark coals, including 5 samples from the Shanxi Formation and 4 samples from the Benxi Formation (Figure 1b). To obtain the basic physical characteristics of the coal samples, a Leica DM4P photometer microscope was used for observations, and maximum vitrinite reflectance ($R_{o,max}$) measurements (50 points) and maceral analyses (500 points) were carried out randomly under reflected light with oil immersion, strictly following the national standards GB/T 6948−2008 and GB/T 8899−2013, respectively. According to national standard GB/T 30732−2014, the moisture content (M_{ad}), ash content (A_d), volatile matter content (V_{daf}) and fixed carbon content (FC_{ad}) of the coal samples were analysed [38].

LPA and LTA experiments were performed using a Quantachrome Instruments Au-tosorb IQ-MP automatic gas adsorption analyser according to national standards GB/T 21650.2-2008 and GB/T 21650.3-2011. The coal and rock samples were ground with an agate mortar and screened to 60~80 mesh. The samples were weighed to approximately 2~3 g, and the test temperatures were 273 K and 77 K. An FEI Helios 650 field emission scanning electron microscopy (FE-SEM) device was used to image the coal and rock samples and observe their pore morphology. The implementation standard was China's petroleum industry standard SY/T 5162-2014. The HPMA experiments were carried out by Gravimetric Isotherm Rig 3. According to the national standard GB/T 19560-2008, the test sample size was approximately 80 g of dry sample of size 60–80 mesh, and the maximum pressure and temperature were set to 25 MPa and 70 °C, respectively.

4. Results

4.1. Coal Rock Coal Quality Characteristics

The results show that the maturity increases with increasing coalification degree. The R_o values of the collected coal and rock samples range from 2.93% to 3.30% (Table 1). The average R_o values of the Shanxi Formation and Benxi Formation are 3.13% and 3.17%, respectively, which are considered high-rank coals according to standard ISO 11760:2018. The macerals are mainly vitrinite (54.0% average), which is considered a medium vitrinite coal according to standard ISO 11760:2018, followed by inertinite (40.1% average), and exinite is not visible. The mineral group is relatively low, accounting for 2.2–9.8% of the coal rocks and are mainly clay minerals, silica, carbonate and iron sulfide (Table 1).

Table 1. Basic characteristics of coal samples.

Samples	Strata	Coal Seam	Depth (m)	$R_{o,max}$%	Proximate Analysis (%)				Macerals (%)		
					M_{ad}	A_d	V_{daf}	FC_{ad}	Vitrinite	Inertinite	Minerals
PM-1	Shanxi	5 #	2195.3	2.93	1.1	12.6	7.2	79.1	62.7	27.8	9.5
PM-2	Shanxi	5 #	2195.7	3.13	0.8	10.3	6.8	82.2	52.9	39.5	7.6
PM-3	Shanxi	5 #	2196.5	3.14	0.8	5.8	6.8	86.7	41.8	52.5	5.7
PM-4	Shanxi	5 #	2197	3.30	1.0	6.8	6.5	85.7	62.7	35.1	2.2
PM-5	Benxi	8 #	2274.1	3.15	1.2	12.7	7.0	79.2	52	43.9	4.1
PM-6	Benxi	8 #	2274.4	3.15	0.8	12.6	10.1	76.5	64.3	26.6	9.1
PM-7	Benxi	8 #	2275.7	3.17	0.7	7.3	6.3	85.7	34.1	61.3	4.6
PM-8	Benxi	8 #	2276.4	3.21	1.3	6.4	6.6	85.8	58	38.5	3.5
PM-9	Benxi	8 #	2277.1	3.15	1.1	8.3	7.3	83.3	57.83	35.37	6.8

Note: $R_{o,max}$ = maximum oil vitrinite reflectance; M_{ad} = moisture content; A_d = ash content; V_{daf} = volatile matter content; F_{Cad} = fixed carbon content.

The moisture contents (M_{ad}) of the coal rocks in the Shanxi and Benxi Formations range from 0.7% to 1.3% (1.0% average). The ash contents (A_d) range from 5.8% to 12.7% (9.2% average), corresponding to a low–medium ash coal according to standard ISO 11760:2018. The volatile matter contents (V_{daf}) range from 6.3% to 10.1% (7.2% average), which is low.

The fixed carbon contents (FC_{ad}) range from 76.5% to 86.7% (82.7% average), which is very high (Table 1). When coal is ranked high, FC_{ad} is usually negatively correlated with A_{d} [38].

4.2. Pore Morphology Characteristics

The pore morphology of coal is clearly observable by FE-SEM. According to the origin and distribution characteristics of the pores, they can be divided into two categories: (1) organic pores, composed of gaseous pores and shrinkage pores/fractures, and (2) mineral-related pores, consisting of intraparticle (IntraP) pores within minerals and interparticle (InterP) pores between matrix particles [39,40]. Figure 2 shows the pore types of 9 representative coal samples in FE-SEM images. The results show that organic pores and InterP pores are widely distributed in the coal samples in the study area, with various shapes, abundant nanopores and a small number of microscale pores/cracks (Figure 2a,b). The gaseous pores are round, oval and slit-shaped and form a pore network (Figure 2c), which greatly increases the pore connectivity and results in a good storage capacity. The pore widths are mainly in the range of approximately 200 nm to 2.0 μm. Wang (2019) and Li (2019) et al. show that the pore shapes are generally spherical for low rank coal and they are mainly ellipsoidal for high rank coal [17,40]. High-order coal seams in the study area are buried deep (>2000 m) and have a high degree of thermal evolution; under the high pressure conditions of overlying strata, pores are compressed, forming various irregular forms such as wedges and slits (Figure 2f,h,i). In contrast to the organic matter pores, the pores in grains generally exist between mineral particles or between minerals and organic matter and are polygonal and elongated (Figure 2f,g). FE-SEM images show that the clay minerals are closely bound to the organic matter: most of the internal pores associated with the organic matter are slit-shaped and form along a clay boundary; these pores are more than 200 nm wide (Figure 2f). Among them, the clay minerals in PM-6 are vermicular and stacked, which can produce shrinkage cracks (Figure 2d,f,g). The clay minerals in the PM-9 coal sample are massive and form a large number of polygonal grain pores (Figure 2g–i).

4.3. Quantitative Analyses of Pore Structure

4.3.1. CO_2 Adsorption Isotherms

The LPA method to determine the pores in coal generally reveals monolayer adsorption or micropore filling at the <2 nm scale [41–43]. The CO_2 adsorption isotherms of the coal samples are shown in Figure 3, which show similar characteristics. Their CO_2 adsorption capacity increases steadily with increasing pressure [44]. According to the IUPAC standards, the CO_2 adsorption isotherms of coal and rock samples all have typical type I isotherm characteristics, indicating that all coal and rock samples have microporous properties. Sample PM-8 (29.9 cm^3/g STP) has the highest adsorption capacity for CO_2, indicating the highest microporosity, while sample PM-1 (21.6 cm^3/g STP) has the lowest adsorption capacity for CO_2, indicating the lowest microporosity.

The DA, DR, GCMC and NLDFT models in ASiQwin software were used to calculate the PV and SSA distribution of all coal and rock samples, and the results are shown in the corresponding Table 2. The SSA and PV of the same coal sample vary greatly under different models. As the DA and DR models are traditional macroscopic thermodynamic models, they are based on Polanyi potential theory and Dubinin micropore filling theory [45,46]. The PVs calculated by the DA model and DR model are 0.078~0.113 cm^3/g and 0.065~0.084 cm^3/g, respectively. The SSAs obtained by the DR model are 182.437~236.571 m^2/g (Table 2). GCMC and NLDFT are molecular dynamics models that describe the microscopic theory of fluid adsorption and phase behaviour in narrow pores at the molecular level [47,48], the properties of adsorbed gas molecules linked to their adsorption properties in pores of different sizes. The GCMC and NLDFT models provide a more ac-curate method for pore size analysis. The PVs calculated by the GCMC model and NLDFT model are 0.056~0.092 cm^3/g and 0.062~0.092 cm^3/g, respectively, and the calculated SSAs are 187.447~277.147 m^2/g and 209.408~291.810 m^2/g, respectively (Table 2).

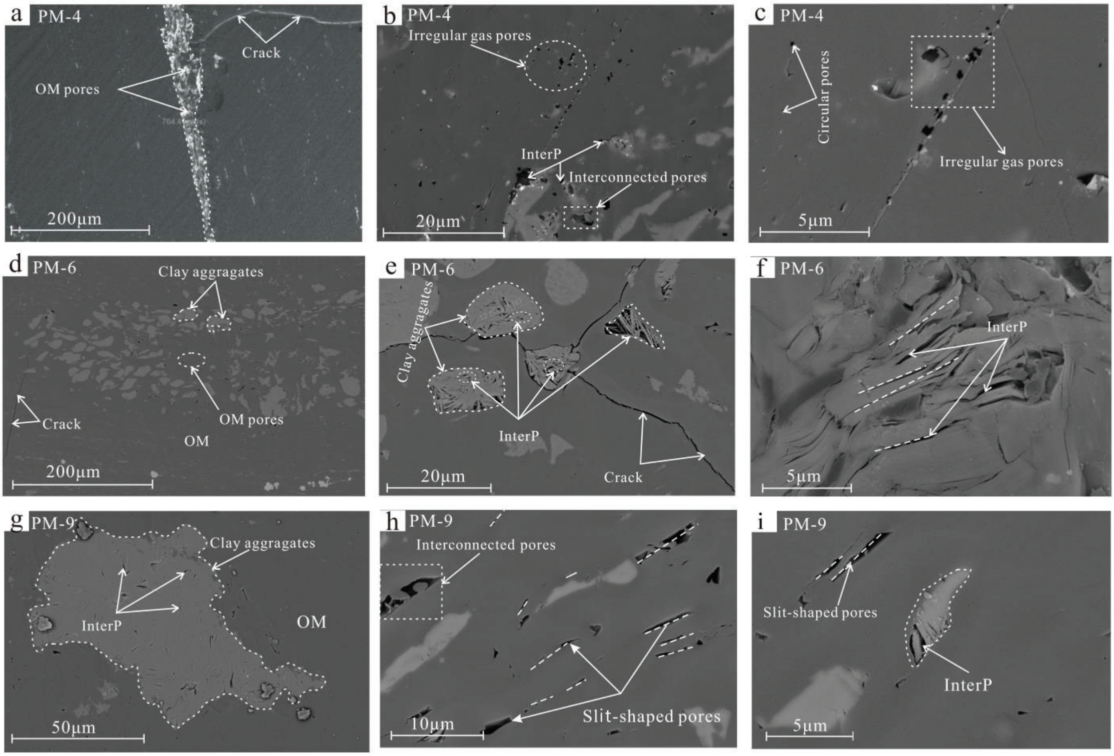

Figure 2. FE—SEM images of the organic and inorganic pores in selected coal samples. (**a**–**c**) The pore–fracture distribution and irregular gas pores, sample PM-4. (**d**–**f**) The coal matrix and clay mineral distribution and InterP pores, sample PM-6. (**g**–**i**) Directional alignment and some slit-shaped pores, sample PM-9.

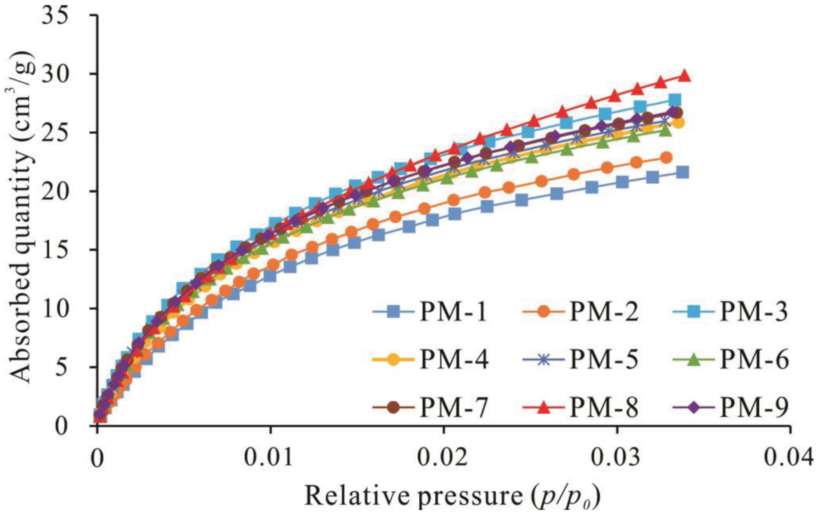

Figure 3. CO_2 adsorption isotherms obtained at 273 K for different samples.

Table 2. The PV and SSA of LP-CO_2/N_2GA calculated by different models.

Model		Parameters	PM-1	PM-2	PM-3	PM-4	PM-5	PM-6	PM-7	PM-8	PM-9
CO_2 adsorption	DR	PV (cm^3/g)	0.065	0.071	0.076	0.075	0.075	0.073	0.084	0.079	0.077
		SSA (m^2/g)	182.437	199.568	214.939	212.133	211.343	204.318	236.571	222.042	216.809
	DA	PV (cm^3/g)	0.078	0.086	0.083	0.090	0.082	0.079	0.113	0.094	0.092
	GCMC	PV (cm^3/g)	0.056	0.063	0.070	0.068	0.073	0.071	0.092	0.076	0.075
		SSA (m^2/g)	187.447	205.006	236.368	227.242	238.084	230.864	277.147	250.915	244.416
	NLDFT	PV (cm^3/g)	0.062	0.066	0.079	0.078	0.077	0.075	0.092	0.081	0.079
		SSA (m^2/g)	209.408	224.502	266.137	257.523	260.323	252.787	291.810	275.762	267.185
N_2 adsorption	BET	SSA (m^2/g)	0.269	0.302	0.305	0.449	0.515	0.376	0.173	0.291	0.454
	BJH	PV (cm^3/g)	0.002	0.001	0.001	0.002	0.003	0.002	0.001	0.002	0.001
		SSA (m^2/g)	0.638	0.557	0.451	0.873	0.835	0.688	0.458	0.558	0.613
	NLDFT	PV (cm^3/g)	0.001	0.001	0.001	0.002	0.002	0.001	0.001	0.001	0.001
		SSA (m^2/g)	0.388	0.349	0.337	0.522	0.592	0.449	0.281	0.390	0.414
Total micropore		PV (cm^3/g)	0.059	0.063	0.074	0.073	0.072	0.070	0.086	0.076	0.074
		SSA (m^2/g)	204.380	219.385	258.675	250.065	253.102	245.765	282.415	268.210	259.860

Note: DR = Dubinin—Radushkevich; DA = Dubinin–Astakhov; GCMC = grand canonical Monte Carlo; NLDFT = Nonlocal density functional theory; BET = Brunauer–Emmett–Teller; BJH = Barrett—Joyner—Halenda; PV = pore volume; SSA = specific surface area.

Although the PV and SSA measured by the DA, GCMC and NLDFT models are similar, the PSD is obviously different, the PSD calculated by the GCMC model and NLDFT model has multiple peaks, and the pore sizes are mainly 0.4–0.7 nm and 0.8–0.9 nm, respectively (Figure 4). The DA calculation results show a single peak, and the pore sizes are mainly between 1.5 and 3.5 nm. Because the thermodynamic properties of fluid in micropores are very different from those in the free state, the critical point, freezing point and triple point change [9]. However, the DA and DR models do not take into account the changes in these parameters or the effect of pore shape on gas molecular aggregation, so the results calculated by these models may be more biased. Blacher et al. (2000) and El-Merraoui et al. (2000) also analysed and compared the activated carbon micropores of different models, and the results showed that the NLDFT model was more reliable due to its smaller fitting error [1,49]. Jie et al. (2018) measured isotherms and calculated the fit-ting error of isotherms by comparing different models and determined that the fitting error of the NLDFT model was smaller than that of the GCMC model [50]. Song et al. (2020) showed that the fitting curves of the DR and DA models deviated greatly from the measured isotherms, with relative errors of 27.2% and 18.4%, respectively [9]. However, the fitting curves of the GCMC and NLDFT models are basically consistent, and the relative errors are 0.37% and 0.23%, respectively. These results show that the NLDFT model is more accurate for analysing the PSD of micropores in coal under LPA.

4.3.2. N_2 Adsorption Isotherm

The LTA isotherms of the coal and rock samples are shown in Figure 5, indicating that the N_2 adsorption volumes of all coal and rock samples are within 0.79~1.97 cm^3/g. According to the IUPAC classification, the main form of coal in the study area is type IV [3]. When the relative pressure $p/p_0 > 0.1$, the adsorption curve increases rapidly, indicating that these samples have a strong adsorption effect on N_2. Initially, the adsorption curve rises slowly with increasing pressure, indicating that the sample is slowly transformed from monolayer adsorption to multimolecular adsorption. When $p/p_0 \approx 1$, the capillary condensation effect leads to a sharp rise in the curve, and the coal sample does not show adsorption saturation equilibrium, indicating that there are certain large pores in the coal sample. For desorption branches, when $p/p_0 \approx 0.5$, the curve is above the adsorption branch. In addition, when $p/p_0 \approx 0.5$, the curve shows a rapid decline; after this point, the desorption branch and the adsorption branch basically coincide.

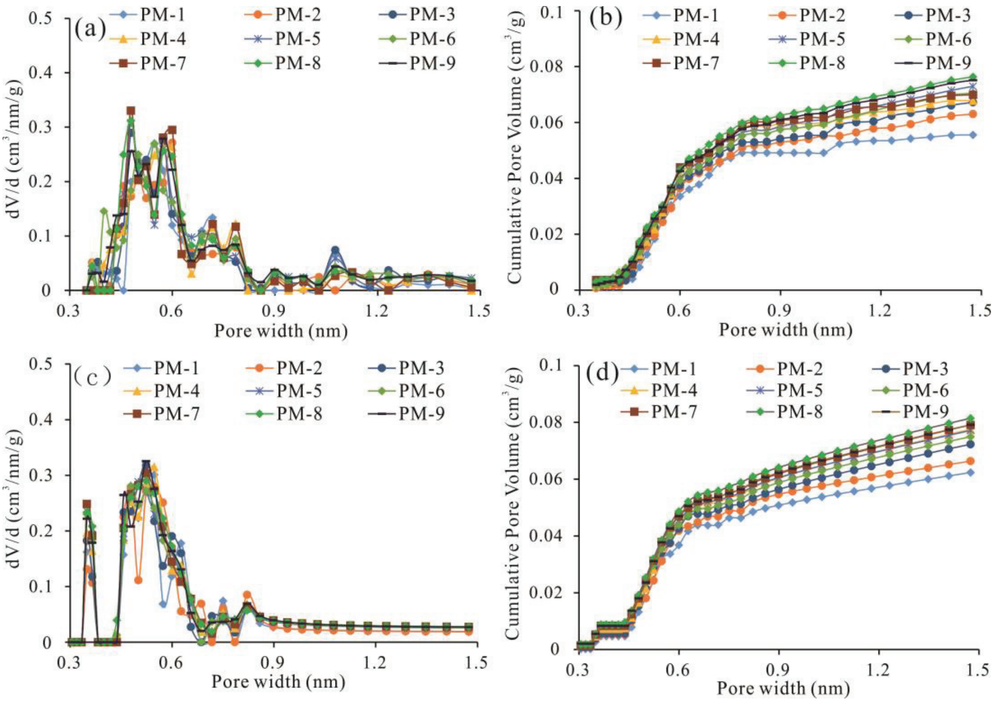

Figure 4. Distribution of the PV calculated by different models for different pores sizes. (**a**,**b**) GCMC model, (**c**,**d**) NLDFT model.

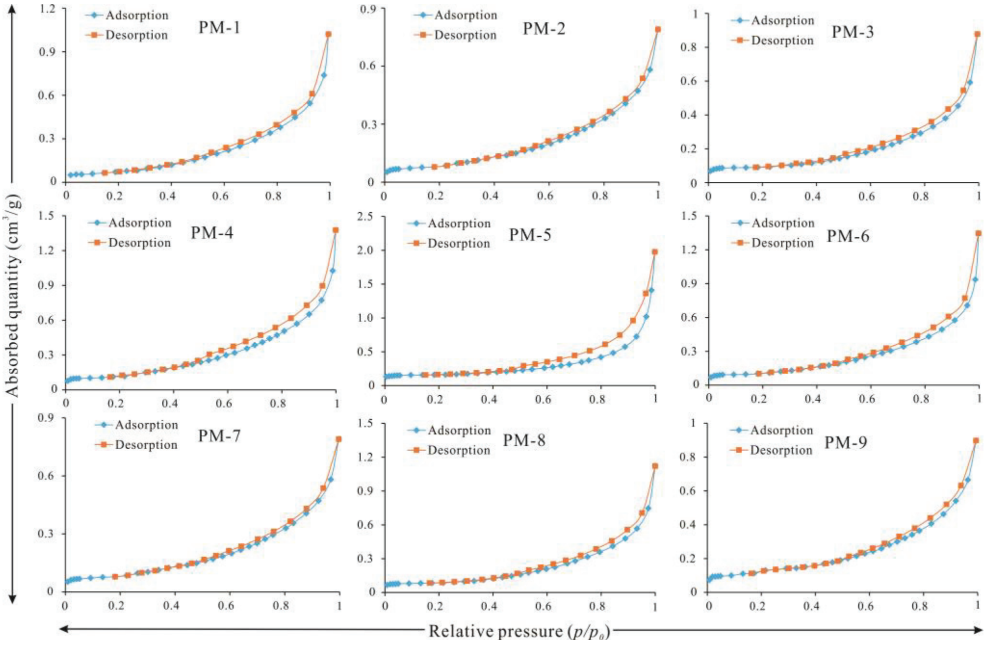

Figure 5. N_2 adsorption isotherm of ten samples at 77 K.

The shape of the hysteresis loop can yield important information about the pore structure. According to adsorption aggregation theory, different relative pressures on the same pore lead to the formation of an adsorption ring between the adsorption curve and the desorption curve during the agglomeration and evaporation processes, which are mainly caused by the complex combination of different pore morphologies [13,44,51]. Pore types can be divided by shape into cylindrical, ink bottle, parallel plate, slit, etc. Ac-cording to the IUPAC classification of hysteresis loops, the hysteresis loops of the coal and rock samples in the study area are mainly classified as the H3 type (Figure 5). The hysteretic curves of all coal samples are similar to those of the H3 type. When the relative pressure is low ($p/p_0 \approx 0.5$), the adsorption and desorption curves basically coincide, indicating that the pore types are mainly cylindrical, conical and anvil-shaped. When p/p_0 is large, there is a slight hysteresis loop, indicating the existence of open pores.

ASiQwin software was used to calculate the experimental data of LTA. The Brunauer–Emmett–Teller (BET), Barrett—Joyner—Halenda (BJH) and NLDFT models were used to calculate the results, as shown in Table 2. The results of the NLDFT model and BJH model are similar (Figure 6). The BJH model and NLDFT model were used to calculate PVs of 0.001~0.003 cm^3/g and 0.001~0.002 cm^3/g, respectively. The BET, BJH and NLDFT models were used to calculate SSAs of 0.173~0.515 m^2/g, 0.451~0.873 m^2/g and 0.281~0.592 m^2/g, respectively. Groen et al. (2003) and Song et al. (2020) proved experimentally and theoretically that the DFT model is more accurate than other models. Considering the fitting error and convergence of the pore size range [5,9]. Jie et al. (2018) determined that the total PV and total SSA of pores obtained by the BJH model were generally slightly higher than those obtained by the NLDFT model [50]. By comparing the fitting errors of the calculated isotherms and measured isotherms, it is determined that the fitting errors of the NLDFT model are less than those of the BJH model (Table 3) [52]. Because the anisotropy and surface roughness of nanopores are considered in the NLDFT model, it is more accurate to analyse the PSD of nanopores in coal.

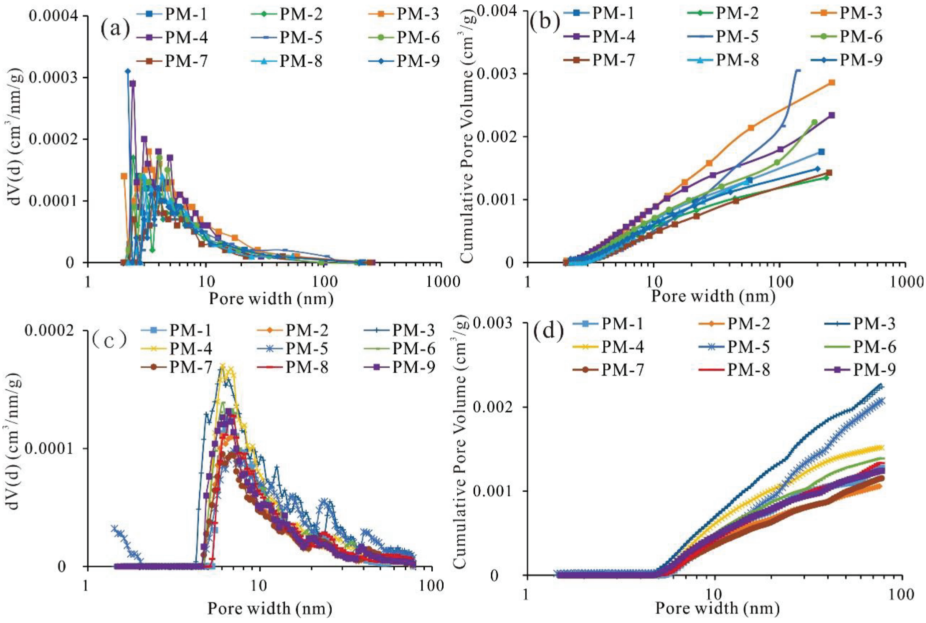

Figure 6. Distribution of the PV calculated by the BJH and NLDFT models. (**a**,**b**) BJH model, (**c**,**d**) NLDFT model.

Table 3. Pore analysis results of the BJH and NLDFT models.

Samples	Model					
	BJH			NLDFT		
	PV (cm^3/g)	SSA (m^2/g)	Fitting Error (%)	PV (cm^3/g)	SSA (m^2/g)	Fitting Error (%)
PM-1	0.002	0.638	1.37	0.001	0.388	0.44
PM-2	0.001	0.557	0.84	0.001	0.349	0.16
PM-3	0.001	0.451	0.48	0.001	0.337	0.11
PM-4	0.002	0.873	0.94	0.002	0.522	0.16
PM-5	0.003	0.835	0.62	0.002	0.592	0.15
PM-6	0.002	0.688	0.83	0.001	0.449	0.19
PM-7	0.001	0.458	1.65	0.001	0.281	0.62
PM-8	0.002	0.558	0.92	0.001	0.390	0.34
PM-9	0.001	0.613	0.35	0.001	0.414	0.09

Note: NLDFT = Nonlocal density functional theory; BJH = Barrett—Joyner—Halenda; PV = pore volume; SSA = specific surface area.

4.4. Pore Fractal Characteristics

Currently, the fractal dimension based on the high-pressure mercury injection method and gas adsorption method is the most commonly used method to study reservoir heterogeneity [42,53,54]. However, due to the limitation of measurement accuracy and the gas occurrence mechanism, the two methods are most applicable to the range of macro- and mesopores and cannot accurately characterize the heterogeneity of micropores. Previous studies have shown that adsorbent molecules in micropores are usually filled with micropores [55,56]. Jaroniec et al. (1993), via the adsorption test of microporous activated carbon, determined that the pore size distribution of micropores is the core factor affecting its heterogeneity [55]. According to the DA equation, the adsorption process of micropores is the filling of their inner volume rather than the layered adsorption on the pore wall. The pore packing degree θ was used to characterize the adsorption capacity:

$$\theta = \frac{n}{n_{max}} = \int_0^\infty exp[-(Az/\beta)^3]F(z)dz, \tag{1}$$

where

$$A = RTLn(p_0/p), \tag{2}$$

and

$$z = 1/E_0. \tag{3}$$

In the above equations, θ is the packing degree of CO_2 molecules in micropores; n and n_{max} are, respectively, the amount and maximum amount adsorbed in the micropores, cm^3/g; A is the adsorption potential, kJ/mol; β is a similarity constant, which is related to the adsorbent, 0.38; $F(z)$ is the normalized distribution function; E_0 is the characteristic energy, kJ/mol; p/p_0 is the relative pressure; z is the inverse of E_0, mol/kJ; T is the absolute temperature, K; and R is the universal gas constant, 8.314 J/(mol·K). According to Jaroniec et al. (1993) [57], the normalized distribution function $F(z)$ of z is represented by a gamma distribution:

$$F(z) = \frac{3\rho^v}{\Gamma\left(\frac{v}{3}\right)} \cdot z^{v-1} \cdot e^{-(\rho z)^3}, \tag{4}$$

where

$$\Gamma(x) = \int_0^\infty t^{x-1} e^{-t} dt, \tag{5}$$

where ρ and v are related parameters of the $F(z)$ distribution function; ρ is the scale parameter, kJ/mol; and v is the shape parameter. The analytical solution of the integral

Equation (1) with the gamma distribution (Equation (5)) provides a very simple expression for the overall adsorption θ:

$$\theta = \frac{n}{n_{max}} = \left[1 + \left(\frac{A}{\beta\rho}\right)^3\right]^{-\frac{V}{3}}. \tag{6}$$

According to Stoeckli et al. (2009) [58] research results on the relationship between adsorption characteristic energy and pore size of micropores, empirical formulas for x and z can be obtained as follows:

$$x = 15z + 2852.5z^3 + 0.014z^{-1} - 0.75, \tag{7}$$

and

$$J(x) = F(z)\frac{dz}{dx}. \tag{8}$$

The combination of Equations (4), (7) and (8) provides the following expression for the micropore size distribution $J(x)$:

$$J(x) = \frac{3\rho^v}{\Gamma\left(\frac{v}{3}\right)} \cdot \frac{z^{v-1} \cdot e^{-(\rho z)^3}}{15 + 8557.5z^2 - 0.014z^{-2}}. \tag{9}$$

According to Jaroniec (1993) [57], the following relationship between the micropore size distribution function $J(x)$ and the micropore dimension x is proposed:

$$lnJ(x) = (2 - D)lnx + C. \tag{10}$$

In summary, the steps to calculate the fractal dimension of micropores by using CO_2 adsorption data are as follows: First, the adsorption volume data are obtained by using CO_2 adsorption data and the DR equation; then, the parameters ρ and v are obtained by nonlinear fitting, z is calculated by using the pore size distribution data, and then Equation (9) is applied to obtain the pore size distribution function $J(x)$, Finally, lnx and $lnJ(x)$ are fitted by Equation (10) to obtain the slope of the logarithmic curve, and the fractal dimension D of micropores is further obtained.

Figure 7 shows the fitting curves of lnx and lnJ(x) of the CO_2 adsorption samples. The linear fitting slope, correlation coefficient (R^2) and fractal dimension of each sample are shown in the Table 4, and R^2 is greater than 0.91. The D values of all coal and rock samples are distributed between 2 and 3, which proves that they conform to fractal theory. The D values are distributed between 2.4441 and 2.6646, with an average of 2.603, which is basically the same as the results of Xiong et al. (2020) from their study on the coal of the Shanxi, Taiyuan and Benxi Formations in the eastern Ordos Basin (D value is 2.63–2.80, with an average value of 2.75) and the results of Li et al. (2019) from their study on lean coal and anthracite in the Qinshui Basin (D values are 2.38–2.63 and 2.31–2.68, respectively) [44,54,59].

4.5. Methane Adsorption Characteristics

Numerous HPMA studies on coal have shown that the Langmuir equation is the most straightforward and widely accepted model to describe the relationship between the gas pressure and the amount of CH_4 adsorbed on coal [60–63]. According to Langmuir theory, the outer surface of the coal sample is uniform in terms of energy, CH_4 molecules are absorbed only on the outer surface of the coal sample in the form of a monolayer covering, and the adsorption amount of CH_4 depends on the SSA of the outer surface [64,65]. The results show that the Langmuir volume (V_L) and Langmuir pressure (P_L) ranges of the seven selected coal samples are 24.46~32.83 m^3/t and 2.91~3.46 MPa, respectively (Figure 8). Among them, the V_L and P_L of PM-7 are the largest, and the corresponding SSA and PV of PM-7 are large, indicating that the micropores are well developed and provide a large amount of SSA. The V_L and P_L of PM-1 are the smallest, and the corresponding micro-SSA and micro-PV are small. Previous studies have shown that the adsorbent–adsorptive interaction in micropores is enhanced; thus, CH4 molecules are adsorbed only in the microporous structure in the form of micropore filling, and the adsorption capacity of CH_4 is limited by the micro-PV [35,38].

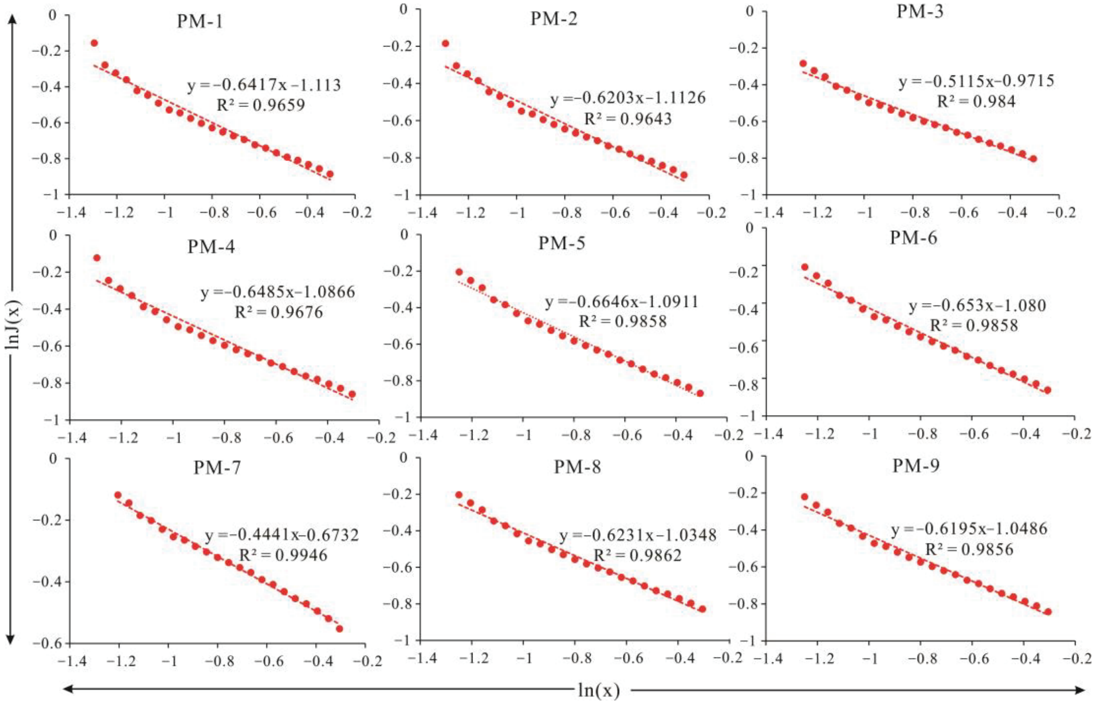

Figure 7. Fractal dimension fitting of the CO_2 adsorption data of coal samples.

Table 4. Fractal dimension of the CO_2 adsorption data of coal samples.

Samples	Fitting Equation	Slope	Fractal Dimension	Degree of Fitting
PM-1	$\ln J(x) = -0.6417\ln x - 1.113$	−0.6417	2.6417	0.9659
PM-2	$\ln J(x) = -0.6203\ln x - 1.1126$	−0.6203	2.6203	0.9643
PM-3	$\ln J(x) = -5115\ln x - 0.9715$	−0.5115	2.5115	0.984
PM-4	$\ln J(x) = -0.6485\ln x - 1.0866$	−0.6485	2.6485	0.9676
PM-5	$\ln J(x) = -0.6646\ln x - 1.0911$	−0.6646	2.6646	0.9858
PM-6	$\ln J(x) = -0.6530\ln x - 1.0800$	−0.653	2.653	0.9858
PM-7	$\ln J(x) = -0.4441\ln x - 0.6732$	−0.4441	2.4441	0.9946
PM-8	$\ln J(x) = -0.6231\ln x - 1.0348$	−0.6231	2.6231	0.9862
PM-9	$\ln J(x) = -0.6195\ln x - 1.0486$	−0.6195	2.6195	0.9856

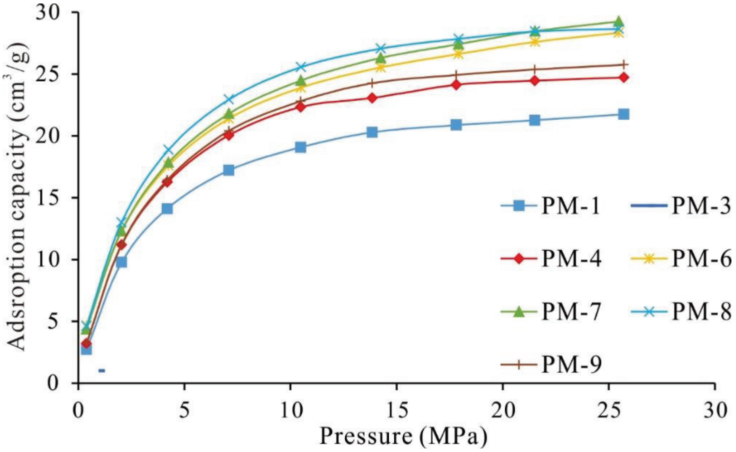

Figure 8. Isothermal adsorption curves of seven selected coal samples.

5. Discussion

5.1. Development and Pore Size Distribution of Micropores

LPA data can be calculated based on the NLDFT model to obtain the SSA, PV, PSD and other relevant information of the effective pore size range of 0.3~1.5 nm. LTA data can be calculated based on the NLDFT model to obtain the SSA, PV, PSD and other relevant information of the effective pore size measurement range of 1.06~77.7 nm. The overlap of the two models is 1.06~1.50 nm. Since the results of the two experiments are different in the overlap range [9], the arithmetic mean of the two models is used in this paper to determine the PV, SSA and PSD in the range of 1.06~1.50 nm. The PV, SSA and PSD of micropores were calculated by LTA and LPA (Figure 9a,b). The micro-PV and micro-SSA values of the coal samples range from 0.059 to 0.086 cm^3/g and from 204.380 to 282.415 m^2/g, respectively. These results show that the coal samples in the study area are extremely well developed, and the micro-PV in coal is several hundred times higher than that of marine shale in the Sichuan Basin and transitional facies in the Ordos Basin [44,54,63] but close to that of coal in eastern Yunnan [13].

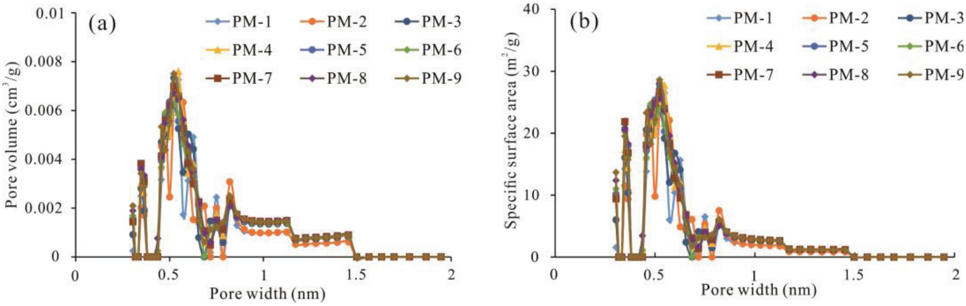

Figure 9. Distributions of the PV and SSA results of different sizes of micropores. (**a**) PV; (**b**) SSA.

Although the size range of micropores is very small, the PSD shows a certain regularity [9,20]. As shown in Figure 9a,b, the PSD has multiple peaks, which are mainly in the ranges of 0.3–0.4 nm, 0.4–0.7 nm and 0.7–2.0 nm. Among them, the degree of development of nanopores in the coal samples is similar. The PV and SSA of 0.4–0.7 nm are the most developed, accounting for more than 60% of the PV and SSA (Table 5 and Figure 10). The PV and SSA in the pore size range of 0.7–2.0 nm follow, and the PV and SSA in the pore size range of 0.3–0.4 nm are the least developed. The PSD of coal rock is similar to that of activated carbon and shale at pore sizes < 1.0 nm, but the PV and SSA of coal rock at pore sizes of 1.0–2.0 nm are significantly lower than those of activated carbon and higher than those of shale [9,56,66].

Table 5. PV and SSA results of different sizes of micropores.

Samples	**PV (cm^3/g)**			**SSA (m^2/g)**		
	<0.4 nm	**0.4–0.7 nm**	**0.7–2.0 nm**	**<0.4 nm**	**0.4–0.7 nm**	**0.7–2.0 nm**
PM-1	0.0047	0.039	0.0153	26.66	145.66	32.06
PM-2	0.0053	0.0416	0.0161	30.93	154.63	33.83
PM-3	0.0083	0.0449	0.021	48.15	167.48	43.05
PM-4	0.0073	0.044	0.0213	42.48	163.59	44
PM-5	0.0085	0.0435	0.0204	48.86	162.25	41.99
PM-6	0.0082	0.0414	0.0207	47.48	155.15	43.14
PM-7	0.0068	0.0482	0.0308	38.6	178.78	65.05
PM-8	0.0088	0.0465	0.0211	51.19	173.51	43.51
PM-9	0.0084	0.0443	0.0216	48.94	165.89	45.03

Note: PV = pore volume; SSA = specific surface area.

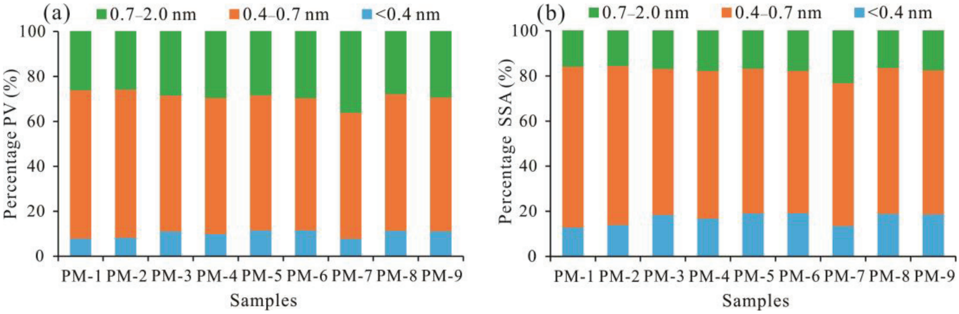

Figure 10. Distributions of different pore sizes acquired from CO_2/N_2 adsorption in terms of the (**a**) per-centage of pore volume and (**b**) percentage of SSA.

5.2. Proportion of Micropores in Total Pores

Micropores are widely distributed and abundant in coal and are usually the main space for gas adsorption and initial gas migration in coal seams. The qualitative and quantitative description of micropore development characteristics can play a very important role in determining the scale and form of gas migration in coal, so it is necessary to further analyse and study the development scale, pore morphology and pore structure of coal micropores.

To explore the contribution degree of micropores to the total PV and total SSA of pores in coal, the above established quantitative characterization method of pores in coal was used to calculate the total PV and total SSA of pores in the pore size range of 0.3–100 nm. The results are shown in Figure 11 and Table 6, and the proportions of nano-PVs and SSAs are different for different pore size ranges. The micro-PVs contribute 97.25%~99.03%, with an average of 98.18%. The meso-PV contributes 0.92%~2.31%, with an average of 1.60%. The macro-PV contributes 0.05%~0.44%, with an average of 0.21%. These results indicate that the contribution of PV in coal mainly originates from micropores, while the contribution of mesopores and macropores is relatively small. The micro-SSA contributes 99.79%~99.90%, with an average of 99.84%. The meso-SSA contributes 0.10%~0.21%, with an average of 0.16%. These results indicate that the contribution of SSA in coal mainly originates from the micropores, followed by the mesopores, and the contribution of the macropores can be ignored. As shown in Figure 10a,b, the distribution trend of PV and SSA of the same coal sample has a good consistency, and the pore SSA of the pore segment with PV development also develops. In coal sample, both PV and SSA are mainly contributed by micropores. These results indicate that the large number of micropores with large surface are the main adsorption and occurrence sites of CBM, as well as the effective channels for initial migration and diffusion of CBM after desorption, so it is necessary to further study and analyze their development and structural characteristics.

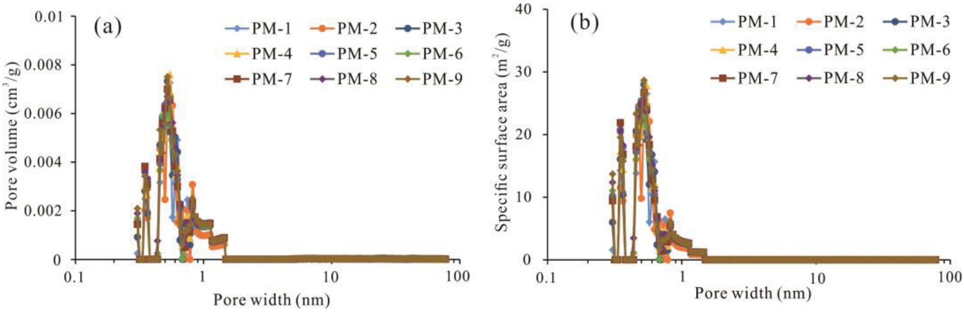

Figure 11. PV and SSA rates of change for all the pore sizes by using two models: (**a**) pore volume, (**b**) specific surface area.

Table 6. The PV, SSA and proportions of micro, meso-, and macropores in different coals.

Samples	PV (cm^3/g)			SSA (m^2/g)			PV Proportion (%)			SSA Proportion (%)		
	Micro	Meso	Macro	Micro	Meso	Macro	Micro	Meso	Macro	Micro	Meso	Macro
PM-1	0.0591	0.0011	0.0002	204.38	0.38	0.01	97.89	1.81	0.31	99.81	0.18	0.01
PM-2	0.063	0.0009	0.0001	219.39	0.34	0.01	98.35	1.48	0.17	99.83	0.16	0.01
PM-3	0.0742	0.001	0.0002	258.68	0.33	0.01	98.47	1.3	0.23	99.86	0.13	0.01
PM-4	0.0726	0.0014	0.0001	250.07	0.52	0.01	97.95	1.92	0.12	99.78	0.21	0.01
PM-5	0.0724	0.0017	0.0003	253.1	0.46	0.02	97.25	2.31	0.44	99.81	0.18	0.01
PM-6	0.0703	0.0013	0.0001	245.77	0.44	0.01	98.06	1.78	0.16	99.81	0.18	0.01
PM-7	0.0858	0.0008	0.0001	282.42	0.28	0.01	99.03	0.92	0.05	99.89	0.1	0.01
PM-8	0.0765	0.0011	0.0002	268.21	0.38	0.01	98.28	1.43	0.29	99.85	0.14	0.01
PM-9	0.0743	0.0011	0.0001	259.86	0.41	0.01	98.36	1.48	0.16	99.83	0.16	0.01

Note: PV = pore volume; SSA = specific surface area; Micro = micropores; Meso = mesopores; Macro = macropores.

5.3. Pore Structural Parameters and Fractal Dimensions

Previous studies on the factors influencing the pore structure of coal rock suggest that coal rank and coal composition (moisture, ash, vitrinite and mineral composition) are the main factors controlling PV and SSA [9,10,13,20]. As shown in Figure 12a, there is no significant correlation between the micro-PV and micro-SSA results of coal samples and vitrinite content. This finding differs from those of previous studies [10,18]; this difference may be due to the small number of samples and narrow reflectivity range between samples. The micro-PV and micro-SSA are negatively correlated with the mineral content in coal samples. There are two main aspects: on the one hand, the minerals can form pores; on the other hand, minerals can fill some of the existing pores, resulting in a decrease in the PV and SSA (Figure 12d), which is consistent with the results of previous studies [11,54]. The relationships between the micro-PV and micro-SSA and proximate analysis parameters (M_{ad} and A_d) are shown in Figure 12c,d, and there is no obvious relationship between the micro-PV or micro-SSA and M_{ad}. Due to the relatively low water content of coal and rock in the study area, there is no correlation between the micro-PV or micro-SSA and Mad. The micro-PV and micro-SSA show linear negative correlations with A_d. As A_d is a derivative of the minerals in coal, it is formed by complex reactions, such as de-composition and combination reactions [13]. The negative correlations of PV, SSA and A_d are consistent with that of mineral content, that is, the development of pores in these samples is controlled by both the organic matter and mineral content; and minerals can increase the value of A_d. When the minerals in coal fill in some of the pores, this leads to decreases in PV and SSA.

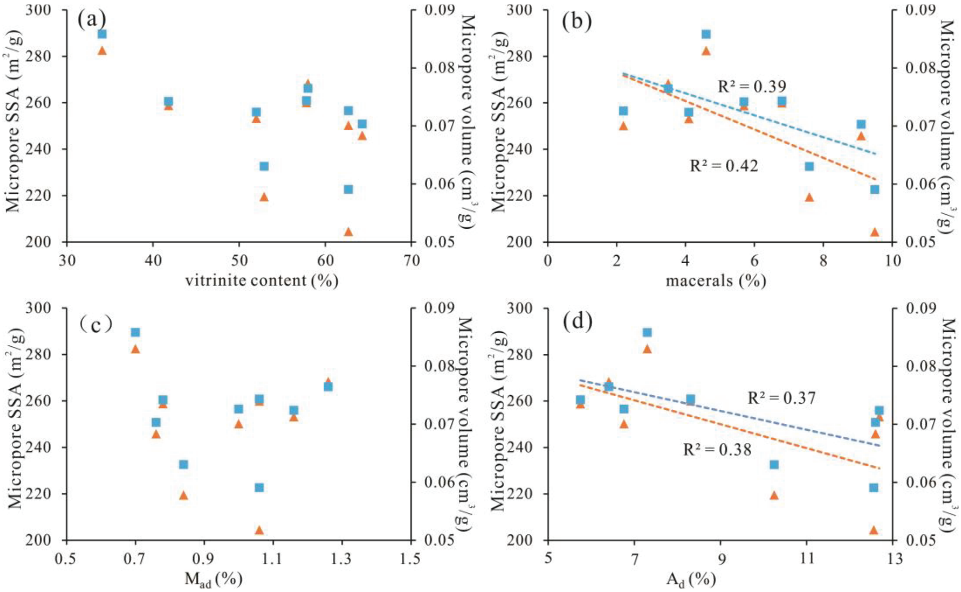

Figure 12. Relationships between the micro-PV, micro-SSA and (**a**) vitrinite content, and (**b**) macerals, (**c**) M_{ad}, and (**d**) V_d.

5.4. Influence on the Fractal Dimensions

To investigate the influence of the maceral composition and proximate analysis parameters on deep coal micropores fractal dimensions, the related plots are illustrated in Figure 13. The D value increases with increasing vitrinite content (Figure 13a), indicating that vitrinite has a positive effect on the fractal dimension. This result is consistent with the views of Clarkson and Bustin (2008) and Fu et al. (2017) [66–69]. The higher the content of vitrinite in the coal samples, the more micropores tend to develop. As the mineral component content increases, the D value shows no obvious trend of change (Figure 13b). Due to the relatively low mineral content of coal samples in the study area, there is no obvious correlation between the fractal dimension of micropores and mineral components. There is a weak positive correlation between the D value and M_{ad} (Figure 13c), which may be because a higher M_{ad} of the coal sample indicates that the water molecules in the gas–liquid phase form tension on the pore surface of the coal, thus exerting a great influence on the fractal dimension [51,70]. The positive correlation between D and A_d is weak (Figure 13d); as A_d increases, the coal pore structure becomes complicated. Yao et al. (2012) believed that ash in coal would fill the pores, resulting in the enhancement of the heterogeneity of the coal pore structure and an increase in the fractal dimension [24]. In conclusion, due to the relatively low mineral content, its influence on the fractal dimension of pores is limited. The influences of A_d and M_{ad} on the fractal dimension of coal pores are not obvious, indicating that the factors controlling the fractal dimension of deep coal pores are more complex and may be affected by many factors. The factors controlling the pore fractal dimension of deep coal rocks need to be studied in more detail in the future.

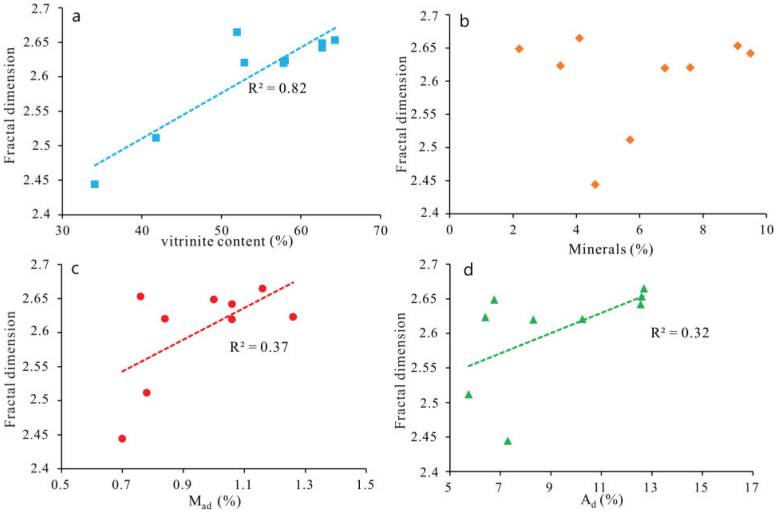

Figure 13. Relationship between the micropore fractal dimension and vitrinite content (**a**), and minerals (**b**), d M_{ad} (**c**) and A_d (**d**).

This study shows that the pores of coal are mainly micropores, the micro-PV and micro-SSA contribute more than 90% of the total pores, and the mesopores and macropores are rarely or almost undeveloped [22,71]. Mesopores and macropores are mainly developed in shale pores, occupying approximately 90% of the total PV and 60% of the total SSA [10,72]. Figure 14 shows the relationship between the fractal dimension (D) and pore structure parameters. D has a negative linear correlation with the micro-SSA and micro-PV, but the correlation is poor, which may be caused by the high heterogeneity of coal and rock samples. This result is consistent with coal sample data obtained by Xiong et al. (2020). The fractal dimension of micropores decreases with the increase in the micro-SSA and micro-PV, indicating that the smaller the storage space and SSA of pores, the stronger the homogeneity of coal and rock, and the more complex the pore structure.

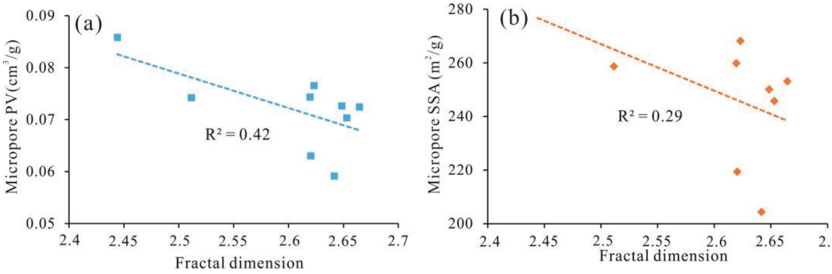

Figure 14. Relationships between the micropore fractal dimension and (**a**) micro-PV and (**b**) micro-SSA.

5.5. Adsorption Capacity of Micropores

CBM is mainly retained on the inner surfaces of coal micropores in the adsorbed state, so the SSA of coal is of great significance to its adsorption capacity and enrichment characteristics [7,20]. According to the basic physical adsorption theory of solid surfaces, the adsorption capacity of an object is proportional to the SSA [9]. Zhong et al. (2002)

conducted LTA and methane adsorption experiments on coal samples and determined that the adsorption capacity of coal to CH_4 was positively correlated with the total PV, total SSA and micro-SSA [73]. Sang et al. (2003) determined that the SSA of coal was negatively correlated with the adsorption capacity [74]. Chen et al. (2017) discovered a strong linear positive correlation between CO_2-SSA and V_L [20]. Regarding the cause of the difference, previous researchers have used different determination and precision methods of the SSA of coal [9,20]. Figure 15 shows scatter diagrams of the correlations between the V_L and the micro-PV and micro-SSA. V_L has an obvious positive linear correlation with micro-PV and micro-SSA (Figure 15b). This correlation shows that micropores have an obvious influence on the adsorption gas of coal and rock.

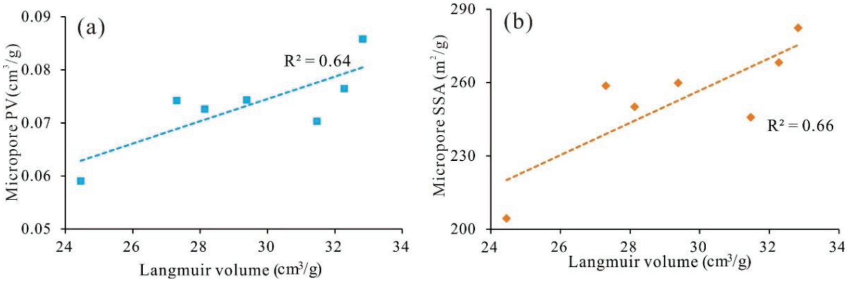

Figure 15. Relationships between the high-pressure CH_4 adsorption capacities and (**a**) micro-PV and (**b**) micro-SSA.

Table 6 shows that the contribution of the micro-SSA to the total SSA reaches 99%, indicating that methane is mainly absorbed in the micropores of a coal reservoir and that the gas adsorption capacity of a coal reservoir depends on the total PV and distribution frequency of pores in this part [20]. In addition, it is known that LPA absorbs carbon dioxide with a smaller molecular diameter than N_2 as the adsorbent, not only to avoid the disadvantage of carbon dioxide not being completely adsorbed when the micropore size is close to the molecular size of nitrogen, but also quickly reach adsorption equilibrium [20,75]; therefore, the SSA and PV of micropore can be accurately measured. This study shows that the combination of LPA and LTA can more accurately reveal the pore structure and adsorption capacity of coal reservoirs than either method, especially for micropores <2 nm in size.

6. Conclusions

This paper uses deep coal samples of the Daning–Jixian block from the eastern margin of the Ordos Basin as the research object. Using LPA and LTA experiments, FE-SEM and other pore structure analysis methods, a research method for the precise determination and quantitative characterization of micropores in coal is proposed. Considering fractal theory, the factors affecting the fractal dimension of micropores are discussed from the perspective of the physical properties of coal samples. HPMA experiments are carried out to explore the gas adsorption capacity of micropores. The following conclusions are drawn:

(1) The LPA method based on the NLDFT model is the best method to measure and calculate the PV, SSA and PSD corresponding to the pore size range from 0.3~1.5 nm, as validated by comparing the results of the LPA and LTA experiments and different calculation models. Combining the LPA method with the LTA method based on the NLDFT model, all micropores smaller than 2.0 nm can be measured.

(2) The pores developed in deep coal rocks are mainly organic pores, InterP pores and microfractures, and the pore size distribution patterns of different coal samples have multiple peaks, among which micropores are the main contributors to the total PV and total SSA, with the micro-PV ranging from 0.059 to 0.086 cm^3/g and the micro-SSA ranging from 204.380 to 282.415 m^2/g.

(3) Different coal samples in the study area have great differences in the degree of micropore development, but the pore distribution characteristics are basically the same. The PV and SSA of the 0.4–0.7 nm pore size range are the most developed, accounting for more than 60%. Micropore structure development is mainly affected by the maceral and mineral components. With increasing mineral content and A_{d}, micro-PV and micro-SSA decrease rapidly.

(4) The micropore fractal dimension (D) is calculated based on LPA data. The D values range from 2.4441 to 2.6646, with an average of 2.603. The relationship between the D value and mineral content is not obvious, but D is positively correlated with vitrinite content, M_{ad} and A_{d}.

(5) The contribution rate of micro-SSA to total SSA of coal samples in the study area reaches 99%, and V_L is linearly positively correlated with micro-SSA, which shows that the adsorption capacity of coal reservoir depends on the development degree of micro-SSA.

Author Contributions: Conceptualization, T.W. and Z.D.; methodology, T.W. and H.H.; software, T.W.; validation, T.W., Z.D. and H.H.; formal analysis, T.W.; investigation, T.W. and F.T.; resources, Z.D.; data curation, Z.D.; writing—original draft preparation, T.W.; writing—review and editing, T.W.; visualization, T.W.; supervision, F.T.; project administration, F.T.; funding acquisition, Z.D. All authors have read and agreed to the published version of the manuscript.

Funding: This research was jointly supported by the Research and Experiment on Scale Benefit Development Technology of Deep Coalbed Methane in Daning-Jixian (Grant No. 2022KT1401) and In Situ Bio-gasification Mechanism and Experimental Study of Coalbed Methane (Grant No. 2021DJ2302). We thank PetroChina Exploration and Development Research Institute and PetroChina Coalbed Methane Company Limited for picking up the samples.

Data Availability Statement: The data used to support the findings of this study are included within the article.

Acknowledgments: We thank PetroChina Exploration and Development Research Institute and PetroChina Coalbed Methane Company Limited for picking up the samples.

Conflicts of Interest: The authors declare no conflict of interest.

References

1. Blacher, S.; Sahouli, B.; Heinrichs, B.; Lodewyckx, P.; Pirard, R.; Pirard, J.P. Micropore size distributions of activated carbons. *Langmuir* **2000**, *16*, 6754–6756. [CrossRef]
2. Tao, S.; Chen, S.; Tang, D.; Zhao, X.; Xu, H.; Li, S. Material composition, pore structure and adsorption capacity of low-rank coals around the first coalification jump: A case of eastern Junggar Basin, China. *Fuel* **2018**, *211*, 804–815. [CrossRef]
3. Sing, K.S.W.; Everett, D.H.; Haul, R.A.W. Reporting physisorption data for gas/solid systems with special reference to the determination of surface area and porosity. *Pure Appl. Chem.* **1985**, *57*, 603–619. [CrossRef]
4. Cui, X.; Bustin, R.M.; Dipple, G. Selective transport of CO_2, CH_4, and N_2 in coals: Insights from modeling of experimental gas adsorption data. *Fuel* **2004**, *83*, 293–303. [CrossRef]
5. Groen, J.C.; Peffer, L.A.; Pérez-Ramırέz, J. Pore size determination in modified microand mesoporous materials. Pitfalls and limitations in gas adsorption data analysis. *Microporous Mesoporous Mater.* **2003**, *60*, 1–17. [CrossRef]
6. Hou, S.; Wang, X.; Wang, X.; Yuan, Y.; Pan, S.; Wang, X. Pore structure characterization of low volatile bituminous coals with different particle size and tectonic deformation using low pressure gas adsorption. *Int. J. Coal Geol.* **2017**, *183*, 1–13. [CrossRef]
7. Hu, B.; Cheng, Y.; He, X.; Wang, Z.; Wang, L.; Jiang, Z.; Wang, C.; Wei, L.; Wang, L. New insights into the CH_4 adsorption capacity of coal based on microscopic pore properties. *Fuel* **2019**, *262*, 116675. [CrossRef]
8. Li, C.; Jiang, B.; Ju, W.; Cheng, G.; Song, Y. Characteristics of tectonic deformation in the Daning-Jixian region, eastern Ordos Basin: Implications for the exploration and development of coalbed methane. *Energy Explor. Exploit.* **2019**, *37*, 907–921. [CrossRef]
9. Song, D.; Ji, F.; Li, Y.; Zhao, H.; Song, B.; He, K. Heterogeneous development of micropores in medium-high rank coal and its relationship with adsorption capacity. *Int. J. Coal Geol.* **2020**, *226*, 103497. [CrossRef]
10. Ma, X.; Guo, S.; Shi, D.; Zhou, Z.; Liu, G. Investigation of pore structure and fractal characteristics of marine-continental transitional shales from Longtan Formation using MICP, gas adsorption, and NMR (Guizhou, China). *Mar. Pet. Geol.* **2019**, *107*, 555–571. [CrossRef]
11. Li, G.; Qin, Y.; Wu, M.; Zhang, B.; Wu, X.; Tong, G.; Liu, J. The pore structure of the transitional shale in the Taiyuan formation, Linxing area, Ordos Basin. *J. Pet. Sci. Eng.* **2019**, *189*, 106183. [CrossRef]
12. Lu, W.; Zhuang, Z.; Zhang, W.; Zhang, C.; Song, S.; Wang, R.; Kong, B. Study on the Pore and Crack Change Characteristics of Bituminous Coal and Anthracite after Different Temperature Gradient Baking. *Energy Fuels* **2021**, *35*, 19448–19463. [CrossRef]

13. Zhang, S.; Wu, C.; Liu, H. Comprehensive characteristics of pore structure and factors influencing micropore development in the Laochang mining area, eastern Yunnan, China. *J. Pet. Sci. Eng.* **2020**, *190*, 107090. [CrossRef]
14. Wei, Y.; Li, J.; Du, Y.; Lu, S.; Li, W.; Yang, J.; Feng, W.; Song, Z.; Zhang, Y. Classification Evaluation of Gas Shales Based on High-Pressure Mercury Injection: A Case Study on Wufeng and Longmaxi Formations in Southeast Sichuan, China. *Energy Fuels* **2021**, *35*, 9382–9395. [CrossRef]
15. Chalmers, G.R.; Bustin, R.M.; Power, I.M. Characterization of gas shale pore systems by porosimetry, pycnometry, surface area, and field emission scanning electron microscopy/transmission electron microscopy image analyses: Examples from the Barnett, Woodford, Haynesville, Marcellus, and Doig units. *AAPG Bull.* **2012**, *96*, 1099–1119.
16. Zhou, S.; Liu, D.; Cai, Y.; Karpyn, Z.; Yao, Y. Comparative analysis of nanopore structure and its effect on methane adsorption capacity of Southern Junggar coalfield coals by gas adsorption and FIB-SEM tomography. *Microporous Mesoporous Mater.* **2018**, *272*, 117–128. [CrossRef]
17. Li, Z.; Liu, D.; Cai, Y.; Wang, Y.; Teng, J. Adsorption pore structure and its fractal characteristics of coals by N_2 adsorption/desorption and FESEM image analyses. *Fuel* **2019**, *257*, 116031. [CrossRef]
18. Wang, X.; Jiang, Z.; Shu, S.; Chang, J.; Zhu, L.; Li, X.; Li, J. Full-Scale Pore Structure and Fractal Dimension of the Longmaxi Shale from the Southern Sichuan Basin: Investigations Using FE-SEM, Gas Adsorption and Mercury Intrusion Porosimetry. *Minerals* **2019**, *9*, 3–26. [CrossRef]
19. Mastalerz, M.; Drobniak, A.; Rupp, J. Meso-and micropore characteristics of coal lithotypes: Implications for CO_2 adsorption. *Energy Fuels* **2008**, *22*, 4049–4061. [CrossRef]
20. Chen, S.; Tao, S.; Tang, D.; Xu, H.; Li, S.; Zhao, J.; Jiang, Q.; Yang, H. Pore structure characterization of different rank coals using N_2 and CO_2 adsorption and its effect on CH_4 adsorption capacity: A case in Panguan Syncline, Western Guizhou, China. *Energy Fuels* **2017**, *31*, 6034–6044. [CrossRef]
21. Li, Y.; Song, D.; Liu, S.; Pan, J. Characterization of Ultra-Micropores and Analysis of Their Evolution in Tectonically Deformed Coals by Low-Pressure CO_2 Adsorption, XRD and HRTEM Techniques. *Energy Fuels* **2020**, *34*, 9436–9449. [CrossRef]
22. Han, W.; Zhou, G.; Gao, D.; Zhang, Z.; Wei, Z.; Wang, H.; Yang, H. Experimental analysis of the pore structure and fractal characteristics of different metamorphic coal based on mercury intrusionnitrogen adsorption porosimetry. *Powder Technol.* **2020**, *362*, 386–398. [CrossRef]
23. Ma, Y.; Wang, M.; Zhao, X.; Dai, X.; He, Y. Study of the Microstructural Characteristics of Low-Rank Coal under Different Degassing Pressures. *Energies* **2022**, *15*, 3691. [CrossRef]
24. Yao, Y.; Liu, D. Comparison of low-field NMR and mercury intrusion porosimetry in characterizing pore size distributions of coals. *Fuel* **2012**, *95*, 152–158. [CrossRef]
25. Okolo, G.N.; Everson, R.C.; Neomagus, H.W.J.P.; Roberts, M.J.; Sakurovs, R. Comparing the porosity and surface areas of coal as measured by gas adsorption, mercury intrusion and SAXS techniques. *Fuel* **2015**, *141*, 293–304. [CrossRef]
26. Zhao, Y.; Sun, Y.; Liu, S.; Chen, Z.; Yuan, L. Pore structure characterization of coal by synchrotron radiation nano-CT. *Fuel* **2018**, *215*, 102–110. [CrossRef]
27. Yu, S.; Bo, J.; Meijun, Q. Molecular dynamic simulation of self-and transport diffusion for $CO_2/CH_4/N_2$ in low-rank coal vitrinite. *Energy Fuel* **2018**, *32*, 3085–3096. [CrossRef]
28. Amarasekera, G.; Scarlett, M.J.; Mainwaring, D.E. Micropore size distributions and specific interactions in coals. *Fuel* **1995**, *74*, 115–118. [CrossRef]
29. Clarkson, C.R.; Bustin, R.M. Variation in micropore capacity and size distribution with composition in bituminous coal of the Western Canadian Sedimentary Basin: Implications for coalbed methane potential. *Fuel* **1996**, *75*, 1483–1498. [CrossRef]
30. Centeno, T.A.; Stoeckli, F. The assessment of surface areas in porous carbons by two model-independent techniques, the DR equation and DFT. *Carbon* **2010**, *48*, 2478–2486. [CrossRef]
31. Landers, J.; Gor, G.Y.; Neimark, A.V. Density functional theory methods for characterization of porous materials. *Colloids Surf. A Physicochem. Eng. Asp.* **2013**, *437*, 3–32. [CrossRef]
32. Zhu, H.; Ju, Y.; Lu, W.; Han, K.; Qi, Y.; Neupane, B. The characteristics and evolution of micro-nano scale pores in shales and coals. *J. Nanosci. Nanotechnol.* **2017**, *17*, 6124–6138. [CrossRef]
33. Guo, S.B.; Mao, W.J. Division of diagenesis and pore evolution of a Permian Shanxi shale in the Ordos Basin, China. *J. Pet. Sci. Eng.* **2019**, *182*, 920–4105. [CrossRef]
34. Kuang, L.; Dong, D.; He, W.; Wen, S.; Sun, S.; Li, S.; Qiu, Z.; Liao, X.; Li, Y.; Wu, J.; et al. Geological characteristics and development potential of transitional shale gas in the east margin of the Ordos Basin, NW China. *Pet. Explor. Dev.* **2020**, *47*, 471–482. [CrossRef]
35. Liu, Y.; Zhu, Y.; Liu, S.; Chen, S.; Li, W.; Wang, Y. Molecular structure controls on micropore evolution in coal vitrinite during coalification. *Int. J. Coal Geol.* **2018**, *199*, 19–30. [CrossRef]
36. Liu, C.; Zhong, J.; Wang, X.; Cao, M.; Wu, J.; Zhang, S.; Wu, X.; Sun, N.; Du, Y.; Liu, Y. Petrological characteristics and the impact of mineral content on reservoir quality in coal-bearing strata of Linxing area, eastern margin of Ordos Basin, China. *Energy Explor. Exploit.* **2018**, *36*, 872–894. [CrossRef]
37. Zhao, L.P.; Lu, J.; Li, X.; Li, Y.; He, Q.; Ma, Z. Logging calculation method and application of geochemical parameters of source rocks with different lithologies in marine-continental transitional facies in Ordos Basin, China. *Arab. J. Geosci.* **2022**, *15*, 1111. [CrossRef]

38. Zhang, M.; Fu, X. Characterization of pore structure and its impact on methane adsorption capacity for semi-anthracite in Shizhuangnan Block, Qinshui Basin. *J. Nat. Gas Sci. Eng.* **2018**, *53*, 370–384. [CrossRef]
39. Loucks, R.G.; Reed, R.M.; Ruppel, S.C.; Jarvie, D.M. Morphology, Genesis, and Distribution of Nanometer-scale Pores in Siliceous Mudstones of the Mississippian Barnett Shale. *J. Sediment. Res.* **2009**, *79*, 848–861. [CrossRef]
40. Wang, Y.; Liu, D.; Cai, Y.; Li, X. Variation of petrophysical properties and adsorption capacity in different rank coals: An experimental study of coals from the Junggar, Ordos and Qinshui Basins in China. *Energies* **2019**, *12*, 986. [CrossRef]
41. Ravikovitch, P.I.; Haller, G.L.; Neimark, A.V. Density functional theory model for calculating pore size distributions: Pore structure of nanoporous catalysts. *Adv. Colloid Interface Sci.* **1998**, *76*, 203–226. [CrossRef]
42. Mahamud, M.; Lopez, O.; Pis, J.J.; Pajares, J.A. Textural characterization of coals using fractal analysis. *Fuel Process. Technol.* **2003**, *81*, 127–142. [CrossRef]
43. Thommes, M.; Kaneko, K.; Neimark, A.V.; Olivier, J.P.; Rodriguez-Reinoso, F.; Rouquerol, J. Physisorption of gases, with special reference to the evaluation of surface area and pore size distribution (IUPAC Technical Report). *Pure Appl. Chem.* **2015**, *87*, 1051–1069. [CrossRef]
44. Li, Y.; Wang, Z.; Pan, Z.; Niu, X.; Meng, S. Pore structure and its fractal dimensions of transitional shale: A cross-section from east margin of the Ordos Basin, China. *Fuel* **2019**, *241*, 417–431. [CrossRef]
45. Dubinin, M.M. Adsorption in micropores. *J. Colloid Interface Sci.* **1967**, *23*, 487–499. [CrossRef]
46. Marsh, H.; Rand, B. The characterization of microporous carbons by means of the Dubinin-Radushkevich equation. *J. Colloid Interface Sci.* **1970**, *33*, 101–116. [CrossRef]
47. Evans, R.; Marconi, U.M.B.; Tarazona, P. Capillary condensation and adsorption in cylindrical and slit-like pores. *J. Chem. Soc.* **1986**, *82*, 1763–1787. [CrossRef]
48. Gelb, L.D.; Gubbins, K.E.; Radhakrishnan, R.; Sliwinska-Bartkowiak, M. Phase separation in confined systems. *Rep. Prog. Phys.* **1999**, *62*, 1573–1659. [CrossRef]
49. El-Merraoui, M.; Aoshima, M.; Kaneko, K. Micropore size distribution of activated carbon fiber using the density functional theory and other methods. *Langmuir* **2000**, *16*, 4300–4304. [CrossRef]
50. Ji, X.; Song, D.; Ni, X.; Li, Y.; Zhao, H. Coal Matrix Deformation and Pore Structure Change in High-Pressure Nitrogen Replacement of Methane. *Energies* **2018**, *11*, 2–18. [CrossRef]
51. Wei, Z.; Fu, X.; Hao, M.; Li, G.; Pan, J.; Niu, Q.; Zhou, H. Experimental insights into the adsorption-desorption of CH_4/N_2 and induced strain for medium-rank coals. *J. Petrol. Sci. Eng.* **2021**, *204*, 108705.
52. Jagiello, J.; Thommes, M. Comparison of DFT characterization methods based on N2, Ar, CO2, and H2 adsorption applied to carbons with various pore size distributions. *Carbon* **2004**, *42*, 1227–1232. [CrossRef]
53. Pan, J.; Wang, K.; Hou, Q.; Niu, Q.; Wang, H.; Ji, Z. Micro-pores and fractures of coals analysed by field emission scanning electron microscopy and fractal theory. *Fuel* **2016**, *164*, 277–285. [CrossRef]
54. Zhang, J.; Li, X.; Wei, Q.; Sun, K.; Zhang, G.; Wang, F. Characterization of Full-Sized Pore Structure and Fractal Characteristics of Marine–Continental Transitional Longtan Formation Shale of Sichuan Basin, South China. *Energy Fuels* **2017**, *31*, 10490–10504. [CrossRef]
55. Jaroniec, M.; Lu, X.; Madey, R.; Choma, J. Evaluation of structural heterogeneities and surface irregularities of microporous solids. *Mater. Chem. Phys.* **1990**, *26*, 87–97. [CrossRef]
56. Machin, W.D. Temperature dependence of hysteresis and the pore size distributions of two mesoporous adsorbents. *Langmuir* **1994**, *10*, 1235–1240. [CrossRef]
57. Jaroniec, M.; Gilpin, R.K.; Choma, J. Correlation between microporosity and fractal dimension of active carbons. *Carbon* **1993**, *31*, 325–331. [CrossRef]
58. Stoeckli, H.F.; Ballerini, L.; Bernardini, S.D. On the evolution of micropore widths and areas in the course of activation. *Carbon* **2009**, *27*, 501–502. [CrossRef]
59. Xiong, Y.; Zhou, S.; Jiao, P.; Yang, M.; Zhou, J.; Wei, W.; Cai, J. Fractal analysis of micropore structures in coal and shale based on lowtemperature CO_2 adsorption. *Nat. Gas Geosci.* **2020**, *31*, 1028–1040.
60. Reucroft, P.J.; Sethuraman, A.R. Effect of pressure on carbon dioxide induced coal swelling. *Energy Fuels* **1987**, *1*, 72–75. [CrossRef]
61. Clarkson, C.R.; Bustin, R.M. The effect of pore structure and gas pressure upon the transport properties of coal: A laboratory and modeling study. 1. Isotherms and pore volume distributions. *Fuel* **1999**, *78*, 1345–1362. [CrossRef]
62. Li, J.; Li, B.; Ren, C.; Yang, K.; Zhang, Y. Characterization of Methane Adsorption Behavior on Wet Shale under Different Temperature Conditions. *Energy Fuels* **2020**, *34*, 2832–2848. [CrossRef]
63. Yang, Y.; Liu, S.; Zhao, W.; Wang, L. Intrinsic relationship between Langmuir sorption volume and pressure for coal: Experimental and thermodynamic modeling study. *Fuel* **2019**, *241*, 105–117. [CrossRef]
64. Langmuir, I. The adsorption of gases on plane surfaces of glass, mica and platinum. *J. Am. Chem. Soc.* **1918**, *40*, 1361–1403. [CrossRef]
65. Mosher, K.; He, J.; Liu, Y.; Rupp, E.; Wilcox, J. Molecular simulation of methane adsorption in micro-and mesoporous carbons with applications to coal and gas shale systems. *Int. J. Coal Geol.* **2013**, *109*, 36–44. [CrossRef]
66. Jia, A.; Hu, D.; He, S. Variations of Pore Structure in Organic-Rich Shales with Different Lithofacies from the Jiangdong Block, Fuling Shale Gas Field, SW China: Insights into Gas Storage and Pore Evolution. *Energy Fuels* **2020**, *34*, 12457–12475. [CrossRef]

67. Zhou, L.; Qian, Y.; Zhang, L.; Lan, X.; Wu, Y.; Wang, Q.; Zhang, G. Seismic prediction of oolitic beach thin-bed reservoir based on favorable facies belt constraints: Taking the second member of Feixianguan Formation in Jiulongshan area, Northwest Sichuan, China. *J. Nat. Gas Geosci.* **2021**, *6*, 329–344. [CrossRef]
68. Bustin, R.M.; Bustin, A.M.M.; Cui, X.; Ross, D.J.K.; Murthy, P.V.S. Impact of shale properties on pore structureand storage characteristics. In Proceedings of the Shale Gas Production Conference, Fort Worth, TX, USA, 16–18 November 2008.
69. Fu, H.J.; Tang, D.Z.; Xu, T.; Tan, S.; Yin, Z.Y.; Chen, B.L.; Zhang, C.; Wang, L.L. Characteristics of pore structure and fractural dimension of low-rank coal: A case study of Lower Jurassic Xishayao coal in the southern Junggar Basin, NW China. *Fuel* **2017**, *193*, 254–264. [CrossRef]
70. Shang, Z.; Dong, L.; Niu, L.; Shi, H. Adsorption of Methane, Nitrogen, and Carbon Dioxide in Atomic-Scale Fractal Nanopores by Monte Carlo Simulation I: Single-Component Adsorption. *Energy Fuels* **2019**, *33*, 10457–10475. [CrossRef]
71. Zhang, C.; Yao, Y.; Dong, Y. Heterogeneous development of micro- and meso-pores in shale kerogen: New insights from chemical structure analysis. *J. Nat. Gas Sci. Eng.* **2022**, *102*, 104552. [CrossRef]
72. Sun, Y.; Guo, S. Characterization of whole-aperture pore structure and its effect on methane adsorption capacity for transitional shales. *Energy Fuels* **2018**, *32*, 3176–3188. [CrossRef]
73. Zhong, L.W.; Zhang, H.; Yuan, Z.R.; Lei, C.L. Influence of specific pore area and pore volume of coal on adsorption capacity. *Coal Geol. Explor.* **2002**, *30*, 26–28.
74. Sang, S.X.; Qin, Y.; Guo, X.B.; Chen, Y.H. Storing characteristics of Jurassic coalbed gas in Junggar and Tuha Basins. *Geol. J. China Univ.* **2003**, *9*, 365–372.
75. Thommes, M.; Cychosz, K.A. Physical adsorption characterization of nanoporous materials: Progress and challenges. *Adsorption* **2014**, *20*, 233–250. [CrossRef]

applied sciences

Article

An Experimental Investigation on Mechanical Properties and Failure Characteristics of Layered Rock Mass

Yongxiang Zheng [1,2,3], Tongjing Zhang [3,*], Haotian Yang [3], Wei Wang [1,2,3], Qinghe Niu [1,2,3] and Haiyang Wei [3]

[1] Key Laboratory of Road and Railway Engineering Safety Guarantee, Ministry of Education, Shijiazhuang Tiedao University, Shijiazhuang 050043, China; zhengyx@stdu.edu.cn (Y.Z.); wangweiuuu@163.com (W.W.); qinghniu@163.com (Q.N.)
[2] Hebei Metal Mine Safe and Efficient Mining Technology Innovation Center, Shijiazhuang 050043, China
[3] School of Civil Engineering, Shijiazhuang Tiedao University, Shijiazhuang 050043, China; Yanghaotian1125@outlook.com (H.Y.); 13462565425@163.com (H.W.)
* Correspondence: 1202101309@student.stdu.edu.cn

Abstract: Layered rock mass is a common rock mass structure with diverse forms and complex mechanical properties. Three types of composite layered rock mass prepared using sandstone and shale can be divided into sandwiched type, interbedded type and superimposed type. The total height of the combined rock mass is 50 mm, which is a cylinder composed of sandstone and shale with a diameter of 25 mm and different thickness. Uniaxial compression tests on sandstone, shale and combined rock mass were performed. The results show that, with the increase in the content of soft components, the compressive strength and elastic modulus of the combined rock mass tend to decrease. The mechanical properties of the superimposed rock mass will be between the two components and close to the soft component in numerical value. The mechanical properties of sandwiched rock mass are obviously affected by the properties of the sandwiched rock. When the content of the components is consistent, interbedded rock mass often shows higher strength and elastic modulus. Compared with other rock mass, interbedded rock mass has more stable mechanical properties. The stress–strain curve can be divided into the compaction stage, elastic stage, plastic development stage and post-fracture stage. The composition content of the rock mass plays a decisive role in the compaction stage. The failure modes are mainly shear failure and tensile failure. With the increase in soft rock content, the failure degree of soft rock is gradually weakened, and the failure modes show a trend from tensile failure to shear failure. The experimental results provide theorical guidance for underground engineering construction.

Keywords: layered rock mass; combination rock; uniaxial compression experiment; mechanical properties; failure characteristic

Citation: Zheng, Y.; Zhang, T.; Yang, H.; Wang, W.; Niu, Q.; Wei, H. An Experimental Investigation on Mechanical Properties and Failure Characteristics of Layered Rock Mass. *Appl. Sci.* **2023**, *13*, 7537. https://doi.org/10.3390/app13137537

Academic Editor: Tiago Miranda

Received: 25 May 2023
Revised: 21 June 2023
Accepted: 25 June 2023
Published: 26 June 2023

1. Introduction

In recent years, with the depletion of fossil energy worldwide and the rapid development of guidance technology, more and more underground mining projects have shifted from shallow excavation to deeper excavation. The research on the mechanical properties of layered rock has been gradually paid attention to and intensified [1]. As early as 1967, Wager [2] put forward the concept of layered rock mass in the study of igneous rock, which had an important influence on geological research. Subsequently, many scholars [3–8] have conducted a lot of studies on the properties of single-layered rock mass such as shale and sandstone. However, in deep engineering, more and more problems of layered rock masses, which are different from general rock mechanics, have been found. Additionally, these rock masses often have various shapes and complex mechanical properties. It brings challenges to underground engineering construction such as hydraulic fracturing, oil and gas exploitation, underground excavation, and so on [9–12]. Therefore, it is of great significance to explore the mechanical properties of layered rock for underground engineering construction.

In 1981, Duffault [13] introduced the term of sandwiched rock mass when classifying rock mass. According to the research progress, the layered rock mass can be divided into soft sandwiched rock mass, hard sandwiched rock mass, interbedded rock mass and so on. The current studies into layered rock mainly focuses on mechanical properties and deformation mechanism. In terms of mechanical properties, Chen et al. [14] used coal and oil shale with high strength and low elastic modulus to prepare the sandwich type and superposition type combination rock samples. Through uniaxial compression test, they found that the difference in the mechanical properties of coal and oil shale affected the stress state near the interface, resulting in the increase in coal strength and the decrease in oil shale strength. Sun et al. [15] found that, based on mineral composition, the uniaxial compressive strength and triaxial compression tests of shale reservoir, it was found that the mechanical properties of the shale reservoir in parallel bedding direction are less affected by lithology under uniaxial conditions. There is an increase in the compressive strength of rock, with a higher confinement in triaxial tests. The change in stress state is an important factor leading to the change in rock strength in the sample. Later, many scholars proved that the mechanical properties of combined rock mass are closely related to the content and strength of components. Wang et al. [16] studied the uniaxial compressive strength of the sandwich rock mass with different strength ratios of original materials. The relationship between the strength difference of lithological units, the percentage of soft rock and uniaxial compressive strength in soft rock and hard rock with alternating layered rock mass is revealed. Huang et al. [17] studied the influence of water pressure on the mechanical properties and permeability of layered rock mass through triaxial compression tests under different water pressures and low confining pressures. The results show that the increase in water pressure reduces the peak strength of layered rock mass, but accelerates the expansion of cracks and significantly enhances the peak permeability of layered rock mass. Li et al. [18] conducted uniaxial compression tests on combination rock samples to reveal their mechanical properties. The conclusion is that combination rocks with thick interlayers are more likely to fail than combination rocks with thin interlayers. Li et al. [19] prepared superimposed and sandwiched rock masses using coal and rock coal bi-material samples. Uniaxial compression tests showed that the strength of coal determines the overall strength of the bi-material sample. Lisanne et al. [20] studied the influence of the difference in rock strength between adjacent rock strata on cracks. The results show that the increase in strength difference can prevent the crack from expanding into a stronger layer. Li et al. [21] analyzed the stress–strain curve characteristics, strength characteristics and failure characteristics of interbedded sandstones with different sandwiched thicknesses under uniaxial and conventional triaxial compression conditions. The research results show that, with the increase in sandwiched thickness, the uniaxial compressive strength of sandwiched sandstones first decreases first and then increases. In terms of deformation, Zhang et al. [22] proposed the constitutive relation and elastic parameter calculation model of parallel, vertical, and inclined layered rock mass by combining Hooke spring model and coordinate transformation method. Through the analysis of sensitivity, it is concluded that the elastic parameters of layered rock mass are controlled by the thickness, elastic parameters and dip angle of layer and sandwich rock. Then, Wei et al. [23] derived the calculation formula of deformation parameters of layered rock mass based on elastic theory.

At present, although relevant scholars have performed a lot of research into the mechanical properties of sandwiched rock mass, including interbedded rock mass superimposed rock mass after compression, there is a lack of comparative analysis for these complex strata. Thus, by using sandstone and shale to make sandwiched rock mass, interbedded rock mass and superimposed rock mass, uniaxial compression tests are carried out on combination samples with different thicknesses as well as different layers and different combination methods. The mechanical properties such as compressive strength, elastic modulus and failure mode are analyzed from the aspects of combination mode, rock content and the layer number of each specimen, and the variation law of mechanical properties after uniaxial compression is discussed.

2. Uniaxial Compression Test of Layered Rock Mass

2.1. Test Scheme

Berisavljević et al. [24] carried out a series of uniaxial compression tests on the combination specimens of sandstone and siltstone. The experimental results show that the inhomogeneity of sample strength seriously affects the accuracy of the experiment. This is because the rocks collected in the field have certain limitations and it is difficult to ensure the uniformity and integrity of the rocks. Therefore, the most common method of preparing samples is to collect rocks with different lithological properties, cut, polish and shape them to the desired size separately, and finally assemble them. The same cementation is used between layers and the same thickness is applied. In this experiment, the sandstone and shale were made into cylindrical samples with diameters of 25 mm and different thicknesses, and the height of the combined samples was 50 mm. In order to analyze the influence of different combination characteristics, the samples are divided into four types. As shown in Table 1, these are single rock, superimposed rock mass, sandwiched rock mass and interbedded rock mass. The schematic diagram of the sample design scheme is shown in Figure 1. This study discusses that soft rock and hard rock are not the mechanical classification of engineering rock mass, but are divided into soft rock and hard rock according to their relative strength. When the uniaxial compressive strength of hard rock is more than one times that of soft rock, they can be divided into soft rock and hard rock.

Table 1. Uniqueness of each rock.

Category	Type	Characteristic
1	Single rock mass	Shale and sandstone are sedimentary rocks, whose mechanical characteristics are closely related to structural composition.
2	Superimposed rock mass	It is composed of two kinds of rock mass with different strength. The thickness of each rock mass is relatively thick, and its mechanical properties are determined by two kinds of components.
3	Sandwiched rock mass	The sandwiched rock mass has a layered or banded soft (hard) thin layer, and its mechanical properties such as mechanical strength and elastic modulus are smaller (larger) than those of surrounding rock.
4	Interbedded rock mass	The interbedded rock mass is a kind of sedimentary type in which soft rock and hard rock alternate with each other in longitudinal direction and the thickness is small. The lithology shows frequent vertical alternations between soft and hard.

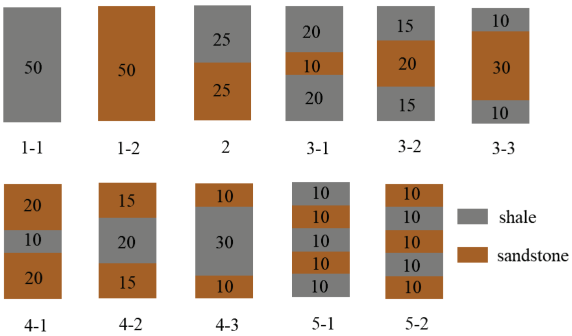

Figure 1. Schematic diagram of sample scheme.

2.2. Test Results

The uniaxial compression test of the prepared combination rock mass was carried out by TAW-2000 rock triaxial shear tester, and a continuous loading method was used to load the sample to failure. The compressive strength, elastic modulus and stress–strain curves of the samples were obtained. The average value of each group of experimental data was used as the test result. The test data are shown in Table 2.

Table 2. Test results.

Grouping	Lithology	Proportion (H:S)	Number of Layers	Hierarchical Feature	Compressive Strength/MPa	Modulus of Elasticity/GPa
1-1	Shale		1		200.67	34.72
1-2	Sandstone		1		37.37	9.66
2	Shale-Sandstone Association	1:1	2	HS	40.8	9.39
3-1		4:1	3	HSH	76.88	15.65
3-2		3:2	3	HSH	41.77	12.63
3-3		2:3	3	HSH	29.04	9.14
4-1		1:4	3	SHS	29.64	6.02
4-2		2:3	3	SHS	48.34	10.19
4-3		3:2	3	SHS	67.05	10.93
5-1		3:2	5	HSHSH	44.22	8.89
5-2		2:3	5	SHSHS	48.17	8.28

Note: H (hard) stands for shale S (soft) stands for sandstone.

3. Mechanical Properties of Layered Rock Mass

3.1. Comparative Analysis of Compressive Strength

The compressive strength characterizes the ability of rock to resist damage, so the combined characteristics of the compressive strength of the rock mass are analyzed. It is of great significance for understanding the fracture behavior of deep layered rock mass. Figure 2 summarizes the compressive strength values of all rock masses. According to the compressive strength of the single rock mass, the average uniaxial compressive strength of sandstone is 37.37 MPa, and that of shale is 200.67 MPa. This is because the shale used in this experiment has good compactness, while the mineral component particles of sandstone are larger and weakly cemented, so there is a large difference in strength. The compressive strength of shale is five times that of sandstone. The uniaxial compressive strength of the combination is between 29 and 80 MPa, which is between the strength of sandstone and shale. In combination rock samples, both sandstone and shale bear the stress of loading at both ends. As the existence of high-strength shale improves the overall bearing capacity, the compressive strength of the combination rock samples is higher than that of single sandstone rock samples. However, due to the low compressive strength of sandstone, the stress in the loading process first reaches the maximum bearing capacity of sandstone. Although it does not reach the bearing capacity of shale, the combined sample has lost its bearing capacity. Thus, the strength of the combined sample is lower than that of a single shale sample. In addition, the compressive strength of the combined samples is more similar to that of sandstone. This indicates that low strength rock mass plays a key role in the overall strength of rock mass in different lithologic assemblage strata.

In summary, the compressive strength of the combined sample is between the compressive strength of the combined component, which is biased towards the compressive strength of the soft rock. The soft rock of the combination plays a decisive role in the strength of the combination.

Figure 3 analyzes the strength characteristics of the superimposed rock mass. The strength of 1-1 shale is 200.67 MPa, The strength of 1-2 sandstone is 37.37 MPa. Additionally, the compressive strength of superimposed rock mass 2 is 40.8 MPa, which is 1.09 times that of sandstone, but only 0.203 times that of shale. This shows that the strength of soft and hard superimposed rock mass is slightly higher than that of sandstone. Compared with the strength of shale, the strength will decrease greatly. Therefore, for the soft and hard superimposed rock mass, the strength is greatly affected by sandstone (relatively soft rock mass). When the content of each component is the same, its strength will be close to the strength of soft rock mass. Relevant scholars' research [12] also shows that the strength of composite rock will be between the compressive strength of two kinds of rock [14].

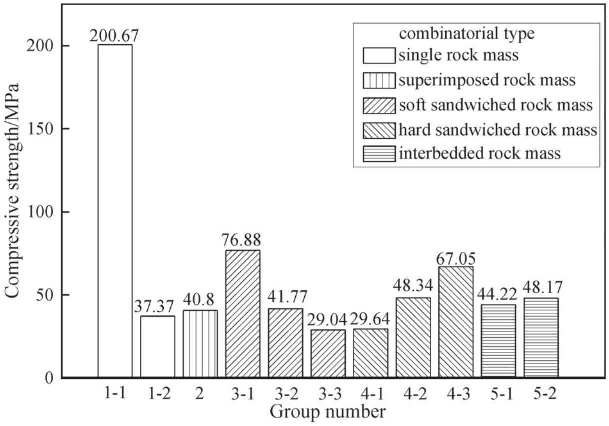

Figure 2. Comparative analysis of the compressive strength of the combination.

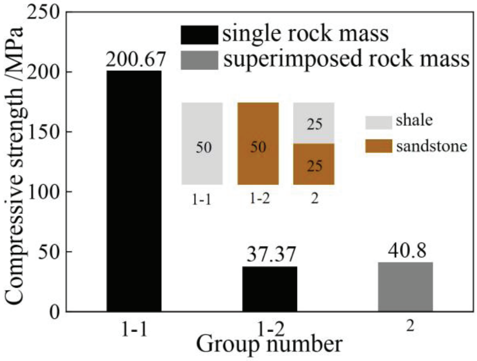

Figure 3. Strength characteristics of superimposed rock mass.

Figure 4a shows the soft sandwiched rock mass with different component content. The sandwich height of the samples from groups 3-1, 3-2 and 3-3 increased successively, and the compressive strength of samples with sandstone content of 20%, 40% and 60% were 76.88 MPa, 41.77 MPa and 29.04 MPa, respectively. It can be observed that the strength of combination was continuously weakened with the increase in the content of sandwiched sandstone. Figure 4b shows hard interbedded rock mass with a different component content. The interlayer height of samples in groups 4-1, 4-2 and 4-3 successively increased, the shale content was 20%, 40% and 60%, respectively, and the compressive strength was 29.64 MPa, 48.34 MPa and 67.05 MPa, respectively. It can be observed that the strength of combination body increases with the increase in shale content. This also indicates that, for the interbedded rock mass, the strength of the rock mass mainly depends on the lithology and content of the rock strata. When the sandwich is sandstone (soft rock mass), the strength of the assemblage increases with the decrease in the sandwiched rock mass content. When the sandwich is shale (hard rock), the strength of the combination decreases with the decrease in sandwich content.

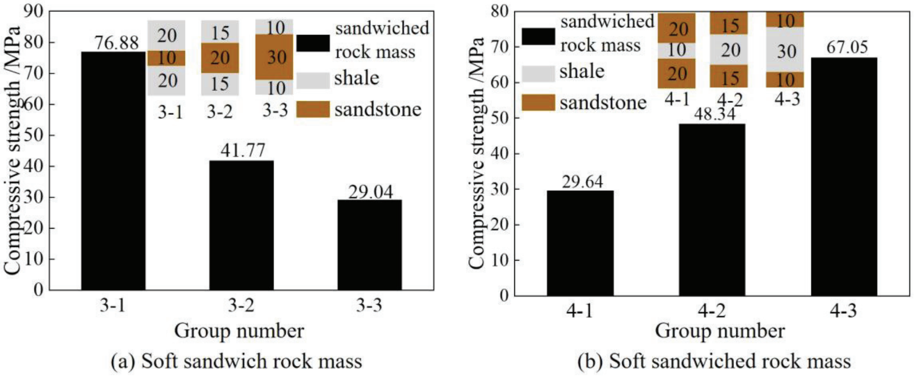

(a) Soft sandwich rock mass (b) Soft sandwiched rock mass

Figure 4. Influence of interlayer thickness on the strength of interlayer rock mass.

In summary, the effect of the sandwich on the overall strength of the rock mass is as follows, when the strength of the sandwich is lower than that of surrounding rock, the overall strength of the rock layer decreases with the increase in the thickness of sandwich. When the strength of the sandwich is higher than that of surrounding rock, the overall strength of the rock stratum increases with the increase in sandwiched thickness.

Figure 5 analyzes the effect of rock position on strength. The shale content of samples 3-2 and 4-3 is 60%, and the compressive strength is 41.77 MPa and 67.05 MPa, respectively. When the soft rock layer is in the sandwich, the strength of the sample will be low. In Figure 5b, the shale content of samples 3-3 and 4-2 is 40%, and the compressive strength is 29.04 MPa and 48.31 MPa, respectively. When the hard rock layer is in the sandwich, the strength of the sample will be higher.

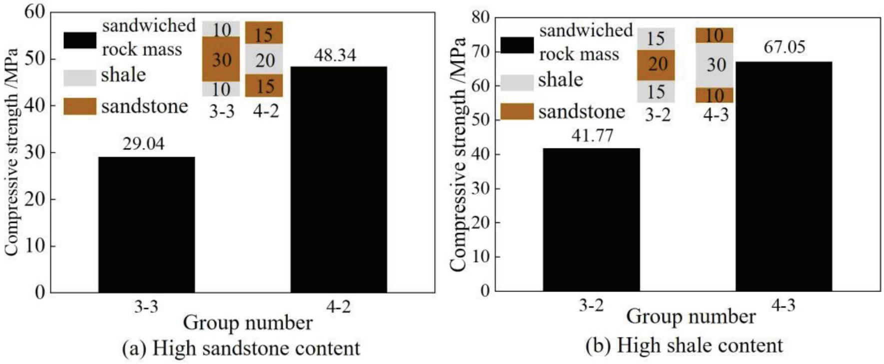

(a) High sandstone content (b) High shale content

Figure 5. Influence of rock position on the strength of the sandwich rock mass.

In conclusion, when the content of each component of the sample is unchanged, the influence of the sandwich on the strength is the strongest. When the sandwich is a weak rock layer, the sample shows smaller strength. When the sandwich is a hard rock layer, the sample shows greater strength.

Figure 6 compares and analyzes the influence law of the number of rock layers on the strength of the superimposed rock mass and interbedded rock mass. The strength of the superimposed rock mass is 40.8 MPa, and that of the interbedded rock mass is 44.22 MPa and 48.17 MPa. From the perspective of the component content, taking shale as an example, the shale content of superimposed rock mass is 50%, and that of interbedded rock mass is 60% and 40%, respectively, between the superimposed rock mass. From the perspective of the component content alone, the strength of the superimposed rock mass is between the two groups of interbedded rock mass, but the strength of interbedded rock mass is higher than that of superimposed rock mass. This indicates that the number of layers has an important effect on the strength. When the composition content of the combination is similar, the overall strength will increase with the increase in the number of layers.

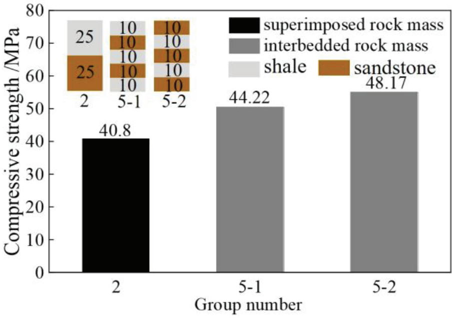

Figure 6. The influence of the number of layers on the strength of rock mass.

Figure 7 analyzes the strength characteristics of sandwiched rock mass and interbedded rock mass with the same component content. The strength of samples 3-2 and 5-1 are 41.77 MPa and 44.22 MPa, respectively. The strength of samples 4-2 and 5-2 are 48.34 MPa and 48.17 MPa, respectively. The intensity is very similar. This indicates that the level of component content has an important effect on the rock mass of interbedded and sandwiched rock mass. The strength is similar when the component content is the same and the surrounding rock type is the same.

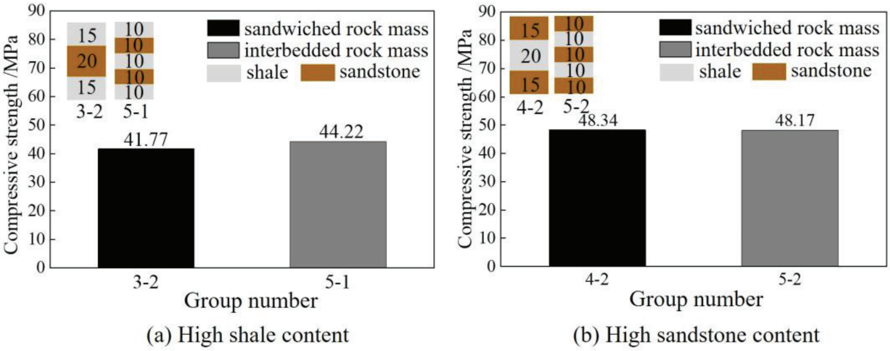

Figure 7. Comparison between sandwich type and interbedded type with the same content.

In conclusion, the composition content has an important effect on the rock mass. The greater the proportion of hard rock, the easier it is for the combination to show greater strength. In addition, the strength of the superimposed rock mass is greatly affected by the type of components. The strength value of the superimposed rock mass is between the strength of each component, which is slightly higher than that of the weak component, but significantly lower than that of the hard component. The strength of the sandwiched rock mass is closely related to the thickness of the sandwich and the strength of the sandwich and surrounding rock. Interbedded rock mass has the largest number of layers, the strength of interbedded rock mass is similar to that of sandwiched rock mass when the composition content is the same or similar and the type of surrounding rock is the same. When the composition content is similar, the strength of interbedded rock mass is slightly higher than that of superimposed rock mass. It is similar to the current research results [14]. The strength of composite rock mass will be between the strength of two kinds of rock and close to low strength [19].

3.2. Comparative Analysis of Elastic Modulus

Elastic modulus is the ratio of stress to strain change value of the object in the elastic deformation stage, that is, the stress required for the unit elastic deformation of the material under the action of external force. The elastic modulus characterizes the ability of the object to resist elastic deformation. Therefore, it is of great significance to clarify the influence of combination characteristics on the elastic modulus for understanding the deformation law of rock in deep combined strata.

To compare the elastic modulus, Figure 8 is drawn according to the order of the elastic modulus and the component content and layered characteristics of the sample. The values of the elastic modulus was closely related to the component content. The higher the shale content is, the lower the sandstone content is, and the higher the elastic modulus of the rock mass is. In addition, the number of layers and the location of the rock layer also affect the elastic modulus. When the component content is the same, the elastic modulus of the hard sandwich is smaller than that of the soft sandwich. The elastic modulus of the interbedded rock mass with the same component content is smaller than that of the sandwich rock mass.

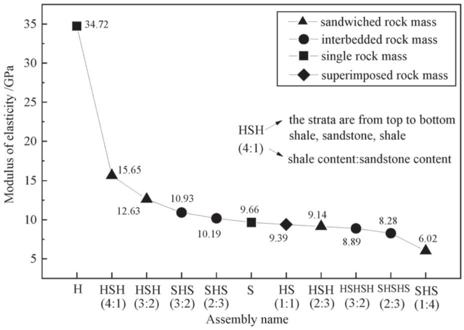

Figure 8. Analysis diagram of elastic modulus.

Figure 9 shows the stress diagram of superimposed, sandwiched and interbedded rock masses. Assuming that the stress between layers is equal, according to Hooke's law, the shape variable of the assemblage can be expressed by Equation (1), and that of each rock layer can be expressed by Equation (2).

$$\Delta h = \frac{Fh}{EA} \tag{1}$$

$$\Delta h_i = \frac{Fh_i}{E_i A} \tag{2}$$

where *h* represents the height of rock strata, *F* represents the pressure of the rock mass, *E* represents the elastic modulus and *A* represents the upper and lower area of the rock mass.

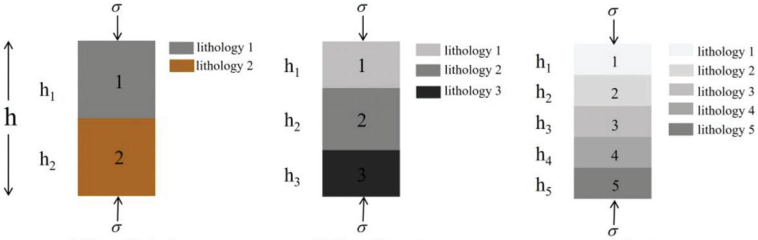

(a) Two lithologic combinations
(b) Three lithologic combinations
(c) Five lithologic combinations

Figure 9. Stress analysis diagram of layered rock mass.

The total deformation is the sum of the deformation of the rock layer, as shown in Equation (3). Thus, the elastic modulus of the combination can be expressed by Equation (4).

$$\Delta h = \sum h_i \tag{3}$$

$$\frac{1}{E} = \frac{1}{h}\left(\frac{h_1}{E_1} + \frac{h_2}{E_2}\right) \tag{4}$$

For Figure 9b,c, the elastic modulus of the combination can be expressed by Equations (5) and (6) as

$$\frac{1}{E} = \frac{1}{h}\left(\frac{h_1}{E_1} + \frac{h_2}{E_2} + \frac{h_3}{E_3}\right) \tag{5}$$

$$\frac{1}{E} = \frac{1}{h}\left(\frac{h_1}{E_1} + \frac{h_2}{E_2} + \frac{h_3}{E_3} + \frac{h_4}{E_4} + \frac{h_5}{E_5}\right) \tag{6}$$

The elastic model of the combination is only related to the elastic modulus of each component and the height of the rock layer. For the combination containing only two materials, the elastic modulus can be expressed by Equation (7).

$$\frac{1}{E} = \frac{\alpha}{E_1} + \frac{\beta}{E_2} \tag{7}$$

The percentage of the height of the material with a surface elastic modulus of E_1 to the total height of the combination. The percentage of the height of the material whose modulus of elasticity is E_2 in the total height of the combination. Substitute $\beta = 1 - \alpha$ into Equation (8) to obtain:

$$E = \frac{E_1 E_2}{\alpha(E_2 - E_1) + E_1} \tag{8}$$

If $E_2 > E_1$, the larger α (the higher the total height of the material whose elastic modulus is E_1), the lower the elastic modulus of the combination. If $E_2 < E_1$, the larger α (the higher the total height of the material whose elastic modulus is E_1), the higher the elastic modulus of the combination will be. Therefore, for the elastic modulus of a combination containing only two materials, when the component with a large elastic modulus accounts for a large number, the elastic modulus of the combination will be larger. On the contrary, when the component with a small elastic modulus accounts for a large number, the elastic modulus of the combination will be smaller.

Figure 10 shows the comparison of the elastic modulus between the sandwiched rock mass and interbedded rock mass with the same component content. When the component content is the same, the elastic modulus of the rock mass should be the same or remain similar. However, it can be seen from Figure 10 that the elastic modulus of the interbedded rock mass in the two groups of samples is significantly lower than that of the sandwiched rock mass. The reason is that there are structural planes between the upper and lower layers on the stratified interface. In contrast to the intact rock mass without stratification, the contact mode between two walls under the structural plane is several points or a local structural plane. Although the layered interface was treated before the experiment, the structural plane effect was broken to a certain extent, and the upper and lower structural planes were still in incomplete contact, which would lead to the decline of the mechanical properties of similar materials. The more layers there are, the more severely the mechanical properties of similar materials will decline. The discontinuity between layers will increase, which will increase the deformation of rock mass, so the elastic modulus will decrease.

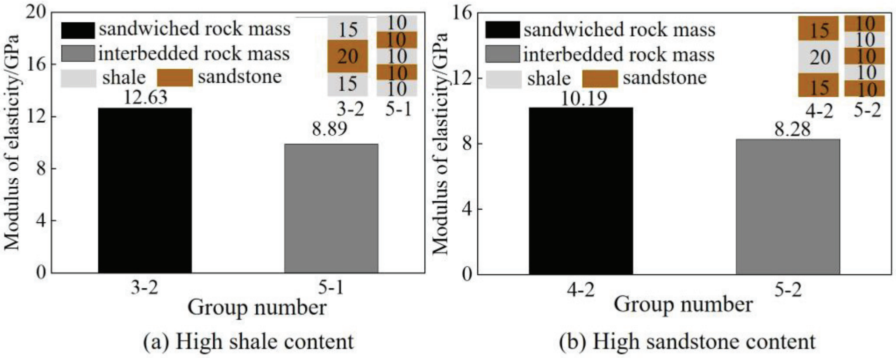

Figure 10. Influence of the number of layers on the elastic modulus.

In conclusion, the elastic modulus of the combination is mainly affected by the content of components and the number of layers. The greater the content of hard components, the lesser the deformation and the greater the elastic modulus of rock mass. When the component content is the same, the increase in the number of layers will form more structural planes and generate larger shape variables, and the elastic modulus will decrease. Previous study has suggested that the elastic modulus of the combination will be close to that of the rock with a high content [16]. This study draws more detailed conclusions through formula derivation and experimental data.

4. Failure Characteristics of Layered Rock Mass

4.1. Analysis of Stress–Strain Curve

The uniaxial compression stress–strain curve of the combination can be roughly divided into four stages, similarly to a previous study [21]. As shown in Figure 11 OA stage, the compaction stage, there are micro-cracks in the rock mass itself. With the increase in stress, these micro-cracks gradually close, and the rock will be compacted to form early nonlinear deformation, and the stress–strain curve is concave. The AB stage, elastic deformation stage the stress–strain curve of this stage shows an approximately linear shape, which can be approximated as elastic deformation. In the BC stage, the plastic deformation stage from the elastic stage after the test block began to enter the plastic stage, the development of micro-fracture undergoes a qualitative change, the fracture continues to develop, the micro-cracks in the specimen under the action of pressure gradually formed a semi-through joint in the test block, the specimen has a volume compression into a volume expansion and the axial strain increases sharply. After the C point, the post-fracture stage, after the bearing capacity of the test block reaches the peak strength, its internal structure is seriously damaged. The crack penetrates the entire test block to form a macroscopic fracture surface. The bearing capacity decreases sharply with the deformation of the test block; however, it does not drop to zero, indicating that the test block after failure still has a certain bearing capacity.

According to the composition content of the rock sample, the number of strata and the combination way, the stress–strain curve of the assemblage will also show different characteristics. The stress–strain curve was plotted in Figure 12 for comparative analysis. The maximum strain value of sandstone is 0.62, and that of shale is 0.83, which is related to the material of the sample itself and its own micro-cracks. Similarly to the conclusion drawn above, the maximum strain value of the combination body is basically between the two. Figure 12a shows the comparison between the superimposed rock mass and sandstone or shale. It can be seen that the stress–strain curve of the superimposed rock mass has the same trend as that of sandstone, indicating that the mechanical properties of the assemblage are mainly affected by sandstone and shale. Figure 12b shows the soft sandwiched rock mass with different component contents. As can be seen from the curve, the peak strain of the HSH (4:1) sample with the lowest sandstone content is above 0.7, while the other two groups of samples have a relatively high interlayer content and the maximum strain value is approximately 0.4. This indicates that, when the thickness of the soft sandwiched rock mass is small, the rock mass is more likely to have a greater strain value. Figure 12c shows the hard sandwiched rock mass with a different content. The SHS (1:4) sample shows an obvious stress drop phenomenon, while the other two groups of samples with a higher sandwiched content have smooth curves. This indicates that the mechanical properties of the combination are more unstable when the content difference of components is relatively large. The compaction stages of the curves in Figure 12d are almost identical. This indicates that the component content of the sandwiched rock mass and superimposed rock mass plays a decisive role in the mechanical properties of the samples at the initial loading stage.

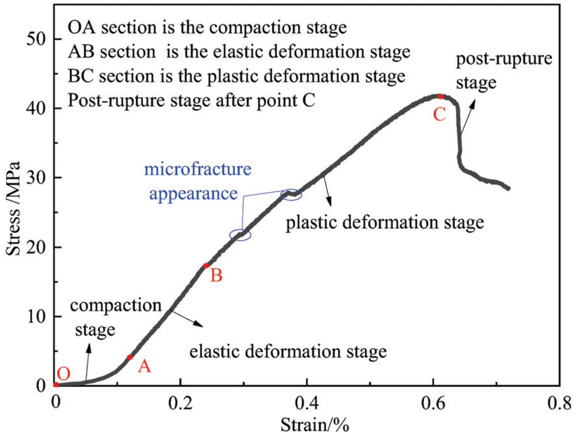

Figure 11. Analysis of combination stress–strain curve.

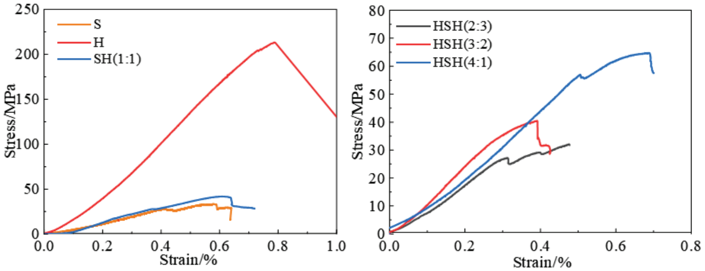

(a) Comparison of single and superimposed rock mass

(b) Soft sandwich with different contents

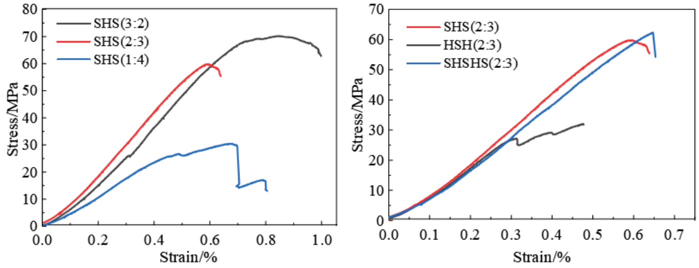

(c) Hard sandwich with different contents

(d) Sandwich and interbedding with the same content

Figure 12. Comparative analysis of stress–strain curves.

4.2. Damage Pattern of Rock Sample

Figure 13 shows the fracture characteristics of the soft sandwiched rock mass with different component contents. When the content of the interlayer is 20%, as shown in Figure 13a, the sandstone layer in the sample falls off, and the shale part cracks along the direction of the sandstone falling off. Under the vertical load, the sandstone part first expands and a part of the rock mass falls off, forming a highly concentrated area of stress at the interface between the soft and hard layers. Finally, the axial fracture failure occurs in the shale part. When the interlayer content is 40%, as shown in Figure 13b, shear failure occurs in sandstone, and two approximately parallel oblique fractures appear, with volume dilatation, but not as obvious as the former. When the content of the interlayer is 60%, as shown in Figure 13c, shear failure occurs in the sandstone part. Due to the high proportion of sandstone, the failure characteristics are similar to that of sandstone.

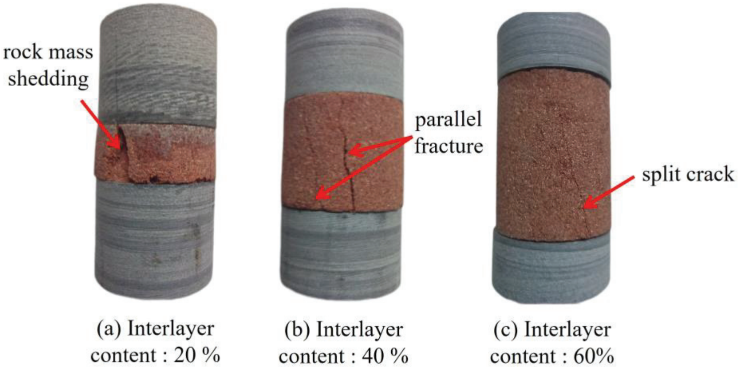

(a) Interlayer content : 20 %
(b) Interlayer content : 40 %
(c) Interlayer content : 60%

Figure 13. Failure characteristics of weak interlayer.

Therefore, the failure mode of the rock mass containing a soft sandwich is related to the content of rock strata. With the increase in the content of sandstone, the failure degree of sandstone gradually weakens, and the failure mode presents the trend of splitting failure to shear failure.

Figure 14 shows the failure characteristics of the hard sandwiched rock mass with different component contents. When the sandwich content is 60%, as shown in Figure 14a, splitting failure occurs in the sandstone part, and longitudinal fractures of the sample are concentrated in the sandstone, without obvious phenomena on the shale surface. When the sandwich content is 40%, as shown in Figure 14b, the sandstone is also split failure, with three vertical fractures at the lower end and one vertical fracture at the upper end penetrating through the shale. When the sandwich content is 20%, as shown in Figure 14c, a large area of volume shedding occurs in the lower surrounding rock.

Therefore, the failure characteristics of hard sandwiched rock mass are related to the component content. When the content of the sandwiched rock is high or low enough, the failure of the rock mass mainly occurs in the surrounding rock. When the content of sandwiched rock is similar to that of surrounding rock, the failure of both the sandwiched rock mass and surrounding rock mass will occur.

Figure 15 shows the failure characteristics of the interbedded rock mass. As shown in Figure 15a, the top sandstone part has a vertical crack, but without crossing the shale section, there is no obvious phenomenon. The rest of Figure 15b shows a sample surface without apparent damage. It can be seen that the strength of the soft and hard interbedded rock mass is similar to that of other rock mass under the condition of constant lithology and proportion. However, the damage degree shown after compression will be significantly weakened. It is difficult to produce cracks.

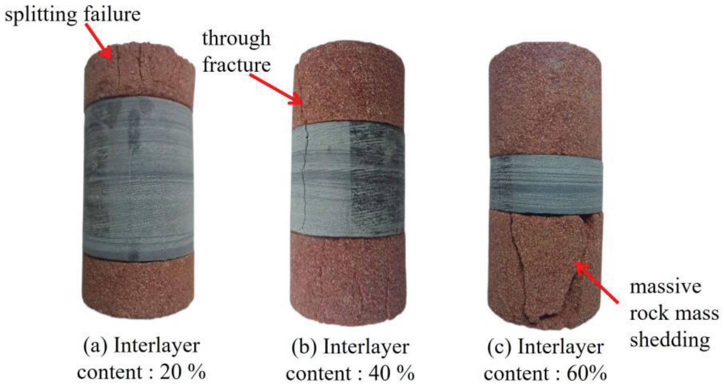

Figure 14. Failure characteristics of the hard interlayer.

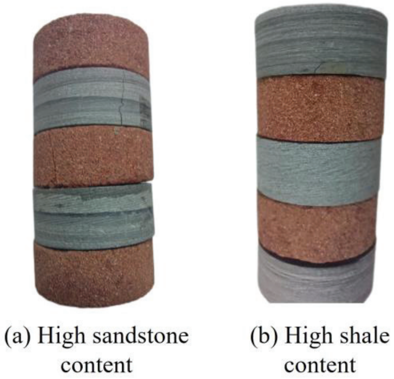
(a) High sandstone content
(b) High shale content

Figure 15. Failure characteristics of interbedded rock mass.

5. Conclusions

Through uniaxial compression experiments on different types of rock masses, the compressive strength, elastic modulus and failure characteristics of the samples were obtained. The influence of component content, number of layers and rock position on the combined rock mass was analyzed. The conclusions are as follows:

(1) The mechanical properties of the superimposed rock mass, such as strength and elastic modulus, are between the sandstone and shale. The strength and elastic modulus of superimposed rock mass decrease greatly compared with the shale, but increase little compared with sandstone. Sandwiched rock mass can be divided into soft sandwiched rock mass and hard sandwiched rock mass. The overall strength of the soft sandwiched rock mass decreases with the increase in sandwich thickness, while the overall strength of hard sandwiched rock mass increases with the increase in rock thickness. Compared with the former, the mechanical properties of the interbedded rock mass tend to be more stable; the strength and elastic modulus of the interbedded rock mass only change a little after changing the composition content and formation location. Compared with the sandwiched rock mass, the strength of the interbedded rock mass is similar to that of the sandwiched rock mass, but the elastic modulus of the interbedded rock mass decreases with the increase in the number of layers.

(2) The stress–strain curve of the combination can be divided into the compaction stage, elastic stage, plastic stage and post-peak bearing stage. The component content of rock mass plays a decisive role in the compaction stage. When the component content is unchanged, the interbedded rock mass will produce a larger strain value.

(3) The failure modes of the combination are mainly shear failure and splitting failure. The failure mode of the rock mass with the soft sandwich is related to the content of the rock layer. With the increase in the sandwich content, the failure degree of sandstone is gradually weakened, and the failure mode shows the trend of splitting failure to shear failure. For hard sandwich rock mass, when the sandwich content is high or low enough, the failure of the rock mass mainly occurs in the surrounding rock. When the content of the sandwich is similar to that of the surrounding rock, both the sandwich and surrounding rock will appear. The properties of soft and hard interbedded rock mass are more stable and the damage degree is less.

(4) Layered rock mass is the most common type of rock mass in practical engineering. The research results of this paper can provide a reference for the complex layered rock mass problems encountered in oil and gas exploitation and underground excavation. The cementation between the layered rock samples prepared in this experiment is the same. In fact, the cementation between the rock layers also affects the strength of the rock mass. Therefore, the cementation between rock layers can be further studied as a variable.

Author Contributions: Conceptualization, Y.Z.; methodology, Y.Z. and H.W.; software, T.Z.; validation, Y.Z.; formal analysis, Q.N.; investigation, Y.Z.; resources, Y.Z.; data curation, T.Z. and H.Y.; writing—original draft preparation, T.Z.; writing—review and editing, Y.Z.; visualization, Y.Z.; supervision, Y.Z. and W.W.; project administration, Y.Z.; funding acquisition, Y.Z. All authors have read and agreed to the published version of the manuscript.

Funding: This study was funded by the Natural Science Foundation of Hebei Province (E2021210036 and E2021210128).

Institutional Review Board Statement: Not applicable.

Informed Consent Statement: Not applicable.

Data Availability Statement: Due to the need for follow-up research, participants of this study did not agree for their data to be shared publicly, so supporting data is not available.

Conflicts of Interest: All authors certify that they have no affiliations with or involvement in any organization or entity with any financial interest or non-financial interest in the subject matter or materials discussed in this manuscript.

References

1. Wagner, H. Deep Mining: A Rock Engineering Challenge. *Rock Mech. Rock Eng.* **2019**, *52*, 1417–1446. [CrossRef]
2. Buddington, A.F. Layered igneous rocks. *Chem. Geol.* **1970**, *6*, 241–243. [CrossRef]
3. Suo, Y.; Chen, Z.; Rahman, S.S.; Chen, X. Experimental study on mechanical and anisotropic properties of shale and estimation of uniaxial compressive strength. *Energy Sources Part A Recovery Util. Environ. Eff.* **2020**. [CrossRef]
4. Hou, P.; Gao, F.; Yang, Y.; Zhang, X.; Zhang, Z. Effect of the layer orientation on mechanics and energy evolution characteristics of shales under uniaxial loading. *Int. J. Min. Sci. Technol.* **2016**, *26*, 857–862. [CrossRef]
5. Li, H.; Yang, Z.; Li, H. Mechanical Characteristics and Failure Mechanism of Siltstone with Different Joint Thickness. *Adv. Civ. Eng.* **2020**, *2020*, 3824538. [CrossRef]
6. Abdi, Y.; Khanlari, G.-R.; Jamshidi, A. Correlation between Mechanical Properties of Sandstones and P-Wave Velocity in Different Degrees of Saturation. *Geotech. Geol. Eng.* **2018**. [CrossRef]
7. Ma, J.; Jiang, N.; Wang, X.; Jia, X.; Yao, D. Numerical Study of the Strength and Characteristics of Sandstone Samples with Combined Double Hole and Double Fissure Defects. *Sustainability* **2021**, *13*, 7090. [CrossRef]
8. Yan, C.; Deng, J.; Hu, L.; Chen, Z.; Yan, X.; Lin, H.; Tan, Q.; Yu, B. Brittle failure of shale under uniaxial compression. *Arab. J. Geosci.* **2015**, *8*, 2467–2475.
9. Zhang, J. Borehole stability analysis accounting for anisotropies in drilling to weak bedding planes. *Int. J. Rock Mech. Min. Sci.* **2013**, *60*, 160–170. [CrossRef]
10. Everitt, R.A.; Lajtai, E.Z. The influence of rock fabric on excavation damage in the Lac du Bonnett granite. *Int. J. Rock Mech. Min. Sci.* **2004**, *41*, 1277–1303. [CrossRef]
11. Zheng, Y.; He, R.; Huang, L.; Bai, Y.; Wang, C.; Chen, W.; Wang, W. Exploring the effect of engineering parameters on the penetration of hydraulic fractures through bedding planes in different propagation regimes. *Comput. Geotech.* **2022**, *146*, 104736. [CrossRef]
12. Huang, L.; Liu, J.; Zhang, F.; Dontsov, E.; Damjanac, B. Exploring the influence of rock inherent heterogeneity and grain size on hydraulic fracturing using discrete element modeling. *Int. J. Solids Struct.* **2019**, *176–177*, 207–220. [CrossRef]

13. Duffaut, P. Structural Weaknesses in Rocks and Rock Masses Tentative Classification and Behaviour. In Proceedings of the Isrm International Symposium, ISRM-IS, Tokyo, Japan, 21–24 September 1981.
14. Chen, S.; Yin, D.; Jiang, N.; Wang, F.; Zhao, Z. Mechanical properties of oil shale-coal composite samples. *Int. J. Rock Mech. Min. Sci.* **2019**, *123*, 104120. [CrossRef]
15. Sun, W.-T.; Li, Z.-H.; Lou, Y.-S.; Zhu, L.; Wu, H.-M.; Lenwoue, A.R.K.; Liu, Q. Mechanical Properties of Shale-Reservoir Rocks Based on Stress–Strain Curves and Mineral Content. *Geofluids* **2022**, *2022*, 2562872. [CrossRef]
16. Wang, Z.; Wang, M.; Zhou, L.; Zhu, Z.; Shu, Y.; Peng, T. Research on uniaxial compression strength and failure properties of stratified rock mass. *Theor. Appl. Fract. Mech.* **2022**, *121*, 103499. [CrossRef]
17. Huang, W.; Wang, H.; Zhang, T.; He, M.; Yan, L. Hydraulic pressure effect on mechanical properties and permeabilities of layered rock mass: An experimental study. *Eur. J. Environ. Civ. Eng.* **2023**, *27*, 2422–2433. [CrossRef]
18. Li, H.; Wang, J.; Li, H.; Wei, S.; Li, X. Experimental Study on Deformation and Strength Characteristics of Interbedded Sandstone with Different Interlayer Thickness under Uniaxial and Triaxial Compression. *Processes* **2022**, *10*, 285. [CrossRef]
19. Li, F.; Yin, D.; Wang, F.; Jiang, N.; Li, X. Effects of combination mode on mechanical properties of bi-material samples consisting of rock and coal. *J. Mater. Res. Technol.* **2022**, *19*, 2156–2170. [CrossRef]
20. Douma, L.A.; Regelink, J.A.; Bertotti, G.; Boersma, Q.D.; Barnhoorn, A. The mechanical contrast between layers controls fracture containment in layered rocks. *J. Struct. Geol.* **2019**, *127*, 103856. [CrossRef]
21. Li, J.; Yu, Z.; Zhou, Z.; Wang, Y.; Li, J. Mechanical analysis and failure modes prediction of composite rock under uniaxial compression. *Sci. Rep.* **2021**, *11*, 22826. [CrossRef]
22. Zhang, L.; Qu, G.; Qu, S.; Liu, Z. Constitutive model and elastic parameters for layered rock mass based on combined Hooke spring. *Strength Fract. Complex.* **2017**, *10*, 145–156.
23. Wei, W.; Zhu, L.; Liu, H. Anisotropy of deformation parameters of stratified rock mass. *Arab. J. Geosci.* **2021**, *14*, 1675. [CrossRef]
24. Berisavljević, Z.; Berisavljević, D.; Rakić, D.; Hadži-Niković, G.; Radić, Z. Strength of composite flysch samples under uniaxial compression. *Bull. Eng. Geol. Environ.* **2018**, *77*, 791–802. [CrossRef]

energies

MDPI

Article

Effects of Changes in Physical Properties of Porous Media and Fluid under Supercritical CO_2 Huff-n-Puff in Low-Permeability Reservoir

Guohui Qu *, Xuebin Tian, Yikun Liu, Bowen Li and Xiunan Li

Key Laboratory for Oil and Gas Recovery Improvement of the Ministry of Education, Northeast Petroleum University, Daqing 163000, China; 218003020722@stu.nepu.edu.cn (X.T.); liuyikun@nepu.edu.cn (Y.L.); 228002020098@stu.nepu.edu.cn (B.L.); 228002020095@stu.nepu.edu.cn (X.L.)
* Correspondence: quguohui@nepu.edu.cn

Abstract: The low-permeability reservoirs have abundant reserves and broad development prospects, and the supplementary energy methods have gradually become a hot research topic. In addition, the technology of enhanced oil recovery through supercritical CO_2 injection is becoming increasingly mature; however, the changes in reservoir properties at the microscopic level still need further investigation. In this study, natural rock cores from low-permeability reservoirs were used to simulate reservoir conditions and conduct supercritical CO_2 injection experiments for energy supplementation. The study aimed to investigate the changes in reservoir microstructure, minerals, and crude oil properties before and after the experiments. The research results indicate that after supercritical CO_2 injection into the reservoir, it dissolves in the formation water to form carbonic acid. Under the effect of dissolution, the porosity of the low-permeability reservoir increases by 1.06–5.68%, and permeability can be improved by 40–60%. The rock becomes more water-wet and less oil-wet. The content of calcite and feldspar in the rock minerals decreases due to the dissolution of carbonic acid, resulting in a reduction in plagioclase and calcite. After the CO_2 injection, the light components (C_8–C_{10}) in the crude oil in the rock cores decreased by approximately 14.6%, while the heavy components (C_{16}–C_{39}) increased by 6.99%. The viscosity of the crude oil decreases, and its flowability is further enhanced.

Keywords: low-permeability; supercritical CO_2 huff-n-puff; permeability; porosity; wettability; viscosity

Citation: Qu, G.; Tian, X.; Liu, Y.; Li, B.; Li, X. Effects of Changes in Physical Properties of Porous Media and Fluid under Supercritical CO_2 Huff-n-Puff in Low-Permeability Reservoir. *Energies* **2023**, *16*, 6813. https://doi.org/10.3390/en16196813

Academic Editors: Ali Habibi, Jan Vinogradov and Zhengyuan Luo

Received: 31 August 2023
Revised: 16 September 2023
Accepted: 22 September 2023
Published: 26 September 2023

1. Introduction

In the context of carbon neutrality, the technology of using CO_2 for oil extraction has garnered significant attention [1–3]. Compared to other swelling agents, such as nitrogen, deoxygenated air, and reactive water, carbon dioxide is more soluble in crude oil under extraction conditions, providing additional reservoir energy [4–6]. Carbon dioxide can reach a supercritical state at temperatures above 31 °C and pressures of 7.50 MPa. In this state, carbon dioxide exhibits excellent dissolving capabilities for both crude oil and water, leading to an increased oil recovery through mechanisms such as expanding the volume of oil, reducing oil viscosity, lowering oil–water interfacial tension, dissolving-gas-drive, and enhancing core permeability [7–11].

Low-permeability reservoirs in Daqing Oilfield are primarily concentrated in the peripheral fields and the exterior reservoirs of Changyuan Oilfield. These reservoirs are characterized by poor physical properties, low permeability, low movable fluid saturation, poor pore connectivity, and high clay content [12]. Studies have shown that injecting supercritical CO_2 into low-permeability reservoirs is an effective method for improving oil recovery in these reservoirs. Additionally, it enables the utilization and geological storage of CO_2, thereby mitigating the greenhouse effect [13–15]. However, in practical applications in Daqing Oilfield, the injection of supercritical CO_2 to enhance oil recovery has not yielded the expected results, limiting the widespread application of this technology. After the injection of supercritical CO_2 into low-permeability reservoirs, CO_2 dissolves in the connate water within the reservoir, forming carbonic acid. Under certain conditions, carbonic acid can react with the minerals in the reservoir, thereby altering the reservoir's physical properties and microstructure to some extent. Moreover, supercritical CO_2 in the reservoir state can not only extract light components from the crude oil but can also dissolve in the oil itself, leading to oil volume expansion and viscosity reduction [16–19].

Rathnaweera et al. [20] studied the impact of supercritical CO_2 and saline water on the mechanical properties of sandstone. The results showed significant dissolution of quartz minerals and dissolution of calcite and siderite in both the supercritical CO_2–water and saline–water systems. This indicates that the chemical dissolution of minerals and rock promotes the collapse of rock pores, leading to damage to the mechanical properties of the rock. Isaka et al. [21] investigated the changes in uniaxial and triaxial mechanical properties of granite under long-term exposure to supercritical CO_2 over two months. They found that changes in the mineral structure of granite were caused by the dissolution of silicate minerals and feldspar minerals, resulting in a decrease in rock strength. The dissolution and precipitation of minerals also affected the corrosive action of supercritical CO_2 on granite, exhibiting time-dependent degradation. Wang Shaopeng [22] and others determined the solubility, density, and volume coefficient of CO_2 in Daqing crude oil and reservoir water at different pressures using the PVT method. The study found that the solubility of CO_2 increased linearly with increasing pressure, and the volume coefficient of the saturated CO_2–oil–water mixture depended on the experimental pressure and the amount of dissolved gas, while it was less influenced by the liquid-phase composition. Li Yuxing [23] conducted experiments on viscosity reduction and solubility of super-heavy oil using supercritical CO_2 and simulated the properties using a fluid equilibrium model. They derived the calculation formulas for the solubility and volume coefficient of supercritical CO_2 in super-heavy oil.

Currently, the characterization of rock porosity evolution under the action of supercritical CO_2 primarily relies on porosity, permeability, or adsorption characteristics. There is insufficient understanding of the dissolution behavior of supercritical CO_2 under high-temperature and high-pressure conditions, a lack of research on other physical properties of rock minerals, and insufficient analysis of mineral compositions in core samples. Therefore, this study is based on laboratory experiments simulating the physical simulation of supercritical CO_2 injection. It focuses on the changes in reservoir properties and crude oil properties before and after the experiments using natural low-permeability core samples. The study quantitatively analyzes the changes in permeability and porosity of the core, investigates the variations in mineral composition, and examines the changes in the hydrocarbon composition of crude oil. Unlike conventional viscosity analysis of extracted crude oil, this study uses the falling ball method to simulate and analyze the viscosity changes of the crude oil under the temperature and pressure conditions of the experiments.

2. Experimental Section

2.1. Materials and Instruments

The low-permeability natural rock cores used in the experiment were obtained from the target block of Daqing Oilfield. The dimensions of the cores were $\phi 2.5$ cm × 5 cm, and their main characteristic parameters are shown in Table 1. The crude oil used in the experiment was Daqing Oilfield's crude oil, with a surface density of 0.8268 g/cm^3 (20 °C, 0.101 MPa) and a viscosity of 4 mPa·s (71 °C, 0.101 MPa). The water used in the experiment was laboratory-prepared simulated formation water with a salinity of 12,500 mg/L and predominantly contained sodium ions. The water type was $NaHCO_3$. The CO_2 used in the experiment was provided by Qingdao China Gas Co., Ltd., with a purity of 99.99%.

Table 1. Characteristic parameters of natural core.

Core Number	Length (cm)	Diameter (cm)	Raw Permeability (10^{-3} μm^2)	Raw Porosity (%)
Z1	5.01	2.51	1.541	12.32
Z2	5.10	2.51	0.431	14.11
Z3	4.98	2.50	0.982	10.72
Z4	5.11	2.50	0.361	11.24
Z5	5.00	2.49	1.425	15.42
Z6	5.00	2.50	0.742	9.88

The QKY-2 Porosity Determination Instrument is manufactured by Hai'an China Co., Ltd. The GASPERM Gas Permeability Measurement Instrument is produced by Vinci Technologies, a company based in Paris France. The Agilent 5973I Gas Chromatography-Mass Spectrometry System is manufactured by Agilent Technologies in the United States. The CHY-Π Viscometer is a product of Brookfield, a company based in the United States. The D8 Advance X-ray Diffraction Instrument is manufactured by Bruker, a company from Berlin, Germany. The OCA25 Contact Angle Measurement Instrument is produced by Dataphysics, a company based in Berlin, Germany. The displacement experiment equipment mainly includes an ISCO syringe pump (manufactured by Teledyne ISCO, United States, with a flow accuracy of 0.001 mL/min), a temperature- and pressure-resistant piston container, core holders, a hand pump, a temperature-controlled chamber, a data acquisition device, pressure gauge, etc. For more detailed information, please refer to Figure 1.

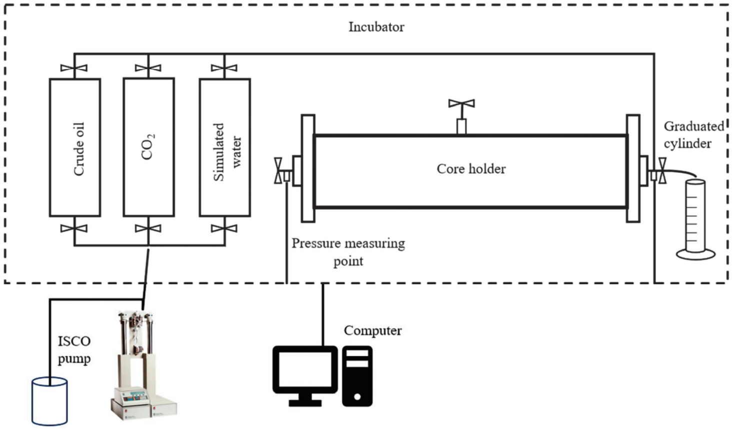

Figure 1. Displacing experimental device.

2.2. Experimental Method

To investigate the changes in the physical properties of the porous media and fluids in low-permeability cores after supercritical CO_2 flooding, the following experimental procedure was designed: (a) The natural rock cores were first washed with xylene and then dried in a temperature-controlled chamber at 71 °C for 24 h. After drying, the cores were weighed and sampled for scanning electron microscope (SEM) observation to obtain the initial microstructure of the cores.

(b) The dried natural rock cores were subjected to a permeability measurement using the gas permeability measurement instrument and porosity determination using the porosity determination instrument. Subsequently, a vacuum was applied for 24 h to achieve a pressure below 1 Pa, followed by saturation with water. (c) The prepared rock cores were placed in core holders, connected with pipelines, and checked for airtightness. The temperature of the temperature-controlled chamber was set to 71 °C. After a thermal stabilization period of 24 h, the cores were saturated with oil at a rate of 0.01 mL/min. (d) Supercritical CO_2 huff-n-puff experiments were carried out on natural cores. CO_2 was injected into the core gripper at an injection pressure of 16 MPa for 5 min to ensure the internal stability of the core gripper at 16 Mpa, and then the valves at both ends of the core gripper were closed. After 24 h of braising, the liquid was extracted from the same end of the core gripper and huff-n-puff was repeated for 3 rounds.

(1) Determination of permeability and porosity of natural rock cores before and after the experiment.

After drying the natural rock cores before and after the experiment, the permeability and porosity are measured using gas permeability measurement instruments and gas porosity determination instruments. This provides information about the changes in the physical properties of the natural rock cores before and after the supercritical CO_2 flooding experiment. (To reduce experimental errors, ensure that each rock core is measured for the same duration when using the gas permeability measurement instrument and porosity measurement instrument).

(2) Determination of the mineral composition of natural rock cores before and after the experiment.

Before and after the experiment, the natural rock cores are dried, sliced, and ground into powder. X-ray diffraction analysis is conducted to determine the mineral composition of the natural rock cores before and after the supercritical CO_2 flooding.

(3) Determination of wettability of natural rock cores before and after the experiment.

After drying the natural rock cores, prepare 2 mm thick slices and measure the water contact angle to assess the wettability changes before and after the huff-n-puff experiment. Prior to the contact angle measurement, ensure that the rock core slices and water are thermally stabilized at 71 °C for 1 h.

(4) Determination of total hydrocarbon composition in crude oil.

First, the intermediate container is cleaned, and 100 mL of the crude oil sample is poured into it. The temperature of the temperature-controlled chamber is set to 71 °C. After a thermal stabilization period of 24 h, CO_2 is injected into the intermediate container to achieve an internal pressure of 16 MPa. The intermediate container is rotated to ensure sufficient contact between the crude oil and CO_2. After 12 h, the crude oil is extracted, and its structural characterization is performed using a gas chromatography-mass spectrometry (GC-MS) instrument. The temperature program for gas chromatography is as follows: hold at an initial temperature of 50 °C for 10 min, then increase the temperature at a rate of 5 °C/min until reaching 300 °C, and hold for 20 min.

(5) Determination of crude oil viscosity under experimental conditions.

First, the intermediate container is cleaned, and 500 mL of the crude oil sample is poured into it. The viscosity meter temperature is set to 71 °C. After a thermal stabilization period of 1 h, CO_2 is injected into the intermediate container to achieve an internal pressure of 16 MPa. The intermediate container is rotated to ensure sufficient contact between the crude oil and CO_2. After 2 h, the drop time is measured at different drop angles, and the crude oil viscosity is calculated using Equation (1). Five pressure points are simulated, and the viscosity meter is used to measure the changes in the crude oil viscosity under different supercritical CO_2 injection pressure conditions (10 MPa, 12 MPa, 14 MPa, 16 MPa, and 18 MPa). (The ball drop angle and time can be captured by a camera, and the data can be automatically recorded by an information collection system to minimize measurement errors).

$$\mu = kt(\rho_a - \rho_f) \tag{1}$$

t—Ball fall time;
ρ_a—Pellet density;
ρ_f—Crude oil density;
k—Fixed parameter (related to the drop angle of the ball).

3. Results and Discussion

3.1. Changes in Core Permeability before and after Huff-n-Puff

After supercritical CO_2 flooding in low-permeability reservoirs, the physical properties of the natural rock cores can be affected by the presence of supercritical CO_2. The permeability and porosity of the rock cores are essential parameters in this study. The permeability of natural rock cores Z1–Z6 before and after the supercritical CO_2 flooding was determined, and the experimental results are shown in Table 2 and Figure 2.

Table 2. Changes in core permeability.

Core Number	Raw Permeability (10^{-3} μm^2)	Post-Experimental Permeability (10^{-3} μm^2)
Z1	1.541	2.157
Z2	0.431	0.664
Z3	0.982	1.449
Z4	0.361	0.578
Z5	1.425	2.025
Z6	0.742	1.122

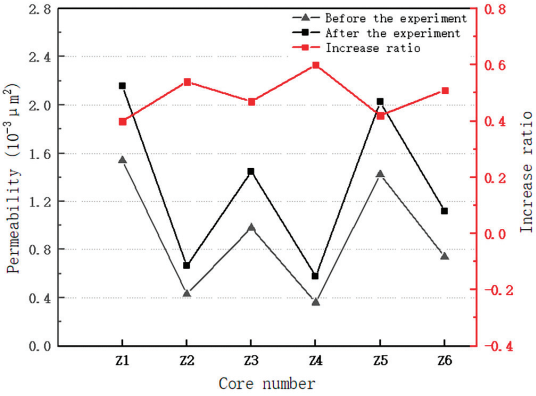

Figure 2. Permeability change curve.

The injected supercritical CO_2 dissolves in the remaining water within the rock cores, forming carbonic acid. After a prolonged soaking period, the minerals in the rock cores can undergo dissolution. The target zone rock cores contain a significant amount of feldspar and calcite, which readily reacts with carbonic acid, leading to dissolution and the creation of etched pores, thereby increasing the permeability of the rock cores. From Figure 2, it can be observed that the permeability of the natural rock cores undergoes varying degrees of increase after supercritical CO_2 flooding, with an increased ratio ranging from 40% to 60%. Among them, the increase in permeability is relatively small for Z2, Z3, Z4, and Z6 rock cores, with a permeability lower than 1×10^{-3} μm^2, while Z1 and Z5 exhibit a greater increase in permeability. This is because compared to rock cores with higher permeability, rock cores with lower permeability have a larger surface area of internal pore solid particles, making the dissolution effect of carbonic acid more pronounced.

3.2. Changes in Core Porosity before and after Huff-n-Puff

After supercritical CO_2 flooding, another property closely related to the permeability of low-permeability natural rock cores, the porosity of the rock cores, exhibits a more pronounced increase. This is mainly due to the injected supercritical CO_2 dissolving in the remaining water within the rock cores, forming carbonic acid, which has a dissolution effect on the minerals in the rock cores, resulting in etched pores and an increase in the porosity of the rock cores. The specific results can be seen in Table 3. Supercritical CO_2 can not only dissolve the matrix cement and increase the content of small pores but also dissolve medium-sized pores into larger ones. From Table 3 and Figure 3, it can be observed that the porosity of the experimental rock cores increases by 1.06% to 5.68% after supercritical CO_2 flooding. The increase in porosity is not significant for Z1 and Z6, which may be mainly due to the high content of calcite in the rock cores of this area. When calcite is dissolved by acid, the generated Ca^{2+} reacts with the subsequently produced carbonic acid to form secondary precipitation. As a result, the porosity of the natural rock cores initially decreases and then increases during the experimental process, leading to a relatively small overall change in porosity.

Table 3. Changes in core porosity.

Core Number	Raw Porosity/%	Post-Experimental Porosity/%
Z1	12.32	12.45
Z2	14.11	14.91
Z3	10.72	10.98
Z4	11.24	11.72
Z5	15.42	15.93
Z6	9.88	10.11

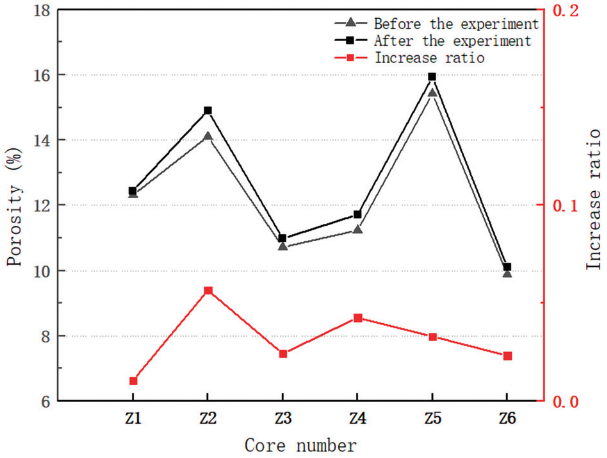

Figure 3. Porosity change curve.

As an acidic gas, CO_2 can generate weak acid when in contact with formation water. It can react with certain cementing materials and also inhibit the expansion of some viscosity particles. Additionally, it can react with abundant calcium carbonate present in the formation, forming bicarbonate. This reaction enables the slight dissolution of the rock surface, optimizing the pore structure and enhancing the permeability of the formation. As a result, the rock's fluid flow capacity is improved. This mechanism plays a crucial role in the enhanced oil recovery achieved through supercritical CO_2 injection.

3.3. Changes in Mineral Composition of Natural Core

After prolonged and multiple rounds of supercritical CO_2 flooding, a series of dissolution reactions between carbonic acid and pores, as well as other chemical reactions, result in changes in the mineral composition within the natural rock cores. The changes in the internal mineral composition of the natural rock cores before and after supercritical CO_2 flooding are shown in Table 4.

Table 4. Changes in core mineral composition before and after the experiment.

Core Number	Quartz Content/%		Feldspar Content/%		Calcite Content/%		Other Mineral Content/%	
	Before	**After**	**Before**	**After**	**Before**	**After**	**Before**	**After**
Z1	43.5	44.7	45.8	44.8	8.5	7.9	2.2	2.6
Z2	42.3	42.7	48.7	47.8	6.2	5.8	2.8	3.6
Z3	46.3	47.2	43.9	42.8	7.3	6.9	2.5	3.1
Z4	45.2	46.3	41.3	39.8	6.4	5.2	7.1	8.7
Z5	41.6	42.5	42.3	41.2	6.9	6.3	9.2	9.9
Z6	42.3	43.5	42.6	41.2	7.9	7.0	7.2	8.3

The natural rock cores in this area are mainly composed of quartz, feldspar (plagioclase + potassium feldspar), and calcite. From Table 4, it can be observed that before the experiment, the dominant component in the rock cores of this area was feldspar (plagioclase + potassium feldspar), accounting for approximately 50% of the total mineral content. Quartz was the second most abundant mineral, accounting for approximately 30–40% of the total mineral content, while calcite had the lowest abundance, accounting for approximately 10% of the total mineral content. The remaining minerals were other minerals (siderite + dolomite + clay). After supercritical CO_2 flooding, the content of quartz in the natural rock cores remained relatively stable or slightly increased. This is because quartz is not significantly involved in the physical and chemical reactions that occur during the experiment. However, the decrease in the content of other reacting components indirectly increases the proportion of quartz. During the experiment, carbonic acid mainly reacts with feldspar (plagioclase + potassium feldspar) and calcite, leading to a varying degree of reduction in the content of feldspar (plagioclase + potassium feldspar) and calcite within the natural rock cores. After supercritical CO_2 flooding, various changes occur within the natural rock cores, resulting in an increase in the proportion of other minerals.

3.4. Change in Oil–Water Wettability of Natural Core

After prolonged and multiple rounds of supercritical CO_2 flooding, the oil–water wettability of the natural rock cores changes due to the dissolution effect of carbonic acid on the porous medium. The variation in wettability of natural rock core Z4 before and after supercritical CO_2 flooding is shown in Figure 4.

(**a**) Before the experiment (**b**) Post-experiment

Figure 4. Z4 core water-phase wetting angle.

According to Figure 4, it can be observed that the water-phase contact angle of natural rock core Z4 decreased from 33.118° before the experiment to 25.336° after the experiment, representing a reduction of 23.5%. The strength of hydrophilicity varies among different minerals. In the studied block, the major minerals in the natural rock cores are quartz, feldspar (plagioclase + potassium feldspar), and calcite, with different degrees of hydrophilicity. The hydrophilicity of feldspar (plagioclase + potassium feldspar) and calcite is similar, while quartz exhibits higher hydrophilicity compared to these two minerals. The influence of the remaining minerals (siderite + dolomite + clay) can be neglected due to their relatively small proportion.

After prolonged and multiple rounds of supercritical CO_2 flooding, carbonic acid reacts with the internal pores of the rock cores, primarily involving feldspar (plagioclase + potassium feldspar) and calcite. As the content of these two minerals decreases, the content of quartz and other minerals (siderite + dolomite + clay), which do not participate in the reaction, increases. Due to the strong hydrophilicity of quartz, the natural rock core exhibits an enhancement in hydrophilicity after undergoing supercritical CO_2 flooding. Furthermore, when CO_2 dissolves in formation water, the resulting carbonic acid reacts with the rock, leading to the removal of the oil film on the rock's surface. As CO_2 continues to dissolve in the formation water, the aqueous CO_2 solution adsorbs on the surface of rock particles, forming a thin film of CO_2 solution, which alters the wettability of the rock.

3.5. Microscopic Changes in Porous Media

Based on the analysis above, it is evident that after the injection of supercritical CO_2 into the rock core pores, the carbonic acid formed by the dissolution of supercritical CO_2 in water reacts with the minerals in the rock core. This reaction leads to an increase in the permeability and porosity of the rock core. To further investigate the changes in the rock core pores after supercritical CO_2 injection, electron microscopy scans were conducted on sliced samples of all the experimental rocks. The results, using rock core Z2 as an example, are shown in Figure 5.

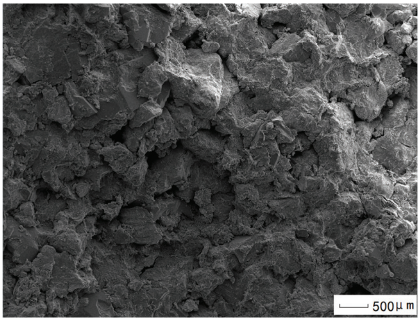

(**a**) Before the experiment

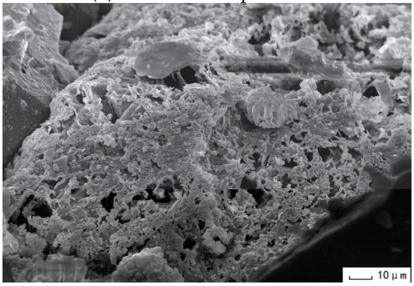

(**b**) Post-experiment

Figure 5. Comparison of micromorphology of natural core Z2 before and after the experiment.

From Figure 5a, it is evident that the internal porous medium of the rock core, without undergoing supercritical CO_2 flooding, is relatively dense, with poor connectivity and limited development of pores between particles. However, upon observing Figure 5b, it becomes clear that after supercritical CO_2 flooding, numerous small pores have appeared on the surface of the rock core particles. These small pores are formed due to the dissolution of the rock core particles by the carbonic acid generated during the supercritical CO_2 flooding process.

Furthermore, as a result of the reaction between calcite and the formed carbonic acid, the clay minerals that were bound by the cemented calcite undergo detachment. This causes the rock core to become more porous, improves connectivity, and facilitates the development of intergranular pores. Consequently, the permeability and porosity of the rock core increase.

3.6. Changes in the Properties of Crude Oil

To study the extraction characteristics of supercritical CO_2 on crude oil, a simulated contact reaction between crude oil and supercritical CO_2 was conducted under experimental conditions. After sufficient contact between crude oil and supercritical CO_2 under the experimental conditions, a comparison of the crude oil's total hydrocarbon composition before and after the experiment was measured using a gas chromatograph, as shown in Figure 6.

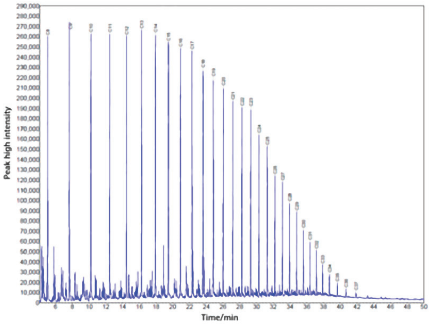

(**a**) Total hydrocarbon distribution of crude oil before experiment.

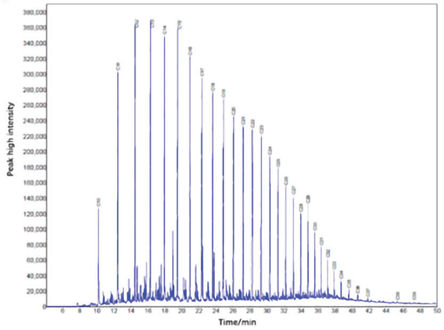

(**b**) Total hydrocarbon distribution of crude oil after experiment.

Figure 6. Change of total hydrocarbon of crude oil.

From Figure 6a, it is evident that the carbon number distribution of the crude oil sample in the experimental block is mainly concentrated in the range of C_8–C_{17}, with approximately 54.33% of the content being C_{17} and below. By comparing the two data graphs, it is clear that the crude oil undergoes significant changes in its total hydrocarbon composition due to the extraction effect of supercritical CO_2. Lighter components such as C_8–C_{10} are extracted by supercritical CO_2, resulting in a decrease of approximately 14.6% in their content. Specifically, C_8 and C_9 show a reduction of nearly 100%. As a result, heavier components such as C_{16}–C_{39} experience an increase in content by 6.99%. Therefore, supercritical CO_2 can extract light hydrocarbon components from crude oil, which can help improve the oil recovery rate.

The experimental study investigated the variation of crude oil viscosity under different supercritical CO_2 injection pressure conditions (10 MPa, 12 MPa, 14 MPa, 16 MPa, and 18 MPa). The data obtained from the experiment are presented in Table 5 and Figure 7.

Table 5. Crude oil viscosity under different CO_2 injection pressures.

Injection Pressure (Mpa)	Angle of Drop (°)	Drop Time (s)			Average Time (s)	Viscosity (mPa·s)	Average Viscosity (mPa·s)
		1	2	3			
10	22.5	1.17	1.17	1.17	1.17	3.94	4.64
	45	0.75	0.76	0.76	0.75	4.73	
	67	0.61	0.61	0.61	0.61	5.25	
12	22.5	1.19	1.20	1.19	1.19	4.02	4.49
	45	0.70	0.70	0.70	0.70	4.40	
	67	0.59	0.58	0.59	0.59	5.05	
14	22.5	1.14	1.14	1.14	1.14	3.84	4.34
	45	0.69	0.69	0.69	0.69	4.34	
	67	0.57	0.56	0.56	0.56	4.85	
16	22.5	1.12	1.12	1.13	1.12	3.79	4.26
	45	0.70	0.71	0.71	0.71	4.45	
	67	0.53	0.53	0.53	0.53	4.56	
18	22.5	1.08	1.08	1.08	1.08	3.64	3.96
	45	0.61	0.61	0.62	0.61	3.85	
	67	0.51	0.51	0.51	0.51	4.39	

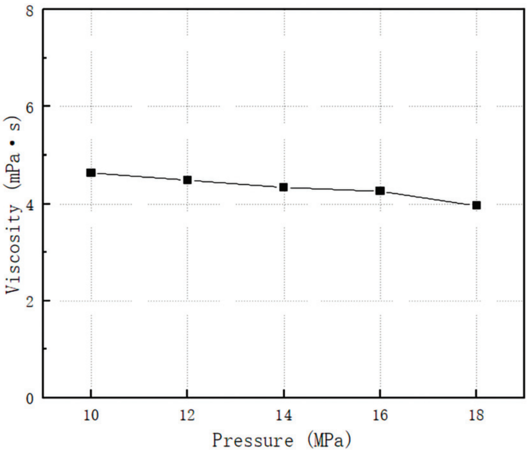

Figure 7. Crude oil viscosity under different CO_2 injection pressures.

From Table 5 and Figure 7, it is evident that supercritical CO_2 has a viscosity-reducing effect on crude oil. Consequently, the oil–water mobility ratio in the reservoir decreases after injecting supercritical CO_2. The reduction in the oil–water mobility ratio can enhance sweep efficiency, thereby increasing the oil recovery rate. Therefore, it can be observed that through supercritical CO_2 flooding, the light hydrocarbon components of the reservoir's crude oil are extracted, leading to a decrease in crude oil viscosity. This improves the fluid properties of the crude oil and enhances its flowability, which is beneficial for reducing residual oil saturation and, consequently, increasing the oil recovery rate.

Furthermore, the dissolution of CO_2 in crude oil reduces its viscosity. Therefore, the oil–water mobility ratio in the reservoir also decreases after CO_2 injection. The decrease in the oil–water mobility ratio can enhance sweep efficiency and thus increase the oil recovery rate. Additionally, some data indicate that the viscosity of water increases by more than 20% when CO_2 is dissolved in it [24,25]. With the increased viscosity of water and the decreased viscosity of crude oil, the oil–water mobility ratio is further reduced, which can improve sweep efficiency and ultimately enhance the oil recovery rate through the injection of supercritical CO_2.

3.7. Practical Application

The W119 fault block is located in the Ba County sag of the Jizhong Depression, with a structure resembling a castle-shaped nose on the Wen'an slope—the geological reserves in this block amount to 245.39 million metric tons (Mt). The average porosity of the fault block is 21%, with an average permeability of 20.8×10^{-3} μm^2. The viscosity of the reservoir crude oil is 18.8 mPa·s. Currently, the block has a daily oil production of 16.59 metric tons (t) with a high water cut of 95.59% and a recovery factor of 21.14%. The reservoir exhibits strong heterogeneity, and the main layers have long been the primary production zones. Additionally, the intrusion of bottom water has formed dominant water flow channels, leading to a decreasing effectiveness of water flooding over the years and severely constraining the development of the fault block.

In 2021, CO_2-flooding pilot tests were conducted in two well groups, W119-11 and W119-23. The test wells consisted of two injection wells and twelve production wells. By the end of 2022, a total of 1.8 thousand metric tons (kt) of CO_2 had been injected, resulting in an incremental oil production of 1.2 kt. However, after CO_2 flooding, the reservoir oil and its properties have changed, altering the flow characteristics and displacement mechanism. Due to the high gas–oil ratio, 87% of the shut-in wells are currently out of production in the test area, significantly affecting the development effectiveness of the experimental block.

To address this issue, adjustments were made to the injection parameters and methods of the two injection wells based on laboratory experiments and the dynamic production analysis of the oil wells (see Table 6). After adjusting the injection parameters in the pilot test-well group, the gas–oil ratio decreased to below 400 m/m, and the well opening rate increased to 95%. The daily oil production increased from 5.6 t to 15 t, resulting in a cumulative incremental oil of 5760 t. The recovery factor in the swept area improved by 0.23%, and the injection pressure increased by 3.5 MPa. By optimizing the injection method and reducing the amount of CO_2 injected, the cost per ton of oil was reduced by 10.2%.

Table 6. Comparison of injection parameters before and after adjustment in the test area.

Pound Sign	Before the Adjustment		After the Adjustment			
	Injection Volume/(t·d^{-1})	Injection Mode	Injection Volume/(t·d^{-1})		Injection Mode	Water-Air Ratio
			Supercritical CO_2	Water		
W119-11	30	Continuous gas injection	15	10	Alternation of water and air	1.5:1
W119-23	30		20	10		1:1

4. Conclusions and Suggestions

To address the lack of clear understanding regarding the changes in reservoir porous media and the fluid properties induced by supercritical CO_2 flooding, a study was conducted based on physical simulation experiments of supercritical CO_2 flooding on low-permeability natural rock cores. The aim was to investigate the variations in reservoir microstructure, permeability, porosity, mineral composition, and fluid composition before and after the experiments. The study analyzed the interaction patterns between supercritical CO_2 and the original reservoir, aiming to provide insights for enhancing development efficiency in low-permeability reservoirs in the Daqing Oilfield through the use of supercritical CO_2 flooding. However, this study mainly focuses on the changes in porosity, permeability, and mineral composition, and the experimental scope is relatively narrow. In future research, additional experiments related to capillary pressure and other relevant factors will be included to gain a more comprehensive understanding of reservoir dynamics and provide guidance for field operations.

(1) After prolonged supercritical CO_2 flooding, low-permeability natural rock cores exhibit a significant increase in permeability and porosity. This is primarily due to the reaction between the injected CO_2 and the simulated formation water, resulting in the formation of carbonic acid. Carbonic acid, being a weak acid, slowly acidifies the interior of the natural rock cores through its unique chemical properties. This reaction causes various minerals to react, ultimately leading to changes in the internal structure of the natural rock cores, improving the pore structure and physical properties. Therefore, supercritical CO_2 huff-n-puff can enhance the permeability of the formation and reduce gas injection pressure. However, reducing the injection pressure may result in a smaller affected area. Therefore, in subsequent injection adjustment processes, the addition of blocking agents should be considered for sealing off larger pathways and improving gas sweep efficiency.

(2) Under the erosive action of supercritical CO_2, the wettability of natural rock cores also changes, with increased inherent hydrophilicity. This is because different natural minerals exhibit varying wettability towards oil and water. Under the erosive action of supercritical CO_2, the content of less hydrophilic minerals like feldspar and calcite decreases, while the content of more hydrophilic quartz thus increases. As a result, the overall change in the physical properties of the natural rock cores is an enhancement in water-phase wettability. It is worth considering a transition from injecting pure supercritical CO_2 to alternating huff-n-puff with supercritical CO_2 and water injection, which can help achieve cost reduction objectives.

(3) Due to the decrease in the content of feldspar (plagioclase + potassium feldspar) and calcite, which participate in the erosive reaction, the proportion of quartz and other minerals not involved in the reaction significantly increases.

(4) By observing the microscopic morphology of the internal porous media of the rock cores before and after supercritical CO_2 flooding, we can observe that the pre-experiment porous media exhibits characteristics such as density, poor connectivity, and underdeveloped intergranular porosity. However, after the experiment, the porous media showed evident erosive phenomena, displaying loose, improved connectivity, and well-developed intergranular porosity, indicating favorable physical properties.

(5) Supercritical CO_2 exhibits a significant extraction effect on the experimental oil sample. After the flooding experiment, there are noticeable changes in the total light hydrocarbon components of the oil, with a decrease of approximately 14.6% in components such as C_8–C_{10} and an increase of 6.99% in heavier components such as C_{16}–C_{39}. Under the experimental conditions, the viscosity of the oil also decreases to a certain extent, indicating that supercritical CO_2 has a viscosity-reducing effect on the oil.

Therefore, in the field application of injecting supercritical CO_2 to enhance oil recovery, it is necessary to analyze the relationship between dissolution and extraction based on the interaction mechanism between supercritical CO_2 and crude oil (C) in conjunction with the reservoir pressure and temperature conditions. Optimal parameters for supercritical CO_2 huff-n-puff should be selected to improve the effectiveness of the technical application.

Using laboratory high-pressure experimental methods, the study investigated the changes in crude oil properties after supercritical CO_2 dissolution and quantitatively evaluated the variations in formation water and rock properties following CO_2 dissolution. It was found that after CO_2 dissolved in formation water, the pH of the water became acidic, leading to the rapid dissolution of reservoir minerals. As a result, the formation permeability increased by 40–60%, porosity increased by 1.06–5.68%, and the water contact angle decreased by 23.5%. The dual improvement of CO_2 on both crude oil and reservoir properties enhanced the oil's ability to flow within the formation, providing a theoretical basis for the development of heavy oil and low-permeability reservoirs.

In the CO_2 huff-n-puff pilot test wells of the W119 block, the development performance deteriorated after injecting 1.8×10^3 metric tons of carbon dioxide. Through laboratory experiments and dynamic analysis, adjustments were made to the injection parameters and methods, resulting in a daily oil production increase of 9.4 metric tons and effectively improving the development performance. This provides technical reserves for the design and dynamic adjustment of the injection and production parameters for the subsequent industrial-scale promotion of CO_2 flooding, with significant lessons and reference value.

Author Contributions: Methodology, G.Q.; Formal analysis, X.L.; Data curation, B.L.; Writing—original draft, X.T.; Funding acquisition, Y.L. All authors have read and agreed to the published version of the manuscript.

Funding: This work was supported by the General Program of the National Natural Science Foundation of China, titled "Research on the Multifield Coupled Percolation Mechanism of Fracturing Percolation Oil Displacement Method" (52074087).

Data Availability Statement: Data sharing not applicable.

Conflicts of Interest: The authors declare no conflict of interest.

References

1. Meng, C.; Zhigang, Y.; Ming, Z. Progress and Prospect of CCUS-EOR Engineering Technology. *Pet. Sci. Technol. Forum* **2023**, *42*, 49–56.
2. Song, X.; Wang, F.; Ma, D.; Gao, M.; Zhang, Y. Progress and prospect of carbon dioxide capture, utilization, and storage in CNPC oilfields. *Pet. Explor. Dev.* **2023**, *50*, 206–218. [CrossRef]
3. Hill, L.B.; Li, X.C.; Wei, N. CO_2-EOR in China: A comparative review. *Int. J. Greenh. Gas Control.* **2020**, *103*, 103173. [CrossRef]
4. Li, B.; Bai, H.; Li, A.; Zhang, L.; Zhang, Q. Experimental investigation on influencing factors of CO_2 huff and puff under fractured low-permeability conditions. *Energy Sci. Eng.* **2019**, *7*, 1621–1631. [CrossRef]
5. Min, R. The indissoluble bond between carbon dioxide and oil. *Pet. Knowl.* **2016**, *05*, 8–9.
6. Qin, J.; Han, H.; Liu, X. Application and enlightenment of carbon dioxide flooding in the United States of America. *Pet. Explor. Dev.* **2015**, *42*, 209–216. [CrossRef]
7. Abedini, A.; Torabi, F. On the CO_2, storage potential of cyclic CO_2, injection process for enhanced oil recovery. *Fuel* **2014**, *124*, 14–27. [CrossRef]
8. Jiang, H.; Shen, P.; Lu, Y.; Jiang, L.; Luo, J. Research on the current situation of CO_2 enhancing oil and gas recovery in the world. *Spec. Oil Gas Reserv.* **2010**, *17*, 5–10+120.
9. Zhao, L.; Jiang, E.; Wang, S.; Luo, Q.; Li, B.; Zhu, D.; Bai, H. Effect of carbon dioxide injection on mineral and pore structure in low permeability reservoir. *Oilfield Chem.* **2021**, *38*, 659–664+670.
10. Wang, X.; Zhang, Y.; Yan, X.; Wang, H.; Zhao, Y.; Tian, M.; Wang, W.; Wang, L.; Guo, Y. Analysis of supercritical carbon dioxide extraction on crude oil. *Oilfield Chem.* **2023**, *40*, 317–321.
11. Zhang, M.; Wang, L.; Cui, Q.; Hu, Y.; He, S. Experimental study on reservoir physical property change of carbon dioxide flooding. *World Pet. Ind.* **2023**, *30*, 90–96.
12. Liu, J.; Li, L.; Gao, M. Interaction of CO_2 and crude oil in low permeability reservoir. *Oilfield Chem.* **2021**, *38*, 464–469.
13. Chen, X.; Fan, Y. Study on CO_2 huff and puff technology in tight reservoir. *Petrochem. Ind. Appl.* **2021**, *40*, 8–12.
14. Shi, L. Damage characteristics of CO_2 huff and huff asphaltene deposits to reservoirs in tight sandstone reservoirs. *Oilfield Chem.* **2022**, *39*, 343–348.
15. Li, M.; Shan, W.; Liu, X.; Shang, G. Laboratory study on miscible oil displacement mechanism of supercritical carbon dioxide. *Acta Petrolei Sinica* **2006**, *27*, 80–83.
16. Wang, Q.; Yang, S.; Han, H.; Kun, Q.; Wang, L. Impact of CO_2 displacement methods on changes in physical properties of ultra-low permeability sandstone reservoirs. *J. China Univ. Pet. Ed. Nat. Sci.* **2020**, *44*, 124–133.
17. Zhou, T.; Liu, X.; Yang, Z.; Li, X.; Wang, S. Experimental analysis on reservoir blockage mechanism for CO_2 flooding. *Pet. Explor. Dev.* **2015**, *42*, 502–506. [CrossRef]
18. Sun, H.; Zhu, Y.; Wei, Y.; Gao, Y. Influence mechanism of acidification on oil recovery during CO_2 flooding. *Lithol. Reserv.* **2020**, *32*, 136–142.
19. Xia, H.; Xu, Y. Study on the Mechanism and Application of CO_2 Flooding in Low Permeability Reservoirs. *Contemp. Chem. Ind.* **2017**, *46*, 471–474.
20. Rathnaweera, T.D.; Ranjith, P.G.; Perera, M.S.A.; Haque, A.; Lashin, A.; Al Arifi, N.; Chandrasekharam, D.; Yang, S.Q.; Xu, T.; Wang, S.H.; et al. CO_2-induced mechanical behaviour of Hawkesbury sandstone in the Gosford basin: An experimental study. *Mater. Sci. Eng. A* **2015**, *641*, 123–137. [CrossRef]

21. Isaka, B.L.A.; Gamage, R.P.; Rathnaweera, T.D.; Perera, M.S.A.; Chandrasekharam, D.; Kumari, W.G.P. An influence of thermally-induced micro-cracking under cooling treatments: Mechanical characteristics of Australian granite. *Energies* **2018**, *11*, 1338. [CrossRef]
22. Wang, S.; Hou, J.; Zhao, F. Solubility of CO_2 in oil-water mixture and density of saturated CO_2 oil-water. *J. Xi'an Shiyou Univ. Nat. Sci. Ed.* **2012**, *27*, 39–42+57+8.
23. Li, Y.; Zhang, J.; Li, M. Study on Supercritical CO_2 Solubility in Heavy Oil and Heavy Oil Formation Volume Factor. *Sci. Technol. Eng.* **2013**, *13*, 53–57.
24. Lu, J. Numerical Simulation Study of CO_2 Huff and Puff about the Laws on the Control of Water in the Horizontal Wells of Heavy Oil. Ph.D. Thesis, China Petroleum of University, Beijing, China, 2016.
25. Lu, X.; Lu, P. Mechanism and application status of enhancing oil recovery by CO_2 immiscible flooding. *Pet. Geol. Eng.* **2007**, *02*, 58–61.

energies

Article

Mechanical and Acoustic Response of Low-Permeability Sandstone under Multilevel Cyclic Loading-Unloading Stress Paths

Hongying Tan [1,2], Hejuan Liu [2,3,*], Xilin Shi [2,3], Hongling Ma [2,3], Xiaosong Qiu [4], Yintong Guo [2,3] and Shengnan Ban [2,3]

[1] State Key Laboratory of Coal Mine Disaster and Control, Chongqing University, Chongqing 400044, China; tanhongying2021@126.com
[2] State Key Laboratory of Geomechanics and Geotechnical Engineering, Institute of Rock and Soil Mechanics, Chinese Academy of Sciences, Wuhan 430071, China; xlshi@whrsm.ac.cn (X.S.); hlma@whrsm.ac.cn (H.M.); ytguo@whrsm.ac.cn (Y.G.); b1270808901@163.com (S.B.)
[3] University of Chinese Academy of Sciences, Beijing 100049, China
[4] Key Laboratory of Underground Storage of Oil and Gas Engineer of China National Petroleum Corporation, Langfang 065007, China; qiuxiaos69@petrochina.com.cn
* Correspondence: hjliu@whrsm.ac.cn

Abstract: Low-permeability sandstone reservoirs have been widely used as a gas storage medium worldwide. Compared with the high porosity and high permeability of sandstone, low-permeability sandstone may present different mechanical (deformation, damage or failure) and acoustic responses under cyclic loading-unloading processes caused by the high-rate injection–production of underground gas storage. In this paper, multistage triaxial loading–unloading tests with a continuously increased upper limit of stress were carried out on low-permeability sandstone under six different confining pressures. The results showed that the superposition of stress–strain curves become much denser in the process of each level of stress. Based on the variation of the elastic modulus of low-permeability sandstone under alternating loads, the mechanical behavior of low-permeability sandstone under cyclic loading is divided into three stages: cyclic hardening, stability and cyclic softening. According to the evolution of acoustic emission (AE) signal parameters, AE counts appear intensively at the initial stage of each level of stress and then gradually stabilize. The peak frequency presents the zonal distribution, which is divided into low-frequency, intermediate-frequency and high-frequency zones. Low confining pressure leads to a small b-value. The RA–AF distribution implies that the mixed tensile–shear cracks are continuously generated in low-permeability sandstone during the cyclic loading process, and the shear cracks are more obviously developed.

Keywords: low-permeability sandstone; multilevel cyclic loading; confining stress; deformation; acoustic emission; microscopic cracks

Citation: Tan, H.; Liu, H.; Shi, X.; Ma, H.; Qiu, X.; Guo, Y.; Ban, S. Mechanical and Acoustic Response of Low-Permeability Sandstone under Multilevel Cyclic Loading-Unloading Stress Paths. *Energies* **2023**, *16*, 6821. https://doi.org/10.3390/en16196821

Academic Editor: Mofazzal Hossain

Received: 4 August 2023
Revised: 13 September 2023
Accepted: 21 September 2023
Published: 26 September 2023

1. Introduction

Sandstone is the main lithology type of depleted natural gas reservoirs converted into underground gas storage (UGSD), accounting for more than 60% of UGSDs [1–3]. The operation of UGSDs is characterized by cyclic high-rate injection and production of natural gas and frequent perturbation in the local stress state, which may strengthen the damage to the sandstone structure and affect the operation efficiency of the storage [4–8]. Therefore, it is important to study the effect of cyclic injection and extraction of gas in sandstone reservoirs on the damage evolution and development of fractures [9–12].

In recent years, extensive work has been carried out to study the mechanical behavior response of sandstone under complex stress paths [13–15]. Through a large number of experiments, it was found that the loading frequency [16], amplitude [17], stress level [13] and other factors of cyclic loading will affect the deformation behavior of sandstone. In addition, compared with simple cyclic loading, the current research pays more attention to the influence of multifactor synergy on the rock response, including temperature [18], crack angle [19], dry–wet cycles [20], confining pressure [21], permeability [22], etc. Many researchers have studied the mechanical response of reservoir low-permeability sandstone under complex stress paths [23–26]. However, research on cyclic loading under multi-stage constant amplitude cyclic loading at different formation depths (different confining pressures) is still limited.

The deformation characteristics of rocks during cyclic loading are difficult to monitor in real time [27]. The essence of the rock deformation process is the evolution, development, expansion and combination of microcracks [28,29]. In this process, the strain energy stored in the rock will be rapidly released in the form of transient elastic waves to produce acoustic emission (AE) [30]. Therefore, there is a close relationship regarding the deformation mechanism between the rock and AE. As a nondestructive testing method, AE is widely used to monitor the crack propagation and damage fracture process in real-time [31]. AE signals include a series of parameters, such as the number of AE events, energy, frequency and amplitude [32]. At present, most studies have studied the acoustic evolution mechanism in the process of rock deformation by analyzing the above parameters [33,34]. Most of them focus on the AE characteristics of rock failure under a single stress state, and research on the AE characteristics of rock under a complex stress state is limited.

In this paper, a series of triaxial cyclic compression experiments were carried out on low-permeability sandstone under different confining pressures. The loading path was a combination of constant amplitude cyclic loading and increasing amplitude cyclic loading. Macroscopically, the failure and deformation mechanism of low-permeability sandstone is revealed by analyzing the variations in typical mechanical parameters. Microscopically, the damage evolution process of internal cracks in rocks is analyzed based on real-time acoustic emission detection.

2. Materials and Methods

2.1. Low-Permeability Sandstone Samples and Test Equipment

The low-permeability sandstone samples used in this experiment were obtained from Shuanglong Town, ZiZhong County, Neijiang City, Sichuan Province, China. The bulk density of the low-permeability sandstone was 2400 kg/m^3. The porosity and permeability were 9.3% and 2.7 mD, respectively. The sandstone was composed mainly of quartz (83%), while clay minerals (e.g., chlorite, illite, kaolinite) accounted for 12.6% and carbonate minerals (calcite and iron dolomite) accounted for 4.4%. The microstructure of the low-permeability sandstone, observed by SEM imaging, is shown in Figure 1.

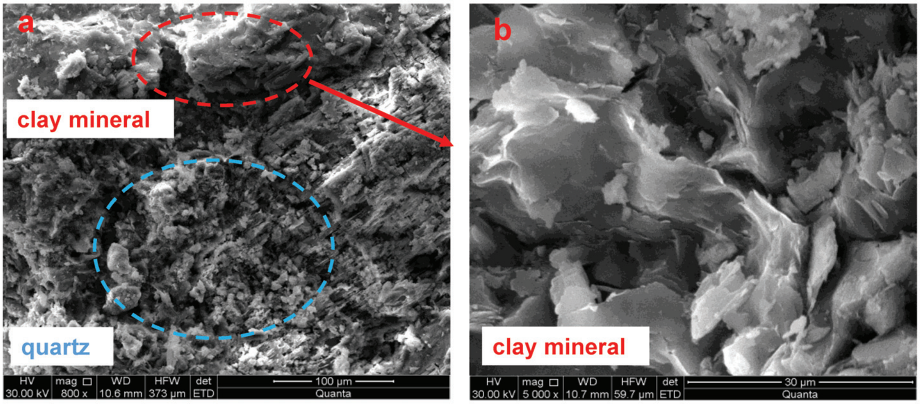

Figure 1. Microstructure of low-permeability sandstone observed by scanning electron microscopy (**a**), and partial enlarged view of clay minerals (**b**).

Fifteen cylindrical samples (50 mm in diameter and 100 mm in height) were used in triaxial compression experiments that were performed on an electrohydraulic servo-controlled rock mechanical rigidity tester (MTS815.04), as shown in Figure 2. It consists of a control system, oil source, loading frame, confining pressure system and various test fixtures and sensors. The cylindrical sample was enclosed in a heat-shrinkable tube, and the top and bottom of the rock sample were clamped by pads. Axial and transverse strains were obtained through strain sensors and extensometers fixed on the surface of the rock sample with chains.

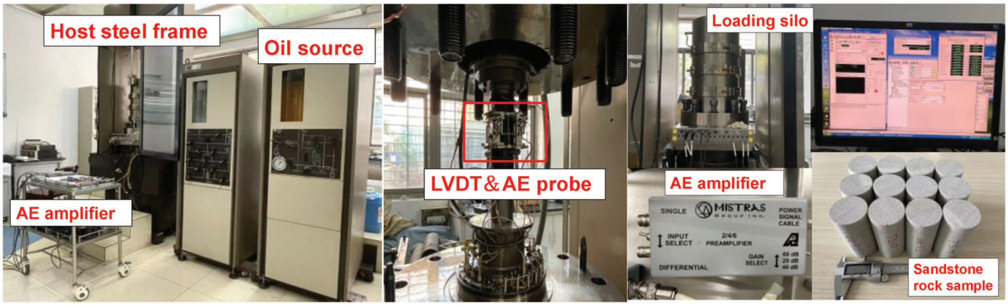

Figure 2. MTS815 experimental equipment and low-permeability sandstone samples.

2.2. Experimental Schemes

2.2.1. Experimental Parameters

Low-permeability sandstone reservoirs can also be used to store natural gas in underground gas storage (UGS) projects. Taking the Wen 23 UGS located in the Dongpu depression in the Henan Province of China as an example, the average porosity and permeability of low tertiary sandstone are 12.2% and 3.42 mD, respectively. It is designed as the largest UGS in east-central China, with a storage capacity of 10.4 billion m^3 [35].

The depths of UGSs in the world vary greatly. Most of the UGSs in Europe and the United States are constructed at depths of 300–1500 m, while the depths of UGSs in China are often in the range of 1000~5500 m, mostly at depths below 2000 m. It is meaningful to study the mechanical characteristics of low-permeability sandstone at different depths (i.e., different stress states) considering the alternating loading conditions in UGSs [36]. In this paper, confining pressures of 5 MPa, 10 MPa, 15 MPa, 20 MPa, 30 MPa and 40 MPa at a loading rate of 0.05 MPa/min were applied to simulate different buried depths of UGSs. Two types of triaxial compression tests were carried out. Conventional triaxial compression experiments can obtain the peak strength of low-permeability sandstone under different confining pressures. Cyclic loading experiments can be used to simulate the stress-path variation of a low-permeability sandstone reservoir during the gas injection and extraction process. The cyclic loading upper limits of 0.4, 0.6, 0.7, 0.8, 0.9 and 1.0 σ_m were designed based on the results of Martin et al. [37], considering crack initiation and expansion.

2.2.2. Experimental Procedures

In the conventional triaxial compression tests, the confining pressure was loaded to the desired value at a rate of 0.05 MPa/s, and then the axial stress was applied to the top of the sample at a constant displacement loading rate of 0.06 mm/min until the sample was completely damaged and the peak strength σ was obtained. In the triaxial cyclic compression experiments, six levels of loading stress (defined as the ratio of loading stress to static compressive strength) were set at 0.4, 0.6, 0.7, 0.8, 0.9 and 1.0. The lower limit stress of the cycle was 10 MPa. Each stress level was repeated twenty times. The specimen was loaded at a rate of 4 kN/s. If failure occured for the sample during the cyclic loading-unloading process, the experiment was terminated. If failure did not occur after the designed cyclic loading-unloading experiments, the conventional compression test was performed until the sample was destroyed. As shown in Figure 3, the stress path is a combination of constant-amplitude and incremental-amplitude cyclic loading.

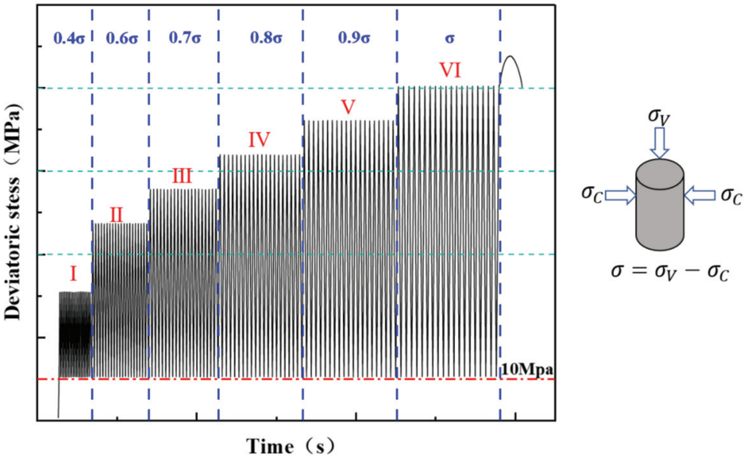

Figure 3. Schematic diagram of multilevel and multicycle loading paths (I–VI represent six maximum axial stress levels 0.4σ_c, 0.6σ_c, 0.7σ_c, 0.8σ_c, 0.9σ_c, σ_c).

3. Results and Discussion

3.1. Stress-Strain Curves under Different Confining Stresses

3.1.1. Stress-Strain Curves after Conventional Triaxial Compression Tests

Conventional triaxial compression tests were performed to obtain the peak strength of the low-permeability sandstone. Figure 4 shows the deviatoric stress-strain curves under confining pressures of 5 MPa, 10 MPa, 15 MPa, 20 MPa, 30 MPa and 40 MPa. According to the experimental results, the triaxial compressive strength increases with the increase in confining pressure. With the rise of confining pressure, the brittleness of the rock decreases and the plasticity increases. The conventional triaxial compression test results are summarized in Table 1. The elastic modulus of the rocks increases accordingly with the confining pressure, but the Poisson's ratio has no obvious fluctuation.

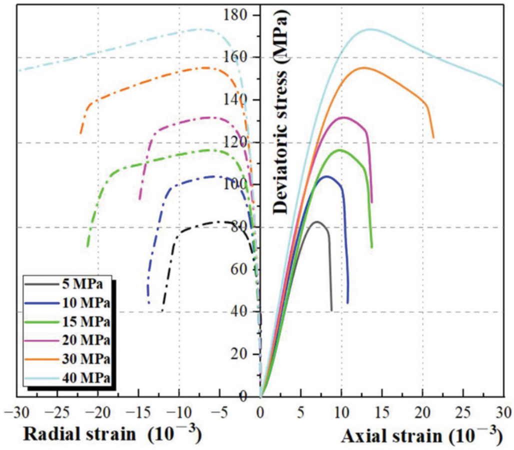

Figure 4. Stress-strain curve of low-permeability sandstone under different confining pressures (The dotted line represents the radial strain curve, and the solid line represent the axial strain curve).

Table 1. Basic geometric and mechanical parameters of low-permeability sandstone samples.

Confining Pressure (MPa)	Length (mm)	Diameter (mm)	Peak Strength (MPa)	Peak Strength under Cyclic Load (MPa)	Increment (%)	Elastic Modulus (GPa)	Poisson's Ratio (-)
5	100.44	49.77	83.14	87.51	5.26	16.39	0.29
10	100.45	49.80	104.51	108.27	3.64	18.31	0.32
15	100.65	49.86	116.99	125.38	7.17	17.86	0.29
20	100.56	49.80	132.24	138.31	4.59	19.74	0.24
30	100.57	49.83	155.87	163.63	4.98	19.63	0.24
40	100.42	49.97	173.43	178.16	2.73	22.07	0.29

3.1.2. Stress-Strain Curves after Cyclic Loading-Unloading Triaxial Compression Tests

The deviatoric stress-axial strain curves obtained by multistage cyclic loading-unloading experiments are shown in Figure 5. Under cyclic loading-unloading processes, the stress-strain curves of low-permeability sandstone do not overlap, and hysteresis loops appear [38,39]. The strain evolution under different confining pressures presents similar trends, and the hysteresis loops of each level gradually become dense with the increase in the number of loading-unloading cycles. At the beginning of the experiments, large plastic deformation occurred due to the instantaneous increase in the stress, and more plastic strain energy was absorbed due to the mutual friction between the crystals and the extension of microcracks, and then the plastic deformation was limited [14]. The larger area of the plastic hysteresis loop occurred at a high level of the stress state, indicating the accumulation of plastic deformation related to the sprouting, expansion and merging of cracks in low-permeability sandstone. In addition, the peak strength of the low-permeability sandstone after multistage cyclic loading-unloading processes was greater than that of the conventional loading triaxial compression experiments, which can be explained by the hardening phenomenon due to the cyclic loading-unloading process [17].

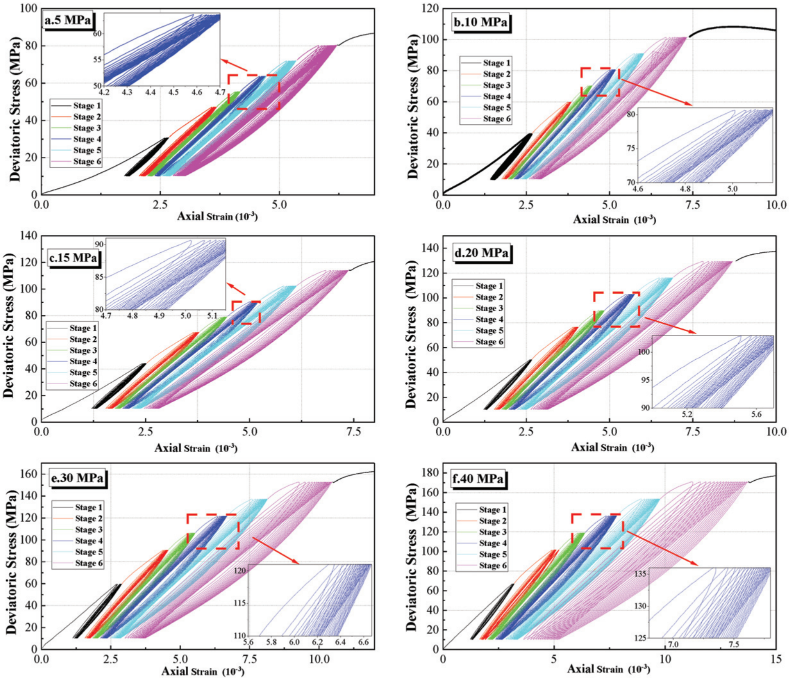

Figure 5. Deviatoric stress-axial strain curves after cyclic loading-unloading experiments with different confining pressures. ((**a**–**f**): 5 MPa, 10 MPa, 15 MPa, 20 MPa, 30 MPa and 40 MPa).

3.2. Evolution of Deformation Parameters after Cyclic Loading-Unloading Tests

3.2.1. Evolution of the Elastic Modulus

The linear part of the stress-strain curve at each cyclic loading phase was used to calculate the dynamic elastic modulus of low-permeability sandstone [40]. Figure 6a shows the trend of the elastic modulus of low-permeability sandstone samples under different confining pressures with increasing cycles and stress levels. It can be seen that the evolution of the elastic modulus has a strong consistency, presenting an obvious step-down trend with increasing stress level and cycle number, and the decreasing rate is accelerated with increasing confining pressure.

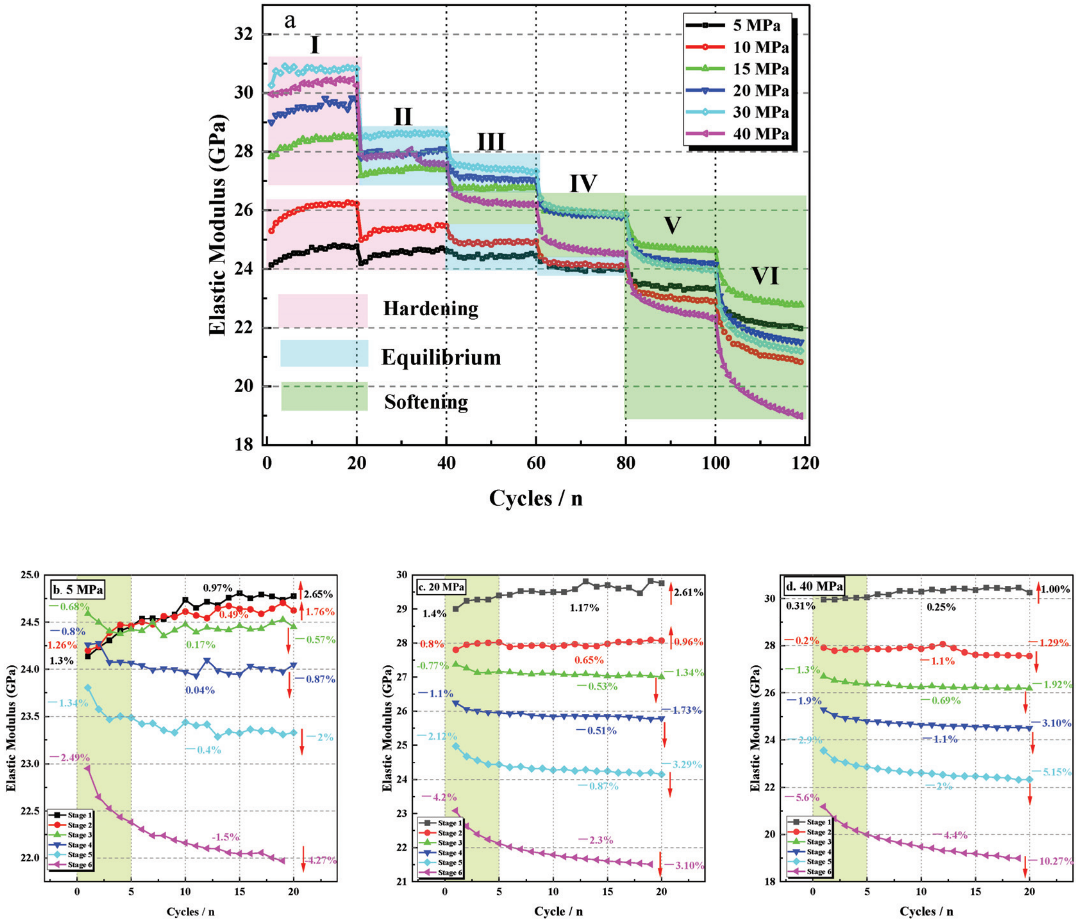

Figure 6. Evolution of the elastic modulus: (**a**) under different confining pressures (I–VI represent six maximum axial stress levels $0.4\sigma_c$, $0.6\sigma_c$, $0.7\sigma_c$, $0.8\sigma_c$, $0.9\sigma_c$, σ_c); (**b**–**d**) under confining pressures of 5, 20 and 40 MPa, respectively.

The evolution of the elastic modulus during the cyclic loading-unloading processes can be divided into three stages: (I) The growth stage (or the cyclic hardening stage) occurs when the designed upper limit stress is low. During this stage, the deformation of low-permeability sandstone caused by cyclic loading is small because the rock is compressed and the connection between the particles is strengthened under high confining pressures, which greatly restricts the damage extension [41,42]. (II) The equilibrium stage is represented by a near-stable elastic modulus at intermediate stress levels. The equilibrium section appears earlier under high confining pressure, indicating that a high confining pressure plays a role in suppressing damage. (III) The decline stage (or the cyclic softening stage) occurs when the designed upper limit stress is high. After the equilibrium stage, the high stress level and the increasing number of cycles lead to new cracks and pores, resulting in an obvious damage effect, especially for rocks under high confining pressure, and the decline in the elastic modulus is most obvious. Figure 6b–d, taking 5 MPa, 20 MPa and 40 MPa as examples, shows the elastic modulus increments of the first 5 cycles, the last 15 cycles and each stress level. The elastic modulus change at each stress level can be divided into two modes: (I) a rapid increasing or decreasing trend of the elastic modulus at the beginning of cyclic loading due to obvious deformation under the initiation, connection or closure of microcracks or pores, and (II) gradual stabilization in subsequent cyclic loading-unloading processes.

3.2.2. Evolution of Irreversible Strain

The elastic deformation of rocks is recovered during unloading, but the irreversible deformation, also called residual deformation, remains [42,43]. Figure 7a,b shows the variation in the irreversible axial strain with the number of cycles under different confining pressures. When the confining pressure is low (5 MPa, 10 MPa and 15 MPa), the irreversible axial strain of the low-permeability sandstone decreases with an increase in confining pressure, reflecting that a high confining pressure can inhibit the initiation and development of cracks [14]. However, when the confining pressure is high (20 MPa, 30 MPa and 40 MPa), the plastic strain increases with an increase in confining pressure.

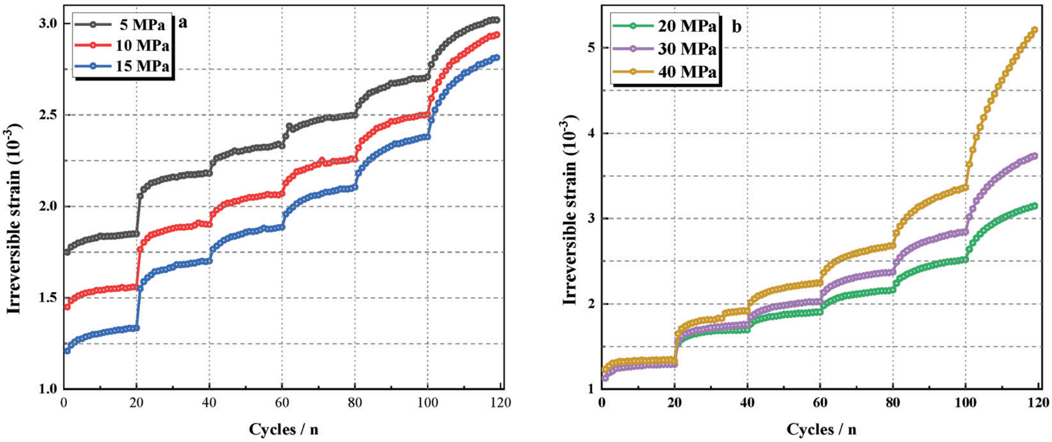

Figure 7. Variation in the axial irreversible strain with the number of cycles under the cyclic loading process: (**a**) with confining pressures of 5, 10 and 15 MPa; (**b**) with confining pressures of 20, 30 and 40 MPa.

3.3. Acoustic Emission (AE) Characteristics during Cyclic Loading-Unloading on Low-Permeability Sandstone

3.3.1. AE Count Characteristic Analysis

Time domain features such as acoustic emission (AE) count, AE energy, RMS and information entropy can be used to analyze the deformation, damage and failure evolution of rocks [44–46]. AE count analysis can reveal the development of internal microcracks during the stress loading-unloading process. Figure 8 shows the relationship between axial stress, AE counts (cumulative counts) and test time under different confining pressures. With increasing stress level, the accumulated AE counts showed a step increase trend, and the increase rate of the accumulated AE counts gradually increased. This indicates that the development rate of cracks and microcracks in the rocks gradually increases with increasing stress level. At the beginning of the loading phase, a large number of intensive AE count signals are generated, and then the count signals are sparse and remain constant. This is because the rock sample is instantaneously compressed in the axial direction at the beginning of each stress level, resulting in the variation in internal structure with the initiation and expansion of microcracks; thus, the AE activity increases accordingly [33]. Afterwards, the cracks develop slowly, and the internal structure does not change, stabilizing AE activity. Several jump points of AE counts occur during the steady deformation of one loading stage, as shown in Figure 8, indicating that the interior structure of the rock samples is damaged, causing the accumulated strain energy to be released and the sudden changes in the AE count.

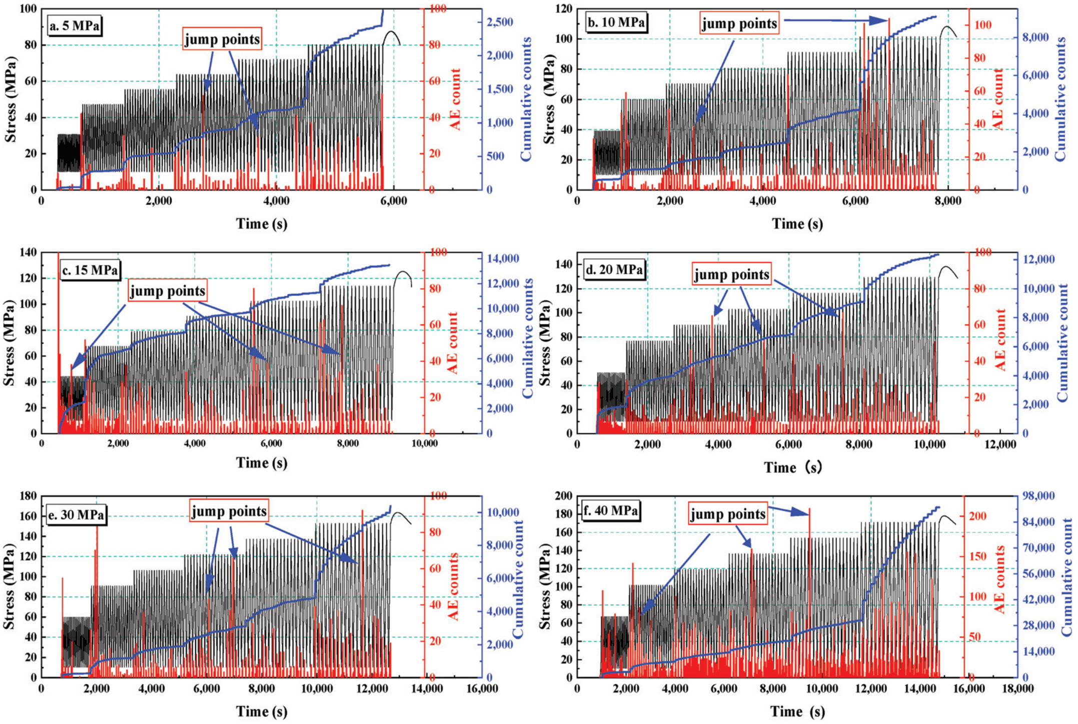

Figure 8. Relationship between axial stress, AE count (cumulative count) and time under different confining pressures: (**a**–**f**) represent 5 MPa, 10 MPa, 15 MPa, 20 MPa, 30 MPa and 40 MPa, respectively. (Red: AE count; Blue: AE Cumulative Count; Black: Axial Stress).

To further investigate the continuous development of cracks in low-permeability sandstone in a single cycle at different stress levels, Figure 9a–f shows the relationship between AE counts and time at the first five cycles of each stress level stage with a confining pressure of 10 MPa. Frequent and intensive AE count signals appeared in the initial period of each level, and then the activity of AE signals gradually decreases with the increase in the number of cycles. This corresponds to the initial and stable deformation in the rock samples at each level of stress. With increasing stress level (stages 1–6), the peak value and activity of the AE signal gradually increase, indicating that the internal microcracks in the rock sample continue to develop as the stress level increases. Compared with the unloading stage, there are more AE count signals in the loading stage, which indicates that the microcracks in the rock sample are obviously developed in the bearing stage.

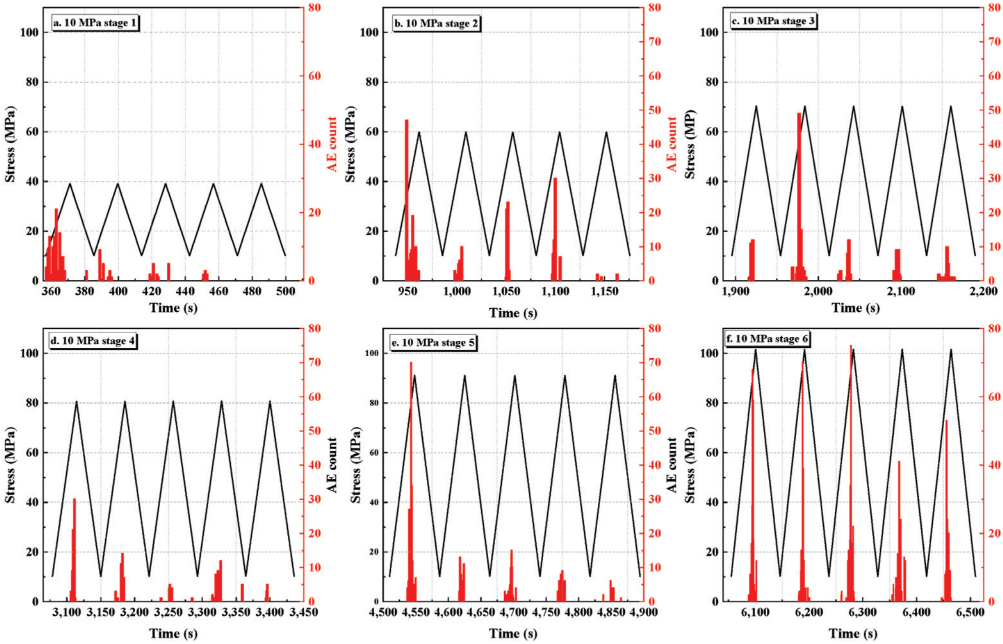

Figure 9. The evolution of AE counts with time in the first 5 cycles of axial stress loading and unloading process under a confining pressure of 10 MPa. (stage 1~stage 6 represent six different maximum axial stress levels $0.4\sigma_c$, $0.6\sigma_c$, $0.7\sigma_c$, $0.8\sigma_c$, $0.9\sigma_c$, σ_c).

3.3.2. Frequency–Amplitude Characteristics Analysis

Frequency is a critical parameter for analyzing the rock failure mechanism and revealing the internal stress state of rocks during loading. Different AE frequencies reflect different source mechanisms and types of cracks. Low-frequency AE signals correspond to large-scale cracks, whereas high-frequency AE signals correlate with small-scale cracks.

Figure 10 shows the variation in peak frequencies with time during the cyclic loading-unloading process. The peak frequency of rocks under cyclic loading is mainly concentrated in three frequency bands: low frequency, medium frequency and high frequency. Medium-frequency signal events widely exist throughout the cycle, and low-frequency and high-frequency signal events are few. Under low confining pressures (5 MPa, 10 MPa and 15 MPa), low-frequency signals only appear when the stress level increases, and their number is small; a high-frequency signal is concentrated in the final monotonic loading section. Under high confining pressures (20 MPa and 30 MPa), low-frequency signals and high-frequency signals only appear at high stress levels and in the final monotonic loading section; however, some lower-frequency (approximately 100 kHz) signals appear in the intermediate-frequency signal range. When the confining pressure is 40 MPa, the high-frequency signal is continuous and dense. This indicates that a higher stress level and confining pressure tend to cause denser cracks. Under high confining pressure, the intermediate-frequency signal of each stress level gradually decreases with the increase of the number of cycles, which may be because the sudden increase in stress level leads to the formation of cracks, and then the crack development gradually stabilizes. It is worth mentioning that when the number of AE events of low, intermediate and high frequencies increases simultaneously (simultaneous multifrequency response) due to the initiation of cracks, the range of the peak frequency zone becomes wider [47], as shown in Figure 10.

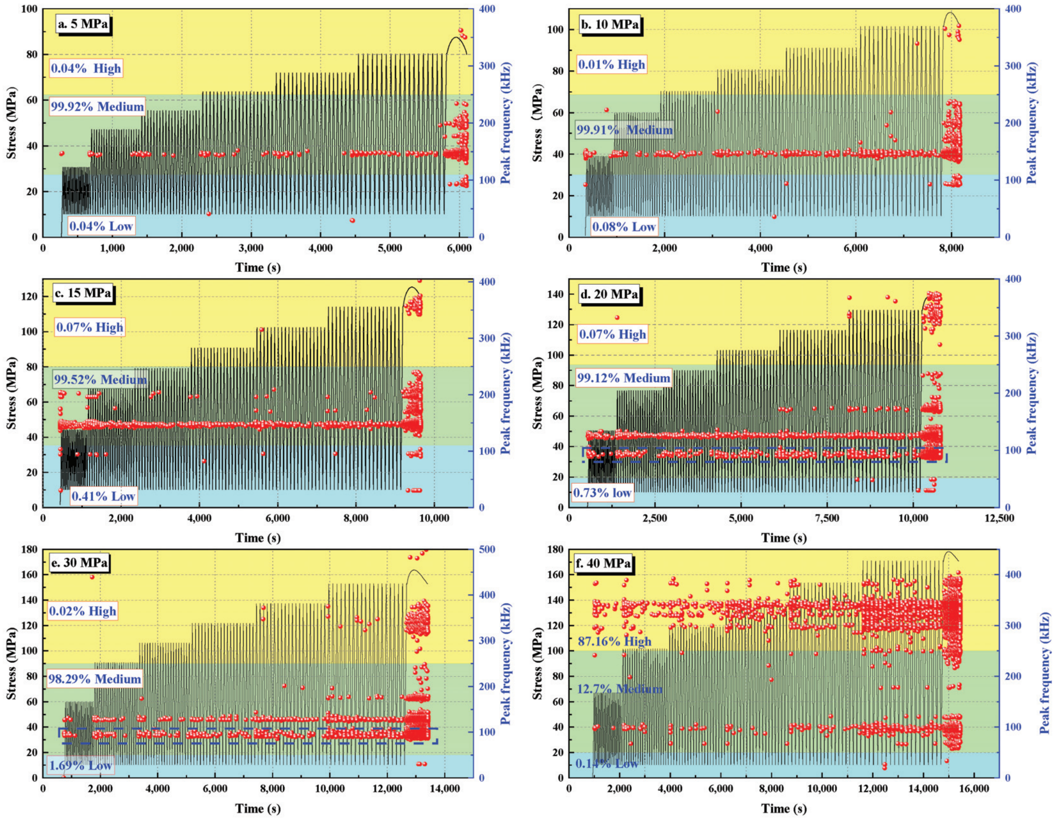

Figure 10. Variations in peak frequency with time during cyclic loading: (**a**–**f**) represent 5, 10, 15, 20, 30 and 40 MPa confining pressure. (Blue part is low frequency, green part is intermediate frequency and yellow part is high frequency).

The amplitude signal is also a key factor in describing the damage and failure of rocks [48]. Figure 11a–f show the relationship between the peak frequency and the normalized peak amplitude of AE. The medians after the peak amplitudes were normalized are 0.518 at 5 MPa, 0.55 at 10 MPa, 0.479 at 15 MPa, 0.62 at 20 MPa, 0.56 at 30 MPa and 0.55 at 40 MPa, respectively. The peak amplitude is accordingly divided into low and high components. AE signals with median and high-peak frequencies are generally characterized by high-peak amplitude, and different confining pressures present similar trends. The higher the confining pressure is, the denser the high-frequency signal is, which indicates that the internal cracks of the high confining pressure rock sample develop actively.

To better analyze the spectral frequency characteristics, the AE signals are classified into six types according to the peak frequency (low, intermediate and high) and amplitude (low and high) [33], as shown in Figure 12, which shows the variation in peak frequency, amplitude and stress with time under different confining pressures. Overall, the high-amplitude medium-frequency (HAMF) signal and the low-amplitude medium-frequency (LAMF) signal always existed throughout the experiment, and the initial appearance time of the other signals are described in Table 2. High-amplitude high-frequency (HAHF) signals appear sparsely when the low permeability sandstone is damaged under low confining pressures (5, 10 and 15 MPa). HAHF signals appear densely when the cyclic stress is close to peak strength and the sandstone samples are at failure under high confining pressures (20, 30 and 40 MPa). This means that the appearance of HAHF signals represents a drastic change in the upper limit of the cyclic stress on the sandstone or that the sandstone samples are damaged. The appearance of low-amplitude low-frequency (LALF) signals and low-amplitude high-frequency (LAHF) signals indicates that samples have begun to rupture.

Table 2. Statistics of the initial occurrence time of different signals.

Samples	HAHF	LAHF	HALF	LALF
TS-5	Failure	--	Stage4-No.2	Stage6-No.1
TS-10	Stage1-No.1	--	--	Stage4-No.17
TS-15	Stage4-No.2	Failure	Stage1-No.1	Stage1-No.1
TS-20	Stage2-No.1	Stage6-No.1 (More at Failure)	Failure	Stage1-No.3 (More at Failure)
TS-30	Stage5-No.1	Failure	--	Failure
TS-40	Stage1-No.1	Stage1-No.1	--	Stage6-No.6

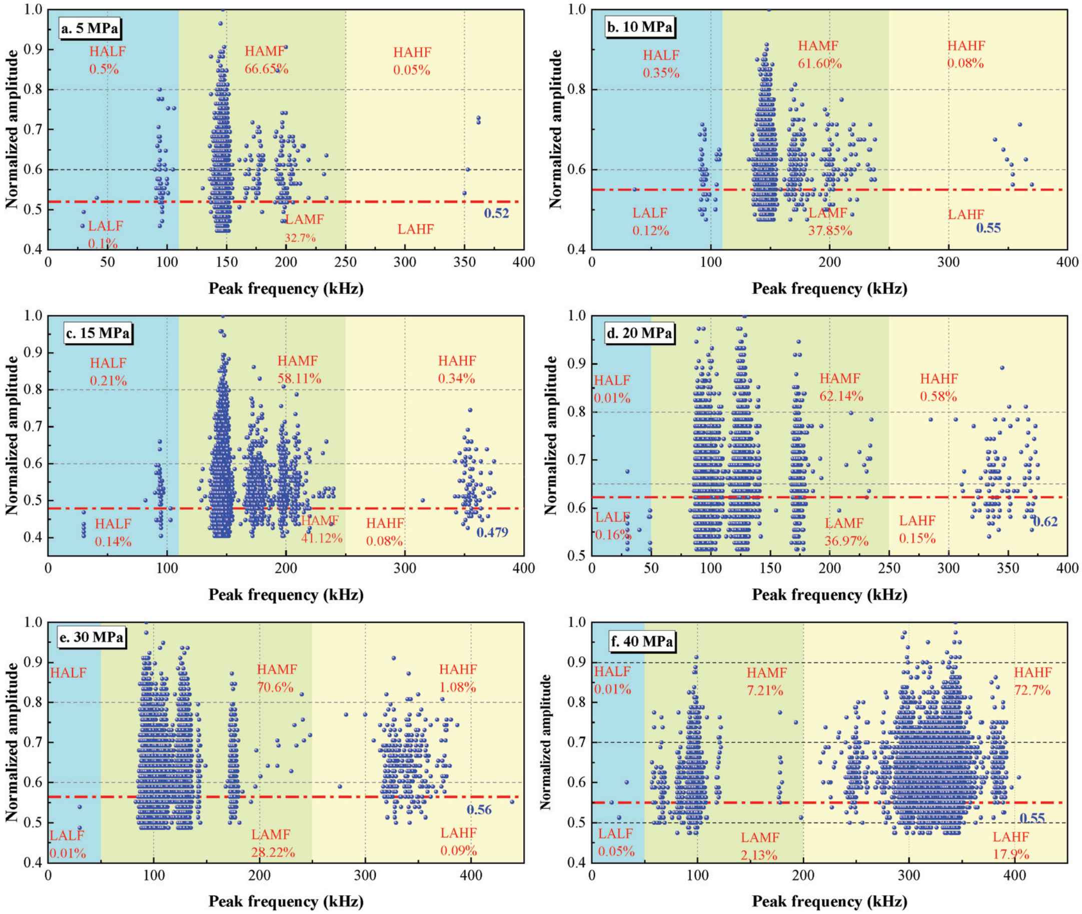

Figure 11. Relationship between peak frequency and normalized amplitude under different confining pressures ((**a**–**f**): 5 MPa, 10 MPa, 15 MPa, 20 MPa, 30 MPa and 40 MPa; the red line is the median after normalization of the amplitude).

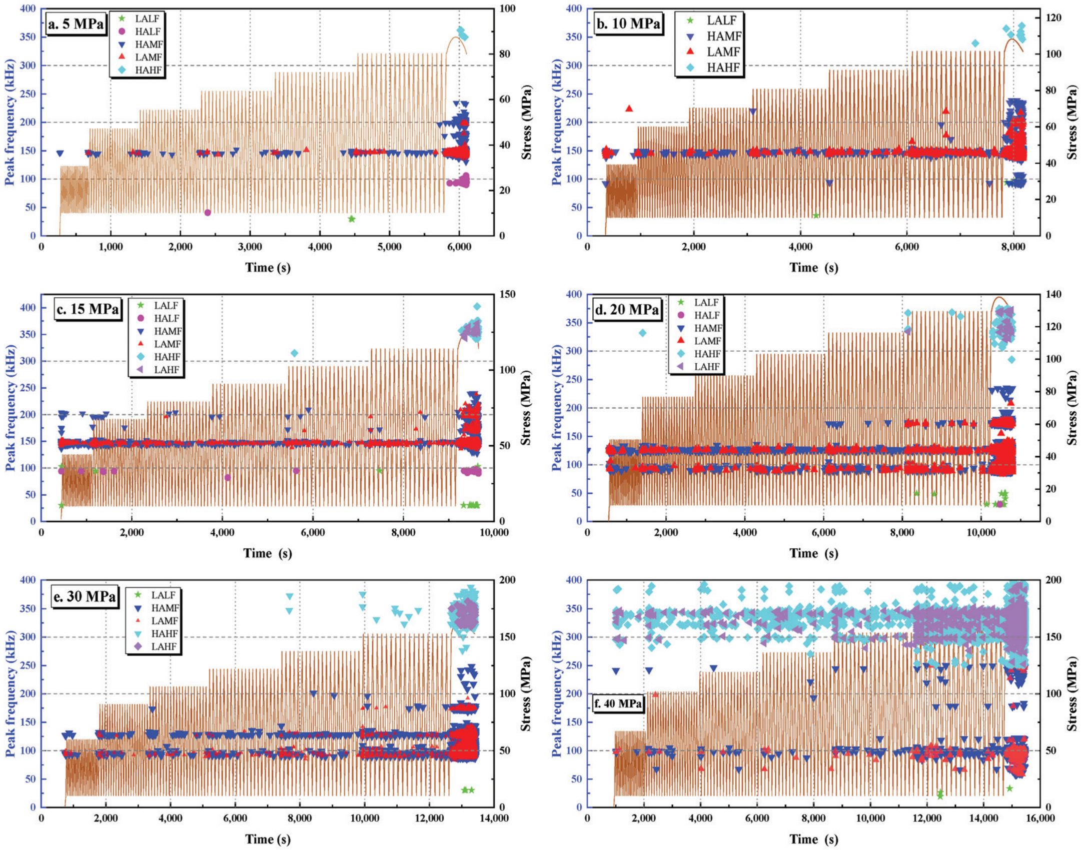

Figure 12. Variations in peak frequency, amplitude and axial stress with time under different confining pressures ((**a**–**f**): 5 MPa, 10 MPa, 15 MPa, 20 MPa, 30 MPa and 40 MPa).

3.3.3. b-Value Analysis

The b-value is widely used to describe the evolution of crack initiation and development to distinguish between macroscopic and microscopic cracks [49]. The well-known "G-R" law can describe the relationship between frequency and amplitude [50]:

$$M = \frac{A_{dB}}{20} \tag{1}$$

$$\log_{10} N = a - bM \tag{2}$$

where M denotes the AE magnitude, A_{dB} is the peak amplitude of the AE event, N is the number of AE signals with amplitudes greater than A_{dB}, a is the fitting parameter and b is the b-value. According to the acquisition frequency of the acoustic emission experiment, every $5A_{dB}$ is set as a calculation period to prevent a large error due to a small calculation interval; that is, the magnitude M increases sequentially by 0.25.

The overall magnitude and variation trend of the b-value are closely related to the development of cracks in the rocks. A high b-value indicates slow initiation and expansion of microcracks and an increased proportion of small-amplitude AE events. Conversely, a low b-value indicates rapid or unstable crack initiation and an increased proportion of large-amplitude AE events [51,52].

To quantitatively study the amplitude characteristics of the AE signal during cyclic loading, Figure 13a–f show the statistical distribution of the peak amplitude of low-permeability sandstone during cyclic loading under different confining pressures. With an increase in confining pressure, the amplitude range of AE has no obvious change. The AE amplitude of low-permeability sandstone under different confining pressures is mainly in the range of 40–45 dB, the average value of AE amplitude is approximately 45 dB, and the median value is 44–45 dB. With the increase in AE amplitude, the AE count and amplitude under different confining pressures show similar variation trends. The AE counts in each amplitude range gradually decrease. The relationship between AE count and amplitude can be described by an exponential function, and the coefficients of determination (R^2) are 0.97, 0.85, 0.82, 0.96, 0.91 and 0.92 under confining pressures from 5 MPa to 40 MPa (Figure 13).

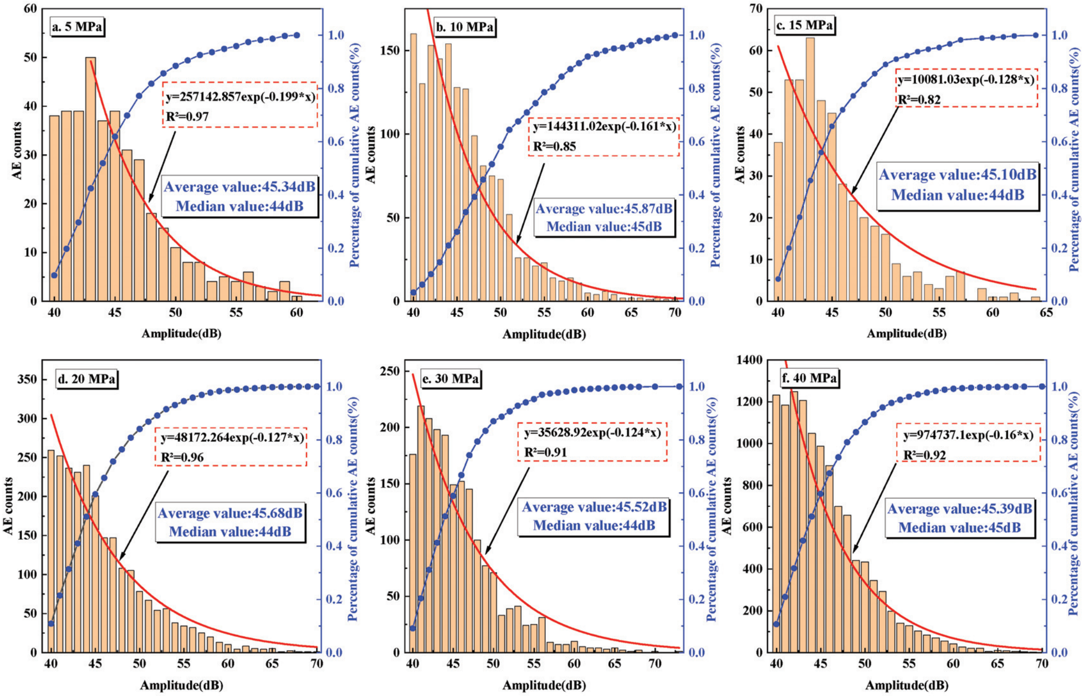

Figure 13. Statistical distribution of macroscopic AE counts under cyclic loading ((**a**–**f**) represent the confining pressures of 5 MPa, 10 MPa, 15 MPa, 20 MPa, 30 MPa and 40 MPa; blue line is the cumulative curve of macroscopic AE counts, and the red line is the fitting curve of amplitude and macroscopic AE counts).

By fitting the straight-line part of the accumulated magnitude distribution curve, the slope of the fitted line is b, and the intercept is a. Figure 14a shows the b-value of the AE signal and the fitting curve used to determine the b-value. The fitting coefficient is high, which shows that the b-value obtained by using the AE data is relatively accurate [53]. The b-values at confining pressures of 5, 10, 15, 20, 30 and 40 MPa are 1.976, 2.055, 2.069, 2.1746, 1.968 and 2.3273, respectively. This indicates that the b-value shows an increasing trend with increasing confining pressure, indicating that crack initiation is faster and more unstable at low confining pressure than under high confining pressure.

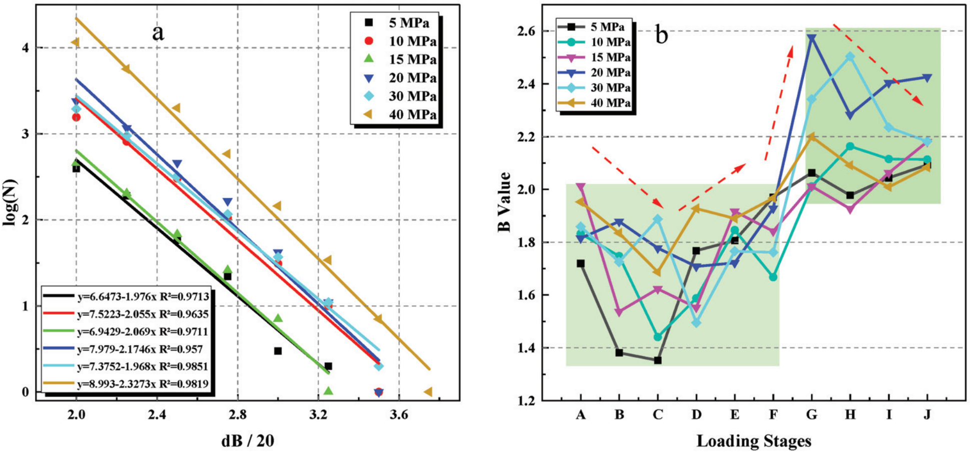

Figure 14. Changes in the b-value in the process of cyclic loading: (**a**) equation fitting to obtain the b-value; (**b**) the relationship between the b-value and loading stages. A–F refer to the first to sixth stages, respectively, and G–J refer to 1/4, 1/2, 3/4 and 1 of the monotonous loading stage, respectively.

To better reflect the damage mechanisms of low-permeability sandstone during cyclic loading and unloading, Figure 14b shows the evolution of the b-value under different confining pressures with increasing cycle number and stress level. It can be divided into the fluctuation stage of cyclic loading (first to sixth stress level) and the decreasing stage of monotonic loading. At the beginning of the cyclic phase, the b-value fluctuates slightly, showing a decreasing trend at first, and gradually increasing as the stress level increases. In the monotonic loading phase, the b-value is greater than that of the cyclic loading phase, and it shows a declining trend. Larger b-values indicate relatively larger fractures in rocks [53], and decreasing b-values indicate that the rocks are approaching the damage state [54,55]. Thus, a decreasing and then increasing b-value implies that internal damage gradually occurs in rocks during the cyclic loading-unloading process, followed by unstable extension and coalescence of fractures. Larger-scale cracks occurred in the monotonic loading process compared with those of the cyclic phase. The b-value underwent a drastic fluctuation throughout the loading process, which indicates that the damage behavior of the rocks is more complex during the experiment and should be further analyzed.

3.3.4. RA–AF Distribution Analysis

The RA (ratio of the rise time to the amplitude)–AF (ratio of the number of hits to the duration) distribution of AE events is widely used to determine the failure modes of various materials [36,49–52]. Generally, AE signals due to tensile damage of rocks are characterized by high AF and low RA, while AE signals obtained from shear damage exhibit the opposite characteristics [34,56,57]. Therefore, the damage pattern and evolution of damage in low-permeability sandstone under a complex stress state can be analyzed by the RA–AF value.

Figure 15 shows the trend of the RA–AF distribution during cyclic loading and unloading of low-permeability sandstone under different confining pressures and the range of distribution of RA and AF (90% of the values are within the general value range). The RA and AF values of samples with different confining pressures (5–30 MPa) exhibited similar variation trends. At a low stress level (stage 1–5), the RA–AF value only rises when the stress level increases, and then the fluctuation gradually stabilizes. As the stress level gradually reaches the peak strength of low-permeability sandstone, the RA–AF value gradually increases. This indicates that the abrupt increase in stress causes obvious initiation and propagation of cracks in rocks. The AF value increases slightly at the beginning of each stress level and then fluctuates steadily. The RA value not only increases significantly at the initial stage of each stress level, but also has multiple jump points that increase sharply by several times in the constant amplitude period. This may imply that the tensile and shear cracks are continuously generated in rocks, and shear cracks develop distinctly. At high stress levels (stage 6), the RA–AF values are continuous and intensive. In addition, the RA–AF value under a high confining pressure (40 MPa) is generally larger than that under other confining pressures.

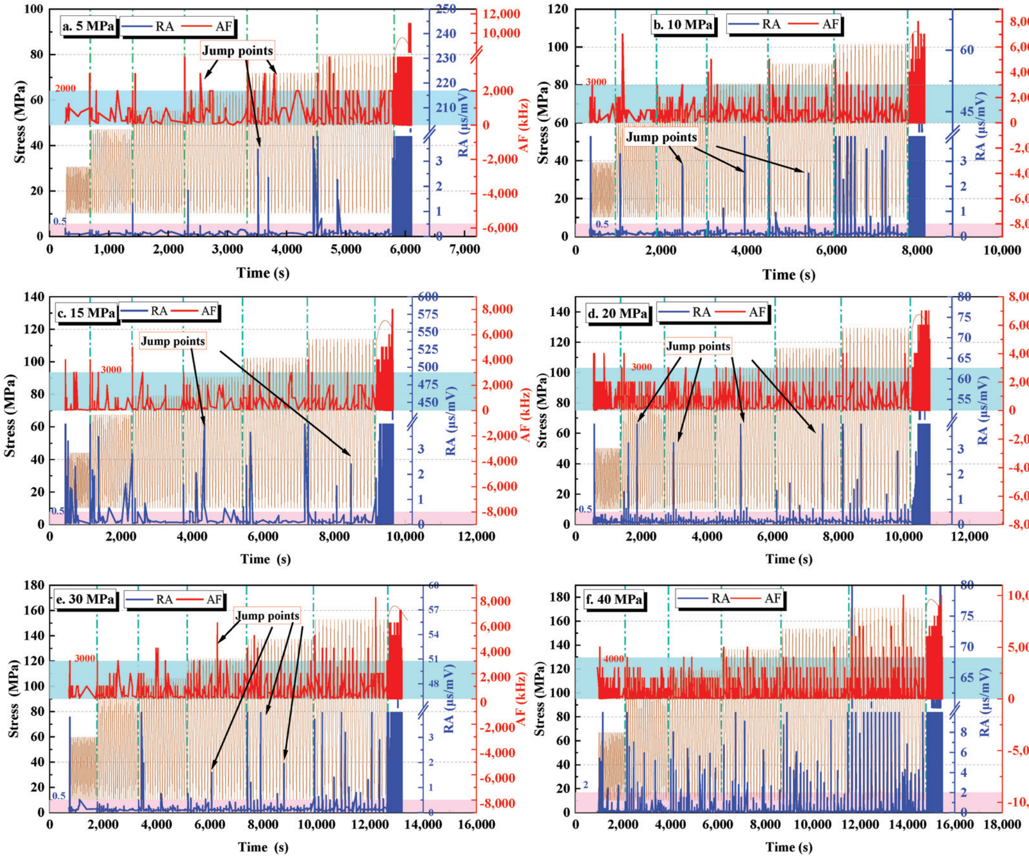

Figure 15. Variation in RA and AF during cyclic loading under different confining pressures (red and blue lines represent RA and AF, respectively, and brown lines represent stress paths).

4. Conclusions

Low-permeability sandstone reservoirs of depleted gas fields can also be used to store natural gas. In this paper, both conventional triaxial compression tests and multistage constant and incremental amplitude cyclic loading-unloading experiments were carried out on low-permeability sandstone specimens under different confining pressures. The mechanical properties of low-permeability sandstone were systematically studied considering the impacts of confining pressure, number of cycles and cyclic stress level, and the analysis of acoustic emission signals was used to indirectly reflect the initiation and propagation of microcracks in rocks. Some main conclusions are drawn as follows:

1. Compared with conventional triaxial compression experiments, the peak strength of the low-permeability sandstone increased slightly (less than 10%) after multi-stage

constant-amplitude cyclic loading and unloading processes. Based on the variation characteristics of the elastic modulus, the mechanical behavior of low-permeability sandstone under cyclic loading is divided into three stages: the cyclic hardening stage, the mechanical stability stage and the cyclic softening stage.

2. The evolution of AE counts implies that microcracks in rocks develop actively and then gradually stabilize at the initial stage of each level of stress. The evolution of the AE cumulative count shows that the internal cracks of low-permeability sandstone develop obviously with an increase in confining pressure and stress level.
3. The AE frequency signals show a zonal distribution, and they present the same trends under different confining pressures. The intermediate-frequency signals are the dominant type, and the low-frequency and high-frequency signals only appear under high stress, indicating that large cracks appeared under high-stress conditions.
4. The variation of the AE b-value reflects that the internal cracks of rocks initiate faster under low confining pressure than under high confining pressure. The decrease in the b-value in the cyclic loading and unloading stage indicates that damage occurs in the rocks, while the increase in the b-value in the monotonic compression stage indicates that larger cracks initiate in the rocks. The distribution of the RA–AF value shows that the mixed tensile–shear cracks are continuously generated in low-permeability sandstone during the cyclic loading process, and the development of shear cracks is more obvious.

Author Contributions: H.T.: Writing—original draft, Investigation, Methodology. H.L.: Investigation, Visualization, Conceptualization, Review and editing. X.S.: Conceptualization, Funding acquisition. H.M.: Data curation, Review and editing. X.Q.: Project administration. Y.G.: Formal analysis. S.B.: Visualization. All authors have read and agreed to the published version of the manuscript.

Funding: The authors would gratefully like to acknowledge the financial support from the CAS Pioneer Hundred Talents Program (Y826031C01), National Natural Science Foundation (U22A20166), Key Research and Development Program of Hubei Province (Nos. 2022BAA093, 2022BAD163), Major Science and Technology Research and Development Special Program of Jiangxi Provincial (2023ACG01004).

Data Availability Statement: Data will be made available on request.

Conflicts of Interest: The authors declare that they have no known competing financial interest or personal relationships that could have appeared to influence the work reported in this paper.

References

1. Yang, X.; Cheng, L.; He, X.; Geng, T.; Li, C. A Prediction Method for Multi-Stage Injection and Recovery Capacity of Underground Gas Storage. *Nat. Gas Ind.* **2013**, *33*, 96–99. [CrossRef]
2. Matos, C.R.; Carneiro, J.F.; Silva, P.P. Overview of Large-Scale Underground Energy Storage Technologies for Integration of Renewable Energies and Criteria for Reservoir Identification. *J. Energy Storage* **2019**, *21*, 241–258. [CrossRef]
3. Liu, H.; Yang, C.; Liu, J.; Hou, Z.; Xie, Y.; Shi, X. An Overview of Underground Energy Storage in Porous Media and Development in China. *Gas Sci. Eng.* **2023**, *117*, 205079. [CrossRef]
4. Qiu, X.; Liu, H.; Liu, M.; Mao, H.; Wang, D.; Ying, Q.; Ban, S. Pore Structure Evolution in Sandstone of Underground Gas Storage during Cyclic Injection and Production Based on Nuclear Magnetic Resonance Technology. *Energies* **2023**, *16*, 2096. [CrossRef]
5. Molíková, A.; Vítězová, M.; Vítěz, T.; Buriánková, I.; Huber, H.; Dengler, L.; Hanišáková, N.; Onderka, V.; Urbanová, I. Underground Gas Storage as a Promising Natural Methane Bioreactor and Reservoir? *J. Energy Storage* **2022**, *47*, 103631. [CrossRef]
6. Tang, Y.; Hu, S.; He, Y.; Wang, Y.; Wan, X.; Cui, S.; Long, K. Experiment on CO_2-Brine-Rock Interaction during CO_2 Injection and Storage in Gas Reservoirs with Aquifer. *Chem. Eng. J.* **2021**, *413*, 127567. [CrossRef]
7. Song, R.; Wang, Y.; Tang, Y.; Peng, J.; Liu, J.; Yang, C. 3D Printing of Natural Sandstone at Pore Scale and Comparative Analysis on Micro-Structure and Single/Two-Phase Flow Properties. *Energy* **2022**, *261*, 125226. [CrossRef]
8. Liu, H.; Hou, Z.; Were, P.; Gou, Y.; Sun, X. Numerical Investigation of the Formation Displacement and Caprock Integrity in the Ordos Basin (China) during CO_2 Injection Operation. *J. Pet. Sci. Eng.* **2016**, *147*, 168–180. [CrossRef]
9. Song, R.; Liu, J.; Yang, C.; Sun, S. Study on the Multiphase Heat and Mass Transfer Mechanism in the Dissociation of Methane Hydrate in Reconstructed Real-Shape Porous Sediments. *Energy* **2022**, *254*, 124421. [CrossRef]

10. Mahmoodpour, S.; Singh, M.; Bär, K.; Sass, I. Thermo-Hydro-Mechanical Modeling of an Enhanced Geothermal System in a Fractured Reservoir Using Carbon Dioxide as Heat Transmission Fluid—A Sensitivity Investigation. *Energy* **2022**, *254*, 124266. [CrossRef]
11. Mahmoodpour, S.; Singh, M.; Turan, A.; Bär, K.; Sass, I. Simulations and Global Sensitivity Analysis of the Thermo-Hydraulic-Mechanical Processes in a Fractured Geothermal Reservoir. *Energy* **2022**, *247*, 123511. [CrossRef]
12. Shaibu, R.; Sambo, C.; Guo, B.; Dudun, A. An Assessment of Methane Gas Production from Natural Gas Hydrates: Challenges, Technology and Market Outlook. *Adv. Geo-Energy Res.* **2021**, *5*, 318–332. [CrossRef]
13. Hu, M.; Xu, W.; Wang, H.; Ning, Y.; Wang, R.; Lyu, C.; Zhang, T. Deformation Characteristics of Muddy Sandstones during Cyclic Loading and Unloading with Different Stress Lower Limits under Pore Pressure. *Int. J. Fatigue* **2023**, *172*, 107606. [CrossRef]
14. Jia, C.; Xu, W.; Wang, R.; Wang, W.; Zhang, J.; Yu, J. Characterization of the Deformation Behavior of Fine-Grained Sandstone by Triaxial Cyclic Loading. *Constr. Build. Mater.* **2018**, *162*, 113–123. [CrossRef]
15. Xu, T.; Tian, H.; Zhu, H.; Cai, J. China Actively Promotes CO_2 Capture, Utilization and Storage Research to Achieve Carbon Peak and Carbon Neutrality. *Adv. Geo-Energy Res.* **2022**, *6*, 1–3. [CrossRef]
16. Liu, E.; Huang, R.; He, S. Effects of Frequency on the Dynamic Properties of Intact Rock Samples Subjected to Cyclic Loading under Confining Pressure Conditions. *Rock Mech. Rock Eng.* **2012**, *45*, 89–102. [CrossRef]
17. Bagde, M.N.; Petroš, V. Fatigue Properties of Intact Sandstone Samples Subjected to Dynamic Uniaxial Cyclical Loading. *Int. J. Rock Mech. Min. Sci.* **2005**, *42*, 237–250. [CrossRef]
18. Wang, M.; Li, J.; Tan, H.; Wang, J.; Shi, Z.; Li, K. Study on Fatigue Characteristics and Thermal Damage Mechanism of Red Sandstone under High Temperature-Cyclic Load Coupling. *Int. J. Fatigue* **2023**, *168*, 107405. [CrossRef]
19. Wang, J.; Li, J.; Shi, Z.; Chen, J. Fatigue Damage and Fracture Evolution Characteristics of Sandstone under Multistage Intermittent Cyclic Loading. *Theor. Appl. Fract. Mech.* **2022**, *119*, 103375. [CrossRef]
20. Tan, H.; Li, J.; Shi, Z.; Wang, M.; Wang, J.; Li, J. Damage Evolution and Failure Characteristics of Red Sandstone with Prefabricated Crack under Coupled Dry–Wet Cycle-Fatigue Loading. *Int. J. Fatigue* **2023**, *175*, 107751. [CrossRef]
21. Yang, S.-Q.; Ranjith, P.G.; Huang, Y.-H.; Yin, P.-F.; Jing, H.-W.; Gui, Y.-L.; Yu, Q.-L. Experimental Investigation on Mechanical Damage Characteristics of Sandstone under Triaxial Cyclic Loading. *Geophys. J. Int.* **2015**, *201*, 662–682. [CrossRef]
22. Zhou, J.; Deng, G.; Tian, S.; Xian, X.; Yang, K.; Zhang, C.; Dong, Z. Experimental Study on the Permeability Variation of Sandstone at Cyclic Stress: Implication for Underground Gas Storage. *J. Energy Storage* **2023**, *60*, 106677. [CrossRef]
23. Bagde, M.N.; Petroš, V. Waveform Effect on Fatigue Properties of Intact Sandstone in Uniaxial Cyclical Loading. *Rock Mech. Rock Eng.* **2005**, *38*, 169–196. [CrossRef]
24. Ray, S.K.; Sarkar, M.; Singh, T.N. Effect of Cyclic Loading and Strain Rate on the Mechanical Behaviour of Sandstone. *Int. J. Rock Mech. Min. Sci.* **1999**, *36*, 543–549. [CrossRef]
25. Shirani Faradonbeh, R.; Taheri, A.; Karakus, M. Failure Behaviour of a Sandstone Subjected to the Systematic Cyclic Loading: Insights from the Double-Criteria Damage-Controlled Test Method. *Rock Mech. Rock Eng.* **2021**, *54*, 5555–5575. [CrossRef]
26. Yang, C.; Liu, J. Petroleum Rock Mechanics: An Area Worthy of Focus in Geo-Energy Research. *Adv. Geo-Energy Res.* **2021**, *5*, 351–352. [CrossRef]
27. Li, H.; Ma, H.; Yang, C.; Zhao, K.; Hu, Z.; Daemen, J.J.K. Acoustic Emission Characteristics of Rock Salt under Multi-Stage Cyclic Loading. *Int. J. Fatigue* **2023**, *176*, 107911. [CrossRef]
28. Rodríguez, P.; Celestino, T.B. Application of Acoustic Emission Monitoring and Signal Analysis to the Qualitative and Quantitative Characterization of the Fracturing Process in Rocks. *Eng. Fract. Mech.* **2019**, *210*, 54–69. [CrossRef]
29. Zhao, K.; Yang, D.; Zeng, P.; Huang, Z.; Wu, W.; Li, B.; Teng, T. Effect of Water Content on the Failure Pattern and Acoustic Emission Characteristics of Red Sandstone. *Int. J. Rock Mech. Min. Sci.* **2021**, *142*, 104709. [CrossRef]
30. Li, S.; Yang, D.; Huang, Z.; Gu, Q.; Zhao, K. Acoustic Emission Characteristics and Failure Mode Analysis of Rock Failure under Complex Stress State. *Theor. Appl. Fract. Mech.* **2022**, *122*, 103666. [CrossRef]
31. Fan, J.; Chen, J.; Jiang, D.; Chemenda, A.; Chen, J.; Ambre, J. Discontinuous Cyclic Loading Tests of Salt with Acoustic Emission Monitoring. *Int. J. Fatigue* **2017**, *94*, 140–144. [CrossRef]
32. Zhao, K.; Ma, H.; Liang, X.; Li, X.; Liu, Y.; Cai, R.; Ye, L.; Yang, C. Damage Evaluation of Rock Salt under Multilevel Cyclic Loading with Constant Stress Intervals Using AE Monitoring and CT Scanning. *J. Pet. Sci. Eng.* **2022**, *208*, 109517. [CrossRef]
33. Zhao, K.; Ma, H.; Yang, C.; Daemen, J.J.K. The Role of Prior Creep Duration on the Acoustic Emission Characteristics of Rock Salt under Cyclic Loading. *Int. J. Rock Mech. Min. Sci.* **2022**, *157*, 105166. [CrossRef]
34. Li, Z.; Suo, J.; Fan, J.; Fourmeau, M.; Jiang, D.; Nelias, D. Damage Evolution of Rock Salt under Multilevel Amplitude Creep–Fatigue Loading with Acoustic Emission Monitoring. *Int. J. Rock Mech. Min. Sci.* **2023**, *164*, 105346. [CrossRef]
35. Chang, D.; Hu, J.; Guo, H.; Duo, T.; Yang, J.; Cheng, F. Dynamic Analysis of Wen 23 Gas Storage. *Highlights Sci. Eng. Technol.* **2022**, *25*, 175–180. [CrossRef]
36. Ma, X.; Zheng, D.; Wei, G.; Ding, G.; Zheng, S. Development directions of major scientific theories and technologies for underground gas storage. *Nat. Gas Ind.* **2022**, *42*, 93–99.
37. Martin, C.D.; Chandler, N.A. The Progressive Fracture of Lac Du Bonnet Granite. *Int. J. Rock Mech. Min. Sci. Geomech. Abstr.* **1994**, *31*, 643–659. [CrossRef]
38. Jaeger, J.; Cook, N.; Zimmerman, R. *Fundamental of Rock Mechanics*; Wiley: Hoboken, NJ, USA, 2007.

39. Zhao, G.; Guo, Y.; Chang, X.; Jin, P.; Hu, Y. Effects of Temperature and Increasing Amplitude Cyclic Loading on the Mechanical Properties and Energy Characteristics of Granite. *Bull. Eng. Geol. Environ.* **2022**, *81*, 155. [CrossRef]
40. Lin, H.; Liu, J.; Yang, J.; Ran, L.; Ding, G.; Wu, Z.; Lyu, C.; Bian, Y. Analysis of Damage Characteristics and Energy Evolution of Salt Rock under Triaxial Cyclic Loading and Unloading. *J. Energy Storage* **2022**, *56*, 106145. [CrossRef]
41. Xie, H.; Gao, F.; Ju, Y. Research and development of rock mechanics in deep ground engineering. *Chin. J. Rock Mech. Eng.* **2015**, *34*, 2161–2178. [CrossRef]
42. Zhao, G.; Chang, X.; Guo, Y.; Yang, H.; Guo, W.; Hu, Y. Fatigue of Granite Subjected to Cyclic Loading at Various Temperatures: Experimental Insights from Deformation and Energy Conversion. *Geomech. Geophys. Geo-Energy Geo-Resour.* **2022**, *8*, 64. [CrossRef]
43. Liu, Y.; Ma, T.; Wu, H.; Chen, P. Investigation on Mechanical Behaviors of Shale Cap Rock for Geological Energy Storage by Linking Macroscopic to Mesoscopic Failures. *J. Energy Storage* **2020**, *29*, 101326. [CrossRef]
44. Du, K.; Li, X.; Tao, M.; Wang, S. Experimental Study on Acoustic Emission (AE) Characteristics and Crack Classification during Rock Fracture in Several Basic Lab Tests. *Int. J. Rock Mech. Min. Sci.* **2020**, *133*, 104411. [CrossRef]
45. Barile, C.; Casavola, C.; Pappalettera, G.; Kannan, V.P. Application of Different Acoustic Emission Descriptors in Damage Assessment of Fiber Reinforced Plastics: A Comprehensive Review. *Eng. Fract. Mech.* **2020**, *235*, 107083. [CrossRef]
46. Chai, M.; Hou, X.; Zhang, Z.; Duan, Q. Identification and Prediction of Fatigue Crack Growth under Different Stress Ratios Using Acoustic Emission Data. *Int. J. Fatigue* **2022**, *160*, 106860. [CrossRef]
47. Jiang, Z.; Li, Q.; Hu, Q.; Liang, Y.; Xu, Y.; Liu, L.; Wu, X.; Li, X.; Wang, X.; Hu, L.; et al. Acoustic Emission Characteristics in Hydraulic Fracturing of Stratified Rocks: A Laboratory Study. *Powder Technol.* **2020**, *371*, 267–276. [CrossRef]
48. Scholz, C.H. Microfracturing and the Inelastic Deformation of Rock in Compression. *J. Geophys. Res.* **1968**, *73*, 1417–1432. [CrossRef]
49. Liu, M.; Lu, J.; Ming, P.; Song, J. AE-Based Damage Identification of Concrete Structures under Monotonic and Fatigue Loading. *Constr. Build. Mater.* **2023**, *377*, 131112. [CrossRef]
50. Shi, Z.; Li, J.; Wang, J. Effect of Creep Load on Fatigue Behavior and Acoustic Emission Characteristics of Sandstone Containing Pre-Existing Crack during Fatigue Loading. *Theor. Appl. Fract. Mech.* **2022**, *119*, 103296. [CrossRef]
51. Zhang, Q.; Zhang, X.-P. A Numerical Study on Cracking Processes in Limestone by the B-Value Analysis of Acoustic Emissions. *Comput. Geotech.* **2017**, *92*, 1–10. [CrossRef]
52. Sagasta, F.; Zitto, M.E.; Piotrkowski, R.; Benavent-Climent, A.; Suarez, E.; Gallego, A. Acoustic Emission Energy B-Value for Local Damage Evaluation in Reinforced Concrete Structures Subjected to Seismic Loadings. *Mech. Syst. Signal Process.* **2018**, *102*, 262–277. [CrossRef]
53. Wang, Y.; Han, J.Q.; Song, Z.Y.; Zhu, C. Macro-Meso Failure Behavior of Pre-Flawed Hollow-Cylinder Granite under Multi-Level Cyclic Loads: Insights from Acoustic Emission and Post-Test CT Scanning. *Eng. Fract. Mech.* **2021**, *258*, 108074. [CrossRef]
54. Lockner, D. The Role of Acoustic Emission in the Study of Rock Fracture. *Int. J. Rock Mech. Min. Sci. Geomech. Abstr.* **1993**, *30*, 883–899. [CrossRef]
55. Song, D.; Wang, E.; Song, X.; Jin, P.; Qiu, L. Changes in Frequency of Electromagnetic Radiation from Loaded Coal Rock. *Rock Mech. Rock Eng.* **2016**, *49*, 291–302. Available online: https://link.springer.com/article/10.1007/s00603-015-0738-6 (accessed on 21 June 2023). [CrossRef]
56. Soulioti, D.; Barkoula, N.M.; Paipetis, A.; Matikas, T.E.; Shiotani, T.; Aggelis, D.G. Acoustic Emission Behavior of Steel Fibre Reinforced Concrete under Bending. *Constr. Build. Mater.* **2009**, *23*, 3532–3536. [CrossRef]
57. Aggelis, D.G. Classification of Cracking Mode in Concrete by Acoustic Emission Parameters. *Mech. Res. Commun.* **2011**, *38*, 153–157. [CrossRef]

water

Article

Effect of Confining Pressure on CO_2-Brine Relative Permeability Characteristics of Sandstone in Ordos Basin

Ligen Tang [1,2], Guosheng Ding [1,2], Shijie Song [3], Huimin Wang [3], Wuqiang Xie [3], Yiyang Zhou [4], Zhiyong Song [4], Chiyu Xie [4] and Hongqing Song [4,*]

[1] Research Institute of Petroleum Exploration & Development, PetroChina, Beijing 100083, China
[2] National Energy Underground Gas Storage R&D Center, Beijing 100083, China
[3] Shaanxi Coal and Chemical Industry Group Co., Ltd., Xi’an 710100, China
[4] School of Civil and Resource Engineering, University of Science and Technology Beijing, Beijing 100083, China
* Correspondence: songhongqing@ustb.edu.cn

Abstract: CO_2-brine relative permeability significantly impacts CO_2 injection and is a key parameter for carbon dioxide storage simulation in saline aquifers. In the study of relative permeability, factors such as temperature, pressure, and reservoir rock physical properties play a crucial role. To better understand the impact of confining pressure on the CO_2-brine relative permeability characteristics of sandstone in the Ordos Basin, five sets of CO_2-brine relative permeability data were obtained through unsteady-state displacement tests conducted at various confining pressures ranging from 12 to 20 MPa. The research findings indicate that with an increase in confining pressure there is a slight decrease in irreducible brine saturation. Furthermore, the CO_2 relative permeability in the irreducible brine state decreased by 57% as the pressure increased from 12 MPa to 20 MPa. The study demonstrates notable differences in the CO_2-brine relative permeability curves under varying confining pressure conditions. As the confining pressure increases, the CO_2 relative permeability curve decreases, while the brine relative permeability increases. The change in brine relative permeability is not as pronounced as that of CO_2. These experimental results offer essential support for subsequent numerical calculations and practical applications in engineering. Experimental research holds significant importance in the assessment of storage potential and the prediction of the evolutionary patterns of CO_2 migration.

Keywords: CO_2-brine relative permeability; confining pressure; unsteady-state experiment; Carbon Capture and Storage

Citation: Tang, L.; Ding, G.; Song, S.; Wang, H.; Xie, W.; Zhou, Y.; Song, Z.; Xie, C.; Song, H. Effect of Confining Pressure on CO_2-Brine Relative Permeability Characteristics of Sandstone in Ordos Basin. *Water* **2023**, *15*, 4235. https://doi.org/10.3390/w15244235

Academic Editor: Fernando António Leal Pacheco

Received: 31 October 2023
Revised: 29 November 2023
Accepted: 5 December 2023
Published: 9 December 2023

1. Introduction

Climate change has been identified as one of the most significant global environmental issues due to the continuous increase in carbon dioxide (CO_2) and other greenhouse gas emissions in recent years. Consequently, reducing atmospheric CO_2 content has become a critical area of research within the international scientific community [1]. Carbon Capture and Storage (CCS) technology has emerged as a highly effective method for reducing significant CO_2 emissions into the atmosphere [2]. One of the potential sites for large-scale CO_2 storage is deep saline aquifers. This is because the rocks in saline aquifers are often permeable sandstones, and the depth of the reservoir allows CO_2 to be maintained in a dense supercritical state. In these deep saline aquifers, supercritical CO_2 can be permanently stored through structural, solubility, mineral, and residual trapping mechanisms [3].

The flow and distribution of CO_2 in saline aquifers are highly complex processes influenced by reservoir characteristics, interactions between CO_2 and brine, as well as flow and transport properties [4]. Relative permeability (RP) is an important basic parameter for predicting CO_2 reserves in deep saline aquifers; it significantly affects the CO_2 injection capacity and transportation capacity [5]. Currently, the primary method of obtaining RP is laboratory testing, usually using steady-state and unsteady-state methods [6].

Several studies have reported data on the CO_2-brine RP in common sedimentary formations, including Berea sandstone, carbonate rocks, and other rock types [7–21]. Most of these studies discussed the impacts of temperature, injection pressure, and porosity on RP. Apart from the aforementioned influencing factors, confining pressure (CP) is also an important parameter. Given that the stress state can influence the rock physical properties of the reservoir [22], studying the impact of alterations in CP on RP is essential. In previous studies, research efforts have explored the influence of CP on absolute permeability, and these studies typically arrive at consistent conclusions [23–26]. However, there is limited research focusing on RP, and the existing studies have presented conflicting conclusions regarding the impact of CP on RP.

Fatt [27] was the first to investigate the correlation between RP and CP in sandstone. There are no effects on non-wetting RP at all considering CP. Zhang et al. [28] employed the unsteady-state method and identified significant variations in gas–water two-phase RP curves under various CP conditions. With an increase in CP, the water RP experiences a significant decrease. Additionally, when the water saturation is below 80%, the gas RP exhibits a discernible increasing trend. Liu et al. [29], through experiments, demonstrated that with an increase in CP the gas RP increases while the water RP decreases. Lai and Miskimins [30] observed the influence of CP on the gas–water RP curve through experiments. With an increase in CP, the gas RP decreases significantly, whereas the water RP shows minimal change. Thomas and Ward [31] believed that the RP of both the gas and water phases would remain unaffected by changes in CP. It is evident that researchers hold varying opinions on the impact of CP on RP, and there are very limited studies on the effect of CP on CO_2-brine RP. There are numerous factors influencing the RP of two-phase fluids, encompassing temperature, pressure, rock type, wettability, and interfacial tension [32–34]. Changes in CP can modify pore properties, wettability, and interfacial tension within rocks, thereby inducing notable correlations in the two-phase fluid flow characteristics and varying CPs [35,36]. Adenutsi et al. [37] and others conducted comparisons of NMR T2 spectra before and after applying CP, revealing a decrease in pore volume with increasing CP. This corresponding reduction in the local pore throat radius heightens the capillary resistance of the oil phase through the pores, resulting in a diminished RP of the oil phase as CP rises. Lei et al. [38] and Zhang et al. [28] applied fractal theory to investigate the pressure correlation with the RP. The pressure correlation was expounded by analyzing the relationship between fractal dimensions, pore radius ratios, wettability, and RP. Existing studies generally concentrate on a singular factor, and observing changes in pore properties, wettability, and interfacial tension in rocks is challenging. This results in a lack of clarity regarding the potential causes of changes in RP due to variations in CP. Therefore, in the absence of CO_2-brine RP CP correlation data, it is imperative to conduct CO_2-brine RP tests on cores under various CPs. This is crucial for enhancing our understanding of CO_2 storage in saline aquifers, particularly in the geographical locations where the cores are obtained.

This article explores the influence of CP on the CO_2-brine RP characteristics of sandstone in the Ordos Basin. Unsteady-state drainage experiments were performed in five sets under varying CP conditions (12, 14, 16, 18, 20 MPa). The 'J.B.N' method was employed to calculate CO_2-brine RP. The study analyzed the impacts of CP on irreducible brine saturation, CO_2 RP in the irreducible brine state, and CO_2-brine RP curves. The results of the experiments provide necessary data support for numerical calculations of CO_2 storage in saline aquifers.

2. Materials and Methods

2.1. Experimental Sample and Conditions

The experiment was conducted using a natural sandstone core extracted from the Yi-Shan slope in the eastern Ordos Basin. Five cores are shown in Figure 1. These were all drilled from the same original full-diameter core. Each core is approximately 2.5 cm in diameter and 6.0 cm in length. The five cores were tested for their porosity and single-phase gas permeability. Detailed information on the size, porosity, and permeability of each core sample is given in Table 1.

Figure 1. Five cores for CO_2-brine relative permeability experiments, numbered as 1-1, 1-2, 1-3, 1-4, and 1-5, respectively.

Table 1. Detailed information on experimental cores.

Core Number	Length/cm	Diameter/cm	Porosity/%	Dry Weight/g	Permeability/mD
1-1	5.965	2.502	8.9	69.89	97
1-2	5.977	2.506	8.4	70.95	101
1-3	5.965	2.502	8.4	70.28	103
1-4	5.965	2.502	8.1	70.33	97
1-5	5.977	2.506	8.4	70.95	101

An incubator was used in the experiment to maintain a constant temperature of 70 °C, representing the formation temperature. The core holder's inlet pressure was kept at 10 MPa by a constant speed and constant pressure pump. Meanwhile, the back pressure pump maintained the outlet pressure at 8 MPa. The pressure difference between the core's inlet and outlet was always maintained at 2 MPa. Therefore, the physical properties of brine and CO_2 were determined based on the temperature and average core pressure (9 MPa). The salinity of brine is 23.5 g/L, density is 0.984 $g \cdot cm^{-3}$, and viscosity is 0.415 mpa·s at 70 °C [39,40]. For temperatures (T) and pressures (P) exceeding the critical point (Tc = 31.1 °C and Pc = 7.38 MPa), CO_2 exists in the supercritical phase, exhibiting gas-like behavior while possessing the density of a liquid. Therefore, CO_2 is in a supercritical state at a temperature of 70 °C and a pressure of 9 MPa, with a density of 0.208 $g \cdot cm^{-3}$ and a viscosity of 0.021 mpa·s. Five sets of CP conditions were established, namely 12 MPa, 14 MPa, 16 MPa, 18 MPa, and 20 MPa.

2.2. Experimental Equipment and Process

2.2.1. Experimental Setup

Figure 2 illustrates the experimental setup for unsteady CO_2-brine RP testing. The system comprises a CO_2 storage tank, constant speed and constant pressure pump, pressure gauge, incubator, core holder, CP pump, back pressure valve, back pressure pump, gas–liquid separator, and gas–water metering device. The main equipment for the experiment is divided into a core holder, various pressurization devices, and experimental measurement instruments. The core holder fixes the core through the clamping heads at both ends and the rubber sleeve in the middle. The inlet is connected to a CO_2 storage tank and a constant speed and constant pressure pump to provide CO_2 injection pressure, set at 10 MPa for this experiment. The outlet is connected to a back pressure valve and a back pressure pump to maintain the outlet pressure. In the middle of the core holder, there is a connection for a CP pump, which supplies CP by injecting water into the rubber sleeve's outer periphery, simulating the reservoir pressure of the saline aquifer. It can provide five sets of CP conditions from 12 MPa to 20 MPa. After the back pressure valve, the experimental measurement instruments are connected, including a gas–liquid separator, a graduated cylinder, and a gas flow meter, used to measure fluid flow rate.

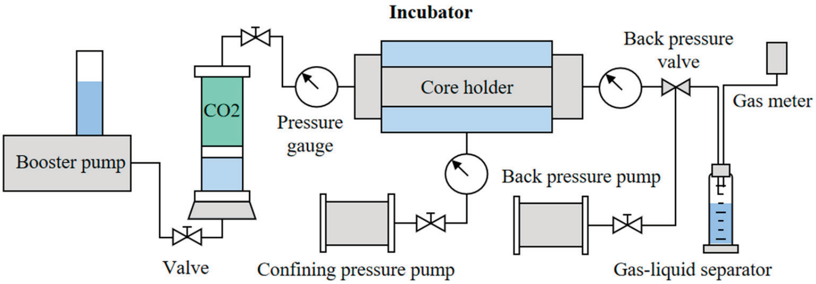

Figure 2. CO_2-brine relative permeability test flow chart.

2.2.2. Experimental Process

In this study, the CO_2-brine RP was measured using the unsteady-state method. Compared with the steady-state method, which is more accurate but also more time-consuming and expensive, the unsteady-state method allows for a significantly shorter experimental time frame. To generate RP curves, different ratios of fluid injection were used to obtain multiple data points [41]. The steady-state method involves the simultaneous injection of CO_2 and brine into the core, which does not reflect the actual injection scenario for CO_2 saline aquifer storage [42]. In contrast, the unsteady-state method displaces one fluid with another, allowing for continuous changes in fluid saturation. This approach better simulates the actual flow conditions of reservoir storage in saline aquifers.

Two types of RP affect CO_2 migration, namely drainage and imbibition RP [43]. This article focuses on the RP of drainage, which corresponds to the injection stage of the geological storage project. The design method of this experiment only obtains the RP of CO_2-displaced brine at irreducible water saturation, that is, the drainage RP.

(a) Dry the core at 60 °C for 24 h and weigh it. Pump to vacuum, then saturate the core with brine. Weigh the rock samples saturated with brine to calculate the effective pore volume of the core.

(b) Before experimenting, CO_2 needs to be pressurized. Open the outlet valve of the CO_2 cylinder to allow CO_2 to enter the piston container. Close the inlet valve of the container and utilize a booster pump to pressurize the CO_2 to the required pressure for the displacement experiment.

(c) Load the rock sample saturated with brine into the core holder. Utilize the CP and back pressure device to apply the necessary back pressure and CP to both ends and to the middle section of the core holder. After completing the pressurization, activate the heating device and maintain the instrument at the experiment's required temperature conditions for 2 h before commencing the experiment.

(d) Activate the booster pump and apply a specific injection pressure to enable the formation brine to pass through the rock sample. Once the pressure difference and flow rate at both ends of the inlet and outlet of the rock sample stabilize, record the flow value.

(e) Utilize the CO_2 displacement brine method and record the time, cumulative brine production, CO_2 production, and pressure conditions at both ends of the rock sample until no brine is produced (visual observation). Reach the irreducible brine state, establish the irreducible brine saturation of the core sample, and measure the effective permeability of the CO_2 in this irreducible brine state.

2.3. Experimental Data Processing Methods

The experiment uses the unsteady-state method to conduct a constant pressure drop CO_2 displacement brine test on the core. Record the flow rate of each fluid at the core outlet. The CO_2-brine RP is calculated using the 'J.B.N' method [44,45]. The method is as follows.

Due to compressibility, the average volume flow rate needs to be used to correct the total fluid production according to Equation (1):

$$\mathrm{V}_t = \Delta\mathrm{V}_w + \mathrm{V}_{t-1} + \frac{2\mathrm{P}_a}{\Delta\mathrm{P} + 2\mathrm{P}_a}\Delta\mathrm{V}_g \tag{1}$$

where V_t denotes the cumulative flow rate of each fluid at time t, mL; V_{t-1} is the cumulative flow rate of each fluid at time $t-1$, mL; $\Delta\mathrm{V}_w$ is the increased flow rate of brine from $t-1$ to time t, mL; P_a is the value of atmospheric pressure; $\Delta\mathrm{P}$ is the value of the displacement pressure difference; and $\Delta\mathrm{V}_g$ represents the measured increase in CO_2 flow rate over a specific time interval under atmospheric pressure, expressed in mL.

After correcting the cumulative CO_2 and brine flow rate according to Equation (1), use Equations (2)–(6) to calculate the unsteady gas-water RP:

$$f_w(S_g) = \frac{d\overline{V_w}(t)}{d\overline{V}(t)} \tag{2}$$

$$K_{rw} = f_w(S_g)\frac{d\left[1/\overline{V}(t)\right]}{d\left\{1/\left[I\cdot\overline{V}(t)\right]\right\}} \tag{3}$$

$$K_{rg} = K_{rw}\frac{\mu_g}{\mu_w}\frac{1-f_w(S_g)}{f_w(S_g)} \tag{4}$$

$$I = (Q(t)/Q_0)(\Delta P_0/\Delta P_t) \tag{5}$$

$$S_g = \overline{V_w}(t) - \overline{V}(t)f_w(S_g) \tag{6}$$

where $f_w(S_g)$ denotes the moisture content; $\overline{V_w}(t)$ represents the dimensionless cumulative brine flow rate, expressed as pore volume fraction; $\overline{V}(t)$ is the dimensionless cumulative CO_2 and brine flow rate; K_{rw} and K_{rg} are the RP of CO_2 and brine, respectively; I is the relative injection capability; Q_0 and $Q(t)$ are the brine flow rate at the core outlet at the initial time and time t, respectively, cm^3/s; ΔP_0 and ΔP_t are the driving pressure drop at the initial time and time t, respectively, MPa. In constant pressure drop displacement experiments, ΔP_0 and ΔP_t are equal. S_g is the CO_2 saturation at the core outlet.

3. Results and Discussion

3.1. Relative Permeability Results for Five Sets of Confining Pressure Conditions

Five sets of CO_2-brine RP were obtained through unsteady-state displacement tests conducted at various CPs ranging from 12 to 20 MPa. The experimental data of CO_2-brine RP at various CPs were calculated using the 'J.B.N' method.

The experimental data were fitted using the Corey model and the Van Genuchten modified model. The basic expression of the Corey model is as follows [46,47]:

$$K_{rw} = K_{rw}\left(S_{gr}\right)\left(\frac{S_w - S_{wr}}{1 - S_{wr} - S_{gr}}\right)^a, \tag{7}$$

$$K_{rg} = K_{rg}(S_{wr})\left(\frac{1 - S_w - S_{gr}}{1 - S_{wr} - S_{gr}}\right)^b \tag{8}$$

where S_{gr} is the irreducible CO_2 saturation and $K_{rw}\left(S_{gr}\right)$ is the RP of brine in the irreducible CO_2 state; similarly, S_{wr} is the irreducible brine saturation, and $K_{rg}(S_{wr})$ is the CO_2 RP in the irreducible brine state. Since the experiment is a drainage process, $S_{gr} = 0$ and $\mathrm{K}_{rw}\left(S_{gr}\right) = 1$ are taken.

The expression of the Van Genuchten modified model is as follows [48]:

$$S^* = (S_w - S_{wr})/(1 - S_{wr}), \tag{9}$$

$$K_{rw} = \sqrt{S^*}[1 - (1 - S^{*1/\lambda})^\lambda]^2 \tag{10}$$

$$K_{rg} = K_{rg}(S_{wr})(1 - S^*)^\gamma(1 - S^{*1/\lambda})^{2\lambda}, \tag{11}$$

Core 1-1 was used for a displacement experiment under a CP of 12 MPa. After processing the experimental data, the irreducible brine saturation was 0.171, and the CO_2 RP under irreducible brine saturation was 0.258. Figure 3 shows the experimental results of CO_2-brine RP, which were fitted using the Corey model—with parameters a = 7.661, b = 3.251—and plotted as the black curve. The Van Genuchten modified model was also used for fitting with parameters of γ = 2.761 and λ = 0.591. The resulting curve is shown in red in Figure 3.

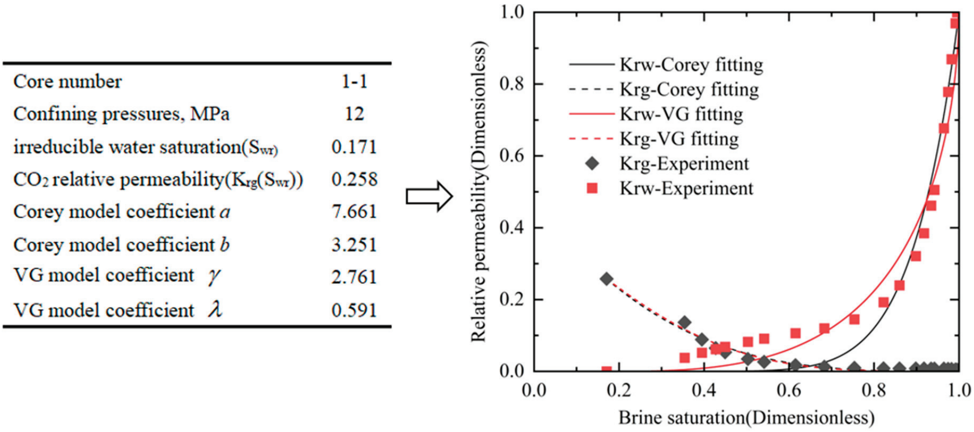

Core number	1-1
Confining pressures, MPa	12
irreducible water saturation(S_{wr})	0.171
CO_2 relative permeability($K_{rg}(S_{wr})$)	0.258
Corey model coefficient a	7.661
Corey model coefficient b	3.251
VG model coefficient γ	2.761
VG model coefficient λ	0.591

Figure 3. Results from experiments and model-fitting for relative permeability under a confining pressure of 12 MPa.

Core 1-2 was used for a displacement experiment under a CP of 14 MPa. The irreducible brine saturation was 0.143, with the CO_2 RP under irreducible brine saturation measured at 0.230. Corey model parameters were found to be a = 5.959 and b = 3.280. Additionally, the Van Genuchten parameters were determined as γ = 2.704 and λ = 0.632. Experimental and model-fitting results are depicted in Figure 4.

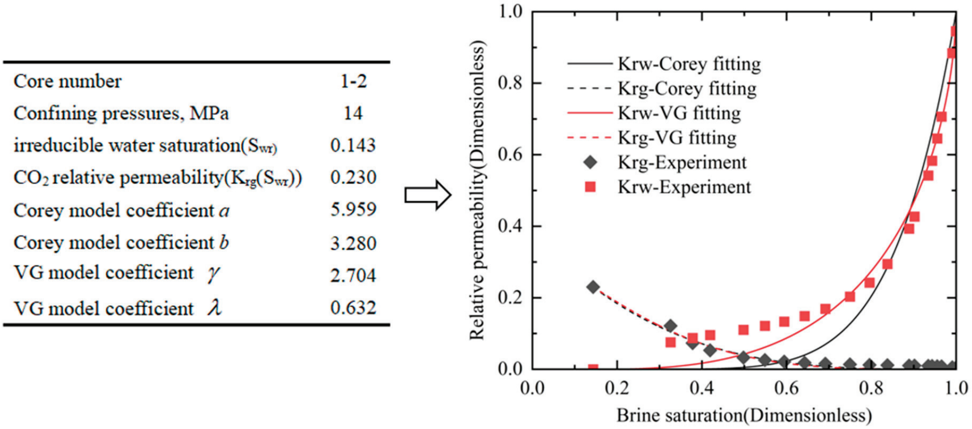

Core number	1-2
Confining pressures, MPa	14
irreducible water saturation(S_{wr})	0.143
CO_2 relative permeability($K_{rg}(S_{wr})$)	0.230
Corey model coefficient *a*	5.959
Corey model coefficient *b*	3.280
VG model coefficient γ	2.704
VG model coefficient λ	0.632

Figure 4. Results from experiments and model-fitting for relative permeability under a confining pressure of 14 MPa.

Core 1-3 was used for a displacement experiment under a CP of 16 MPa. Irreducible brine saturation was 0.138 and CO_2 RP under irreducible brine saturation was 0.166. Corey model parameters were $a = 5.979$ and $b = 2.887$. Van Genuchten parameters were $\gamma = 2.267$ and $\lambda = 0.635$. The results from experiments and model-fitting for RP are shown in Figure 5.

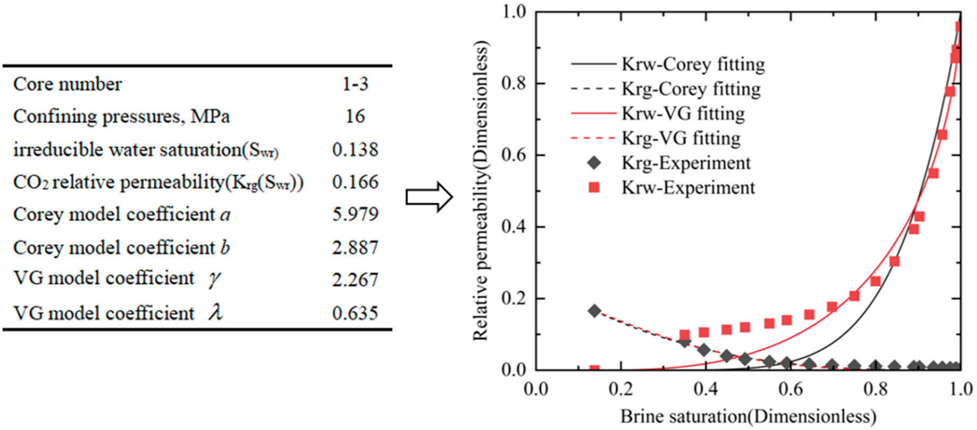

Core number	1-3
Confining pressures, MPa	16
irreducible water saturation(S_{wr})	0.138
CO_2 relative permeability($K_{rg}(S_{wr})$)	0.166
Corey model coefficient *a*	5.979
Corey model coefficient *b*	2.887
VG model coefficient γ	2.267
VG model coefficient λ	0.635

Figure 5. Results from experiments and model-fitting for relative permeability under a confining pressure of 16 MPa.

Core 1-4 was used for a displacement experiment under a CP of 18 MPa. Irreducible brine saturation was 0.136 and CO_2 RP under irreducible brine saturation was 0.117. Corey model parameters were $a = 5.591$ and $b = 2.796$. Van Genuchten parameters were $\gamma = 2.199$ and $\lambda = 0.644$. The results from experiments and model-fitting for RP are shown in Figure 6.

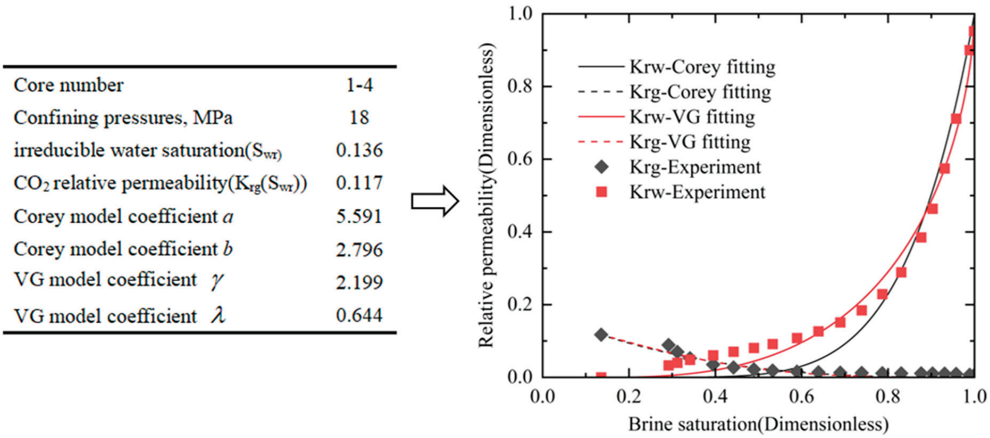

Core number	1-4
Confining pressures, MPa	18
irreducible water saturation(S_{wr})	0.136
CO_2 relative permeability($K_{rg}(S_{wr})$)	0.117
Corey model coefficient *a*	5.591
Corey model coefficient *b*	2.796
VG model coefficient γ	2.199
VG model coefficient λ	0.644

Figure 6. Results from experiments and model-fitting for relative permeability under a confining pressure of 18 MPa.

Core 1-5 was used for a displacement experiment under a CP of 20 MPa. Irreducible brine saturation was 0.133 and CO_2 RP under irreducible brine saturation was 0.110. Corey model parameters were $a = 5.494$ and $b = 2.814$. Van Genuchten parameters were $\gamma = 2.124$ and $\lambda = 0.668$. Experimental and model-fitting results are shown in Figure 7.

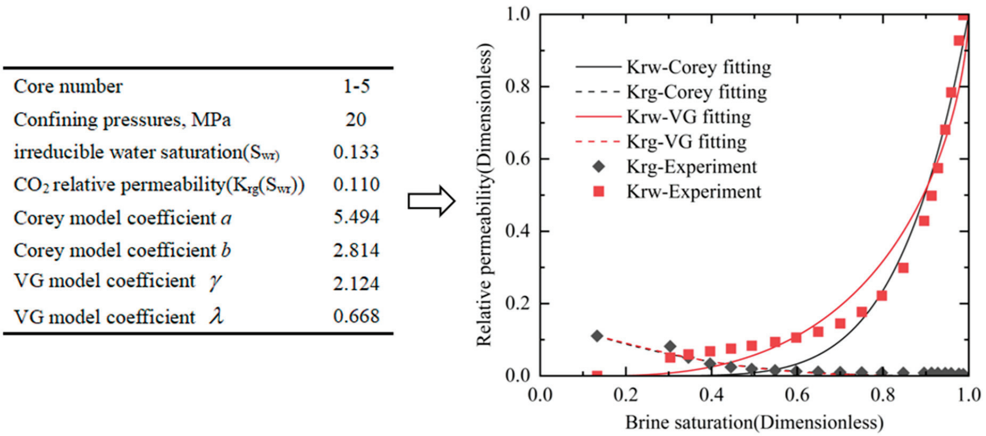

Core number	1-5
Confining pressures, MPa	20
irreducible water saturation(S_{wr})	0.133
CO_2 relative permeability($K_{rg}(S_{wr})$)	0.110
Corey model coefficient *a*	5.494
Corey model coefficient *b*	2.814
VG model coefficient γ	2.124
VG model coefficient λ	0.668

Figure 7. Results from experiments and model-fitting for relative permeability under a confining pressure of 20 MPa.

Based on the images of the results, differences were found in the accuracy of the models used to determine the RP of CO_2 and brine. Both fitting models agree with the experimental results of CO_2 RP. The Van Genuchten modified model was found to be more consistent with experimental results when calculating brine RP. As the CP increased, the coefficient λ in the model also increased, while γ decreased gradually.

The resulting curve in the study clearly shows the process of core drainage, where CO_2 gradually replaces brine in the saturated core, resulting in a decrease in brine saturation. With the decrease in brine saturation, CO_2 RP increases while brine RP decreases gradually. On the left side of the isotonic point, as brine saturation decreases, CO_2 RP increases rapidly. Conversely, on the right side of the isotonic point, as brine saturation increases, brine RP increases rapidly. When brine saturation decreases to the irreducible state, CO_2 RP reaches the maximum while brine RP decreases to 0.

3.2. Effects of Confining Pressures on Irreducible Water Saturation

Irreducible brine refers to the immobile water adsorbed on rock surfaces and trapped in rock pores and throats [49]. Irreducible brine saturation (S_{wr}) is a crucial parameter in reservoir evaluation, directly influencing permeability prediction models and reserve estimations [50]. In the displacement experiment, irreducible brine saturation is reached when the core stops producing brine. The core is weighed, and irreducible brine saturation is calculated.

This study investigates the impact of various CP conditions on irreducible brine saturation. Figure 8 depicts the irreducible brine saturation under varying CP conditions. It can be observed that with the increase in CP, there is a slight decrease in irreducible brine saturation. The elevated CP can alter the rock pore structure [51,52]. Higher pressure may compress larger pores, forming smaller capillary pores, thereby reducing the retention of irreducible brine [53]. This alteration in pore structure might be a primary reason for the decrease in irreducible brine saturation.

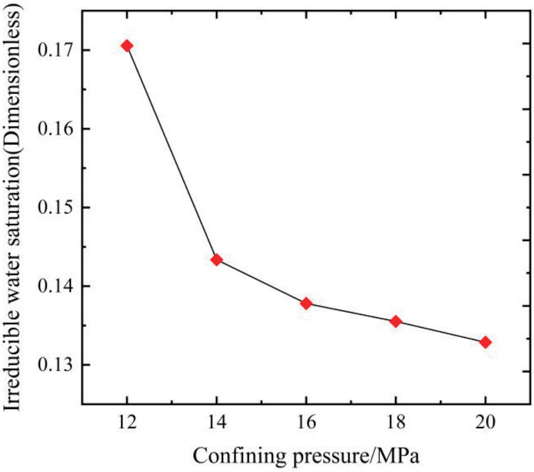

Figure 8. Relationship between irreducible water saturation and confining pressure.

3.3. Effect of Confining Pressure on CO_2 Relative Permeability in the Irreducible Water State

The relationship between CO_2 RP and CP in the irreducible brine state was studied and the results are presented in Figure 9. The experimental findings indicated that as the CP increased from 12 MPa to 14 MPa while in the irreducible water state, the CO_2 RP decreased considerably. However, as the CP was further increased to 20 MPa, the decrease in the CO_2 RP was relatively small.

This phenomenon may be due to alterations in the rock pore structure induced by CP, involving a decrease in pore size and the development of capillary pores [54,55]. Certain larger pores transform into capillary pores with water-binding potential [37]. This shift in pore structure hinders CO_2 flow, causing a decline in CO_2 RP. Simultaneously, the reduction in the pore throat radius results in increased capillary forces. This augmented capillary force hinders CO_2 from displacing bound water, further diminishing the CO_2 RP. The effect of pore structure compression might have been significant under the 14 MPa CP. Consequently, under the 20 MPa CP the alteration in pore structure has a relatively minor impact on CO_2 RP.

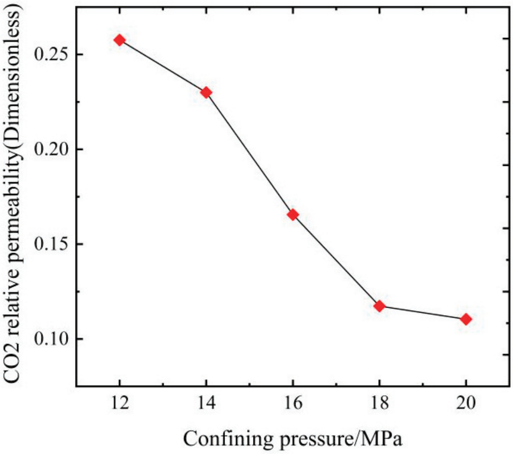

Figure 9. Relationship between CO_2 relative permeability and confining pressure in the irreducible water state.

3.4. Effect of Confining Pressure on CO_2-Brine Relative Permeability Curve

Figure 10 illustrates the CO_2-brine RP curves fitted by five sets of Van Genuchten modified models. The results show significant variations in the CO_2-brine RP curves depending on the CP. The CO_2 RP curve decreases as the CP increases, while the brine RP increases. Specifically, as the pressure was raised from 12 MPa to 20 MPa, the CO_2 RP in the irreducible brine state decreased by 57%. However, the change in brine RP is not as noticeable as that of CO_2. The reduction in CO_2 RP is more apparent when the brine saturation is below the isotonic point saturation. Figure 10's right image provides an enlarged view of the isotonic point area of the RP curve. The isotonic point shifts progressively to the left with increasing CP, while the brine saturation corresponding to the isotonic point decreases. This decrease significantly hampers CO_2 flow.

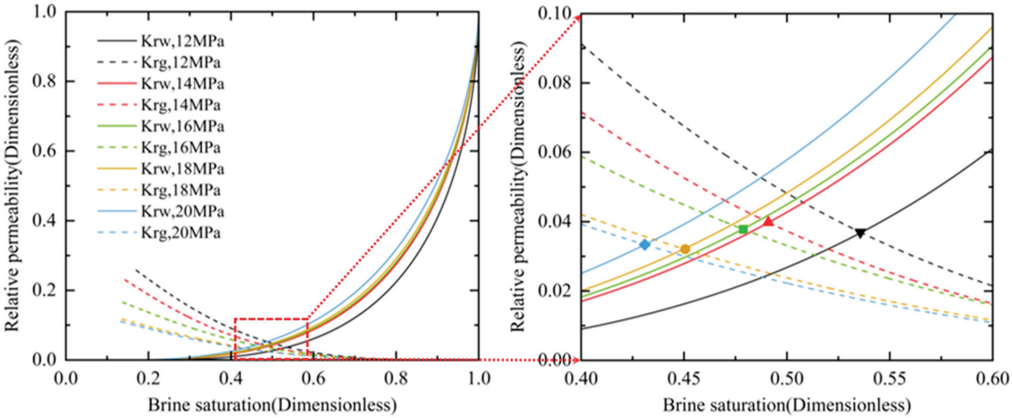

Figure 10. CO_2-brine relative permeability under different confining pressures.

The observed results may be attributed to changes in CP altering rock properties, thereby influencing the RP magnitude [9,56]. These rock properties encompass wettability and pore characteristics. Wettability plays a pivotal role in RP; a shift in rock wettability from strongly water-wetting to gas-wetting leads to a decrease in the RP of gas and an increase in the RP of water [57]. Research on wettability in saline aquifers indicates that increased pressure enhances the wettability of CO_2 [58,59]. Wettability governs the distribution and flow of CO_2 and brine in rock pores. An escalation in CP transforms wettability from water-wetting to mixed-wetting to CO_2-wetting, ultimately resulting in a decrease in the RP of CO_2. Beyond altering wettability, CP may also impact the pore properties of the rock, including porosity, pore size distribution, pore geometry, and pore connectivity. Investigations into CO_2-brine two-phase RP reveal a significant decrease in the RP of CO_2 with decreasing porosity [60]. An increase in CP compacts sand grains, leading to a denser core structure, reduced pore volumes, smaller pore throat sizes, and diminished porosity [61,62]. Small pores are occupied by the wetting phase, forming a thin film on rock particle surfaces. The non-wetting phase occupies larger pores' central region [63,64]. With rising CP, core pore volume decreases, causing pore fluids to redistribute. Some larger pores that originally allowed the unrestricted flow of the non-wetting phase gradually shrink, becoming pores bound by the wetting phase [65]. As the number of pores capable of binding the wetting phase increases, the number of pores permitting non-wetting phase flow decreases. As the CP increases, the local pore throat size decreases, resulting in higher capillary resistance when the non-wetting phase passes through the pore throat. This makes it more challenging for the non-wetting phase to traverse the pores. Consequently, with the increase in CP, the RP of CO_2 decreases. Pore connectivity similarly influences RP [66–68], as fluid can efficiently flow only through connected pores. An increase in CP may isolate pores that were previously interconnected, disrupting fluid flow and decreasing the RP of the terminal gas, even as the final gas saturation increases.

Figure 11 demonstrates that when water saturation is below 80% the ratio of gas RP to water RP (K_{rg}/K_{rw}) decreases as CP increases. The intersection point between the horizontal line and the curve in the figure represents the isotonic point. The brine saturation corresponding to the isotonic point decreases. This suggests that the increase in CP has a more significant impact on gas RP than it does on brine RP.

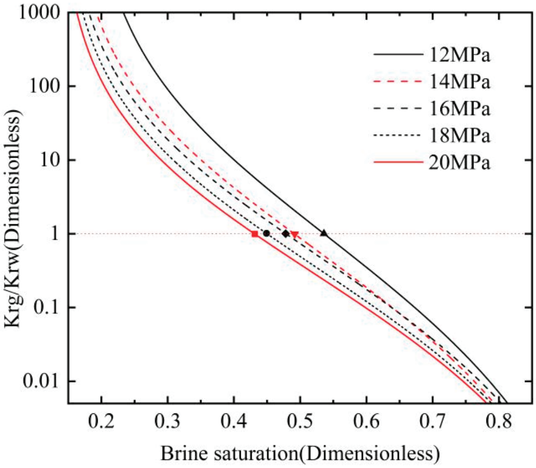

Figure 11. Relationship between relative permeability ratio K_{rg}/K_{rw} and brine saturation under different confining pressures.

Compared with CO_2, the mobility of brine within the core is less influenced by CP. Water molecules may interact with the solid particle surfaces in the formation, and they are more prone to forming water films within the formation pores [69]. At low CP, water molecules can already flow relatively freely in the pores, and increasing the CP has little effect on brine RP.

4. Conclusions

Five sets of unsteady-state drainage experiments were conducted using natural sandstone cores in the Ordos Basin under different CP conditions (12, 14, 16, 18, 20 MPa). The 'J.B.N' method was used to calculate the relative permeability of CO_2-brine. Relative permeability curves for the CO_2-brine system at various confining pressures were plotted. Analyses of confining pressure effects on irreducible brine saturation, CO_2 relative permeability in the irreducible brine state, and CO_2-brine relative permeability curves were conducted.

The research results show that for the sandstone in the Ordos Basin in this study, as the confining pressure increases irreducible brine saturation slightly decreases. As the confining pressure was raised from 12 MPa to 20 MPa, the CO_2 relative permeability in the irreducible brine state decreased by 57%. The results reveal notable differences in the CO_2-brine relative permeability curves at various confining pressures. As the confining pressure increases, the CO_2 relative permeability curve decreases, while the brine relative permeability increases. The change in brine relative permeability is not as pronounced as that of CO_2.

Author Contributions: Conceptualization, L.T. and G.D.; methodology, H.W.; validation, W.X., L.T. and Y.Z.; formal analysis, S.S.; investigation, Z.S.; resources, H.S.; data curation, C.X.; writing—original draft preparation, Y.Z.; writing—review and editing, G.D.; visualization, H.W.; supervision, H.S.; project administration, L.T. All authors have read and agreed to the published version of the manuscript.

Funding: This study was funded by the National Natural Science Foundation of China (Grant No. 52274027 and No. 11972073).

Data Availability Statement: The data is available from the corresponding author on reasonable request.

Conflicts of Interest: Authors Shijie Song, Huimin Wang and Wuqiang Xie were employed by the company Shaanxi Coal and Chemical Industry Group Co., Ltd. The remaining authors declare that the research was conducted in the absence of any commercial or financial relationships that could be construed as a potential conflict of interest.

References

1. Hansen, J.; Johnson, D.; Lacis, A.; Lebedeff, S.; Lee, P.; Rind, D.; Russell, G. Climate impact of increasing atmospheric carbon dioxide. *Science* **1981**, *213*, 957–966. [CrossRef] [PubMed]
2. Leung, D.Y.; Caramanna, G.; Maroto-Valer, M.M. An overview of current status of carbon dioxide capture and storage technologies. *Renew. Sustain. Energy Rev.* **2014**, *39*, 426–443.
3. Kumar, S.; Foroozesh, J.; Edlmann, K.; Rezk, M.G.; Lim, C.Y. A comprehensive review of value-added CO_2 sequestration in subsurface saline aquifers. *J. Nat. Gas Sci. Eng.* **2020**, *81*, 103437. [CrossRef]
4. Cui, G.; Wang, Y.; Rui, Z.; Chen, B.; Ren, S.; Zhang, L. Assessing the combined influence of fluid-rock interactions on reservoir properties and injectivity during CO_2 storage in saline aquifers. *Energy* **2018**, *155*, 281–296. [CrossRef]
5. Xie, C.; Zhu, J.; Yang, H.; Wang, J.; Liu, L.; Song, H. Relative permeability curve prediction from digital rocks with variable sizes using deep learning. *Phys. Fluids* **2023**, *35*, 096605. [CrossRef]
6. Honarpour, M.M. *Relative Permeability of Petroleum Reservoirs*; CRC Press: Boca Raton, FL, USA, 2018.
7. Al-Menhali, A.; Niu, B.; Krevor, S. Capillarity and wetting of carbon dioxide and brine during drainage in b erea sandstone at reservoir conditions. *Water Resour. Res.* **2015**, *51*, 7895–7914. [CrossRef]
8. Bachu, S.; Bennion, B. Effects of in-situ conditions on relative permeability characteristics of CO_2-brine systems. *Environ. Geol.* **2008**, *54*, 1707–1722. [CrossRef]
9. Chen, X. Experimental Studies on CO_2-Brine-Decane Relative Permeabilities in Berea Sandstone with New Steady-State and Unsteady-State Methods. Doctoral Dissertation, UT Austin, Austin, TX, USA, 2016.
10. Levine, J.S.; Goldberg, D.S.; Lackner, K.S.; Matter, J.M.; Supp, M.G.; Ramakrishnan, T.S. Relative permeability experiments of carbon dioxide displacing brine and their implications for carbon sequestration. *Environ. Sci. Technol.* **2014**, *48*, 811–818. [CrossRef]
11. Krevor, S.C.; Pini, R.; Zuo, L.; Benson, S.M. Relative permeability and trapping of CO_2 and water in sandstone rocks at reservoir conditions. *Water Resour. Res.* **2012**, *48*. [CrossRef]
12. Manceau, J.C.; Ma, J.; Li, R.; Audigane, P.; Jiang, P.X.; Xu, R.N.; Tremosa, J.; Lerouge, C. Two-phase flow properties of a sandstone rock for the CO_2/water system: Core-flooding experiments, and focus on impacts of mineralogical changes. *Water Resour. Res.* **2015**, *51*, 2885–2900. [CrossRef]

13. Pini, R.; Krevor, S.C.; Benson, S.M. Capillary pressure and heterogeneity for the CO_2/water system in sandstone rocks at reservoir conditions. *Adv. Water Resour.* **2012**, *38*, 48–59. [CrossRef]
14. Akbarabadi, M.; Piri, M. Relative permeability hysteresis and capillary trapping characteristics of supercritical CO_2/brine systems: An experimental study at reservoir conditions. *Adv. Water Resour.* **2013**, *52*, 190–206. [CrossRef]
15. Chen, X.; DiCarlo, D.A. A new unsteady-state method of determining two-phase relative permeability illustrated by CO_2-brine primary drainage in berea sandstone. *Adv. Water Resour.* **2016**, *96*, 251–265. [CrossRef]
16. Bakhshian, S.; Hosseini, S.A.; Lake, L.W. CO_2-brine relative permeability and capillary pressure of Tuscaloosa sandstone: Effect of anisotropy. *Adv. Water Resour.* **2020**, *135*, 103464. [CrossRef]
17. Ruprecht, C.; Pini, R.; Falta, R.; Benson, S.; Murdoch, L. Hysteretic trapping and relative permeability of CO_2 in sandstone at reservoir conditions. *Int. J. Greenh. Gas Control* **2014**, *27*, 15–27. [CrossRef]
18. Lee, Y.S.; Kim, K.H.; Lee, T.H.; Sung, W.M.; Park, Y.C.; Lee, J.H. Analysis of CO_2 endpoint relative permeability and injectivity by change in pressure, temperature, and phase in saline aquifer. *Energy Sources Recovery Util. Environ. Eff.* **2009**, *32*, 83–99.
19. Farokhpoor, R.; Lindeberg, E.G.B.; Torsæter, O.; Mørk, M.B.; Mørk, A. Permeability and relative permeability measurements for CO_2-brine system at reservoir conditions in low permeable sandstones in Svalbard. *Greenh. Gases Sci. Technol.* **2014**, *4*, 36–52. [CrossRef]
20. Ren, X.; Li, A.; Memon, A. Experimental Study on Gas–Water Relative Permeability Characteristics of Tight Sandstone Reservoir in Ordos Basin. *Geofluids* **2022**, *2022*, 1521837. [CrossRef]
21. Reynolds, C.; Blunt, M.; Krevor, S. Impact of reservoir conditions on CO_2-brine relative permeability in sandstones. *Energy Procedia* **2014**, *63*, 5577–5585. [CrossRef]
22. Raghavan, R.; Chin, L.Y. Productivity changes in reservoirs with stress-dependent permeability. In *SPE Annual Technical Conference and Exhibition?* SPE: Houston, TX, USA, 2002; p. SPE-77535.
23. Alam, A.B.; Niioka, M.; Fujii, Y.; Fukuda, D.; Kodama, J.I. Effects of confining pressure on the permeability of three rock types under compression. *Int. J. Rock Mech. Min. Sci.* **2014**, *65*, 49–61. [CrossRef]
24. Gobran, B.D.; Brigham, W.E.; Ramey, H.J. Absolute permeability as a function of confining pressure, pore pressure, and temperature. *SPE Form. Eval.* **1987**, *2*, 77–84. [CrossRef]
25. Dong, J.J.; Hsu, J.Y.; Wu, W.J.; Shimamoto, T.; Hung, J.H.; Yeh, E.C.; Wu, Y.H.; Sone, H. Stress-dependence of the permeability and porosity of sandstone and shale from TCDP Hole-A. *Int. J. Rock Mech. Min. Sci.* **2010**, *47*, 1141–1157. [CrossRef]
26. Farrell NJ, C.; Healy, D.; Taylor, C.W. Anisotropy of permeability in faulted porous sandstones. *J. Struct. Geol.* **2014**, *63*, 50–67. [CrossRef]
27. Fatt, I. The effect of overburden pressure on relative permeability. *J. Pet. Technol.* **1953**, *5*, 15–16. [CrossRef]
28. Zhang, X.; Wu, C.; Liu, S. Characteristic analysis and fractal model of the gas–water relative permeability of coal under different confining pressures. *J. Pet. Sci. Eng.* **2017**, *159*, 488–496. [CrossRef]
29. Liu, Y.; Pan, Y.; Zhen, X. Influence of rock stress sensitivity in tight gas reservoir on characteristics of gas/water two phase flows. *Complex Hydrocarb. Reserv.* **2013**, *6*, 36–39.
30. Lai, B.; Miskimins, J.L. A new technique for accurately measuring two-phase relative permeability under non-Darcy flow conditions. *J. Pet. Sci. Eng.* **2015**, *127*, 398–408. [CrossRef]
31. Thomas, R.D.; Ward, D.C. Effect of overburden pressure and water saturation on gas permeability of tight sandstone cores. *J. Pet. Technol.* **1972**, *24*, 120–124. [CrossRef]
32. Esmaeili, S.; Modaresghazani, J.; Sarma, H.; Harding, T.; Maini, B. Effect of temperature on relative permeability—Role of viscosity ratio. *Fuel* **2020**, *278*, 118318. [CrossRef]
33. Owens, W.W.; Archer, D. The effect of rock wettability on oil–water relative permeability relationships. *J. Pet. Technol.* **1971**, *23*, 873–878. [CrossRef]
34. Safaei-Farouji, M.; Thanh, H.V.; Dashtgoli, D.S.; Yasin, Q.; Radwan, A.E.; Ashraf, U.; Lee, K.K. Application of robust intelligent schemes for accurate modelling interfacial tension of CO_2 brine systems: Implications for structural CO_2 trapping. *Fuel* **2022**, *319*, 123821. [CrossRef]
35. Lian, P.; Cheng, L. The characteristics of relative permeability curves in naturally fractured carbonate reservoirs. *J. Can. Pet. Technol.* **2012**, *51*, 137–142. [CrossRef]
36. Zheng, X.; Zhigang, C.; Weichuan, L. Gas/water flowing ability influence experimental study of permeability stress sensibility in tight gas reservoir. *Well Logging Technol.* **2013**, *4*, 360–363.
37. Adenutsi, C.D.; Li, Z.; Xu, Z.; Sun, L. Influence of net confining stress on NMR T2 distribution and two-phase relative permeability. *J. Pet. Sci. Eng.* **2019**, *178*, 766–777. [CrossRef]
38. Lei, G.; Mo, S.; Dong, Z.; Wang CA, I.; Li, W. Theoretical and experimental study on stress-dependency of oil–water relative permeability in fractal porous media. *Fractals* **2018**, *26*, 1840010. [CrossRef]

39. Simion, A.I.; Grigoraş, C.G.; Roşu, A.M.; Gavrilă, L. Mathematical modelling of density and viscosity of NaCl aqueous solutions. *J. Agroaliment. Process. Technol* **2015**, *21*, 41–52.
40. Kestin, J.; Khalifa, H.E.; Correia, R.J. Tables of the dynamic and kinematic viscosity of aqueous NaCl solutions in the temperature range 20–150 C and the pressure range 0.1–35 MPa. *J. Phys. Chem. Ref. Data* **1981**, *10*, 71–88. [CrossRef]
41. Honarpour, M.; Mahmood, S.M. Relative-permeability measurements: An overview. *J. Pet. Technol.* **1988**, *40*, 963–966. [CrossRef]
42. Müller, N. Supercritical CO_2-brine relative permeability experiments in reservoir rocks—Literature review and recommendations. *Transp. Porous Media* **2011**, *87*, 367–383. [CrossRef]
43. Flett, M.; Gurton, R.; Taggart, I. The function of gas-water relative permeability hysteresis in the sequestration of carbon dioxide in saline formations. In *SPE Asia Pacific Oil and Gas Conference and Exhibition*; OnePetro: Richardson, TX, USA, 2004.
44. Welge, H.J. A simplified method for computing oil recovery by gas or water drive. *J. Pet. Technol.* **1952**, *4*, 91–98. [CrossRef]
45. Johnson, E.F.; Bossler, D.P.; Bossler, V.N. Calculation of relative permeability from displacement experiments. *Trans. AIME* **1959**, *216*, 370–372. [CrossRef]
46. Corey, A.T. The interrelation between gas and oil relative permeabilities. *Prod. Mon.* **1954**, *19*, 38–41.
47. Brooks, R.H.; Corey, A.T. Hydraulic properties of porous media. *Hydrol. Pap.* **1964**, *3*, 1–27.
48. Van Genuchten, M.T. A closed-form equation for predicting the hydraulic conductivity of unsaturated soils. *Soil Sci. Soc. Am. J.* **1980**, *44*, 892–898. [CrossRef]
49. Cheng, Y.; Zhang, C.; Zhu, L.Q. A fractal irreducible water saturation model for capillary tubes and its application in tight gas reservoir. *J. Pet. Sci. Eng.* **2017**, *159*, 731–739. [CrossRef]
50. Chilingarian, G.V.; Torabzadeh, J.; Rieke, H.H.; Metghalchi, M.; Mazzullo, S.J. Interrelationships among surface area, permeability, porosity, pore size, and residual water saturation. In *Developments in Petroleum Science*; Elsevier: Amsterdam, The Netherlands, 1992; Volume 30, pp. 379–397.
51. Luo, N.; Suo, Y.; Fan, X.; Yuan, Y.; Zhai, C.; Sun, W. Research on confining pressure effect of pore structure of coal-rich in coalbed methane under cyclic impact. *Energy Rep.* **2022**, *8*, 7336–7348. [CrossRef]
52. Blanton, T.L. Deformation of chalk under confining pressure and pore pressure. *Soc. Pet. Eng. J.* **1981**, *21*, 43–50. [CrossRef]
53. Zhang, F.; Jiang, Z.; Sun, W.; Li, Y.; Zhang, X.; Zhu, L.; Wen, M. A multiscale comprehensive study on pore structure of tight sandstone reservoir realized by nuclear magnetic resonance, high pressure mercury injection and constant-rate mercury injection penetration test. *Mar. Pet. Geol.* **2019**, *109*, 208–222. [CrossRef]
54. Liu, B.; Ma, Y.; Liu, N.; Han, Y.; Li, D.; Deng, H. Investigation of pore structure changes in Mesozoic water-rich sandstone induced by freeze-thaw process under different confining pressures using digital rock technology. *Cold Reg. Sci. Technol.* **2019**, *161*, 137–149. [CrossRef]
55. Li, Y.; Wu, Y.; Qiao, W.; Zhang, S.; Li, X. The Permeability Evolution of Sandstones with Different Pore Structures under High Confining Pressures, High Pore Water Pressures and High Temperatures. *Appl. Sci.* **2023**, *13*, 1771. [CrossRef]
56. Alizadeh, A.H.; Piri, M. Three-phase flow in porous media: A review of experimental studies on relative permeability. *Rev. Geophys.* **2014**, *52*, 468–521. [CrossRef]
57. Beltrán, A.; Hernández-Díaz, D.; Chávez, O.; García, A.; Mena, B.; Zenit, R. Experimental study of the effect of wettability on the relative permeability for air–water flow through porous media. *Int. J. Multiph. Flow* **2019**, *120*, 103091. [CrossRef]
58. Broseta, D.; Tonnet, N.; Shah, V. Are rocks still water-wet in the presence of dense CO_2 or H_2S? *Geofluids* **2012**, *12*, 280–294. [CrossRef]
59. Iglauer, S. CO_2–water–rock wettability: Variability, influencing factors, and implications for CO_2 geostorage. *Acc. Chem. Res.* **2017**, *50*, 1134–1142. [CrossRef] [PubMed]
60. Bennion, D.B.; Bachu, S. Drainage and imbibition relative permeability relationships for supercritical CO_2/brine and H_2S/brine systems in intergranular sandstone, carbonate, shale, and anhydrite rocks. *SPE Reserv. Eval. Eng.* **2008**, *11*, 487–496. [CrossRef]
61. Pan, L.; Jones, S.J.; Wang, X.; Guan, W.; Li, L. Re-evaluation of the porosity measurements under different confining pressures: A better appraisal of reservoir porosity. *AAPG Bull.* **2019**, *103*, 515–526. [CrossRef]
62. Handin, J.; Hager, R.V., Jr.; Friedman, M.; Feather, J.N. Experimental deformation of sedimentary rocks under confining pressure: Pore pressure tests. *Aapg Bull.* **1963**, *47*, 717–755.
63. Anderson, W.G. Wettability literature survey part 5: The effects of wettability on relative permeability. *J. Pet. Technol.* **1987**, *39*, 1453–1468. [CrossRef]
64. Anderson, W.G. Wettability literature survey-part 6: The effects of wettability on waterflooding. *J. Pet. Technol.* **1987**, *39*, 1605–1622. [CrossRef]
65. Lei, G.; Liao, Q.; Lin, Q.; Zhang, L.; Xue, L.; Chen, W. Stress dependent gas-water relative permeability in gas hydrates: A theoretical model. *Adv. Geo-Energy Res.* **2020**, *4*, 326–338. [CrossRef]
66. Gharbi, O.; Blunt, M.J. The impact of wettability and connectivity on relative permeability in carbonates: A pore network modeling analysis. *Water Resour. Res.* **2012**, *48*. [CrossRef]
67. Berg, S.; Rücker, M.; Ott, H.; Georgiadis, A.; Van der Linde, H.; Enzmann, F.; Kersten, M.; Armstrong, R.T.; de With, S.; Becker, J.; et al. Connected pathway relative permeability from pore-scale imaging of imbibition. *Adv. Water Resour.* **2016**, *90*, 24–35. [CrossRef]

68. He, M.; Zhou, Y.; Wu, K.; Hu, Y.; Feng, D.; Zhang, T.; Liu, Q.; Li, X. Pore network modeling of thin water film and its influence on relative permeability curves in tight formations. *Fuel* **2021**, *289*, 119828. [CrossRef]
69. Kimmel, G.A.; Stevenson, K.P.; Dohnalek, Z.; Smith, R.S.; Kay, B.D. Control of amorphous solid water morphology using molecular beams. I. Experimental results. *J. Chem. Phys.* **2001**, *114*, 5284–5294. [CrossRef]

MDPI
St. Alban-Anlage 66
4052 Basel
Switzerland
www.mdpi.com

MDPI Books Editorial Office
E-mail: books@mdpi.com
www.mdpi.com/books

Academic Open
Access Publishing

mdpi.com

ISBN 978-3-7258-1384-1